The enhanced wave-induced drift of large floating objects



Qian Xiao

Somerville College

University of Oxford

A thesis submitted for the degree of

Doctor of Philosophy

Trinity 2024

The enhanced wave-induced drift of large floating objects

A thesis submitted for the degree of
Doctor of Philosophy at the University of Oxford

By Qian Xiao, Somerville College, Trinity 2024

At the ocean surface, mass, momentum and energy are transferred between the atmosphere and the ocean. Ocean surface waves, in particular, drive the transport of floating objects such as sediments, pollutants, and man-made structures. In irrotational and progressive surface gravity waves, water particles exhibit a non-closed path over one wave cycle, leading to Stokes drift. The drift can be modified, and indeed enhanced, when an object deviates from being an ideal Lagrangian tracer. This thesis examines the wave-induced drift of two-dimensional (2D) floating objects by surface gravity waves, specifically, deep-water regular waves. A combination of analytical, numerical, and experimental approaches are employed to analyze the drift of objects with varying sizes and shapes under different wave steepness.

A hybrid numerical model encompassing both viscosity and diffraction effects is used to investigate the influence of changing size, shape and wave steepness on the object drift. The drift deviates from the standard Stokes drift and depends on objects' size and shape. Larger objects with less streamlined shapes, resembling box-like structures, exhibit enhanced drift. The enhancement is attributed to the standing wave pattern generated as a result of diffraction of the wave field, and viscosity.

A diffraction-modified Stokes drift model is proposed to predict object drift. The model introduces additional terms to the standard Stokes drift, accommodating incident, diffracted, and radiated wave fields. The results are compared to both experimental measurements and numerical results, demonstrating a close agreement when the object is not too large. The model offers an in-depth understanding of one of the mechanisms contributing to drift enhancement.

A 2D experiment has been conducted in a laboratory flume. The floating objects are specially designed to ensure the experiment is two dimensional. The enhanced drift, along with the associated standing wave pattern, predicted by the model is also observed in experimental data, which validates the theoretically predicted enhanced drift. Distinct drift behaviours are identified for small and large objects at low and high wave steepness. The data reveals that the scaling relationship between the object drift and steepness is characterized by a mixture of linear and second-order terms (in steepness) and is dependent on object size.

The influence of object corner shape on drift is further explored using the hybrid numerical model. In particular, the drift of a bluff body with sharp and round corners has been investigated. It is found that an object's sharp corners can induce vorticity and thus change the pressure distribution around the moving objects, resulting in a significantly altered drift trajectory and unsteadiness in the object's drift.

Acknowledgements

First and foremost, I would like to express my deepest gratitude to my supervisors, Prof. Ton S. van den Bremer and Prof. Thomas A. A. Adcock, whose unwavering support and guidance were indispensable throughout my PhD journey. They have not only provided exceptional academic mentorship in completing the research for this thesis but also offered tremendous help to support my mental health, career development, well-being, and overseas life. I appreciate their considerable patience and encouragement, which have been constant pillars in my doctoral life.

This endeavour would not have been possible without the financial support from the China Scholarship Council-PAG Oxford Scholarship and additional funding from the Department of Engineering Science, including from Ton's Royal Academy of Engineering Research Fellowship. I want to express my great gratitude to Prof. Shiqiang Yan from City, University of London for his invaluable suggestions and guidance, particularly during the early stages of my research. I am also deeply thankful to Dr. Mark McAllister, Dr. Ross Calvert, and Dr. Tianning Tang, Dr. Zheng Li from Shanghai Jiao Tong University for the fruitful discussions, insightful suggestions, and useful guidance.

I would like to extend my sincere thanks to Mr. Anton de Fockert, Mr. Wout Bakker and other colleagues during my stay at Deltares, the Netherlands, where I participated in an experimental campaign funded by the European Space Agency and had a first taste of laboratory experiments. Special thanks are due to Mr. Christopher Hatcher for his invaluable assistance in fabricating the wooden objects and for his steadfast companionship throughout the experiments, ensuring safety at every single moment. I cherish the memories of our collaboration and camaraderie. Many thanks to my colleagues at Somerville College and in the Civil Engineering-Waves and Fluid group and the members of my Transfer and Confirmation committee, Prof. Wouter Mostert and Dr. Takafumi Nishino, for their support and encouragement.

As a researcher, student, and individual, I have been fortunate to learn from a diverse array of mentors and peers. I am deeply indebted to Prof. Renchuan Zhu, who taught me how to approach challenges with resilience and creativity, turning a possible dead-end problem into a new start. I am indebted to Prof. Wei Li, who ignited my passion for scientific research and set me on the right track.

I owe a debt of gratitude to my close friends Jiayao Meng, Zhenghao Shao, Aimeng Liu and Hanzhi Jiang for their support and comfort. I extend special gratitude to my sweetie (boyfriend) Yuchao Wang, for turning the bittersweet journey of my PhD life into an epic adventure filled with joy, love and shared dreams. This experience would never have been as pleasant without all their companionship. Lastly, I am very grateful to my parents for their unconditional love.

Contents

1 Introduction **1**

1.1 Background . . . 1

1.2 Object drift velocity . . . 4

1.3 Synopsis . . . 6

1.4 List of publications and author's contribution . . . 12

2 Literature Review **15**

2.1 Overview . . . 15

2.2 Drift of small particles . . . 17

2.3 Drift of small floating objects . . . 18

2.4 Drift of large floating objects . . . 20

2.5 Drift of objects of various sizes . . . 23

2.6 QaleFOAM—hybrid model . . . 25

2.6.1 Qale-FEM . . . 27

2.6.2 Two-phase NS model . . . 28

2.6.3 Coupling scheme . . . 31

3 Surface gravity wave-induced drift of floating objects in the diffraction regime **33**

3.1 Abstract . . . 33

3.2 Introduction . . . 34

3.3 Models . . . 37

3.3.1 Problem formulation . . . 37

3.3.2 Hybrid numerical model: qaleFOAM . . . 39

3.3.3 Diffraction-modified Stokes drift model . . . 40

3.4 Validation and verification of the hybrid numerical model (qaleFOAM) . . . 43

3.4.1 Drift of a Lagrangian particle . . . 43

3.4.2 Drift of very small objects . . . 47

3.5 Results from the hybrid numerical model (qaleFOAM) . . . 47

3.5.1 Effect of size (category I) . . . 49

3.5.2 Effect of shape and submergence depth (category II) . . . 55

3.5.3 Effect of wave steepness (category III) . . . 57

3.5.4 Effects of viscosity (categories I & III) . . . 60

3.5.5 Relationship between local standing wave pattern and the object drift . . 62
3.6 Comparison between the hybrid numerical model and the diffraction-modified Stokes drift model . . . 64
3.6.1 Oscillatory motion . . . 64
3.6.2 Object drift . . . 66
3.7 Conclusions . . . 71

Appendices **74**
3.A Mathematical formulation and verification of the BEM model . . . 74
3.A.1 Radiation potential . . . 74
3.A.2 Diffraction potential . . . 76
3.A.3 Equations of motion . . . 76
3.A.4 Two-dimensional Green's function method . . . 78
3.A.5 Second derivatives of the velocity potential . . . 78
3.A.6 Verification of the BEM model . . . 80
3.B Convergence of the hybrid numerical model (qaleFOAM) . . . 81
3.C Effects of object rotation and density . . . 85
3.D Effects of viscosity and turbulence . . . 85
3.D.1 Reynolds and Keulegan–Carpenter numbers . . . 85
3.D.2 Turbulent simulations . . . 88

4 Laboratory study of the enhanced wave-induced drift of large rectangular floating objects **90**
4.1 Abstract . . . 90
4.2 Introduction . . . 91
4.3 Experimental method . . . 96
4.3.1 Wave flume and camera setup . . . 96
4.3.2 Floating objects . . . 98
4.3.3 Data acquisition . . . 102
4.4 Existing theoretical and empirical models used for comparison . . . 105
4.4.1 The diffraction-modified Stokes drift of Xiao et al. (2024) . . . 106
4.4.2 The empirical model of Harms (1987) . . . 106
4.5 Results and analysis . . . 108
4.5.1 Eulerian-mean background current . . . 109
4.5.2 Effect of object size and wave steepness . . . 110
4.5.3 Comparison with existing theoretical and empirical models . . . 115
4.6 Conclusion . . . 119

Appendices **124**
4.A Photographs of objects with bearings . . . 124
4.B Measurement error and repeatability . . . 124
4.C A new empirical parametrisation for enhanced Stokes object drift . . . 127

5 Vorticity and turbulent effects on mean drift of bluff bodies **129**
5.1 Abstract . . . 129
5.2 Introduction . . . 130
5.3 Numerical model . . . 134
5.4 Convergence study for stationary objects . . . 138
5.5 Validation and verification for small moving objects . . . 141
5.6 Results . . . 144
5.6.1 Analysis of moving objects . . . 145
5.6.2 Analysis of stationary objects . . . 159
5.7 Conclusion . . . 167

Appendices **169**
5.A Spectral analysis of turbulent kinetic energy . . . 169

6 Conclusions and recommendations **172**
6.1 Summary . . . 172
6.2 Research impact . . . 178
6.3 Recommendations for future work . . . 179

References **183**

A Calibration and testing of the new Wave and Current Flume **204**
A.1 Flume Dimensions . . . 204
A.2 Wave properties . . . 206
A.2.1 Reflection analysis . . . 208
A.2.2 1/2 wave height . . . 212
A.2.3 Wave frequency . . . 215
A.2.4 Time variation . . . 216
A.2.5 Lateral variation . . . 222
A.2.6 Repeatability . . . 223

List of Figures

1.1 Two ways to evaluate the horizontal drift velocity based on the horizontal trajectory or Lagrangian velocity: (a) Linear-fit method: Time history of the horizontal trajectory $x_p(t)$ of objects with initial position x_{P0}. (b) Frequency-filter method: Different components of the horizontal Lagrangian velocity of objects. . 7

3.1 Shapes and dimensions of the two objects considered: round-cornered boxes (RCBs) and round objects (ROs). 38

3.2 Domains, domain boundaries and coordinate system used in the hybrid numerical model qaleFOAM. 38

3.3 Domain and coordinate system in the diffraction-modified Stokes drift model for the two objects considered, also showing object dimensions. 38

3.4 Drift of Lagrangian particles in simulations of the hybrid numerical model (qaleFOAM) without viscosity ($\nu = 0$): (a) time history of the horizontal motion of a Lagrangian particle ($x_{L_0} = 22.5$ m, $z_{L_0} = -25.0$ mm) for $\epsilon = 0.034$ for the lower-frequency case in table 3.1, where the theoretical Stokes drift is evaluated using (3.9). The wave amplitude here is $a_w = 20.0$ mm; thus, the vertical position of the particle is always below the trough of the wave. The black dashed line denotes the time at which a quasi-steady state has been achieved and the drift speed has become constant ($t_s = 32$ s). The drift speed in (b) has been obtained from the average speed for $t > t_s$. (b) comparison of non-dimensional drift velocities of a Lagrangian particle $\overline{u}_L/c$ between numerical solutions (red and blue squares) and theoretical Stokes drift (red and blue lines) as a function of wave steepness for higher and lower frequencies, where $c = \omega/k$ is the phase speed of the waves. 46

3.5 Effect of object size on object motion and drift (category I simulations): (a) horizontal oscillatory motion amplitude A_x, normalized by input wave amplitude a_w, as a function of relative object size; (b) vertical oscillatory motion amplitude A_z, normalized by wave amplitude a_w, as a function of relative object size; (c) celerity-normalized object drift u_O/c as a function of relative object size; (d) non-dimensional amplitude of the local surface elevation $a(x)/a_w$ as a function of horizontal distance (scaled by wavenumber) from the centre of mass x_c without viscosity ($\nu = 0$). The gap between the two vertical red lines in (d) represents the position of the object for $l/\lambda = 10\%$ and corresponds to its left and right sides, respectively. The percentage (%) in (d) represents the relative size of the object l/λ. The results for Calvert et al. (2021) in panels (a), (b) and (c) are their results for spheres with equivalent diameter to our round objects. 50

3.6 Effect of the shape of the submerged part of a round-cornered box as determined by the radius of the rounded corner r, scaled by submergence depth h_d, on object motion and drift (category II simulations, group 1): (a) and (b) non-dimensional amplitudes of oscillatory motion in the horizontal and vertical directions, respectively; (c) celerity-normalized object drift velocity; Blue square markers in (a), (b) and (c) represent the results for round-cornered boxes (RCBs). Red lines in (a) and (b) denote the oscillatory motions of a Lagrangian particle, these in (c) denote the theoretical Stokes drift. (d) non-dimensional amplitude of the local surface elevation $a(x)/a_w$ as a function of horizontal distance (scaled by wavenumber) from the centre of mass x_c. The gap between the two vertical red lines in (d) represents the position of the object and corresponds to its left and right sides, respectively. The line denoted by FEM in (d) corresponds to simulations of the incident wave field only. 53

3.7 Effect of the submergence depth h_d of a round-cornered box on object motion and drift (category II, group 2): (a) and (b) non-dimensional amplitudes of oscillatory motion in the horizontal and vertical directions, respectively; (c) celerity-normalized object drift velocity; Blue square markers in (a), (b) and (c) represent the results for round-cornered boxes (RCBs). Red lines in (a) and (b) denote the oscillatory motions of a Lagrangian particle, these in (c) denote the theoretical Stokes drift. (d) non-dimensional amplitude of the local surface elevation $a(x)/a_w$ as a function of horizontal distance (scaled by wavenumber) from the centre of mass x_c. The gap between the two vertical red lines in (d) represents the position of the object and corresponds to its left and right sides, respectively. The line denoted by FEM in (d) corresponds to simulations of the incident wave field only. 54

3.8 Effect of wave steepness on object motion and drift (category III): (a) non-dimensional horizontal oscillatory motion amplitude; (b) non-dimensional vertical oscillatory motion amplitude; (c) celerity-normalized object drift velocity; (d) Stokes drift-normalized object drift velocity; (e) difference between the local wave amplitude distribution $a(x)$ and the input wave amplitude a_w for three different values of wave steepness for the object size of $l/\lambda = 10\%$; (f) normalized local wave amplitude distribution $a(x)/a_w$ for three different values of wave steepness for the object size of $l/\lambda = 10\%$. Diamond, star and square markers represent the results for round-cornered boxes (RCBs) of $l/\lambda = 5\%$, 8%, 10% relative sizes, respectively. Red lines in (a) and (b) denote input wave amplitudes, while in (c) and (d) they denote theoretical Stokes drift. The local wave amplitude distributions $a(x)$ in (e) and (f) are given as functions of horizontal distance (scaled by wavenumber) from the centre of mass x_c, and the gaps between the two vertical red lines in represent the position of the object ($l/\lambda = 10\%$) and correspond to its left and right sides, respectively. 60

3.9 The celerity-normalized object drift u_O/c as a function of the local maximum wave amplitude normalized by the input wave amplitude $a_{\max}/a_w$: (a) the results for the round-cornered boxes and round objects of different sizes (category I simulations); (b) the results for the objects of $l/\lambda = 10\%$ with different round-corner radii and depths of submergence (category II simulations). All results shown are for the same input wave condition: $a_w = 0.02$ m and $u_S/c = 0.0012$. . 63

3.10 Comparison of amplitudes of oscillatory motion for objects of different sizes and shapes predicted by the qaleFOAM (QF) and BEM models for $ka_w = 0.034$: (a) horizontal oscillatory motion; (b) vertical oscillatory motion of objects. Motion amplitudes in (a) and (b) are normalized by input wave amplitude a_w, with the red lines then corresponding to the behaviour of a Lagrangian particle. Lines correspond to the results from BEM simulations, while markers are those from qaleFOAM (QF) simulations. Square markers represent results for boxes, rectangular boxes (RBs) for BEM simulations and round-cornered boxes (RCBs) for qaleFOAM simulations, and circle markers denote round object (ROs). 65

3.11 Phase difference of the oscillatory motion between a finite-size object and a Lagrangian particle as a function of relative object size from BEM simulations: (a) horizontal direction, (b) vertical direction. Blue lines correspond to rectangular boxes and black lines to round objects. 66

3.12 Diffraction-modified Stokes drift velocity $u_{S,O}$ as a function of object size: (a) comparison between BEM and qaleFOAM (QF) models with ($\nu = 1.00 \times 10^{-6}\mathrm{m}^2\,\mathrm{s}^{-1}$) and without ($\nu = 0$) viscosity for round objects (ROs) and rectangular boxes (RBs, RCBs); (b) different components of the diffraction-modified Stokes drift velocity predicted by the diffraction-modified Stokes drift model, where $u_{S,O,I}$, $u_{S,O,R}$ and $u_{S,O,D}$ respectively represent the incident, radiation and diffraction components of the diffraction-modified Stokes drift velocity. 67

3.13 Decomposition of the diffraction-modified Stokes drift predicted by diffraction-modified Stokes drift model for rectangular boxes according to (3.13) and (3.14): (a) contributions of the incident ($u_{S,O,I}$) and the sum of the radiated and diffracted waves ($u_{S,O,R} + u_{S,O,D}$); and (b) further decomposition into contributions due to horizontal (x) and vertical (z) components of object motion. The diffraction-modified Stokes drift velocity components are normalized by the Stokes drift (of an infinitesimally small object). 68

3.A.1 Non-dimensional added mass (μ_{ii}) and damping (λ_{ii}) coefficients for example 1 ($d/h_d = 3$, $l/h_d = 1$) of the BEM model verification. The black squares are the predictions by the BEM model, the red lines correspond to the theoretical solutions of Zheng et al. (2004) based on (3.24) and (3.25), ρ_0 is the density of water, and d the water depth. 82

3.A.2 Non-dimensional wave-induced forces for example 2 ($d/h_d = 2$, $l/h_d = 2$) and example 3 ($d/h_d = 2$, $l/h_d = 6$) of the BEM model verification. The black and blue squares are the predictions by the BEM model using (3.28) and (3.29), respectively. The red lines correspond to the theoretical solutions of Zheng et al. (2004) based on (3.39). 82

3.B.1 Eulerian-mean velocity scaled by the theoretical Stokes drift u_S a small distance below the wave trough $a_w = 20.0$ mm ($z = -25.0$ mm) for different spatial resolutions as a function of horizontal position; x_l indicates the location of the left boundary of the Navier–Stokes domain. 83

3.C.1 Effects of rotation and density on object drift: (a) celerity-normalized drift velocity as a function of relative size of the objects in table 3.C.1 for three different scenarios; (b) celerity-normalized drift as a function of relative size for objects of density $\rho = 500$ kg/m^3 (cf. table 3.3) and $\rho = 781$ kg/m^3 (cf. table 3.C.1) without rotation and without viscosity. The red lines correspond to the theoretical Stokes drift. 86

4.3.1 Schematic layout of the wave flume and experimental setup, indicating the positions of the two cameras, the coordinate system, and the dimensions of the floating object. 99

4.3.2 Shapes, bearing layouts, and dimensions of the objects used: (a) Object 0: small yellow polypropylene balls with a diameter of 2 cm and a density of $\rho = 920$ kg/m^3), serving as Lagrangian tracers. (b) Object 1: including flange. (c) Object 2: including flange. (d) Object 3: structure with 6 bearings. (e) Object 4: structure with 6 bearings. (f) Object 5: structure with 9 bearings. (g) Top view of the objects with flanges (Objects 1&2). The flanges are made of perspex sheet and have a width of 0.15 m, a height of 0.1 m, and thickness of 0.006 m. . 100

4.3.3 Side and top view of two objects in the wave flume. (a) On the left is the small object with $l = 0.05$ m, and on the right is the large object with $l = 0.35$ m. (b) On the left is the small object with $l = 0.05$ m and on the right is the large object with $l = 0.35$ m. 101

4.3.4 Example time history of objects' horizontal trajectories and surface elevation in regular waves with $f = 0.9$ Hz. (a) Horizontal trajectories of objects with different relative sizes for $ka_w = 0.10$, where x_c is the horizontal position of the objects' centre, and T_w denotes the wave period. (b) Local surface elevation of virtual gauges at various locations for $ka_w = 0.20$, where x is the horizontal position of the virtual gauges, and η is the local wave elevation. During the extraction process of the surface elevation for virtual wave gauges, the data is removed when the gauges are obscured by the flume's structural members or leave the pixel space (that is, when the position of the wave gauges is beyond the scope of the camera). Extraction begins when the object reaches $x_c = 2.3$ m and ends when it reaches $x_c = 8.2$ m, away from the wave maker. 104

4.5.1 Lagrangian drift of small objects and the Eulerian-mean velocity on the surface as a function of wave steepness in waves with frequencies of $f = 0.9$ Hz and $f = 1.0$ Hz. (a) Lagrangian drift, normalised by wave celerity c, of the 3D small yellow balls ($l = D = 0.02$ m) with $l/\lambda = 1.6\%$ and the smallest 2D objects with $l/\lambda = 2.6\%$ and $l/\lambda = 3.2\%$. (b) Comparison of wave-celerity normalised Eulerian-mean velocity derived from experiments and theory (4.6). The values of $\overline{u}_E$ for $l/\lambda = 2.6\%$ and $l/\lambda = 1.6\%$ are obtained by $\overline{u}_E = \overline{u}_{L,O} - u_{O,S} = \overline{u}_{L,O} - u_S$, in which $\overline{u}_{L,O}$ is the Lagrangian drift of the corresponding objects that is directly measured in the wave flume and u_S is the theoretical Stokes drift (4.1), which is equal to the Stokes object drift for such small objects. 110

4.5.2 Linear oscillatory motion amplitudes as a function of wave steepness for objects of different relative size. (a) Magnitude of horizontal motion normalised by wave amplitude. (b) Magnitude of vertical motion normalised by wave amplitude. . . 111

4.5.3 Linear oscillatory motion amplitudes as a function of the relative size of the objects for different wave steepness. (a) Magnitude of horizontal motion normalised by wave amplitude. (b) Magnitude of vertical motion normalised by wave amplitude. 112

4.5.4 Celerity-normalised Stokes object drift velocity (a) as a function of wave steepness for different relative object sizes and (b) as a function of relative size for different wave steepness. 113
4.5.5 Non-dimensional amplitude of the local surface elevation amplitude distribution, $a(x)/a_w$, as a function of horizontal distance (scaled by wavenumber) from the centre of mass of the object, $k(x - x_c)$, for objects of different relative sizes with incident wave steepness $ka_w = 0.21$, and frequency $f = 0.9$ Hz. The red lines represent the left and right sides of the largest object with a relative size of $l/\lambda = 18.3\%$. 115
4.5.6 Local surface elevation amplitude distribution, $a(x)$, as a function of horizontal distance (scaled by wavenumber) from the centre of mass, $k(x - x_c)$, for the largest object with a relative size of $l/\lambda = 18.3\%$ at a frequency of $f = 0.9$ Hz. (a) Difference between the local surface elevation amplitude and the incident wave amplitude, $a(x) - a_w$, for three different wave steepnesses. (b) Ratio of local surface elevation and incident wave amplitudes, $a(x)/a_w$, for three different wave steepnesses. The red lines represent the left and right sides of the object. . 116
4.5.7 Stokes drift-normalised Stokes object drift (a) as a function of wave steepness for different relative object sizes and (b) as a function of relative size for different values of wave steepness. An idealised Lagrangian particle with zero enhanced drift would have $u_{S,O}/u_S = 1$. The red dashed line with red square labelled DMS represents the diffraction-modified Stokes drift given by (4.3). As the diffraction-modified Stokes drift for a certain object size does not change with wave steepness (we use a linear 'BEM' model to solve (4.3), and (4.3) is a second-order accurate quantity), it is shown as a single line in panel (b). 117
4.5.8 Comparison of the Stokes object drift from experiments with the diffraction-modified Stokes drift (4.3) proposed by Xiao et al. (2024) and the empirical formula (4.4) of Harms (1987) as a function of relative object size for different values of wave steepness. The drift is normalised by wave celerity. Markers connected by continuous lines correspond to the results from experiments, dashed lines (of the same colour, corresponding to the colour in figure 4.5.7 (b)) to the diffraction-modified Stokes drift, and dash-dotted lines (of the same colour) to the empirical formula of Harms (1987). 120
4.5.9 Comparison of the amplitudes of oscillatory motion for objects of different sizes and in different wave steepness from experiments to results predicted by a linear BEM model. (a) Horizontal oscillatory motion. (b) Vertical oscillatory motion. The motion amplitudes in (a) and (b) are normalised by the incident wave amplitude a_w. Markers connected by continuous lines correspond to the results from experiments, while dashed lines of the same colour are those from BEM simulations. 120

4.5.10 Domains of validity of the three different models for Stokes object drift within the parameter space covered by experiments in this chapter: the classical Stokes drift for idealised Lagrangian particles (4.1), the diffraction-modified Stokes drift (4.3), and the empirical formula of Harms (1987) (4.4). The black dot represents the experimental data points. 121
4.5.11 Domain of validity of the three models compared to the experiments in this chapter. Each circle represents an experiment, with the colour of the filled circle denoting the model(s) that has an error of less than 20% compared to the experiment. The black circle corresponds to an experiment for which none of the three models is able to predict the drift observed in experiments with an error of less than 20%. Blue and green denote the classical Stokes drift and the diffraction-modified Stokes drift, respectively. Purple denotes the empirical formula of Harms (1987) (4.4). A combination of colours within a circle suggests multiple models have an error of less than 20% compared to experiments. 121
4.A.1 2D type objects. Left panel (a) is the side view of five objects (painted yellow) installed with bearings. Objects 1, 2, 3, 4, and 5 are shown from left to right, top to bottom. Objects 1 and 2 are designed with 'flange' structure shown in figure 4.3.2. The right panel (b) is the front view of objects. 124
4.B.1 Uncertainty envelopes as a function of relative size for different wave steepness; (a) Stokes object drift, this data is shown without normalization, and we only plot data for objects with relative sizes of l/λ = 2.6%, 5.2%, 8.4%, 10.5%, 18.3% and 27.1%; (b) Celerity-normalised Stokes object drift velocity; (c) Wave-amplitude-normalised magnitude of horizontal motion; (d) Wave-amplitude-normalised magnitude of vertical motion. Mean values, denoted by lines, are obtained using 5 repeat experiments. The error bars, shown as shaded areas, correspond to two standard deviations either side of the mean. The transparency of (c) has been adjusted to make it clearer for overlapping parts. 126
4.B.2 Uncertainty envelopes of wave amplitude as a function of wave steepness for different wave frequencies. Mean values, denoted by lines, are obtained using 5 repeated experiments. The error bars, shown as shaded areas, correspond to two standard deviations either side of the mean. 127

5.5.1 Shapes and dimensions of the objects with two different corner types: (a) Sharp-cornered boxes (SCBs) and round-cornered boxes (RCBs). 141
5.5.2 Time history of the horizontal motion of the small object in low-wave steepness waves ($ka_w = 0.034$) for inviscid simulations. x_p is the time-dependent horizontal position of centre of mass of the object and x_{p0} is the initial horizontal position of its centre of mass. 143

5.6.1 Oscillatory Motion of objects with different corner shapes in different types of simulations in both horizontal and vertical directions: (a) and (b) oscillatory motion amplitudes (normalized by input wave amplitude a_w) as a function of relative object size in horizontal and vertical direction, respectively; (c) and (d) phase differences in both directions of the oscillatory motions between a finite-size object θ_x, θ_z and a Lagrangian particle θ_{x0}, θ_{z0}. The red line denotes the results of an ideal Lagrangian particle. 146
5.6.2 Different types of simulations for objects with different corner shapes: (a) celerity-normalized drift velocity u_O/c as a function of relative object size; (b) amplitude of local wave surface elevation $a(x)$ (normalized by incoming wave amplitude a_w) as a function of horizontal distance (scaled by wavenumber) from the centre of mass x_c (i.e., standing wave pattern) for an object with relative size $l/\lambda = 7\%$. The object boundaries represent the left and right sides of the objects. 147
5.6.3 Examining unsteadiness of the drift velocity of sharp-cornered objects: (a) dependence of drift velocity on the assumed start of the quasi-steady state t_s as a function of object relative size for the RANS simulations. For each relative size, seven different values of t_s are shown, ranging from 23 s to 45 s (i.e., $15T$ to 30 T). The red lines are the drift from figure 5.6.2 (a) using $t_s = 21T$; (b) an illustrative example showcasing different types of fits of the horizontal trajectory of the RANS simulation results for $l/\lambda = 10\%$. Here, x_O denotes the horizontal position of the object at time t, with $x_{O,0}$ representing the initial position at $t = 0$ s. The red line denotes the linear fit: $x_{O,LF}(t) = 14.5t - 388.4$, the approach used in section §5.6.1; the blue line corresponds to the second-order fit: $x_{O,SF} = 0.067t^2 + 7.5t + 214.3$, while the exponentially decaying fit is represented by $x_{O,EF} = 740.1e^{-0.0385t} + 18.64t + 710$. The Stokes drift in this case is $u_S = 2.78$ mm/s. Both linear and second-order fits use the trajectory data after $t_s = 32$ s, whereas the exponential decay fit uses all the trajectory data including those before $t \leq 32$ s. 151
5.6.4 Different types of simulation results of (a) unsteadiness ratio R_a (b) mean acceleration ($\overline{a}_O$) as a function of relative size for objects with different corner shapes. 152
5.6.5 Unsteadiness ratio of drift in the laboratory experiment conducted in Chapter 4 as a function of relative object size for different wave steepness ranging from $ka_w = 0.04$ to $ka_w = 0.24$. The unsteadiness ratio experiment data is evaluated for both shorter and longer time duration T_d. $T_d = 1 \times 10^2 T$ given is the minimum time duration in the experiments evaluated for the largest objects in high wave steepness, while for small objects of $l/\lambda \leq 12\%$, the overall evaluation duration can be up to $10^4 T$. 154

5.6.6 Parameters of decaying component of the exponential-decay fit based on (5.6) as a function of relative size for objects with different corner shapes in different types of simulations: (a) magnitude of the decaying term $e_{O.EF}$, (b) decay rate $b_{O.EF}$. 154
5.6.7 Horizontal forces on the object as a function of relative size for objects with different corner shapes in different types of simulations. (a) magnitudes of the oscillatory part of the pressure forces. (b) mean values of pressure forces over the simulated time duration after $t_s = 21T$. (c) magnitudes of the oscillatory part of viscous forces (b) mean value of the viscous forces over the simulated time duration after $t_s = 21T$. The forces are all normalized by the gravitational force mg, where m is the mass of the object and $g = 9.81$ m/s^2. For 'SCB-inviscid' and 'RCB-inviscid', viscous forces are all 0, as viscosity is not included in these simulations. 156
5.6.8 Vorticity magnitude field (the curl of the velocity field) across one wave period for the RANS simulations of a moving sharp-cornered box ($l/\lambda = 10\%$) for $ka_w = 0.034$. Time starts at $t^* = t - 40$s (after $t_s = 32$s) for initial time $t^* = 0$s, as denoted in the figures. Only the submerged part is shown, achieved by only displaying phase fraction values $\alpha \geq 0.5$. 156
5.6.9 Vorticity magnitude field (the curl of the velocity field) across one wave period for the viscid simulations of a moving round-cornered box ($l/\lambda = 10\%$) for $ka_w = 0.034$. Time starts at $t^* = t - 40$s (after $t_s = 32$s) for initial time $t^* = 0$s, as denoted in the figures. Only the submerged part is shown, achieved by only displaying phase fraction value $\alpha \geq 0.5$. 157
5.6.10 Dynamic pressure field (p_d) across one wave period for the RANS simulations of a moving sharp-cornered box ($l/\lambda = 10\%$) for $ka_w = 0.034$. Time starts at $t^* = t - 40$s (after $t_s = 32$s) for initial time $t^* = 0$s, as denoted in the figures. Only the submerged part is shown, achieved by only displaying phase fraction value $\alpha \geq 0.5$. 157
5.6.11 Dynamic pressure field (p_d) across one wave period for the viscid simulations of a moving round-cornered box ($l/\lambda = 10\%$) for $ka_w = 0.034$. Time starts at $t^* = t - 40$s (after $t_s = 32$s) for initial time $t^* = 0$s, as denoted in the figures. Only the submerged part is shown, achieved by only displaying phase fraction value $\alpha \geq 0.5$. 157

5.6.12 Diagram of the stationary box with both types of corner shapes and the locations of sampling points in the fluid field around the box for stationary object simulations. In the diagram, A and D represent two endpoints at the top of the box while A' and D' denote the points of intersection of the box with the still water level. The sampling points are categorized based on their location regions and then vertical positions (denoted by lines such as l_1). Several points are positioned at the same vertical locations. Typically, for the left and right sides of the region, 5 to 6 points are located on each line while for the bottom region, 8 to 10 points are distributed on each line. 160
5.6.13 Time-averaged y^+ distribution over the edges of the stationary object for two values of wave steepnesses for the RANS simulations of a sharp-cornered box. (a) $ka_w = 0.034$,(b) $ka_w = 0.09$. 160
5.6.14 Standing wave pattern: amplitude of local wave surface elevation $a(x)$ as a function of horizontal distance from the centre of mass x_c for a stationary object of relative size $l/\lambda = 10\%$ with two different corner shapes. (a) different types of simulation in low wave steepness $ka_w = 0.034$, (b) different types of simulation in high wave steepness $ka_w = 0.09$. The local wave amplitude $a(x)$ is normalized by incoming wave amplitude a_w and the horizontal distance is scaled by the wavenumber. The object boundaries represent the left and right sides of the object. 161
5.6.15 Vorticity magnitude field (the curl of the velocity field) across one wave period for the RANS simulations of a stationary sharp-cornered box with $l/\lambda = 10\%$ for $ka_w = 0.034$. 163
5.6.16 Vorticity magnitude field (the curl of the velocity field) across one wave period for viscid simulations of a stationary round-cornered box with $l/\lambda = 10\%$ when $ka_w = 0.034$. Time starts at $t^* = t - 40$s (after $t_s = 32$s) for initial time $t^* = 0$s, as denoted in the figures. Only the submerged part is shown, achieved by only displaying phase fraction value $\alpha \geq 0.5$. 163
5.6.17 Dynamic pressure field p_d across one wave period for RANS simulations of a stationary sharp-cornered box with $l/\lambda = 10\%$ when $ka_w = 0.034$. Time starts at $t^* = t - 40$s (after $t_s = 32$s) for initial time $t^* = 0$s, as denoted in the figures. Only the submerged part is shown, achieved by only displaying phase fraction value $\alpha \geq 0.5$. 164
5.6.18 Dynamic pressure field p_d across one wave period for viscid simulations of a stationary round-cornered box with $l/\lambda = 10\%$ when $ka_w = 0.034$. Time starts at $t^* = t - 40$s (after $t_s = 32$s) for initial time $t^* = 0$s, as denoted in the figures. Only the submerged part is shown, achieved by only displaying phase fraction value $\alpha \geq 0.5$. 164

5.6.19 Dynamic pressure p_rgh (scaled by ρgl) distributions over the object boundaries for objects with $l/\lambda = 10\%$ and two different corner shapes for $ka_w = 0.034$. (a) dynamic pressure magnitude (p_rgh), normalized by ρgl, for different types of simulations. (b) mean values of dynamic pressure $\overline{p_rgh}$, normalized by ρgl, for different types of simulations. 165
5.6.20 Non-dimensional horizontal forces as a function of wave steepness for objects with different corner shapes in different types of simulations: (a) magnitudes of the oscillatory part of pressure forces $F_{x,p}$, normalized by ρgl^3; (b) mean values of pressure forces $\overline{F}_{x,p}$, normalized by ρgl^3, over the simulated time duration after $t_s = 21T$; (c) magnitudes of the oscillatory part of viscous forces $F_{x,v}$, normalized by ρgl^3; (d) mean values of viscous forces $\overline{F}_{x,v}$, normalized by ρgl^3, over the simulated time duration after $t_s = 21T$. Notably, for 'SCB-inviscid', viscous forces are all 0 owing to the absence of viscosity in these simulations. . . 166
5.A.1 Power spectral density (PSD) of turbulent kinetic energy (TKE) k_e at sampling points in the fluid field around the object for RANS simulations of stationary objects ($l/\lambda = 10\%$) with sharp corners when $ka = 0.034$. (a) left (front region) (b) rear (right) region (c) bottom region. The red lines represent the theoretical lines of Kolmogorov's 5/3 law in the inertial subrange. The left and right boundaries of the object are located at $x - x_c = -0.5l$ and $x - x_c = 0.5l$, respectively. The bottom boundaries are located at $z/h_d = 1$, $x - x_c = [-0.5l, 0.5l]$. 171

A.1.1 Schematic layout of the wave flume, indicating the positions of the wave gauges, the coordinate system, and the pipe system. 205
A.2.1 Reflection coefficient C_{rw} of the fundamental wave frequency as a function of wave steepness for different frequencies. The calculations are based on approach 1, where the condition $\sin k_n \Delta xqj = 0$ is satisfied. In cases where the condition fails to be satisfied, we use approach 2 as an alternative). 210
A.2.2 Measured gauge 1/2 wave heights as a function of gauge positions in x axis for different wave steepnesses and wave frequencies. a_g is the examined 1/2 wave heights based on time histories of wave gauges and a_w is the input wave amplitude set to the wavemaker system. 213
A.2.3 1/2 Wave heights averaged over all wave gauges as a function of wave steepness ϵ for different wave frequencies. $\overline{a}_g$ is the 1/2 wave heights averaged over a_g of 7 wave gauges and a_w is the input wave amplitude set to the wavemaker system. . 213
A.2.4 Time history of the surface elevation collected by different wave gauges for the wave of $f = 1.2$ Hz and ka_w=0.06. The surface elevation from the i-th wave gauges is denoted as $\eta_{gi} (i = 1, 2, 3, 5, 7)$ and a_w is the input wave amplitude set to the wavemaker system. 216

A.2.4Time variation of the 1/2 wave height over N sections for different wave steepness and wave frequencies based on signals collected by gauge 3, in which N=15. This means the 1/2 wave height of each section is evaluated and averaged by 10 T_w. The scatter data corresponds to the mean value of the time and 1/2 wave height evaluated on the corresponding sections. Time for the waves generated by the wave maker first reach gauge 3, denoted t_0, is calculated by $t_0 = x_{g3}/c$, where $c = w/k$ is the wave celerity, w the wave angular frequency and k wave number. Time for the reflected wave to make a round trip back the gauge 3, denoted by t_f, is calculated by $t_f = t0 + x_f/c$, where $x_f = (9.945 - 6.02) * 2$ m is the traveling distance from the position of gauge 3, hitting the beaches and bouncing back. . 219

A.2.5Time variation of the 1/2 wave height over N sections for different wave frequencies when $\epsilon = 0.10$ ($\epsilon = 0.08$ for $f = 0.5$ Hz as this is the largest wave that we have for this frequency). The data is based on signals collected by different wave gauges (data for gauge 4 and gauge 6 are not presented here as they share the same x-location with gauge 3 and gauge 5), in which N=15. This means the 1/2 wave height of each section is evaluated and averaged by 10 T_w. The scatter data corresponds to the mean value of the time and 1/2 wave height evaluated on the corresponding sections. 221

A.2.6Lateral variations Δ_{lv} as a function of wave steepness for different frequencies based on signals collected by two pairs of gauges 3,4 and gauges 5,6. 222

A.2.7Confidence bands on the 1/2 wave heights (a) as a function of wave frequency for ka_w=0.06 and (b) as a function of wave steepness for waves of $f = 0.9, 1.0, 1.05, 1.1$ Hz. Each case is obtained by 5 repeats with its mean value denoted by the solid lines. The error bars correspond to two standard deviations on either side of the mean as shown in the shading area. 224

List of Tables

3.1 Wave properties and numerical parameter values for the hybrid numerical model (qaleFOAM) simulations, distinguishing the potential-flow (QALE-FEM) and the Navier–Stokes (NS) domains. 45

3.2 Numerically predicted wave amplitude as a fraction of the input amplitude a/a_w and object drift as a fraction of theoretical Stokes drift u_O/u_S for very small objects of two different shapes and for different mesh sizes, with l the length of the object. The horizontal grid size Δx varies with distance to the object from the farthest location where $\Delta x = 0.02$ m to the nearest location where $\Delta x = 0.0005$-0.001 m. The total number of cells of the mesh is denoted by N_c. The amplitude a is the time-averaged wave amplitude at the location of more than one wavelength downstream away from the object (near the outlet, defined in figure 3.2 (b)) scaled by the input wave amplitude a_w. The force $F'_{x,vis} = F_{x,vis}/(\rho g a_w l^2/4)$ is the non-dimensional magnitude of the horizontal viscous force on the object. 48

3.3 For category I simulations exploring the effect of size, object dimensions of the two different objects considered: round-cornered boxes (RCBs) and round objects (ROs) ($\rho = 500$ kg/m^3 for both). 49

3.4 For category II simulations exploring the effect of object shape with fixed height (group 1): object dimensions for different shapes (l=0.37 m, h=0.32 m, $\rho = 781$ kg/m^3). 53

3.5 For category II simulations exploring the effect of submergence depth with fixed radius of the round corners (group 2): object dimensions for different submergence depths ($l = 0.37$ m, $\rho = 781$ kg/m^3). 53

3.B.1 Values of the three target quantities of the convergence tests: wave amplitude a_w, Eulerian-mean velocity $\overline{u}_E$ and drift rate of a Lagrangian particle $\overline{u}_L$. Results are shown for four different spatial resolutions for the low-wave steepness case, where Δx and Δz represent the grid size in x- and z-directions, respectively, N_c is the total number of cells in the Navier–Stokes domain, and a_{in} is the input wave amplitude. 84

3.B.2 Values of the three target quantities of the convergence tests: wave amplitude a_w, Eulerian-mean velocity $\overline{u}_E$ and drift rate of a Lagrangian particle $\overline{u}_L$. Results are shown for four different spatial resolutions for the high-wave steepness case, where Δx and Δz represent the grid size in x- and z-directions, respectively, N_c is the total number of cells in the Navier–Stokes domain, and a_{in} is the input wave amplitude. 84
3.C.1 Object dimensions of round-cornered boxes of different sizes with $\rho = 781$ kg/m^3. 84
3.D.1 For category I simulations exploring the effect of size, Reynolds numbers, smallest mesh sizes near the boundary Δ_{min}, estimates of normal-wall distance y_d, and total numbers of cells in the mesh N_c, and Keulegan–Carpenter numbers K_c for round-cornered boxes (RCBs) and round objects (ROs). 86
3.D.2 For category III simulations exploring the effect of steepness, Reynolds numbers, smallest mesh sizes near the boundary Δ_{min}, estimates of normal-wall distance y_d, and total numbers of cells in the mesh N_c, and Keulegan–Carpenter numbers K_c for round-cornered boxes (RCBs) and round objects (ROs). 87
3.D.3 Near-wall treatment and effect of including a turbulence model for a round-cornered box with $l/\lambda = 10\%$ and $ka_w = 0.034$ for two different boundary conditions (BC1 and BC2) in the URANS simulation. Here, k is the turbulent kinetic energy (its initial value on both BCs is set to a uniform value of $k = 1.00 \times 10^{-12}$ m^2/s ^{2}), ν_t is the turbulent viscosity (its initial value on both BCs is set to a uniform value of $\nu_t = 0$ m^2/s), ω is the specific turbulence dissipation rate (its initial value is calculated as $\omega = 60\nu/(0.075y^2)$, where y is the normal distance from the boundary to the first cell center), $\overline{y}^+$ is the time-averaged mean value of y^+ on the object boundary. 88
3.D.4 Effect of including a turbulence model for round-cornered boxes with $l/\lambda = 8\%$, $ka_w = 0.08$ and $l/\lambda = 10\%$, $ka_w = 0.09$ (category III). The boundary conditions BC1 and BC2 are those in table 3.D.3, $\overline{y}^+$ is the time-averaged mean value of y^+ on the object boundary. 88

4.2.1 Summary of previous laboratory studies of wave-induced drift of freely-floating objects on waves. Some values not explicitly provided in the cited papers were obtained from digitized figures or estimated using the linear dispersion relationship. In 2D experiments, the 'third dimension' shows the approach used to ensure the experiment's 2D nature. l represents the length of the object in the direction of wave propagation, λ the wavelength, h the height of the object, ρ the density of the object, k the wavenumber, d the water depth, and a the wave amplitude. The wave types R, IR, and WG correspond to regular waves, irregular waves, and wave groups, respectively. 96

4.3.1 Experimental matrix showing the different wave parameters. We have examined a total of 48 wave conditions, combining 4 different frequencies, each with 12 different wave steepness values ranging from 0.04 to 0.32. The wave steepness interval was 0.02 for ka values between 0.04 and 0.2, and 0.04 for ka values between 0.2 and 0.31. The table includes the following parameters: f (wave frequency), a_w (measured wave amplitude), k (wavenumber), ϵ (wave steepness), d (water depth), and λ (wavelength). The term Δa_w represents the lateral variation of the wave amplitude calculated by measuring the wave amplitude using two pairs of gauges positioned at $x = 6.02$ m, $y = 0.0$ m; $x = 6.02$ m, $y = 0.275$ m; $x = 6.32$ m, $y = 0.0$ m; and $x = 6.32$ m, $y = 0.275$ m. The average value across all wave steepness values is reported. $R = a_I/a_R$ refers to the reflection coefficient, which corresponds to the ratio of the incident wave amplitude a_I to the reflected wave amplitude a_R. 99

4.3.2 Object dimensions. Object 0 spherical ball, functioning as a current drogue. The number of bearings indicates the number installed at each end of the object. Objects 1-5 are solid and were constructed from teak wood. The density of these objects is $\rho = 6.36 \times 10^2$ kg/m^3. 100

4.3.3 Matrix of relative object size l/λ. For each relative object size, experiments with 12 different values of incident wave steepness were performed. 101

4.4.1 Estimated natural periods of object heave and roll motion. Object numbers 1-5 correspond to the objects specified in table 4.3.2. The periods $T_{O,R,BEM}$ and $T_{O,H,BEM}$ are the estimated natural periods of roll and heave motions for the objects calculated from the BEM simulations; $T_{O,R,H87}$ denotes the natural roll period given by (4.5) from Harms (1987). 107

4.4.2 Estimates of the ratio of natural heave and roll period for objects with different relative sizes to incident wave periods (see table 4.3.3 for object dimensions and table 4.4.1 for values of the natural period). 108

4.B.1 Measurement error of the Lagrangian object drift $\overline{u}_{L,O}$ during fitting of the horizontal trajectory for objects with different sizes and in varying wave steepness. We chose three different sizes of objects to report here: $l/\lambda = 2.6\%$ for object 1 in wave $f = 0.9$ Hz; $l/\lambda = 12.5\%$ for object 3 in wave $f = 1.1$ Hz; $l/\lambda = 22.4\%$ for object 5 in wave $f = 1.0$ Hz. $1 - R^2$ refers to the goodness of fit with R^2 the uncertainty in the prediction of the fitted polynomial. σ refers to the standard deviation (uncertainty of the coefficients) of the linear coefficient determination in the fit, and thus $\sigma/\overline{u}_{L,O}$ represents the standard deviation of the fitted linear coefficient. 127

4.C.1 Coefficients of the regression of wave-celerity normalised Stokes object drift $u_{S,O}/c$ on wave steepness $\epsilon = ka_w$ given by (4.8). The error bounds represent $\pm$ one standard deviation of the coefficients, and R^2 is the coefficient of determination. 128

5.3.1 Setup of boundary conditions for different variables in our numerical simulations. α is the volume phase fraction, p represents the pressure and $\mathbf{u}$ denotes the velocity field. The conditions in italics are the standard conditions available in the OpenFOAM platform and the 'Coupled' conditions represent the boundary conditions that are coupled with the QaleFEM solver. The boundary conditions, as described in the OpenFOAM official user guide and manual, are as follows: '*inletOutlet*' serves as a generic outflow condition, allowing for specified inflow when there is return flow; '$totalPressure$' establishes a total pressure condition; '$fixedFluxPressure$' sets the pressure gradient to a provided value such that the flux on the boundary matches the specified velocity boundary condition; '$pressureInletOutletVelocity$' is a velocity inlet/outlet boundary condition applied to pressure boundaries where pressure is specified. For outflow, a zero-gradient condition is applied based on the flux, while for inflow, the velocity is determined from the patch-face normal component of the internal-cell value; '*slip*' refers to a no-flow, free-slip condition (*slip*); '*noSlip*' restrains velocity to zero at walls; '$movingWallVelocity$' provides a velocity value for moving walls; For the body surface, we use three different types of velocity boundary conditions for different types of simulations: $movingWallVelocity$ is used for the moving object cases (for both viscous and inviscid simulations), *noSlip* is used for the stationary object cases in the viscous simulation, and *slip* is used for inviscid simulation of the stationary object cases. 135

5.3.2 Discretization schemes used in our numerical simulations, where $t, \mathbf{u}$ refers to time and velocity, respectively; μ_{eff} is the effective dynamic viscosity, which encompasses both the molecular dynamic viscosity and the turbulent viscosity. ϕ refers to the mass flux; for incompressible fluid, it is replaced by velocity. α is the volume fraction and α_{rb} is related to an artificial compression term. Turbulent modelling-related terms refer to the convection terms of turbulent kinetic energy (TKE) k_e and the specific rate of dissipation ω in RANS modelling. The column 'Setup in OpenFOAM' corresponding to the terms used in $fvSchemes$ (a setup file name) in OpenFOAM simulation cases. The schemes in italics are standard schemes available in OpenFOAM. 136

5.4.1 Convergence test for low wave steepness ($ka_w = 0.034$), conducted at particle Re $= 1.97 \times 10^4$, KC $= 0.33$. The mesh refinement is reduced in the order M1, M2, M3 with M3 being the most coarse mesh. N_c is the total number of cells in the mesh with the unit 'M' representing million. λ and l represent the wavelength and size of the object, respectively. Δx and Δz indicate the horizontal and vertical mesh sizes, while $\Delta_{\min}$ represents the smallest mesh size near the object surface. $\overline{y}^+$ is the time-averaged value of the average y^+ over the body surface. a represents the local wave amplitude of the sampled location. The sample location of 'Front' and 'Back' are chosen from the distance $0.0155l$ away from the front and back side of the object. F_x and F_z are the magnitudes of the oscillatory parts of the horizontal and vertical forces, which are made non-dimensional as $F'_x = F_x/(\rho g a_w l^2/4)$ and $F'_z = F_z/(\rho g a_w l^2/4)$, respectively. . 139

5.4.2 Convergence test for the highest wave steepness ($ka_w = 0.09$) conducted at particle Re $= 8.0^4$, KC $= 0.87$. Mesh refinement is reduced in the order M1, M2, M3 with M3 being the most coarse mesh. N_c is the total number of cells in the mesh with the unit 'M' representing a million. λ and l are the wavelength and size of the object, respectively. Δx and Δz is the horizontal and vertical mesh sizes, while Δ_{min} represents the smallest mesh size near the object surface. $\overline{y}^+$ denotes the time-averaged value of the average y^+ over the body surface. a represents the local wave amplitude of the sampled location. The sample location of 'Front' and 'Back' are chosen from the distance $0.0155l$ away from the front and back side of the object. F_x and F_z are the magnitudes of oscillatory parts of the horizontal and vertical forces, which are made non-dimensional as $F'_x = F_x/(\rho g a_w l^2/4)$ and $F'_z = F_z/(\rho g a_w l^2/4)$, respectively. 140

5.4.3 Convergence statistics of normalized first-harmonic components of target quantities for low wave steepness $ka_w = 0.034$ with particle Re $= 3.01 \times 10^4$, KC $= 0.34$. F_{px} and F_{pz} are the magnitudes of the first-harmonics parts of the pressure forces in horizontal and vertical directions, respectively, and F_{vx} and F_{vz} are the magnitudes of the first-harmonics parts of the viscous forces in horizontal and vertical directions, respectively. All these forces shown with its non-dimensional form at the table are normalized by $F' = F/(\rho g a_w l^2/4)$. 140

5.4.4 Convergence statistics of normalized 1st harmonic components of target quantities for low wave steepness $ka_w = 0.09$ with particle Re $= 8.0 \times 10^4$, KC $= 0.9$. F_{px} and F_{pz} are the magnitudes of the first-harmonics parts of the pressure forces in horizontal and vertical directions, respectively, and F_{vx} and F_{vz} are the magnitudes of the first-harmonics parts of the viscous forces in horizontal and vertical directions, respectively. All these forces shown with its non-dimensional form at the table are normalized by $F' = F/(\rho g a_w l^2/4)$. 141

5.5.1 Results and mesh sensitivity study of a very small sharp-cornered box in low wave steepness $ka_w = 0.034$. For inviscid simulations, the kinematic viscosity in the simulation is set as $\nu = 0$ and for viscid simulations, $\nu = 1\times10^{-6}$ m^2·s^{-1}. The level of mesh refinement is reduced from M1 to M2, with M1 being the mesh used for later simulations. a is the wave amplitude in the far downstream of the tank, which is a good indicator of a clean wave field with minimal radiated and diffracted disturbance to the waves. u_O is the time-averaged horizontal drift velocity of the object. F_x and F_z are the magnitudes of the oscillatory parts of horizontal and vertical forces, which are made non-dimensional as $F'_x = F_x/(\rho g a_w l^2/4)$ and $F'_z = F_z/(\rho g a_w l^2/4)$. 142

5.6.1 Object dimensions of sharp-cornered boxes and round-cornered boxes with a constant density of $\rho = 781$ kg/m^3 and aspect ratio $h_d/l = 0.67$. 144

5.6.2 Mean values of y^+ for viscid and RANS simulations of sharp-cornered boxes. The mean value is obtained by averaging the time-averaged (over the whole simulation duration) y^+ value over the surface. 145

5.6.3 Reynolds and Keulegan–Carpenter numbers of moving objects for both round-cornered and sharp-cornered bpxes. 148

5.6.4 Detailed coordinates of sampling points in the fluid field shown in figure 5.6.12 for different wave steepness values for stationary objects. The variables x and z represent the horizontal and vertical coordinates of the points, respectively, while x_c is the horizontal coordinates of the centre of object. Variables l and h_d denote the length and draft of the objects, respectively. Consequently, the horizontal locations of lines AB and CD are $x - x_c = -0.5l$ and $x - x_c = 0.5l$, respectively. The vertical locations of lines $A'D'$ and BC are $z/h_d = 0$ and $z/h_d = -1$, respectively. For $ka_w = 0.034$, the sampling points cover the region of $-0.65l \leq x - x_c \leq 0.57l$ and $-0.12h_d \leq z \leq -1.2h_d$. For higher wave steepness values $ka_w = 0.07, 0.09$, the region expands to $-0.76l \leq x - x_c \leq 0.65l$ and $-0.26h_d \leq z \leq -1.32h_d$. 159

5.6.5 Particle Reynolds and Keulegan–Carpenter numbers for stationary objects for different wave steepness. The values of Reynolds and Keulegan–Carpenter numbers are the identical for sharp-cornered and round-cornered boxes. 160

A.1.1 Detailed width dimensions of the flume for each pane. The beaches sit from x=9.945 m to the end x =11.8 m. The variation is calculated by $\delta_{width}/\overline{width}$, $\delta_{width} = \sqrt{\frac{\sum_{i=1}^{5}\left(width_i - \overline{width}\right)^2}{5-1}}$, where $width_i$ represents the i-th location of the corresponding pane and $\overline{width}$ denotes the mean value of the five locations in each pane. 207

A.2.1Reflection coefficient C_{rw} of the fundamental wave frequency for all wave conditions. The calculations are based on approach 1, where the condition $\sin k_n \Delta xqj = 0$ is satisfied. In cases where the condition fails to be satisfied, we use approach 2 as an alternative). The values of $C_{rw} \leq 0.05$ are marked by Green, those of $0.10 \leq C_{rw} \leq 0.20$ are marked by light red, and of $C_{rw} \geq 0.20$ are marked by bright red. 211
A.2.21/2 wave heights averaged over all wave gauges $\overline{a}_g/a_w$ for all wave frequencies f_w and wave steepness ϵ. The values of $0.95 \leq \overline{a}_g/a_w \leq 1.05$ are marked by Green, those of $0.8 \leq \overline{a}_g/a_w \leq 0.9$ and $1.1 \leq \overline{a}_g/a_w \leq 1.2$ are marked by light red, and of $\overline{a}_g/a_w \leq 0.8$ are marked by bright red. 214
A.2.3Gauge variation: Relative standard deviation of 1/2 wave heights examined over all wave gauges $\delta_{a,g}/a_w$ for all wave frequencies f_w and wave steepness ϵ. The values of $\delta_{a,g}/a_w \leq 5\%$ are marked by Green, those of $10\% \leq \delta_{a,g}/a_w \leq 20\%$ are marked by light red, and of $\overline{a}_g/a_w \geq 20\%$ are marked by bright red. 214
A.2.4Time variation: Relative standard deviation (expressed in units of 100%) of 1/2 wave height examined over different time sections after the signal becomes stable, which is denoted as $\delta_{a,t}/a_w$, for all wave frequencies f_w and wave steepness ϵ. The values of $\delta_{a,t}/a_w \leq 1\%$ are marked by Green, those of $3\% \leq \delta_{a,t}/a_w \leq 5\%$ are marked by light red, and of $\delta_{a,t}/a_w \geq 5\%$ are marked by bright red. 220
A.2.5Lateral variations of the first pair of gauge 3,4 Δ_{lv1} (expressed in units of 100%) for all wave frequencies f_w and wave steepness ϵ. The values of $\Delta_{lv1} \leq 1\%$ are marked by Green, those of $3\% \leq \Delta_{lv1} \leq 5\%$ are marked by light red, and of $\Delta_{lv1} \geq 5\%$ are marked by bright red. 223
A.2.6Lateral variations of the second pair of gauge 5,6 Δ_{lv2} (expressed in units of 100%) for all wave frequencies f_w and wave steepness ϵ. The values of $\Delta_{lv2} \leq 1\%$ are marked by Green, those of $3\% \leq \Delta_{lv2} \leq 5\%$ are marked by light red, and of $\Delta_{lv2} \geq 5\%$ are marked by bright red. 223

Chapter 1

Introduction

Assessing the motion of floating objects on the ocean surface has significant implications across various domains, spanning from natural processes to environmental dynamics and engineering applications. This assessment, for example, is critical for understanding the migration and distribution of nutrients, plankton and marine organisms, which are crucial for maintaining marine ecosystems. Moreover, it impacts the redistribution of heat, regulating Earth's climate system and modulating the energy balance, thereby influencing ocean circulation patterns, climate and weather patterns. It also plays a pivotal role in the dispersion of pollutants, contaminants and marine debris which poses threats to marine life and human health.

1.1 Background

Floating objects in the open ocean are subject to forcing, mainly from winds, ocean waves, and currents. In the open ocean, surface gravity waves are mainly induced by winds. The wave field at a certain location and time is considered a superposition of waves originating from previous wind activity at different locations. The influence of wave-induced transport can be a dominating factor (Wadhams, 1983), allowing particles to cross strong currents and winds (Fraser et al., 2018) and thus cannot be ignored. A thorough understanding of wave-induced transport is imperative not only for understanding the migration of these plastic pollutants, ice floes, search and rescue (SAR) but also for addressing concerns such as oil spill mitigation, the migration of larvae and marine algae, and the needs of the maritime and offshore engineering industry.

In September 2015, the United Nations embraced the 2030 Agenda for Sustainable Development– a shared blueprint advocating dignity, peace, and prosperity for both the planet and humanity. At its heart are the 17 Sustainable Development Goals (SDGs). Rooted in the principle of 'leaving no one behind', the SDGs present a universal call to action to end poverty, hunger, AIDS and other problems. They advocate for strategies to combat climate change and preserve our oceans and forests while spurring economic growth. Notably, 50-80 percent of life on Earth resides in the ocean, covering more than 70 percent of Earth's surface (NASA, 2019). SDGs 14, Life Below Water, specifically urges the conservation and sustainable use of oceans, seas, and marine resources. To ensure sustainable consumption and production patterns, it is essential to address marine and ocean pollution including plastic pollution, which poses a huge potential threat to marine life and aquatic ecosystems, human health, and social well-being (Ostle et al., 2019). Floating plastic pollution has emerged as one of the most pressing environmental problems due to its unprecedented rising rate and enduring longevity (Cole et al., 2011). Alarmingly, millions of wild marine animals succumb to plastic-related recurrences annually, primarily through ingestion, suffocation, entanglement and starvation (IUCNPlastic, 2021). Human activities have introduced a staggering 8300 teragrams (millions of metric tons, MMT) of plastic polymers to Earth's surface since 1950 (Sonke et al., 2022). Plastic, widely utilized in packaging, household, and agriculture has witnessed a doubling in global exports since 2005, reaching nearly US $1.2 trillion in 2021 (UNCTADstat., 2022). The rapid rise in single-use plastic item production, coupled with a throw-away culture, results in a substantial volume of plastic waste. Despite the product's brief lifespan, the enduring environmental impact of plastic waste persists for hundreds or thousands of years in the ocean before it decays (Cole et al., 2011).

Every year, 11 million tonnes of plastic waste enters the ocean (Reddy et al., 2020), predominantly originating from land-based plastic debris (Hannah, 2023). Despite concerted efforts spanning decades to chart the global abundance, size, and bulk of plastics on the ocean surface, the overall budget for oceanic plastics remains poorly understood (Van Sebille et al., 2020; Sonke et al., 2022; Lebreton et al., 2019; Isobe and Iwasaki, 2022). A perplexing plastic paradox arises from the apparent incongruity between the observed abundance of plastics in the world's oceans (a relatively small quantity) and the flow of plastic into the ocean (a substantially larger

quantity). Jambeck et al. (2015) estimated an annual emission range of 4.8 to 12.7 MMT of plastic waste entering the ocean in 2010, with projections anticipating the accumulation of tens of MMT of plastic waste on the ocean surface, assuming the waste flows are proportional to global plastic production. Historical data suggests that 25.3 MMT of mismanaged plastic waste has accumulated in the world's oceans. However, observation and numerical modeling estimate only 0.25 MMT of floating ocean plastics including microplastics and large plastic debris, exist (Eriksen et al., 2014; Isobe and Iwasaki, 2022). Unraveling the global plastic mass transfer budget and resolving the mass imbalance necessitates a better understanding of the physical processes governing mass transport and dispersion (Van Sebille et al., 2020; Kaandorp et al., 2023). Given that a significant share of plastic produced possesses relatively large buoyancy and its enduring nature in the ocean, it is of practical interest in predicting its long-distance surface transport (Geyer et al., 2017).

Covering approximately 7% of the Earth's surface and constituting 10% of the world's oceans, sea ice plays a pivotal role in mass, momentum and energy exchanges between the ocean and air, thereby influencing the global climate circulation system (Wadhams, 2014). As climate change induces global warming, the ice in both the Arctic and Antarctic undergoes melting, affecting the planet as a whole. The destabilization and accelerated movement of glaciers and ice sheets toward the ocean contribute to sea level rise and the presence of additional ice floes floating on the ocean surface. The marginal ice zone (MIZ), characterized as the transitional zone between the open ocean and dense drift ice, is crucially important for local ecological environments, biological processes and human activities. In the MIZ, air-ocean-ice interactions reach their zenith (Strong et al., 2017; Untersteiner, 2013), influencing the behaviours of ice floes including drift, collisions (Martin and Becker, 1987), herding (Wadhams, 1983), and rafting (Dai et al., 2004). A comprehensive understanding of mass transport on the ocean surface is essential for assessing and predicting these ice floe behaviours. Furthermore, an understanding of mass transport on the ocean surface is important for trajectory forecasts for search and rescue (SAR) operations. In 2017 alone, the United States Coast Guard (USCG) responded to 16,000 SAR cases, saving 4,000 lives (Futch and Allen, 2019). Accurate forecasts of the drift patterns, whether for lost objects such as aircraft wrecks (Trinanes et al., 2016; Miron et al., 2019; Rypina et al., 2013) or missing persons, are crucial to enhancing the probability of success

of locating individuals alive.

1.2 Object drift velocity

Floating objects on the surface of the ocean, exposed to waves undergo drift. A floating object subjected to waves typically experiences a net drift in the direction of wave propagation in addition to the wave-induced oscillatory motion. This drift velocity is termed Stokes drift (Stokes, 1847). Stokes drift not only affects the movement of objects afloat such as pollutants and man-made structures, in the open sea but also contributes to the exchange of heat, momentum and gases between the ocean and atmosphere (Kraus and Businger, 1994). Consequently, it plays a role in the physics of the ocean surface mixed (boundary) layer (Belcher et al., 2012). To accurately model Langmuir turbulence (the alignment of vortices in the upper layer of the ocean induced by surface waves) and Stokes–Coriolis forcing (an effect induced by Earth's rotation and surface waves on fluid motions) in an oceanic circulation model, the magnitude and shear depth profile of the Stokes drift must be considered. The total Lagrangian mean velocity of a fluid particle u_L is equal to the sum of its Stokes drift u_{SD} and the Eulerian mean flow velocity u_E (Bühler, 2014; van den Bremer and Breivik, 2018).

The Eulerian-mean flow velocity, induced by Eulerian current can transport the object in the opposite direction of the Stokes drift. Excluding currents in the ocean, Eulerian-mean flows typically fall into three main types. In coastal zones, Stokes drift transports the object forward (i.e. in the wave propagation direction) while an opposite return flow, driving the object backward, forms as no-flow boundary conditions are imposed by a beach. This often manifests as undertow or rip currents in the coastal region. To balance the momentum flux of Stokes drift towards the shore, bounded by the no-flow boundary condition of the beach, a return flow (undertow) is required (Svendsen, 1984; Isobe et al., 2014; Kataoka and Akylas, 2015; Pasternak et al., 2018). Similarly, in a closed wave flume, the forward Stokes drift must be accompanied by an Eulerian return current due to the net depth-integrated mass flux being zero. Therefore, in any laboratory studies in a flume (tank), to calculate the Stokes drift of an object on the surface, the Eulerian return flow must be evaluated. Additionally, for periodic surface wave groups, Eulerian return flow, governed by conservation of volume, is induced due to the divergent characteristic of Stokes transport for a wave group (Longuet-Higgins and

Stewart, 1962; van den Bremer and Taylor, 2015; van den Bremer et al., 2019). Generally, Stokes drift dominates near the surface while return flow's importance grows at depth (van den Bremer and Taylor, 2015), resulting in a positive forward Lagrangian velocity on the surface. Thirdly, due to Earth's rotation and turbulent dissipation in the upper-ocean boundary layer, the Coriolis force in combination with Stokes drift drives an Eulerian-mean current shown as the Ekman-Stokes flow (Higgins et al., 2020; Lewis and Belcher, 2004; Onink et al., 2019), which might significantly alter wave-induced transport of floating objects.

The Stokes drift is derived based on the assumption of an ideal fluid (non-viscous and incompressible) and irrotational flow. However, in the presence of viscosity, particularly within the oscillatory surface boundary layer, the drift velocity can significantly deviate from the Stokes drift, leading to additional net transport (Longuet-Higgins, 1953; Grue and Kolaas, 2017; van den Bremer et al., 2019). Analytical theory by Longuet-Higgins (1953) suggests that vorticity transport associated with the surface boundary layer streaming occurs in two regimes, depending on the ratio of wave amplitude to the thickness of the surface boundary layer. In cases where the ratio is small, vorticity diffusion takes place through the viscous conduction regime, while in instances where the ratio is large, convection with the mass-transport velocity governs the diffusion process. Experimental measurements by Grue and Kolaas (2017) revealed that streaming velocities within the boundary layers beneath the free surface significantly enhance the forward drift velocity of fluid particles.

Under the assumption of zero Eulerian-mean velocities, when considering an idealized, infinitely small fluid particle as a floating object, such a particle performs Lagrangian behaviour and is transported by Stokes drift. However, Stokes drift can be expected to be modified for objects of finite size. Unlike small floating objects, which are significantly smaller than the length of the waves and are passively driven by waves, large objects with different shapes exhibit inertial behaviours, resulting in non-Lagrangian drift behaviour (Calvert et al., 2021; DiBenedetto et al., 2022). In this thesis, we examine the drift behaviour of two-dimensional (2D) floating objects with finite size under the excitation of unidirectional regular waves in deep water. We seek to address the following four key questions: (1) What role does the size play in influencing objects' drift in comparison to an infinitely small fluid particle? (2) How does the shape impact the object's drift behaviour? (3) In what manner does the drift of an

object change with variations in wave steepness? (4) To what extent do viscosity and vorticity contribute to the alteration of object drift?

By considering monochromatic regular waves characterized by a single wave frequency, the Eulerian return flow induced by divergent Stokes transport and the vertical Stokes drift component arising for the wave groups become unimportant (van den Bremer and Taylor, 2015). Our focus is solely on horizontal transport, and we exclude the consideration of the Earth's rotation effects. As a result, our examination is limited to the first type of Eulerian flow discussed above. In this study, we focus on the 2D problem in deep water, and we do not account for the reduced Stokes drift due to wave spreading and a multidirectional wave field (Webb and Fox-Kemper, 2015; van den Bremer and Taylor, 2015), nor finite water depth (van den Bremer and Taylor, 2015). The flow in the third dimension is not considered in our analysis. Finally, we do not address the effect of surface tension.

Generally, there are two methods for determining the mean drift velocity, as illustrated in figure 1.1 (a) and (b). The first approach involves applying the best linear fit to the horizontal trajectory after a quasi-steady stage is reached and then determining the slope of the resulting linear trend line. The quasi-steady stage, indicated in the figure 1.1 refers to the phase beyond the initial transitional period where the movement pattern stabilizes. The second method involves evaluating the average value of the sub-harmonic part of Lagrangian velocity, which is assumed to be stable (as depicted by the green line in figure 1.1(b)) after a quasi-steady state is attained. Different velocity components are obtained by applying frequency filters and then transformed back to the time domain. The Lagrangian velocity can be either directly calculated by a numerical model or obtained by taking the first derivative of the trajectory over time. The linear oscillatory motions in both horizontal and vertical directions in this thesis are extracted from the time history of moving trajectories. By applying a frequency filter to the trajectory, we obtain the time history of the linear components. The motion amplitudes of these linear components are then evaluated for each period and averaged over the entire duration.

1.3 Synopsis

This thesis adheres to the integrated thesis format, where the main chapters (chapters 3 to 5) are taken directly from previously published or submitted (or intended to submit) journal

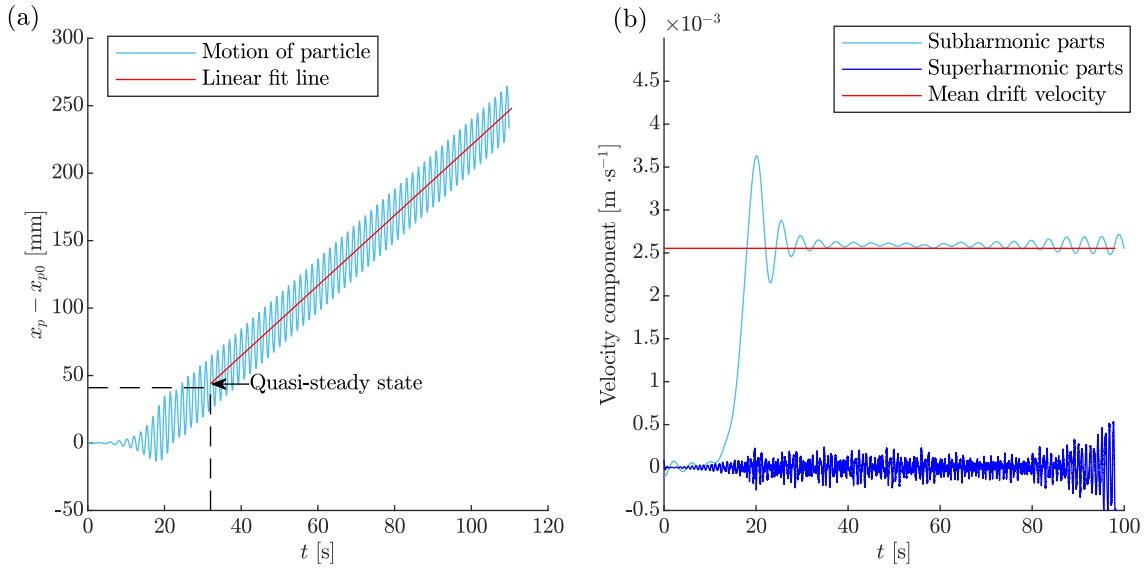


Figure 1.1: Two ways to evaluate the horizontal drift velocity based on the horizontal trajectory or Lagrangian velocity: (a) Linear-fit method: Time history of the horizontal trajectory $x_p(t)$ of objects with initial position x_{P0}. (b) Frequency-filter method: Different components of the horizontal Lagrangian velocity of objects.

papers. The aim of this thesis is to understand and develop suitable models for identifying the mechanisms underlying the transport of finite-sized, differently-shaped floating objects by surface gravity waves in various wave conditions. The investigative approach involves employing an analytical model, numerical simulations and a laboratory study to predict and measure the drift behaviours of 2D unrestrained floating objects. The research commences with numerical simulations using a complex model. In Chapter 3, two mechanisms contributing to the drift enhancement, in comparison to theoretical Stokes drift, are identified. To provide a deeper interpretation of one of the two mechanisms, a mathematical model is derived and compared with the numerical results. The validity of this mechanism is further confirmed through laboratory experiments presented in Chapter 4. Chapter 5 performs an in-depth examination of the identified mechanism associated with viscosity and vorticity effects. A detailed synopsis and the contribution to the literature of each chapter are provided below.

Chapter 2: Literature review

This chapter provides a review of the literature and background pertaining to mass transport on the ocean surface. The discussion starts with an overview and examination of the derivation of Stokes drift to the leading order in deep water, establishing a fundamental context for subsequent exploration. The chapter further details the existing literature encompassing numerical, experimental and analytical studies specifically focusing on floating objects. These objects span

a spectrum of sizes, ranging from infinitely small, to intermediate and large objects. As the object size increases, the dominant mechanisms influencing their behaviour change, necessitating corresponding adjustments in the employed methodologies and models to capture the intricacies of those critical physics. The chapter thus reviews these various approaches and models and underscores the existing research gap regarding the transitional size of the object and the limited efforts in numerical modeling for this specific research topic. In response to this gap, the chapter introduces a hybrid and complex numerical model called QaleFOAM employed in this study to numerically investigate the problem and advance our knowledge of mass transport on the ocean surface.

Chapter 3: Surface gravity wave-induced drift of floating objects in the diffraction regime

Numerical modeling of the drift behaviour of objects has been carried out using QaleFOAM. We examine the net drift of floating objects under the influence of unidirectional regular waves in deep water for objects of relative size l/λ ranging from 1% to 30% where λ is the wavelength. QaleFOAM employs a fully nonlinear potential-flow model to capture the wave field and a Navier–Stokes (NS) model to calculate the detailed flow patterns near objects, our model encompasses both viscous effects and nonlinear wave-body interactions (Gong et al., 2020; Yan et al., 2020b). The validation of the numerical model is first conducted with wave fields and small objects in regular waves, of which the characteristic length is around 1% of the wavelength. The model predicts Lagrangian behaviour of both the fluid particles and small objects, a net drift equal to Stokes drift in the absence of Eulerian mean flow. A series of simulations of objects of different sizes have been conducted on regular waves for both box and sphere shapes in the presence and absence of viscosity in the simulations. The effects of size and shape are investigated with different submergence. The effect of wave steepness is further explored. Viscosity is introduced into the model, and its influence on the mean transport has been investigated. An enhanced drift velocity is found for large objects with deep submergence, and it is shown that the shape of the submerged part of the object plays a role in the drift change. Two mechanisms have been identified for the enhanced drift, one is in the diffraction regime and the other is associated with viscosity.

Then a theoretical diffraction-modified Stokes (DMS) drift is proposed. In this case, we use

the simplified Boundary Element Method (BEM) based on the linearized potential-flow theory to generate the linear wave fields solving the (linear) wave-body interaction problem. The simple Green's function method is applied to compute the radiation and diffraction problems. Consequently, the added mass, radiation damping and wave exciting forces are obtained, and the equations of motions of the objects are established and evaluated. We derive a diffraction-modified Stokes drift akin to Stokes (1847), but based on the combination of the incident, diffracted and radiated wave fields calculated by the BEM model. To validate the model's ability to solve the linear wave field and thus predict the correct linear motions, the added mass, radiation damping and wave exciting forces are calculated in three specific examples and compared with those obtained by an existing theoretical model for linear motions and, a good agreement is achieved. The diffraction-modified Stokes drift model predicts Stokes drift for very small objects, which validates the model for drift prediction. Furthermore, a series of simulations have been conducted for objects with different sizes, submergence and shapes (square and semicircular) and the effects of size, shape, submergence as well as wave steepness are investigated. The corresponding surface elevation distribution around the objects and linear motion of the objects are compared with the results from QaleFOAM.

The results from the proposed model and QaleFOAM are in good agreement. Compared to the complex QaleFOAM model, the theoretical model predicts drift with good accuracy but much less effort, and offers a better understanding behind enhanced drift from a physical tuition perspective. This theory explains both qualitatively and quantitatively the increase in drift. Two effects become clear. First, the increased vertical oscillatory motion of the object causes a greater contribution from the incident wave field to the Stokes object drift (which refers to the drift of objects predicted by the proposed DMS model). Second, the combination of diffracted and radiated waves makes an additional contribution to the Stokes object drift that is not present when the object is small.

Novelty: to the best of the author's knowledge, this is the first attempt to numerically explore wave-induced drift with a complex numerical model that accommodates both diffraction and viscosity. Within this context, two mechanisms are identified to explain the observed enhanced drift compared to theoretical Stokes drift. The second mechanism leads to the development of a new theoretical diffracted-modified Stokes (DMS) model based on a new theory,

incorporating incident, diffraction and radiation fields to predict the wave-induced drift.

Chapter 4: Laboratory study of surface gravity wave-induced drift of floating objects in the diffraction regime

Laboratory studies of two-dimensional type experiments are conducted to examine the drift behaviour of the objects of relative size $l/\lambda = [2.6\%,27\%]$ in regular deep-water waves. This work fills a gap in the drift investigation in the literature (i.e., ranging from very small objects to intermediate object sizes near or crossing the turning points value in Harms (1987)). The design of the object is critical to ensure the experiment is two-dimensional. Substantial preliminary work was carried out before designing the experiment including wave and object design. The wave tank characterisation is carried out in Appendix A. We use carefully designed objects equipped with low-friction plastic light bearings to ensure the free movements of the object in three desirable degrees of freedom while constraining the other three undesirable degrees of freedom (i.e., make the experiment two-dimensional). We verified the Lagrangian drift behaviour of very small objects in a two-dimensional experiment by reporting Stokes drift after deducting the Eulerian mean flow in the tank. We further explore the enhanced drift behaviours of larger objects in different wave steepness and the local surface elevation distributions. The measured data are compared with the results from the diffraction-modified Stokes drift model in Chapter 3 and from an empirical formula by Harms (1987). Good agreement has been found for small objects in low wave steepness. The effects of size and wave steepness have been investigated and the discrepancy between the measured data and theoretical models is explained.

Novelty: to the best of the author's knowledge, this is the first 2D experiment that validates the Lagrangian behaviour of small 2D floating objects and the first to conduct a 2D experiment to systematically investigate the drift behaviour of small objects, spanning from small to intermediate and relatively large sizes. This laboratory study also provides experimental evidence of the mechanism identified by Chapter 3.

Chapter 5: Vorticity and turbulent effects on surface gravity wave-induced drift of bluff bodies

Despite the large body of work on the vorticity and turbulent effects around surface-piercing objects that are either fixed or moored in flows with waves (Palm et al., 2013; Hann et al., 2015;

Palm et al., 2018; Liu et al., 2020), rather less work has been done for the freely floating objects. The primary purpose of Chapter 5 is to investigate the vorticity and turbulent effects induced by the geometry of the object along with the viscous effect on the forces and mean drift velocity of freely floating objects with different sizes and in various wave steepness. The geometry of the object is varied with different corner shapes and submergence. Velocity and pressure fields in the flow fields as well as the vorticity structure are evaluated and analyzed in various cases. We use the hybrid model QaleFOAM (introduced in Chapter 3) to conduct three types of simulations for each case: turbulence modeling, laminar modeling and inviscid simulation with the purpose of investigating turbulent and viscous effects. For turbulence modeling, Reynolds averaged Navier–Stokes (RANS) equations are solved. Following Yu and Li (2013); Li et al. (2018), we use a $k-\omega$ SST turbulence model for our RANS simulations. Laminar modeling solves the incompressible Navier–Stokes equations without any turbulence modeled, which is used to identify and analyze the turbulent flow effects. Inviscid simulations are based on incompressible Euler equations, which are compared with viscous results (using turbulent and laminar modeling) to identify and quantify the viscous effects. Euler simulations do not include the viscosity effects but support flow rotation (i.e. vorticity). Though the Euler equations are not capable of modeling boundary-layer separation effects as there is no near-wall shear stress, it is widely used to study the vortex generated at the regions where a high gradient of pressure and velocity occurs due to high wall curvature, i.e. geometrically induced vorticity, which is inherently triggered by the numerical viscosity from the discretization (Spalart, 1998; Palm et al., 2018). We report a significant difference in the mean drift of relatively large objects due to the corner type (sharp corner vs round corner).

Novelty: this work is the first effort to examine the turbulent and vorticity patterns associated with wave-induced time-averaged drift (a quasi-steady problem) and simulate the flow around unrestrained 2D bluff objects subjected solely to incoming waves.

Appendix: testings on the new Wave and Current Flume at Oxford

As mentioned in Chapter 4, the experiments in this thesis were done in a new wave tank, which required significant preliminary work. There are two main aspects of testing: one with the dimensions of the wave tank (of vital importance is its constant width along the whole tank) and the other associated with the wave properties. We will first give detailed measured

data of the tank dimensions at different sections and report its manufactured tolerance (this is critical as we design our objects and experiment based on this). Then we will present the wave properties covering frequencies ranging from 0.5 Hz to 1.8 Hz with a 0.1 Hz step. For each frequency, we vary the wavesteepness ranging from 0.02 to 0.35. Although not novel in itself, reporting this characterization of a new facility will be valuable to future users of the facility.

1.4 List of publications and author's contribution

Chapter 3 of this thesis is based on a peer-reviewed journal paper. Chapter 4 has been submitted to a peer-reviewed journal, and Chapter 5 is in preparation to be submitted to a peer-reviewed journal paper. Both parts of Chapters 3 and 4 have been published as peer-reviewed conference papers (37th IWWWFB2022 and 39th IWWWFB2024). Material from a combination of Chapters 3 and 4 has been presented in an international conference. Additionally, I contributed to the numerical solver development for Chapter 3, resulting in co-authorship as the second author in a peer-reviewed journal paper (not part of this thesis). Alongside Chapter 4, my participation in a large-scale experimental campaign led to co-authorship as the fourth author in an experimental paper and a joint author of another journal paper (not part of this thesis). In total, I have submitted (or intended to submit) or published three first-author journal papers, two first-author conference papers and three co-authored journal papers at the time of submission of this thesis. They are as follows, where I point out the contributions that I made to each paper:

First-authored journal papers

Xiao Q., Calvert R., Yan S. Q., Adcock T. A. A., and van den Bremer T. S., 2024. Surface gravity wave-induced drift of floating objects in the diffraction regime. Journal of Fluid Mechanics, 980, A27. As the main author of this paper, I contributed to numerical solver development, ran the simulation cases, conducted the data analysis and interpretation, and wrote the manuscript. This paper forms Chapter 3 of this thesis.

Xiao Q., McAllister M. L., Adcock T.A.A., van den Bremer T. S. (under review). Experiment study on wave-induced drift of floating objects with finite size. Journal of Fluid Mechanics. As the main author of this paper, I designed and carried out the experiments, collected and processed the data, and wrote the manuscript. This paper forms Chapter 4 of

this thesis.

Xiao Q., Yan S. Q., Adcock T. A. A., van den Bremer T. S. (2024). Vorticity and turbulent effects on mean drift of bluff bodies. (in preparation)). As the main author of this paper, I designed and ran the numerical cases, analyzed and interpreted the data and wrote the manuscript. This paper forms Chapter 5 of this thesis.

Co-authored journal papers conducted as part of the DPhil but not included in the final thesis

Eeltink D., Calvert R., Swagemakers J. E., **Xiao Q.**, and van den Bremer T. S., 2023. Stochastic particle transport by deep-water irregular breaking waves. Journal of Fluid Mechanics, 971, p.A38. As a contributing author of this paper, I contributed to a large part of the experiment and data collection.

Li Q., **Xiao Q.**, Yan S. Q., etc. (In preparation). Adaptive coupling approach for modelling wave-structure interaction. Renewable Energy. As a contributing author of this paper, I identified the problem of ineffective wave-absorbing boundary and coupling methods, ran the simulations, and provided feedback and took part in discussions.

Eleveld M., Bakker W., Felício J., Soares da Costa T., Vala M., Marques P., Leonor N., Moreira A., Costa J., Caldeirinha R., Matos S., Fernandes C., Fonseca N., Simpson M., Marino A., Gandini E., Camps A., Perez Portero A., Gonga A., Burggraaff O., Garaba S., Salama M., **Xiao Q.**, Calvert R., van den Bremer T. S., de Maagt P. (under review). Assessing the detection of floating plastic litter with advanced remote sensing technologies in a hydrodynamic test facility. Scientific Reports. As a contributing author of this paper, I was part of a larger team conducting the experiments and data collection.

Conferences

Xiao Q., Calvert R., Yan S. Q., Adcock T. A. A., van den Bremer T. S. The wave-induced drift of objects of finite size. In the 37th International Workshop on Water Waves and Floating Bodies, Giardini Naxos, Italy, Apr., 2022 (Oral presentation and conference paper).

Xiao Q., Calvert R., McAllister M., Yan S. Q., Adcock T. A. A., van den Bremer T. S. Study of the enhanced wave-induced drift of large floating objects in the diffraction regime. Ocean Sciences Meeting, New Orleans, USA. Feb. 2024 (Oral presentation).

Xiao Q., McAllister M., Adcock T., van den Bremer T. S. Laboratory study of wave-induced

drift of large floating objects. In the 39th International Workshop on Water Waves and Floating Bodies, 14-17 April 2024, St Andrews, Scotland. (Oral presentation and conference paper).

Chapter 2

Literature Review

2.1 Overview

An understanding of mass transport on the ocean surface is crucial within the context of marine ecosystem health, geophysics , climate and ocean-related industries. Examples include the transport of small biomass, plastic, oil patches and large ice floes, all of which are considered to impact the marine environment. A prediction of drift behaviour is necessary for effective oil spill mitigation (Olascoaga and Haller, 2012; Gough et al., 2019; Law and Huang, 2007). Moreover, a comprehensive understanding of the migration of macro-algae, sediment and pollutants is essential for informed environment management (Brooks et al., 2019; Law et al., 2010; Szanyi et al., 2016). The drift of vessels and offshore oil platforms is of particular interest to ocean engineers. In addition, an assessment of drift behaviour is vitally important for search-and-rescue operations and recovery missions at sea (Breivik et al., 2011, 2013; Bellomo et al., 2015).

Generally, three key mechanisms contribute to drift in the ocean: currents, wind and waves. These mechanisms have been extensively explored (see Martinez et al. (2009); Olascoaga et al. (2020); EI-Tahan et al. (1983)). Arikainen (1972) investigated the wind- and wave-induced drift for ice floes in the tens of meters size range, emphasizing the substantial contribution of wave-induced drift that should not be neglected. Even in the presence of strong winds, Wadhams (1983); Perrie and Hu (1997) suggest that wave-induced drift may still be dominant. The significant impact of ocean waves on the drift speed of floating drifters is demonstrated by Nath (1978). This thesis focuses on wave-induced transport, aiming to establish a robust numerical model that simulates the time-averaged wave-induced drift motions of freely floating

objects across various sizes, densities and shapes.

In the sections below, this thesis commences with a theoretical introduction to the concept of Stokes drift, which represents the mean or time-averaged drift of a fluid particle in waves. There, a fluid particle is regarded as a perfect Lagrangian tracer of infinitely small size. However, the finite size, density, and shape of floating objects can lead to different behaviours compared to such idealized fluid particles. Consequently, a velocity difference between the fluid and the object may arise, giving rise to a drag force acting on the object. Additionally, the relative motions of the object to the water surface including surge and heave motions (Meylan et al., 2015; Calvert et al., 2021) also necessitate consideration.

Depending on the relative size of the object to the wavelength, two methods are typically employed to examine the wave-induced motion of floating objects. One involves potential-flow theory for large objects (Haskind, 1946) and the other employs Morison's equation (Morison et al., 1950) for small objects. Therefore, §2.2 will review the literature exploring the drift of small floating objects, encompassing theoretical models based on Morison's equation and related experimental investigations. This will be followed by a review of both theoretical and experimental literature examining large objects, along with an introduction of models based on potential-flow theory (§2.3).

Despite Morison's equation incorporating viscosity, including a drag force, and potential-flow theory considering the object as a no-flow boundary to the fluid field, thus addressing the diffraction problem, the time-averaged drift of floating objects, encompassing both the effects of viscosity and the disturbances induced by the objects, has not been explored in the literature.

The hybrid model, QaleFOAM, employed here takes advantage of the fast simulation capabilities of potential-flow theory for the large-scale wave field and the ability of the Navier–Stokes (NS) model to resolve viscosity effects and flow separation in proximity to the floating object. As a result, QaleFOAM is capable of capturing small-scale physics associated with viscosity and turbulence at a reasonable computational cost. A description of the hybrid model and the coupling method employed therein is given in §2.6.

2.2 Drift of small particles

In periodic surface gravity waves, the orbits of Lagrangian particles do not fully close, resulting in a net horizontal displacement in the direction of wave propagation over each wave cycle, a phenomenon known as Stokes drift (Stokes, 1847). Thus, the Stokes drift velocity $\overline{\mathbf{u}}_{SD}$ is equal to the difference between wave-averaged Lagrangian velocity $\overline{\mathbf{u}}_L$ and the wave-averaged Eulerian velocity $\overline{\mathbf{u}}_E$, which can be expressed as (Craik, 1988):

$$\overline{\mathbf{u}}_{SD} = \overline{\mathbf{u}}_L - \overline{\mathbf{u}}_E = \overline{\mathbf{u}\left(\boldsymbol{\xi}, t\right)} - \overline{\mathbf{u}(\mathbf{x}, t)}, \tag{2.1}$$

in which $\boldsymbol{\xi}(t) = (\xi_1(t), \xi_2(t))$ refers to the position of a Lagrangian particle, and $\mathbf{x} = (x, z)$ are the Eulerian coordinates for a unidirectional case.

If the fluid is assumed incompressible and inviscid with irrotational motion, then the flow can be represented by a velocity potential ϕ, and the governing equation is the Laplace equation ($\nabla^2\phi = 0$). This thesis considers linearized free surface boundary conditions and assumes $kd \gg 1$ and $\varepsilon = ka \ll 1$, in which k refers to wavenumber, d is the water depth, ε wave steepness and a the wave amplitude. Under these assumptions, a deep-water wave with small wave amplitude is considered, and $\phi = (a\omega/k)\sin(kx - \omega t)\, e^{kz}$. According to Phillips (1966), for the horizontal direction, this thesis employs "Taylor" expansion of the average Lagrangian velocity at the position $\boldsymbol{\xi} = (\xi_1, \xi_2)$ around $\mathbf{x} = (x, z)$. The velocity is denoted by $\mathbf{u}(\mathbf{x}, t) = (u(\mathbf{x}, t), v(\mathbf{x}, t))$ with $u(\mathbf{x}, t)$ representing the horizontal component of the velocity. Then, by reserving the first order quantity and ignore anything higher than the order of O^2, the horizontal component of Stokes drift velocity is obtained as:

$$\begin{aligned}
\overline{u}_{SD} &= \overline{u}_L - \overline{u}_E = \overline{u(\mathbf{x}, t) + \left((\xi_1 - x)\tfrac{\partial^2 \xi_1}{\partial x \partial t} + (\xi_2 - z)\tfrac{\partial^2 \xi_1}{\partial z \partial t}\right) + ... + O^n} - \overline{u(\mathbf{x}, t)} \\
&\approx \overline{\left(-ae^{kz}\sin(kx - \omega t)\right)\left(-a\omega k \sin(kx - \omega t)\, e^{kz}\right) + \left(ae^{kz}\cos(kx - \omega t)\right)\left(a\omega k \cos(kx - \omega t)\, e^{kz}\right)} \\
&= a^2 \omega k e^{2kz} = \varepsilon^2 \tfrac{\omega}{k} e^{2kz}.
\end{aligned} \tag{2.2}$$

Equation (2.2) suggests that the time-averaged horizontal velocity component, first shown in Stokes (1847), is of $O\left(k\omega a^2\right)$ and increases with the wave steepness at a quadratic rate.

There is a rich literature in the theoretical and experimental study of Stokes drift (see reviews in van den Bremer and Breivik (2018)). The seminal work of Stokes (1847) predicted

non-zero mean Lagrangian velocities when the mean (time-averaged) Eulerian velocities in the fluid might be zero by employing the approximation theory derived and formalized for irrotational water waves. Webb and Fox-Kemper (2011) conducted leading-order Stokes drift approximations and investigated the relationship between Stokes drift and different moments of the wave spectra under the assumption of unidirectional waves. They highlighted the third moment of the wave spectrum as the most reliable estimator of Stokes drift and extended their analysis to directional random seas, investigating the effects of wave spreading directionality and multi-directional waves on Stokes drift approximations (Webb and Fox-Kemper, 2015). van den Bremer and Taylor (2015) conducted an approximate analysis by using a multiple-scales expansion (a separation of fast and slow scales expansion) to evaluate the leading-order Stokes drift and return flow for wave groups in realistic sea states. Their investigation considered the impact of finite depth and wave directionality on the return flow and net transport of Lagrangian particles within wave groups. They revealed that for Lagrangian particles near the free surface in directional spreading seas that are not very shallow, the return flow is small and the Stokes drift dominates.

In experimental studies, controlling the effects brought by the finite length of the tank and wave breaking poses challenges (Bagnold, 1947; Longuet-Higgins, 1953; Grue and Kolaas, 2017; van den Bremer et al., 2019; Monismith, 2020). The presence of two ends of the wave flume, housing wave-absorbers and wavemakers where vorticity can be generated, along with the oscillating bottom and surface boundary layers, results in no net flow for measured cross-sections in the tank, thus influencing the mean Eulerian flow. Van den Bremer et al. (2019) studied Lagrangian trajectories under unidirectional wave groups with small amplitude in deep water. For irrotational water waves, they provided experimental evidence confirming that, in the absence of other flows, accurate calculations of mean Lagrangian velocity could be achieved from the lowest-order (first-order) fluid field.

2.3 Drift of small floating objects

For the analytical analysis of the drift behaviour of small objects, it is commonly assumed that the disturbance generated by the presence of the object (diffraction) could be neglected, as suggested by Morison et al. (1950); Wadhams (1983)). Morison's equation considers the motion

of the object at its center of mass and calculates the total wave forces as the sum of the added mass effect (resulting from the acceleration of the water surrounding the object) and the drag effect (caused by the velocity difference between the object and surrounding water). Rumer et al. (1979) conducted pioneering work by extending Morison's equation to study wave-induced drift of small floating objects including inertia, buoyancy, added mass, and drag effects. In their approach, the water free surface is regarded as an oscillating slope. The balance normal to the slope is achieved by the gravity force component and buoyancy, while the tangential component induces the drift movement of the object, termed the slope-sliding effect. In Rumer's model (specifically, in the section on 'Transport by Long Waves'), the equation of motion in the x-direction (the direction of wave propagation) for objects on the surface of unidirectional waves is:

$$\begin{aligned} &m(1+C_m)\tfrac{d^2x}{dt^2} = F_g + F_w = \\ &-\tfrac{1}{2}m(g+\tfrac{\partial^2\zeta_w}{\partial t^2})\sin\left[2\left(\tan^{-1}\tfrac{\partial\zeta_w}{\partial x}\right)\right] + \rho_w C_w A\left|u_{swx}-u\right|(u_{swx}-u), \end{aligned} \tag{2.3}$$

where m refers to the mass of the object, C_m represents the added mass coefficient, F_g, F_w stand for the gravitational force component due to the water surface tilt and drag force at the wetted body surface (the interface of water and object) in x-direction, respectively. $\zeta_w = \zeta_w(x,t)$ is the surface wave elevation relative to the mean water level, ρ_w refers to the water density, C_w is drag coefficient, A is wetted surface area, u_{swx} is x-direction surface water velocity and u is the x-component of object velocity.

Wilson (1982) employed a time-domain numerical model based on Morison's equation to predict the motions and forces of buoys in various ocean environments. Shen and Ackley (1991) applied the slope-sliding concept to study wave-induced ice-floe collisions on deep-water waves. In their model, the forces and moments are estimated by dividing the bodies into discrete elements and applying the Morison-type equation to each element. Shen and Zhong (2001) employed an approximate analytical method that considers wave reflection. They considered specific scenarios where added mass and drag coefficients are alternately set to zero or both set to zero. Grotmaack and Meylan (2006) compared two theoretical models by Rumer et al. (1979) and Marchenko (1999), which differ in the way that the gravity sliding force derives, and noted an incorrect use of vertical inertial force in Rumer's model. They established a new model based on slope-sliding models and verified the correctness of the model by Marchenko (1999).

Huang et al. (2016) extended the slope-sliding model to incorporate object movement, including heave motions. Their study indicated that the slope-sliding model tends to underestimate the wave-induced drift of small floating objects. Their study also showed that the drift velocity is sensitive to the drag coefficient associated with skin friction. Additionally, to investigate the transport of finite-size floating objects in deep-water waves, Calvert et al. (2021) used a transformed coordinate system to ensure the dynamic buoyancy force is in the normal direction to the free surface. Using perturbation methods, they derived a closed-form solution for the drift of round floating objects. Enhanced drift motions are found and explained by two mechanisms. The first is the change of magnitude of the linear orbit, and the second is the dynamic buoyancy force component normal to the local free surface.

For experimental investigation, the problem of the drift velocity of small floating objects on periodic waves with different wave steepness was explored by Nath (1978). They found that the drift speeds of small floating objects for low wave amplitudes are approximately equal to the Stokes drift. Huang et al. (2011) conducted an experimental exploration of drift motions, considering different shapes of objects at two different degrees of submergence, subsequently with different wave-induced inertial forces and drag forces. Larger drift velocities than the Stokes drift are observed for all shapes of objects, with objects having greater submergence exhibiting larger drift velocities regardless of their shape. Furthermore, Calvert et al. (2021) examined the transport of spherical floating bodies with different sizes and densities. Their study revealed that the transport rates of objects with different size and density differ, with larger and heavier buoyant objects displaying more enhanced drift motions.

2.4 Drift of large floating objects

When the relative size of the object to the wavelength is significant, accurate predictions necessitate consideration of the disturbance to the fluid due to the presence of the objects. Consequently, the velocity potential, governed by the Laplace equation, must satisfy various conditions, including the free surface condition (linearized or fully nonlinear), bottom conditions (finite depth or deep water), outgoing-wave radiation condition, and a body condition $\frac{\partial \phi}{\partial n}\big|_{S_B(x,y,z,t)} = \mathbf{n} \cdot \boldsymbol{\nabla} \phi = U_n$. Wave forces and moments exerted on the objects exposed to an incident wave system comprise both unsteady exciting forces, giving rise to unsteady oscillations,

and steady forces due to nonlinear effects. The steady forces, also called drift forces, influence the magnitude and direction of objects' drift velocity, causing an unrestrained floating object to undergo a steady slow drift motion in the direction of wave propagation. Also, in a sea state described by a wave spectrum containing different wave frequencies, the object experiences slow-drift oscillations induced by the difference frequency second-order forces in addition to the rapid oscillations.

Suyehiro (1924) was the first to note the existence of mean wave forces acting on floating vessels from experiments and attributed this force to the reflection effects. Watanabe (1938) proposed that the mean force was of second order and induced by the interaction of incident waves and first-order motions. He expressed mean sway forces in regular waves as the product of first-order roll motion and the Froude–Kryloff component of the roll moment. Considering the mean component of the second-order wave forces in the direction of wave propagation, Havelock (1942) presented expressions involving the interaction between incident wave forces and ship motions.

There are two main ways to calculate second-order forces. One can deduce mean second-order forces in terms of the far-field disturbance of the object based on momentum and energy considerations. This relies on the concept that the change in momentum flux of the fluid is equal to the mean force acting on the object. The other solves second-order disturbance in the near field by direct integration of pressure on the exact wetted surface. Newman (1967) utilized momentum relations to relate drift forces with far-field potential and derived the second-order horizontal steady forces for freely floating bodies in regular waves. In irregular waves, slow drift forces were expressed in terms of a quadratic transfer function of different wave components by Newman (1974), and the steady drift force transfer function was used to calculate the whole quadratic transfer functions.

Pinkster and Hooft (1976); Pinkster and Van Oortmerssen (1977) and Pinkster and Huijsmans (1982) calculated several parts of the mean and low-frequency forces in different directions in regular and irregular waves by directly integrating pressure on the object. Their results were compared with related experiments, achieving reasonable agreement. Expressions of mean and low-frequency second-order forces in terms of time-independent quadratic transfer functions were given by Pinkster (1980) along with comparisons to other analytical results. The

quadratic transfer function was split into contributions arising from five parts: I) a first-order relative wave elevation: $-\frac{1}{2}\rho g \int_{wl} (\zeta^{(1)} - z^{(1)})\vec{n}\mathrm{d}l$, where the superscript $^{(1)}$ denotes corresponding first-order terms, ζ is the surface elevation, z represents the vertical motion relative to the mean water surface, wl refers to the waterline, and $\vec{n}$ is the outward-pointing vector normal to the waterline; II) a pressure drop induced by first-order velocity; III) pressure due to the product of first-order motion and the gradient of first-order pressure; IV) products of first-order angular motions and inertial forces; V) second-order potentials. A detailed analysis of each contribution from these five components was defined and compared for the mean drift force for a freely floating hemisphere in deep-water waves (propagating in the x direction). It is found that regarding the contribution of component I related to relative wave elevation, the magnitude is about twice the total force with the same sign in the direction of wave propagation. Thus, it is believed that if a large difference in relative wave height between both sides of the object exists, this component would be large.

Faltinsen and Løken (1977, 1979) precisely formulated the problem to second order, which includes not only the components arising from products of first-order quantities but also effects induced by second-order velocity potential. Green's theorem was utilized to calculate a solution, and the results of mean and low-frequency transverse forces on two-dimensional cylinders are presented. Ogilvie (1983) gave a survey of the existing methodology for predicting steady and low-frequency forces on marine structures and presented a complete and complicated formulation for second-order wave exciting forces and motions and thus the mean drift forces based on second-order theory. Agnon et al. (1988) carried out both far-field and near-field analysis for slow drift of small displacement of a floating cylinder in narrow-frequency band waves.

Simplified calculations of mean and low-frequency slow drift force have been motivated by the complexity of the problem. In shallow water, Pinkster and Huijsmans (1992); Stansberg and Kristiansen (2011) neglected the interactions between linear waves in incident, diffraction and radiation problems but took into account the effects associated with the setdown phenomenon. Conversely, in deep water, Chen (1994) neglected the free surface integral calculations and this approximation has been shown to work well in deep water. Pessoa and Fonseca (2015) carried out experimental and numerical investigations of problems in bichromatic waves and unidirectional irregular waves. They gave an assessment of different approximation methods

for the second-order low-frequency forces and motions at various water depths. It is shown that the second-order velocity potential cannot be neglected in shallow water, whereas in cases with small difference frequencies, it is reasonable to only consider the second-order velocity potential related to the incident wave.

All above studies focus on the calculation of the steady force when the object's drift speed is zero and/or on the calculation of motion when an object is moored. They do not (directly) predict the drift motion of a freely floating object. The time-averaged drift evaluated in this thesis is a quasi-steady state instead of a net force in the direction of wave propagation. Typically, the objects considered in the above studies are three dimensional with relatively large sizes, often comparable to the wavelength. Moreover, few studies (e.g., Newman (1967)) have examined cases in following waves where objects are travelling in the direction of wave propagation (cf. ships), characterized by heading angles of 0° (most of the cases are in oblique waves or head waves). A floating object travelling with a constant velocity in calm water experiences drag, reflecting the energy required to push the fluid out of the way of the object, known as the wave-making resistance (Michell, 1898; Havelock, 1909). In principle and analogously to this wave-making resistance, the so-called wave drift damping force (Nossen et al., 1991; Aranha, 1994), which acts on a slowly drifting object, could balance the drift force discussed above, perhaps aided by a further viscous or turbulent drag term in realistic flows, leading to force equilibrium and resulting in steady drift motion. However, the authors are unaware of existing work that uses such an equilibrium of drift and drift damping forces to obtain estimates of the (enhanced) drift of floating objects and note that the required analysis would not be straightforward based solely on existing work (e.g., Nossen et al. (1991); Aranha (1994)).

2.5 Drift of objects of various sizes

The mechanism of wave-induced drift motions and speed varies with the relative size between the object and the incoming wavelength. Sections §2.3 and §2.4 present work done on two ends of the problem, covering either the short wavelength problem or the long wavelength problem. However, some studies have examined the drift behaviours of objects ranging from small size to large size, covering the entire wave range. Tanizawa et al. (2002) conducted a series of experiments on two-dimensional and three-dimensional floating bodies in regular and irregular

waves. Their measurements led to the development of an empirical formula for estimating wave-induced drift speed across the entire wave range. It is shown that for a small object (i.e., in long wavelengths), it follows the Stokes drift and the drift speed is proportional to the square of wave steepness, while for a large object (in short wavelengths), its drift is influenced by reflected waves. Its drift speed depends on the equilibrium of the wave-induced drift force and fluid drag and is proportional to the wave steepness. On the basis of these findings, they proposed a second-order polynomial equation for drift speed prediction:

$$u/c = a\epsilon + b\epsilon^2, \tag{2.4}$$

in which u represents the mean drift velocity, c refers to the wave celerity, ϵ is the wave steepness, a, and b are the coefficients of the linear and quadratic terms, respectively.

He et al. (2016) experimentally investigated the nonlinear behaviour of two-dimensional freely-floating objects in regular waves with various wavelengths. Their observations for large-draft objects are consistent with those reported in Tanizawa et al. (2002). They found that for small objects, the drift speed increases quadratically with wave steepness. Enhanced horizontal drift speeds are observed for large objects, with drift enhancement increasing linearly with wave steepness. Furthermore, comparisons between experimental data and results from the slope-sliding model by Grotmaack and Meylan (2006) revealed that the slope-sliding model is not capable of accurately capturing the drift enhancement. The significant differences, observed between the experimental data and the Stokes drift for large objects, indicate that "Stokes drift" has been altered more significantly for large objects compared with those of smaller objects. Besides, they have noticed that the oscillation periods of horizontal, vertical and rotational motions are longer than wave periods and the discrepancies are due to the mean drift motions. Le Boulluec et al. (2008) proposed a simplified theoretical model to calculate the steady drift velocity in regular and irregular waves. The simplified model takes into account second-order drift forces based on potential flow theory and viscous drag, which is of Morison-type formulation. A series of experiments and numerical simulations were conducted for steady drift velocity of cylindrical and box-shape objects with different aspect ratios and submergence. The size of objects in their studies mainly ranges from 10% to 30% of the wavelength.

It was previously believed that when an object is smaller than 20% of the wave length, the

disturbance induced by the object could be ignored (Morison et al., 1950; Wadhams, 1983). Therefore, Morison's equation and slope-sliding model which do not consider wave diffraction effects, can be applied to such objects. For larger objects (i.e., those larger than 20% of the wave length), potential flow theory is used. This 20% threshold is based on the linear motion of objects, whereas the drift examined in this thesis is a second-order effect. Thus, the threshold size might not apply and diffraction effects might be important even for objects smaller than 20%.

2.6 QaleFOAM—hybrid model

Despite the rich literature and extensive investigations presented in the previous sections, there has been limited effort to establish a robust fully nonlinear numerical model for simulating the time-averaged wave-induced drift motions for freely floating objects. On the one hand, the drift of small objects in §2.3 is solved without considering the disturbance caused by the presence of the object. On the other hand, for the drift of large objects in section §2.4, the boundary condition on the intersecting surface between the object and fluid is considered for the boundary-value problem, in the absence of viscosity. The interactions between waves and objects are partly or completely taken into account but only up to the second order in steepness, assuming an ideal fluid and irrotational flow. However, when objects of different scales are exposed to different wave conditions with various wave steepness, complicated physics, such as flow separation and turbulent flow, might be involved. This necessitates a more robust model capable of considering not only the interaction between objects and the fluid up to higher orders but also small-scale physics associated with viscosity and turbulence.

The work involved in Sections §2.3, §2.4 and §2.5 mainly takes the form of analytical and/or experimental investigations, with only a limited number of numerical results. Although some work related to Section §2.4 involves fully numerical simulations (e.g., Pinkster (1980)), the focus is primarily on calculating steady and low-frequency forces and moments or investigating the resonance of restrained/moored objects, rather than exploring the time-averaged drift behaviours of freely-floating objects.

Ren et al. (2015) proposed a new algorithm based on WCSPH (Weakly Compressible Smoothed Particle Hydrodynamic Method) and numerically calculated the nonlinear inter-

actions between waves and a freely floating box. This thesis study uses a Lagrangian meshless method, and attention is primarily given to the vertical oscillation of the object with simple geometries, rather than on the time-averaged drift motions over long duration. Furthermore, the problem is not well-explored in terms of the drift behaviour of floating objects of different sizes with various shapes, and densities in various wave conditions.

For nonlinear wave-structure interactions, a large number of numerical models have been developed based on an Eulerian reference frame using the finite volume method (FVM) to solve the incompressible Navier–Stokes (NS) equation. The small-scale physics associated with viscosity and turbulence and detailed flow patterns near the structure can be resolved based on the multi-phase NS equation (e.g., Xiao et al. (2013); Bai et al. (2016)). Nevertheless, due to the complexity of the governing equations and the high requirements for spatial and temporal resolution to achieve convergence and accuracy, the multi-phase NS model demands large computational resources, making it challenging to conduct large-scale and long-duration simulations for wave propagation and evolution. In contrast, models based on the potential-flow theory are widely accepted for reproducing various wave conditions and modeling the long-time evolution of waves propagating over large computational domains with little computational effort (e.g. Ma and Yan (2006); Wang et al. (2016)). Therefore, hybrid models based on function-splitting (Edmund et al., 2013), time-splitting (Wang et al., 2016) and space-splitting (Colicchio et al., 2006; Yan and Ma, 2010a) approaches have been proposed and developed to achieve accurate long-term simulations of objects on waves over large computational domains. See Sriram et al. (2014); Li et al. (2018) and Zhang et al. (2020) for reviews of the developments of various hybrid models.

The hybrid model QaleFOAM, employed in this thesis study, is based on a domain-decomposition method, which couples the QALE-FEM (Quasi Arbitrary Lagrangian-Eulerian Finite Element method) model with the InterDyMFOAM, a two-phase incompressible NS (Navier–Stokes) model in OpenFOAM (see Ma and Yan (2010); Gong et al. (2020); Li et al. (2018); Yan et al. (2020b) and references therein for details). The fundamental idea of this domain-decomposition approach is to resolve small-scale complex physics (e.g., flow separation and vortex shedding) with an accurate but expensive model within a small region near the objects where these effects play significant roles. The rest of the large domain, where these effects could be neglected,

is calculated by a simplified but cheap model. The following sub-sections provide simple descriptions of Qale-FEM, the two-phase NS model, and the coupling algorithms involved in this domain-decomposition approach.

2.6.1 Qale-FEM

Qale-FEM is based on potential-flow theory, assuming that the fluid is incompressible, inviscid and the flow is irrotational. Thus, the problem can be described by a velocity potential governed by Laplace's equation. The total velocity potential is divided into two parts: $\Phi = \mathbf{r} \cdot \mathbf{U_c} + \phi$, where $\mathbf{r}$ refers to the position vector, $\mathbf{U_c}$ is the velocity of a uniform horizontal current and ϕ is the remaining velocity potential. The boundary value problem related to ϕ is governed by Laplace's equation $\nabla^2\phi = 0$ within the fluid domain Ω_f in Qale-FEM simulation and is subjected to several boundary conditions. On the wavemaker boundaries Γ_{WM}, it satisfies

$$\begin{aligned} \tfrac{D\mathbf{r}}{Dt} &= \boldsymbol{\nabla}\phi + \mathbf{U}_c \\ \tfrac{D\phi}{Dt} &= -gz + \tfrac{1}{2}\left(|\boldsymbol{\nabla}\phi|^2 - |\mathbf{U}_c|^2\right) - \tfrac{P_F}{\rho}, \end{aligned} \tag{2.5}$$

where the pressure P_F is set to be 0. Using this formation, the nodes positioned on the free surface move in tandem with the motion of the fluid particles on the surface. However, nodes located both on the free surface and on the wavemaker boundaries might fail to satisfy both boundary conditions when the current is non-zero. To address this issue, as an alternative to remeshing at every time step as in Ryu et al. (2003), a scheme is employed to move the free-surface nodes. This scheme operates on a principle akin to an arbitrary Lagrangian-Eulerian formulation. Subsequently, the horizontal velocity in the x-direction u (and in the y-direction for a three-dimension problem) is then written as:

$$u = \beta(\frac{\partial\phi}{\partial x} + \sigma U_{cx}), \tag{2.6}$$

where σ and β are weighting coefficients, ranging from 0 to 1, U_{cx} is the value of horizontal velocity of the uniform current. The corresponding modified free-surface boundary conditions

are given by:

$$\begin{aligned} \frac{d\zeta}{dt} &= \frac{\partial \phi}{\partial z} - (\boldsymbol{\nabla}\phi + \mathbf{U}_c + \mathbf{v}) \cdot \boldsymbol{\nabla}\zeta \\ \frac{d\phi}{dt} &= -\tfrac{1}{2}|\boldsymbol{\nabla}\phi|^2 - g\zeta - \mathbf{U}_c \cdot \boldsymbol{\nabla}\zeta - \tfrac{1}{2}|\mathbf{U}_c|^2 + \mathbf{v} \cdot \boldsymbol{\nabla}\phi, \end{aligned} \tag{2.7}$$

where $\frac{d}{dt} = \frac{\partial}{\partial t} + \mathbf{v} \cdot \boldsymbol{\nabla}$ is the time derivative and $\mathbf{v} = (v_x, v_z)$ is the velocity of the nodes. It is obvious that when $\sigma = 1$ and $\beta = 1$, (2.7) reduces to the form in (2.5). The value of the coefficients σ and β varies spatially, and details can be found in Li et al. (2018).

The boundary value problem given above is solved using the finite element method at every time step and advanced in time via a time marching procedure under specified initial conditions. To ensure the computational mesh aligns with the motion of free surface and wavemaker, a purpose-developed spring analogy method is applied, in which (2.7) governs the motion of free surface nodes for most of the time step, with re-allocation occurring at specific time interval to avoid severe separation (Yan and Ma, 2007).

2.6.2 Two-phase NS model

In the two-phase NS model, both the air and water phases are assumed incompressible and the VOF (Volume Of Fluid) method is used to identify the phases and their interfaces. In the VOF method, the location of free surface is described by the volume fraction parameter. The governing equations for the fluid in the NS domain Ω_{NS} include the continuity equation, the two-phase momentum equation (surface tension is ignored), and the transport equation for the volume fraction, they are:

$$\boldsymbol{\nabla} \cdot \rho\mathbf{u} = 0, \tag{2.8}$$

$$\frac{\partial(\rho\mathbf{u})}{\partial t} + \boldsymbol{\nabla} \cdot (\rho\mathbf{u}\mathbf{u}) = -\boldsymbol{\nabla}p + \boldsymbol{\nabla} \cdot (\mu_e \boldsymbol{\nabla}\mathbf{u}) + \boldsymbol{\nabla}\mathbf{u} \cdot \boldsymbol{\nabla}\mu_e - \mathbf{g} \cdot \mathbf{r}\boldsymbol{\nabla}\rho, \tag{2.9}$$

$$\frac{\partial \alpha}{\partial t} + \boldsymbol{\nabla} \cdot \alpha\mathbf{u} + \boldsymbol{\nabla} \cdot \mathbf{u}_c\alpha(1-\alpha) = 0, \tag{2.10}$$

where ρ is the fluid density, $\mathbf{u}$ is the fluid velocity, p denotes the dynamic pressure, μ_e represents the effective dynamic viscosity (the sum of molecular dynamic viscosity and turbulence viscosity if a turbulence model is used) and $\mathbf{u}_c$ indicates the relative compression velocity. The third term in (2.10) is an artificial compression term that is only effective within the interface region

where $0 < \alpha < 1$. On the interfaces, the density and effective viscosity are calculated by:

$$\rho = \rho_{water}\alpha + \rho_{air}(1 - \alpha), \tag{2.11}$$

$$\mu_e = \mu_{e,water}\alpha + \mu_{e,air}(1 - \alpha), \tag{2.12}$$

where $\rho_{water}, \rho_{air}, \mu_{e,water}, \mu_{e,air}$ represent the density and dynamic viscosity coefficient of water and air, respectively. $\alpha = 0$ and $\alpha = 1$ represent pure air and water phases, while the values in between represent the interface. The PIMPLE solver (a combination of PISO and SIMPLE, i.e. Pressure Implicit with Splitting of Operators and Semi-Implicit Method for Pressure-Linked Equations) is used to decouple the velocity-pressure problem. The InterDyMFoam solver is chosen here and details regarding the dynamic mesh handling method can be found in Jasak (2009). Additional information is available on the OpenFOAM website, including online documentation and related papers (Jacobsen et al., 2012; Higuera et al., 2013). When using the VOF method for multi-phase flow models, several effects might affect simulation results, such as spurious velocities and smearing, as discussed below.

Spurious velocity –For the two-phase NS model used here, the fluids (water and air) are incompressible and Newtonian (the fluids obey Newton's law of viscosity in a way that shear stress is proportional to shear rate). It is essential to establish appropriate jump conditions across the sharp interfaces between the two phases (water and air) to solve the momentum equation accurately (Huang et al., 2007; Vukčević et al., 2017; Batchelor and Batchelor, 2000). At the sharp-moving interfaces, the continuity of the velocity field is ensured by enforcing kinematic boundary conditions. Stress balance in tangential and normal directions leads to jump conditions for pressure, pressure gradients and velocity gradients due to the jump in density and viscosity across the interfaces. Implementing the equations that precisely account for these exact jump conditions while maintaining velocity and stress continuity can be complex and challenging without introducing approximations.

The momentum equation (excluding the surface tension term) in (2.9) is derived from a conditional averaging procedure (Batchelor and Batchelor, 2000). This approach considers the variable density of water and air, thus resolving the two-phase coupling between the dynamic pressure p and density ρ. In a hydrostatic case, the dynamic pressure gradient $\boldsymbol{\nabla} p$ and density

gradient $\boldsymbol{\nabla}\rho$ (both nonzero at the sharp interface) are supposed to achieve a balance. However, this balance may not be realized in the simulation model. In the scenario of a hydrostatic case, where terms related to $\boldsymbol{\nabla}\mathbf{u}$ are zero, (2.9) simplifies to:

$$\partial(\rho\mathbf{u})/\partial t = -\boldsymbol{\nabla}p - \mathbf{g}\cdot\mathbf{r}\boldsymbol{\nabla}\rho = \mathbf{S}, \tag{2.13}$$

where $\mathbf{S}$ indicates the imbalance between the dynamic pressure gradient term $\boldsymbol{\nabla}p$ and the density gradient term $\mathbf{g}\cdot\mathbf{r}\boldsymbol{\nabla}\rho$. This source term arises (i.e., becomes nonzero) during numerical solutions with segregated solution schemes (e.g., PIMPLE), leading to a temporal change in the velocity field, which accumulates over the course of the simulation. Notably, this effect is more pronounced in the air phase due to its lower density. Additionally, as denoted by Vukčević et al. (2017), the gradient discretisation schemes applied to calculate dynamic pressure and density gradient are identical for both phases and across the interfaces, leading to insufficient specific treatment for the density-discontinuity issues and contributing to erroneous results. The presence of spurious air velocities is particularly noticeable in cases where viscosity is not considered (i.e., ideal fluid). Vukčević et al. (2017) demonstrated that in a hydrostatic inviscid scenario, with an initially calm water surface and a zero-velocity field, the air velocities on the interfaces calcuated by the multi-phase solver based on conditionally averaged equations could reach values as high as 1500 after the solution of momentum equation, and 0.0015 after pressure correction steps (with the ideal value being 0) after a single time step.

Smearing effect –The VOF method is widely used for simulating moving interfaces in multi-phase problems due to its excellent mass conservation properties (Youngs, 1982; Jacobsen et al., 2012; Higuera et al., 2013). It is an Eulerian method, and the fluid moves on a fixed reference frame, making it challenging to precisely capture the location of the exact free surface on a fixed grid system. Consequently, a numerical smearing effect occurs, where the free surface is situated between some grid points, potentially losing its sharp discontinuous nature during simulations. This is particularly noticeable when significant free surface deformation is present (Kim and Lee, 2003). Several techniques are proposed and developed to mitigate the smearing of interfaces (Kim and Lee, 2003; Ubbink, 1997; Ubbink and Issa, 1999). In our models, we have adopted the approach outlined by Kim and Lee (2003) to counteract this effect.

2.6.3 Coupling scheme

The coupling approach includes weak and strong coupling, namely one-way coupling (Hildebrandt et al., 2013; Yan and Ma, 2010a,b) and two-way coupling (Sriram et al., 2014; Yan et al., 2017). In this thesis study, one-way coupling is employed, where the NS model at the interfaces only takes the solutions from the Qale-FEM solver but does not feed its solutions back. The initial step in establishing successful coupling is to achieve data exchange between the two solvers. In Qale-FEM, the physical quantities defined and solved include velocity potential Φ and surface elevation ζ. In the NS model, however, velocity $\mathbf{u}$, pressure p and volume fraction α are key variables. To set up a bridge to relate these quantities, the definitions of velocity potential and Bernoulli equation help to relate velocity, velocity potential and pressure, which can be expressed by:

$$\mathbf{u}(x,y,z) = \begin{cases} \boldsymbol{\nabla}\phi(x,y,z) + \mathbf{U}_c & z \leq \zeta \\ \boldsymbol{\nabla}\phi(x,y,\zeta) + \mathbf{U}_c & z > \zeta, \end{cases} \tag{2.14}$$

$$p(x,y,z) = \begin{cases} -\rho_{water}\frac{\partial\phi}{\partial t} - \rho_{water}\frac{|\boldsymbol{\nabla}\phi|^2}{2} - \rho_{water}gz & z \leq \zeta \\ 0 & z > \zeta. \end{cases} \tag{2.15}$$

Considering Qale-FEM as a single-phase solver, the velocity of the air phase is determined by employing a smooth transition from the velocity of the water phase to the air phase, ensuring continuity on the free surface. Additionally, the value of the volume fraction α in the overlap zone must be defined, given by:

$$\alpha_c = A_w/A_c, \tag{2.16}$$

where α_c is the volume fraction at a surface cell c within the overlap zone, A_w is the wetted surface area and A_c is the total area of the cell. The second step is to achieve transitions and ensure the continuity/consistency of the solutions across interfaces and the surrounding area. Notably, the governing equations employed by the two solvers differ, with one based on potential theory, ignoring viscosity, while the other incorporates viscosity and turbulence effects. Additionally, the NS solver includes reflected and radiated waves by the structures, which are ignored in Qale-FEM under a one-way coupling approach. These issues are addressed by introducing a

relaxation zone or a damping zone near the interfaces. This zone absorbs the reflected waves from boundaries, preventing the fluid domain results from being contaminated and interfering with the wavemaker boundaries. It also provides a smooth transition of the solutions between the two solvers. The relaxation zone technique is to take a weighted summation of solutions from the two solvers:

$$f(x, y, z) = \gamma f_{qaleFEM}(x, y, z) + (1 - \gamma) f_{NS}, \tag{2.17}$$

in which $f(x, y, z)$ refers to related physical quantities, γ is the chosen weighting function of exponential form:

$$\gamma(r) = 1 - \frac{\exp(r^{3.5}) - 1}{\exp(1) - 1}, \tag{2.18}$$

where $r \in [0, 1]$ is defined such that γ is always 1 at the interface between the non-relaxed part and the relaxed part, and γ must fulfill $\gamma(r = 0) = 1$ and $\gamma^{(3)}(r = 0) = 1$. To achieve coupling, gradient calculations among discretized data (known velocity potential values at related computational nodes) are implemented to obtain $\boldsymbol{\nabla}\phi(x, y, z)$ at each time step and interpolations. Given that the mesh in Qale-FEM is unstructured and dynamically adapts to the motion of free surface, whereas the mesh in the NS domain is an Eulerian grid and mostly fixed, traditional finite difference schemes with regularly distributed data points are unsuitable. To address this challenge, the QSFDI (Quadric Semi-analytical Finite-Difference Interpolation) scheme (Yan et al., 2020a) has been developed. QSFDI achieves comparable levels of convergence and accuracy as the quadratic moving least square method (MLS) but demands the inversion of significantly lower-order matrices, thus requiring less computational effort.

Chapter 3

Surface gravity wave-induced drift of floating objects in the diffraction regime

3.1 Abstract

Floating objects will drift due to the action of surface gravity waves. This drift will depart from that of a perfect Lagrangian tracer due to both viscous effects (non-potential flow) and wave-body interaction (potential flow). We examine the drift of freely floating objects in regular (non-breaking) deep-water wave fields for object sizes that are large enough to cause significant diffraction. Systematic numerical simulations are performed using a hybrid numerical solver, qaleFOAM, which deals with both viscosity and wave-body interaction. For very small objects, the model predicts a wave-induced drift equal to the Stokes drift. For larger objects, the drift is generally greater and increases with object size (we examine object sizes up to 10% of the wavelength). The effects of different shapes, sizes and submergence depths and steepnesses are examined. Furthermore, we derive a 'diffraction-modified Stokes drift' akin to Stokes (1847), but based on the combination of incident, diffracted and radiated wave fields, which are based on potential-flow theory and obtained using the boundary element method (BEM). This 'diffraction-modified Stokes drift' explains both qualitatively and quantitatively the increase in drift. Generally, round objects do not diffract the wave field significantly and do not experience a significant drift enhancement as a result. For box-shape objects, drift en-

hancement is greater for larger objects with greater submergence depths (we report an increase (compared to the theoretical standard Stokes drift) of 92% for simulations without viscosity and 113% with viscosity for a round-cornered box whose size is 10% of the wavelength). We identify the specific standing wave pattern that arises near the object because of diffraction as the main cause of the enhanced drift. Viscosity plays a small positive role in the enhanced drift behaviour of large objects, increasing the drift further by approximately 20%.

3.2 Introduction

Floating marine objects, moored, propelled or freely floating, are all exposed to and influenced by the ocean environment. These objects vary greatly in size, shape and density. The assessment of wave-induced drift of floating objects in the ocean is of importance for environmental and offshore engineering alike (Arikainen, 1972; Wilson, 1982; Perrie and Hu, 1997; Law and Huang, 2007; Webb and Fox-Kemper, 2011; Meylan et al., 2015; van den Bremer et al., 2019; Monismith, 2020). Recently, there has been much interest in the topic because of concerns about marine plastic pollution (e.g., Law et al. (2010); Van Sebille et al. (2020)).

An unrestrained object floating in a surface gravity wave field will normally experience a net drift in the direction of wave propagation, known as the Stokes drift (Stokes, 1847), in addition to the oscillatory motion associated with the waves. This net drift typically only becomes relevant over long time scales due to its small magnitude (typically, of a few cm/s in the ocean). Unlike a perfectly Lagrangian tracer, whose drift is equal to the Stokes drift in the absence of Eulerian-mean flows, an object of finite size may display different behaviour, and a velocity difference between the object and an idealized (i.e., Lagrangian) fluid parcel may emerge (Santamaria et al., 2013; Meylan et al., 2015; Calvert et al., 2021; DiBenedetto et al., 2022).

The drift of small floating objects in periodic waves was investigated experimentally by Nath (1978). For small wave amplitudes, Lagrangian drift behaviour was found for very small objects, while for a spar-type drifting buoy with a deep draft enhanced drift compared to the Stokes drift was reported. Huang et al. (2011) explored the drift motion of objects of different shapes with two different submergence depths. Enhanced drift was found for all shapes, and objects with a larger submergence depth experienced a greater increase in drift regardless of

shape. The studies of Tanizawa et al. (2002) and He et al. (2016) showed that small objects behave like Lagrangian particles, following the Stokes drift, while large objects drift faster than Lagrangian particles with wave reflection off the object evident.

Theoretical models developed for wave-induced loads can be grouped into two main categories: models that take the object to be part of the boundary of the fluid domain allowing for calculation of diffraction effects based on potential-flow theory (Haskind, 1946; Faltinsen and Løken, 1979; Chen, 1994; Stansberg and Kristiansen, 2011; Pessoa and Fonseca, 2015) and a second class of models that express loads in terms of the velocity field in the absence of the object considering both viscosity (drag) and fluid inertia, for example using Morison's equation (Morison et al., 1950) (Shen and Zhong, 2001; Grotmaack and Meylan, 2006; Huang et al., 2016).

For objects of small size relative to the incident wavelength, the disturbance of the wave field by the object can be neglected, and thus Morison's equation can provide an acceptable approximation. Morison's equation is applied by considering the motion of the object at its centre of mass and calculating the total force due to the waves as the sum of the inertial force, including the effect of added mass, and the drag force (caused by the velocity difference between the object and surrounding water). Rumer et al. (1979) conducted pioneering work by extending Morison's equation to study wave-induced drift of small floating objects including inertia, buoyancy, added mass and drag effects. The concept underlying their approach is to regard the free surface as an oscillating slope. A (dynamic) force balance normal to the free surface is achieved through the combined effect of a gravity force component and buoyancy, while the tangential component of gravity causes the drift motion of the object, and this is termed the slope-sliding effect (Rumer et al., 1979). The slope-sliding concept has been applied and developed to study wave-induced motions of various objects by Shen and Ackley (1991) and Huang et al. (2016). They showed that a model that includes the slope-sliding term predicts enhanced drift but tends to underestimate the enhancement of the wave-induced drift of small floating objects compared to experiments. Also making use of a slope-sliding term, Calvert et al. (2021) used a transformed coordinate system and employed perturbation methods to derive a closed-form solution for the drift of spherical floating objects. Enhanced drift motion is explained by two mechanisms in Calvert et al. (2021). First, the magnitude of the linear

motion (normal to the free surface) of a floating particle is enhanced compared to a Lagrangian particle, and, second, the dynamic buoyancy force has a net effect when averaged over the wave cycle in a similar fashion to the slope-sliding term of Rumer et al. (1979).

To accurately predict the drift when the object is large relative to the wavelength it is essential to account for the disturbance in the fluid field caused by the presence of the object. For models based on potential-flow theory, the fluid can be described by a velocity potential, which satisfies the Laplace equation subject to boundary conditions on the wetted body's surface as well as on the free surface, bottom boundary conditions, and a radiation condition. When exposed to an incident wave field, objects experience forces and moments due to the waves. These encompass both unsteady forces, leading to oscillatory motion, and steady (or wave-averaged) forces arising from nonlinear effects. The steady forces, often referred to as drift forces, affect the magnitude and direction of objects' drift, resulting in a slow and steady drift motion unless the object is moored (Suyehiro, 1924; Watanabe, 1938; Havelock, 1942). Two approaches to calculate second-order forces are highlighted here: the first solves for the far-field velocity potential and the second solves for the near-field velocity potential. Newman (1967) utilized conservation of momentum to relate the drift forces to the far-field potential and derived the horizontal steady second-order forces on a freely floating body in regular waves. The drift forces are found to differ considerably both in magnitude and sign depending on the wavelength and direction relative to the object. Pinkster and Hooft (1976); Pinkster and Van Oortmerssen (1977) and Pinkster and Huijsmans (1982) calculated the mean (or low-frequency) forces for different directions in regular and irregular waves by directly integrating the pressure distribution on the object. Their results show that the mean horizontal force due to the relative elevation between the object and surrounding waves can be significant in certain cases. Importantly, viscosity is not included in these calculations, but may have strong effects (Huse, 1977).

This chapter examines the net drift of floating objects under the influence of unidirectional regular waves in deep water for objects that are sufficiently large to diffract the wave field. To do so, we use a hybrid numerical model that employs a fully nonlinear potential-flow model to capture the incident wave field and a Navier–Stokes (NS) model to calculate the detailed flow pattern near the object. Both viscous effects and (nonlinear) wave-body interactions are

modeled. Objects with different sizes, drafts (submergence depths) and shapes in waves with different wave steepness are investigated in the presence and absence of viscosity with the objective of understanding the effect of these variables on drift and the mechanisms involved. To help explain our results, we propose a diffraction-modified Stokes drift. In this case, we use a simplified linear Boundary Element Method (BEM) to generate the linear wave fields solving the (linear) wave-body interaction problem based on potential-flow theory, which in turn forms the basis of the diffraction-modified Stokes drift.

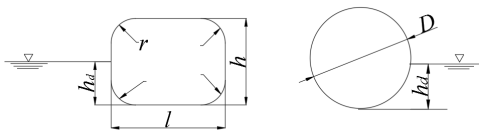
This chapter is laid out as follows. We commence with the description of our two models, the hybrid numerical model qaleFOAM and the diffraction-modified Stokes drift model in §3.3. The validation and verification of the hybrid numerical model are presented in §3.4 (convergence tests are reported in appendix 3.B). In §3.5, drift estimates based on the hybrid numerical model are presented for objects with a range of sizes, different steepnesses, and two different shapes: rectangular boxes with round corners and round objects. The effects of viscosity are explored in each case. For the largest box, different submergence depths (drafts) and different radii of the round corners (corresponding to different submerged shapes) are simulated. In §3.6, the results from non-viscous simulation of the hybrid numerical model are compared to the diffraction-modified Stokes drift model. Finally, conclusions are drawn in §3.7.

3.3 Models

3.3.1 Problem formulation

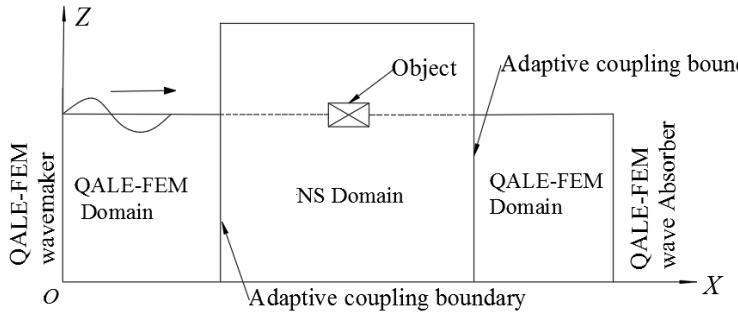
We examine the wave-induced motion and drift of objects with different size, submergence depth and shape. We consider two shapes: a round-cornered box (henceforth abbreviated as RCB) and a round object (henceforth abbreviated as RO) with dimensions shown in figure 3.1. We define the size of the object as its length l in the direction of wave propagation (for round objects, $l = D$ with D the diameter), the submergence depth is h_d, the height of the round-cornered box is h, and the radius of the rounded corner is r. Objects are placed in a regular incident wave field with wave amplitude a_w and angular frequency ω in deep water (i.e., $kd > 3$, where k is the wavenumber and d the depth of the fluid).

Two models are used: the hybrid model qaleFOAM and a diffraction-modified Stokes drift

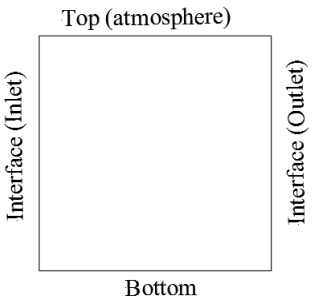


Round-cornered box Round object

Figure 3.1: Shapes and dimensions of the two objects considered: round-cornered boxes (RCBs) and round objects (ROs).



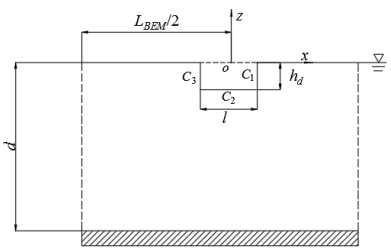
(a) Schematic of the hybrid computational domain.



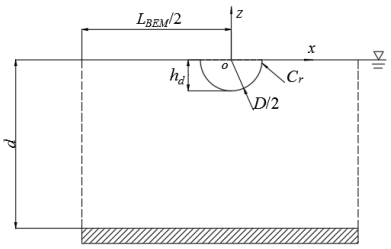
(b) Boundaries of the NS domain.

Figure 3.2: Domains, domain boundaries and coordinate system used in the hybrid numerical model qaleFOAM.

model, which is solved based on the linearized potential-flow BEM. We use both models to conduct two dimensional simulations. In the hybrid qaleFOAM model, an inertial coordinate system (X, Z) is chosen with its origin O located at the bottom left corner of the fluid domain, with waves propagating from left to right, the X-axis positive in the direction of wave propagation, and the Z-axis positive upwards, as shown in figure 3.2 (a). In the diffraction-modified Stokes drift model, we establish a Cartesian coordinate system (x, z) with its origin o located on the still-water level at the horizontal centre of the object, the x-axis in the direction of wave propagation, and the z-axis positive upwards, as shown in figure 3.3. Both coordinate systems, (X, Z) and (x, z), are inertial, earth-fixed coordinate systems and do not move with the objects. The only difference between these two coordinate systems is the position of the origin.



(a) Rectangular box (RB).



(b) Round object (RO).

Figure 3.3: Domain and coordinate system in the diffraction-modified Stokes drift model for the two objects considered, also showing object dimensions.

3.3.2 Hybrid numerical model: qaleFOAM

The hybrid numerical model qaleFOAM is used in this chapter. The model is based on the domain-decomposition method, which couples the QALE-FEM (Quasi Arbitrary Lagrangian-Eulerian Finite Element Method) potential-flow model with the two-phase incompressible Navier–Stokes (NS) model InterDyMFOAM in OpenFOAM. For details, see Ma and Yan (2010); Jacobsen et al. (2012); Li et al. (2018); Gong et al. (2020); Yan et al. (2020b) and references therein. QaleFOAM has been applied to study various wave-structure interaction problems (Li et al., 2018; Yan et al., 2019; Gong et al., 2020). The structures in these studies are either moored or self-propelled, and their sizes are at least 0.2 times the characteristic wavelength. Thus the application of this model to smaller and unmoored objects (down to 0.01 times the wavelength) is new.

In the hybrid numerical model, the larger outer domain is solved by QALE-FEM to capture the incident waves; a smaller inner domain surrounding the object uses OpenFOAM to solve the NS equations, as shown in figure 3.2 (a). In the NS model, both the air and water phases are assumed incompressible, and the VOF (volume of fluid) method is used to identify the phases and their interface. The coupling approach employed in this chapter is a one-way coupling, which means that at the interfaces, the NS model only takes the solutions of the QALE-FEM solver but does not feed its solutions back. The waves are generated first in the QALE-FEM domain using a flap-type wavemaker and then transferred into the NS domain via the left and right interfaces, where the NS domain is coupled with the QALE-FEM solver. Chapter 2.6.3 details the information transfer at these interfaces. The boundaries of the NS domain are shown in figure 3.2 (b). The left and right interfaces of the NS domain are adaptive coupling boundaries equipped with passive wave absorbers (Yan et al., 2020b). These absorbers use adaptive absorbing techniques to efficiently absorb radiated and diffracted waves generated in the NS domain, thus achieving the one-way coupling (i.e., the NS domain does not feedback into the QALE-FEM domain). The wave diffraction problem is thus solved in the NS domain, and we have to ensure that this domain is large enough so its finite size does not affect the solution, while not too large to become computationally prohibitive. By performing simulations with different domain lengths (in the range of 1-4 wavelengths), we demonstrate that our results (notably for object drift) are independent of the length of the NS domain. We note that to

ensure the two-dimensionality of the simulations performed in this chapter (using a numerical model that is, in principle, three dimensional), the front and back interfaces in the NS domain are not used (i.e., the mesh number in the third dimension is 1). Furthermore, a laminar viscosity model is employed (i.e., we do not use a turbulence model).

Waves generated by the QALE-FEM domain get absorbed on the right boundary of the QALE-FEM domain. It takes time for waves generated by the wavemaker to propagate to the NS domain. In order to save computational cost, a reference time period t_R is set, during which the NS model is turned off. The tank length L_x for all simulations in this chapter is chosen to be sufficiently long so that simulations finish before the reflected waves reach the object's location. The distance between the NS domain and the wavemaker is chosen to be at least 3 wavelengths in order to minimise the effects of evanescent waves from the wavemaker.

3.3.3 Diffraction-modified Stokes drift model

To provide an estimate of how object drift is affected by the diffraction of the wave field (without viscosity), we first use a BEM to solve the linearized potential-flow problem. From these linearized potential-flow solutions we obtain an estimate of the object drift (second-order in steepness) in a fashion akin to Stokes (1847) but by taking into account the modified wave field and object motion. To do so, we need to define all the boundaries of the fluid domain (see figure 3.3): d is the depth of the fluid (at $z = -d$ a no-flow bottom boundary condition must be satisfied) and $x = \pm L_{BEM}/2$ correspond to the left and right boundaries of the fluid domain, where the radiation condition must be satisfied. We choose a value of $L_{BEM}/2$ that is large enough for the far-field truncation of the radiation condition not to affect our results. The boundaries C_1, C_2, and C_3 in figure 3.3 (a) and C_r in figure 3.3 (b) require kinematic agreement of the fluid velocity and the (rigid) object's motion for the rectangular box (RB) and the round object (RO), respectively. For the diffraction-modified Stokes drift model, we only consider a rectangular box (RB) with square corners (i.e., $r = 0$), whereas for the hybrid numerical model we explore the effect of the radius of the rounded corner for the round-cornered box (RCB).

At first order in steepness (i.e., for linear waves) the flow is described by a velocity potential Φ, which can be further divided into an incident potential Φ_I, diffraction potential Φ_D and

radiation potential Φ_R:

$$\Phi(x,z,t) = \Phi_I(x,z,t) + \Phi_D(x,z,t) + \Phi_R(x,z,t) = \mathrm{Re}\{\phi_I(x,z)e^{-\iota\omega t}\} + \mathrm{Re}\{\phi_D(x,z)e^{-\iota\omega t}\} + \mathrm{Re}\{\phi_R(x,z)e^{-\iota\omega t}\}, \tag{3.1}$$

where all three components oscillate with the same angular frequency ω. We denote the incident wave amplitude as a_w, and the wavenumber k is obtained from linear dispersion relationship $\omega^2 = gk\tanh(kd)$, where g is the gravitational acceleration. Although we will consider deep-water waves in this chapter (i.e., $kd > 3$ so that $\tanh(kd) \approx 1$), our diffraction-modified Stokes drift model is valid for general water depth. The time-invariant part of the incident wave potential ϕ_I can be expressed as:

$$\phi_I = \frac{a_w g}{\iota\omega}\frac{\cosh k(z+d)}{\cosh kd}e^{\iota kx}. \tag{3.2}$$

The boundary value problems for ϕ_R and ϕ_D are governed by the Laplace equation and solved using the Green's function method; the corresponding forces and equations of motions can then be found using standard methods (e.g., Newman (2018)). We use the implementation of these standard methods by Chen et al. (2018) and Yang et al. (2019a,b) (see appendix 3.A for details).

Estimating wave-induced object drift velocity

To obtain a leading-order (in steepness) estimate of object drift, we perform the same perturbation expansion, up to second order in wave steepness as Stokes (1847) originally used to estimate the Stokes drift (see also van den Bremer and Breivik (2018)). Instead of only the linear incident wave field, we use the total linear wave field (cf. (3.1)) to estimate the 'diffraction-modified Stokes drift' for objects that are large enough to diffract the wave field:

$$u_{S,O} = \overline{\xi_x\frac{\partial^2\Phi}{\partial x^2} + \xi_z\frac{\partial^2\Phi}{\partial x\partial z}} = \overline{\xi_x\left(\frac{\partial^2\Phi_I}{\partial x^2} + \frac{\partial^2\Phi_R}{\partial x^2} + \frac{\partial^2\Phi_D}{\partial x^2}\right) + \xi_z\left(\frac{\partial^2\Phi_I}{\partial x\partial z} + \frac{\partial^2\Phi_R}{\partial x\partial z} + \frac{\partial^2\Phi_D}{\partial x\partial z}\right)}, \tag{3.3}$$

where $\xi_x = \mathrm{Re}\{A_x e^{-\iota\omega t}\}$ and $\xi_z = \mathrm{Re}\{A_z e^{-\iota\omega t}\}$ are the linear horizontal and vertical harmonic oscillatory motions of the object, and the overline denotes averaging over the wave period. We term our estimate of the object drift in (3.3) the 'diffraction-modified Stokes drift', as it is

based on the (linear) diffracted wave field. The diffraction-modified Stokes drift $u_{S,O}$ in (3.3) is calculated conceptually by (a leading-order estimate of) the difference between the Lagrangian-mean object speed and the Eulerian-mean fluid speed (i.e., $u_{S,O} = \overline{u}_{L,O} - \overline{u}_E$, cf. Bühler (2014)). We do not compute the second-order Eulerian-mean flow, as this is generally very small for deep-water waves (e.g., van den Bremer and Taylor (2015); van den Bremer et al. (2019)) in the absence of the Earth's rotation, which is not considered here (cf. Higgins et al. (2020)), and thus set $\overline{u}_E = 0$. Below we will show that we have negligible Eulerian-flow in our simulations.

The different contributions to the diffraction-modified Stokes drift (3.3) can be made more explicit. We denote:

$$\xi_x = A_x e^{\iota\theta_x}, \quad \xi_z = A_z e^{\iota\theta_z}; \tag{3.4a,b}$$

$$\frac{\partial^2\phi_I}{\partial x^2} = k\omega A^I_{xx} e^{\iota\theta^I_{xx}}, \quad \frac{\partial^2\phi_I}{\partial x\partial z} = k\omega A^I_{xz} e^{\iota\theta^I_{xz}}; \tag{3.5a,b}$$

$$\frac{\partial^2\phi_R}{\partial x^2} = k\omega A^R_{xx} e^{\iota\theta^R_{xx}}, \quad \frac{\partial^2\phi_R}{\partial x\partial z} = k\omega A^R_{xz} e^{\iota\theta^R_{xz}}; \tag{3.6a,b}$$

$$\frac{\partial^2\phi_D}{\partial x^2} = k\omega A^D_{xx} e^{\iota\theta^D_{xx}}, \quad \frac{\partial^2\phi_D}{\partial x\partial z} = k\omega A^D_{xz} e^{\iota\theta^D_{xz}}, \tag{3.7a,b}$$

where symbols A denote the (potentially spatially dependent) magnitudes of the terms (given as amplitudes, in meters), and the phase and (oscillatory) spatial dependencies are captured by symbols θ with sub and super-scripts on both A and θ used as to indicate the different terms (and not derivatives). These amplitudes and phases can be obtained from the linear BEM model, which includes the equation of motion of the object. Now, diffraction-modified Stokes drift (3.3) can be rewritten as:

$$\begin{aligned}
\frac{u_{S,O}}{u_S} &= \overline{\mathrm{Re}\{\hat{A}_x e^{\iota(\theta_x-\omega t)}\}\left[\mathrm{Re}\{\hat{A}^I_{xx} e^{\iota(\theta^I_{xx}-\omega t)}\} + \mathrm{Re}\{\hat{A}^R_{xx} e^{\iota(\theta^R_{xx}-\omega t)}\} + \mathrm{Re}\{\hat{A}^D_{xx} e^{\iota(\theta^D_{xx}-\omega t)}\right] + \ldots} \\
&\quad \overline{\mathrm{Re}\{\hat{A}_z e^{\iota(\theta_z-\omega t)}\}\left[\mathrm{Re}\{\hat{A}^I_{xz} e^{\iota(\theta^I_{xz}-\omega t)}\} + \mathrm{Re}\{\hat{A}^R_{xz} e^{\iota(\theta^R_{xz}-\omega t)}\} + \mathrm{Re}\{\hat{A}^D_{xz} e^{\iota(\theta^D_{xz}-\omega t)}\}\right]}, \\
&= \overline{\hat{A}_x\cos(\theta_x-\omega t)\left[\hat{A}^I_{xx}\cos(\theta^I_{xx}-\omega t) + \hat{A}^R_{xx}\cos(\theta^R_{xx}-\omega t) + \hat{A}^D_{xx}\cos(\theta^D_{xx}-\omega t)\right] + \ldots} \\
&\quad \overline{\hat{A}_z\cos(\theta_z-\omega t)\left[\hat{A}^I_{xz}\cos(\theta^I_{xz}-\omega t) + \hat{A}^R_{xz}\cos(\theta^R_{xz}-\omega t) + \hat{A}^D_{xz}\cos(\theta^D_{xz}-\omega t)\right]}, \\
&= \frac{\hat{A}_x}{2}\left[\hat{A}^I_{xx}\cos(\theta_x-\theta^I_{xx}) + \hat{A}^R_{xx}\cos(\theta_x-\theta^R_{xx}) + \hat{A}^D_{xx}\cos(\theta_x-\theta^D_{xx})\right] + \ldots \\
&\quad \frac{\hat{A}_z}{2}\left[\hat{A}^I_{xz}\cos(\theta_z-\theta^I_{xz}) + \hat{A}^R_{xz}\cos(\theta_z-\theta^R_{xz}) + \hat{A}^D_{xz}\cos(\theta_z-\theta^D_{xz})\right],
\end{aligned} \tag{3.8}$$

where the overline denotes wave averaging in time, upon which all the super-harmonic terms (of the form $\cos(2\omega t + \beta)$ with β an arbitrary phase) disappear, and the symbol $\hat{A}$ denotes the normalization of the corresponding magnitude A by the incoming wave amplitude a_w (i.e., $\hat{A} = A/a_w$). The theoretical Stokes drift u_S is given by (Stokes, 1847):

$$u_S = {a_w}^2 \omega k e^{2kz} = \varepsilon^2 \frac{\omega}{k} e^{2kz}, \tag{3.9}$$

in which $\epsilon = ka_w$ is the incident wave steepness, where we have used $z = 0$ in the normalisation in (3.8).

3.4 Validation and verification of the hybrid numerical model (qaleFOAM)

In this section, validation and verification are conducted for the qaleFOAM hybrid numerical model (see appendix 3.A for validation and verification of the BEM model). To do so, we first examine the (Stokes) drift of a Lagrangian particle (i.e., a fluid parcel) through analysis of the Lagrangian-mean velocity (the Eulerian-mean velocity field as well as grid convergence are examined in appendix 3.B). We then examine the Lagrangian drift behaviour of small floating objects.

3.4.1 Drift of a Lagrangian particle

First, we consider, in turn, regular waves in deep water with two different frequencies. For each frequency, a series of waves are simulated with different wave amplitudes, and the horizontal drift velocities of fluid particles are calculated to confirm these are equal to the theoretical Stokes drift based on (3.9). The mean drift velocity of a fluid particle in quasi-steady state is obtained by applying the best linear fit to its horizontal trajectory and determining the slope of the linear fit line. The trajectories themselves are obtained from solving the ordinary differential equation $\mathrm{d}\mathbf{x}_L/\mathrm{d}t = \mathbf{u}(\mathbf{x}_L(t), t)$, where $\mathbf{x}_L(t)$ is the position of a Lagrangian particle.

The properties of the waves and the numerical parameters of the simulations are given in table 3.1, where T_{dur} and $T = 2\pi/\omega$ refer to the total time duration of the simulations and the

wave period, respectively, and L_x is the (horizontal) length of the total domain. The parameters Δx, Δz and Δt denote the horizontal and vertical grid sizes and time steps, respectively. The horizontal positions x_L and x_R represent the left and the right boundary locations of the NS domain, respectively, and z_A denotes the vertical location of the top of the air phase relative to the still-water level in the NS domain. Horizontal grid size is given as a fraction of the wavelength λ and vertical grid size as a fraction of the linear wave amplitude a_w. Finally, the maximum Courant number $\mathrm{Co} = \Delta t \left|\mathbf{u}\right| / \Delta x = 0.25$, in which $|\mathbf{u}|$ refers to the maximum absolute velocity.

We use a Crank–Nicolson scheme for time integration and a non-uniform mesh with finer resolution close to the free surface in the z-direction in both the QALE-FEM and NS domains. Specifically, the grid density in the z-direction in QALE-FEM increases exponentially with distance to the free surface, and the vertical grid size is defined by the number of layers in vertical direction, for which 20 are typically enough for deep-water simulations. The mesh sizes in table 3.1 all refer to those in the region near the free surface.

For InterFoam and InterDyMFoam solvers, Larsen et al. (2019) provide a detailed analysis of different combinations of discretization schemes, mesh sizes and Courant numbers for surface waves to maintain stable amplitudes over long times. For these solvers, Devolder et al. (2015) reported instability of the added-mass term and suggested how to choose the initial values of the added-mass relaxation factor in order to obtain fast convergence and stable motion. Moradi et al. (2015); Palm et al. (2016); Mohseni et al. (2018) and Palm et al. (2018) have investigated wave-body interaction. Based on the above, we choose the PISO algorithm to solve the pressure-velocity coupling, a limited second-order Crank–Nicolson scheme (implicit) with a blending factor of 0.9 is used for time integration (ddtSchemes), a minimally diffusive gradient limiter (cellMDLimited Gauss linear 1, which is second-order and bounded) is used for gradients (gradSchemes) to avoid over and undershooting. To compute the divergence term (divSchemes), a second-order TVD scheme (Gauss MUSCL) is used for the momentum convection term. A second-order and bounded TVD scheme (Gauss vanLeer01 with Gauss interfaceCompression is used to compute the volume fraction.

We vary the steepness of the simulated waves of the two different frequencies from 0.03 to 0.13, and let the relaxation zone vary in length from 1 to 1.5 wavelengths as the wave

Cases	ω (rad/s)	d (m)	kd	T_{dur} (s)	QALE-FEM domain		
					L_x (m)	Δx (m)	Δt (s)
Higher frequency	7.85	3.00	18.84	$65T$=52	75	$\lambda/80$=0.125	$T/533$=0.015
Lower frequency	4.09	5.00	8.53	$65T$=100	210	$\lambda/71$=0.052	$T/496$=0.0031
Cases	Wave steepness	NS domain					
		x_L (m)	x_R (m)	z_A (m)	Δx (m)	Δz (m)	Co
Higher frequency	0.03-0.13	9.00	13.50∼14.50	0.1	$\lambda/750$=0.0013	$a_w/40$	0.25
Lower frequency	0.03-0.13	15.16	31.13∼35.11	0.3	$\lambda/738$=0.0050	$a_w/40$	0.25

Table 3.1: Wave properties and numerical parameter values for the hybrid numerical model (qaleFOAM) simulations, distinguishing the potential-flow (QALE-FEM) and the Navier–Stokes (NS) domains.

steepness increases (Yan et al., 2019). Correspondingly, the location of the right-hand side of the NS domain is adapted so that the length of the NS domain is equal to the relaxation zone length plus the necessary length for particles to move during the proposed time duration of the simulation. The initial position of the tracked particles is chosen to avoid disturbance by transition through the relaxation zone. The initial horizontal position $x_{L,0}$ is chosen some distance to the right of the left relaxation zone, and the initial vertical position $z_{L,0}$ is chosen immediately below the trough of the wave.

Figure 3.4 (a) displays the horizontal trajectory $x_L(t)$ of the tracked particles (x_{L0}, z_{L0}) for $\epsilon = 0.034$, $\omega = 4.09$ rad/s as an example. It is evident that in addition to the oscillatory motion of the waves, the Lagrangian particle undergoes a mean drift that agrees well with the theoretical Stokes drift according to (3.9), in which we set z equal to the initial vertical position of the tracked particle z_{L0}. A comparison between the numerical prediction of the mean drift and the theoretical Stokes drift for different steepnesses is shown in figure 3.4 (b). Excellent agreement is achieved for both higher and lower frequencies and for a range of steepnesses. Finally, we confirm that the Eulerian-mean velocity is negligibly small everywhere in our domain in the case without viscosity (shown in appendix 3.B, so that $\overline{u}_L = u_S$). Together, this validates our model and confirms its ability to predict the drift velocity of an infinitely small object. The deviation from perfectly quadratic behaviour in figure 3.4 (b) results from the initial vertical position z_{L0} being chosen just below the trough for each steepness; this vertical position is also used to evaluate the theoretical Stokes drift according to (3.9), hence the very good agreement.

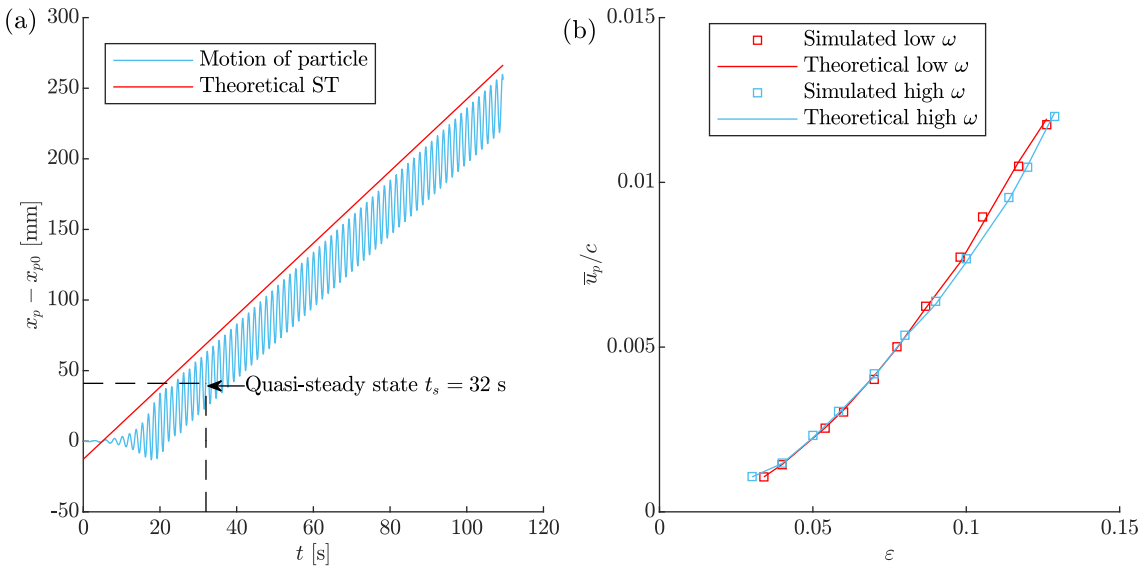


Figure 3.4: Drift of Lagrangian particles in simulations of the hybrid numerical model (qale-FOAM) without viscosity ($\nu = 0$): (a) time history of the horizontal motion of a Lagrangian particle ($x_{L_0} = 22.5$ m, $z_{L_0} = -25.0$ mm) for $\epsilon = 0.034$ for the lower-frequency case in table 3.1, where the theoretical Stokes drift is evaluated using (3.9). The wave amplitude here is $a_w = 20.0$ mm; thus, the vertical position of the particle is always below the trough of the wave. The black dashed line denotes the time at which a quasi-steady state has been achieved and the drift speed has become constant ($t_s = 32$ s). The drift speed in (b) has been obtained from the average speed for $t > t_s$. (b) comparison of non-dimensional drift velocities of a Lagrangian particle $\overline{u}_L/c$ between numerical solutions (red and blue squares) and theoretical Stokes drift (red and blue lines) as a function of wave steepness for higher and lower frequencies, where $c = \omega/k$ is the phase speed of the waves.

3.4.2 Drift of very small objects

To further validate our model, we examine whether it correctly predicts the drift of very small but finite-size objects, which should be equal to the Stokes drift (in the absence of Eulerian-mean flows). Clear experimental evidence exists that when the size of an object is very small, its behaviour is purely Lagrangian (Nath, 1978; van den Bremer et al., 2019). Two different object shapes are examined here: a rectangular box and a round object. We choose the lower-frequency ($\omega = 4.09$ rad/s) wave condition from table 3.1 and a small steepness of $\epsilon = 0.034$. The round-cornered rectangular box has a length (in the direction of wave propagation) of $l = 0.036$ m ($l/\lambda = 0.97\%$), a draft $h_d = 0.025$ m, and the radius of the rounded corner is $r = 0.006$ m. The diameter of the round object is $D = 0.05$ m ($D/\lambda = 1.3\%$). Both of the objects have density of $\rho = 500$ kg/m^3. The height of the box and the radius of the round object are chosen to make sure that the object will not be submerged by the waves.

Table 3.2 gives the object drift velocities of both objects with and without viscous effects modeled in the simulation (i.e., $\nu = 1.00 \times 10^{-6}$ m^2 s^{-1} and $\nu = 0$). The total number of cells of the discretization mesh N_c reported in table 3.2 is the one for the non-viscous simulation, based on which vertical 6 layers are added and one level of refinement is applied near the object for the corresponding viscous simulation. The results confirm the drifts of both very small objects ($\sim 1\%$ of the wavelength) are approximately equal to the theoretical Stokes drift in both the viscous and the non-viscous simulation. By comparing a coarser grid to a finer grid, table 3.2 also shows the convergence of several physical quantities (wave amplitude, horizontal viscous forces on the particle, and the object drift velocity) for both the viscous and the non-viscous simulations. We note the horizontal resolution changes with distance to the object in order to make the grid's aspect ratio approximately unity in the object's near field.

3.5 Results from the hybrid numerical model (qaleFOAM)

In this section, we explore the role played by a variety of factors, namely size, shape, submergence depth, viscosity and wave steepness, in determining an object's drift behaviour. The wave field is equivalent to that considered before in §3.4 (see table 3.1). The two object shapes considered along with the definitions of object dimensions are given in figure 3.1. We use

	l/λ (%)	Δx (m)	$\lambda/\Delta x$	Δz (m)	$a_w/\Delta z$	N_c	$\nu = 0$		$\nu = 1.00 \times 10^{-6}$ m^{2}s^{-1}		
							a/a_w	u_O/u_S	a/a_w	u_O/u_S	$F'_{x,vis}$
Round-cornered box	0.97	0.02∼0.001	185∼3692	0.001	20	353532	1.008	0.987	1.004	0.970	0.00042
	0.97	0.02∼0.0005	185∼7385	0.0005	40	386628	1.007	1.008	1.010	1.040	0.00042
Round object	1.35	0.02∼0.001	185∼3692	0.001	20	394896	1.009	1.045	1.000	1.049	0.00042
	1.35	0.02∼0.0005	185∼7385	0.0005	40	489444	1.003	1.019	1.009	1.035	0.00045

Table 3.2: Numerically predicted wave amplitude as a fraction of the input amplitude a/a_w and object drift as a fraction of theoretical Stokes drift u_O/u_S for very small objects of two different shapes and for different mesh sizes, with l the length of the object. The horizontal grid size Δx varies with distance to the object from the farthest location where $\Delta x = 0.02$ m to the nearest location where $\Delta x = 0.0005$-0.001 m. The total number of cells of the mesh is denoted by N_c. The amplitude a is the time-averaged wave amplitude at the location of more than one wavelength downstream away from the object (near the outlet, defined in figure 3.2 (b)) scaled by the input wave amplitude a_w. The force $F'_{x,vis} = F_{x,vis}/(\rho g a_w l^2/4)$ is the non-dimensional magnitude of the horizontal viscous force on the object.

round-cornered boxes instead of boxes with sharp corners to avoid generation of undesirable vorticity which would complicate the analysis (cf. Moradi et al. (2015)). To organize our findings, we define the following dimensionless parameters: relative object size is described by l/λ (for round objects $l = D$) and the radius of the corners of the round-cornered box by r/h_d. The total duration T_{dur} is around 60-80 s for all simulations; it takes around 25-30 s for object drift to achieve a steady state, and another 25-35T (T is the wave period) is sufficient to estimate the drift velocity. The spatial resolution of the mesh for all cases without viscosity lies in the range from $\Delta x = \lambda/200$, $\Delta z = a_w/20$ at a location 1-1.5λ away from the object to $\Delta x = a_w/20$, $\Delta z = a_w/20$ within a distance of 2-4l surrounding the object. For the cases with viscosity, we add 6 vertical layers near the surface and apply one level of refinement near the object. The maximum Courant number Co = 0.25.

We conduct three categories of simulations. In the first category (category I), we consider the effect of size for a round-cornered box and a round object (§3.5.1). For round-cornered boxes, we keep the aspect ratio h_d/l and submerged shape r/h_d constant, and we consider only round-cornered boxes to avoid the effect of undesirable vorticity from sharp corners. To begin our analysis with a case of the simplest possible geometry, we set the object density $\rho = 500$ kg/m^3, so that both objects are exactly half-submerged. As the round-cornered boxes are hydrodynamically unstable for this density, we constrain the object rotation to be zero in the category I simulations, the consequences of which we discuss in §3.5.1. In the second category (category II), we keep the size of the object constant but vary its submergence depth and submerged shape by changing the radius of the round corner (§3.5.2). Instead of changing

	l/λ (%)	1.0	2.0	3.0	4.0	5.1	6.0	7.0	8.0	9.0	10.0
RCB	l (m)	0.037	0.07	0.11	0.15	0.19	0.22	0.26	0.29	0.33	0.37
	h_d (m)	0.025	0.05	0.075	0.10	0.13	0.15	0.18	0.20	0.23	0.25
	r(m)	0.006	0.012	0.018	0.024	0.03	0.036	0.043	0.048	0.054	0.06
RO	l/λ (%)	1.4	2.0	3.0	4.0	5.1	6.0	7.0	8.0	9.0	10.0
	D (m)	0.05	0.07	0.11	0.15	0.19	0.22	0.26	0.29	0.33	0.37

Table 3.3: For category I simulations exploring the effect of size, object dimensions of the two different objects considered: round-cornered boxes (RCBs) and round objects (ROs) ($\rho = 500$ kg/m^3 for both).

the aspect ratio of the objects, we vary the submergence and roundness of the objects, which is intended to examine the effect of 'streamlining' of objects of constant size. The density of the objects in category II is different from category I, as we no longer wish to constrain the object's rotation; specifically, we choose a density ($\rho = 781$ kg/m^3) that is high enough for round-cornered boxes to become hydrodynamically stable while maintaining the same size and aspect ratio h_d/l as the objects in category I. Unlike the first and second categories, which are all conducted on low-steepness waves, in the third category (category III), we simulate drift behaviour for a range of wave steepnesses (§3.5.3). We examine the role of viscosity explicitly in §3.5.4 for the experiments in categories I and II.

3.5.1 Effect of size (category I)

To study the effect of size, we vary the size of the two objects measured relative to the wavelength from 1% to 10% in 1%-point steps. Detailed object dimensions are given in table 3.3. For the round-cornered box, we set $r/h_d = 0.24$. The differences between a round-cornered box and a round object (RO) of equivalent relative size are the submerged shape and submergence depth of the object. The simulations are performed with and without the inclusion of viscosity. Simulation results are shown in figure 3.5. The non-dimensional magnitude of oscillatory motion in the horizontal and vertical directions are shown in figure 3.5(a) and (b), respectively. The amplitudes of the oscillatory motions A_x and A_z are obtained by filtering out sub- and super-harmonic components, before obtaining amplitudes after the quasi-steady state has been achieved. Figure 3.5 (c) shows the influence of sizes and shape on drift. Finally, figure 3.5(d) depicts the local wave amplitude as a function of its horizontal distance to the centre of mass of the objects for round-cornered boxes of relative sizes $l/\lambda = 1\%$, $l/\lambda = 9\%$ and

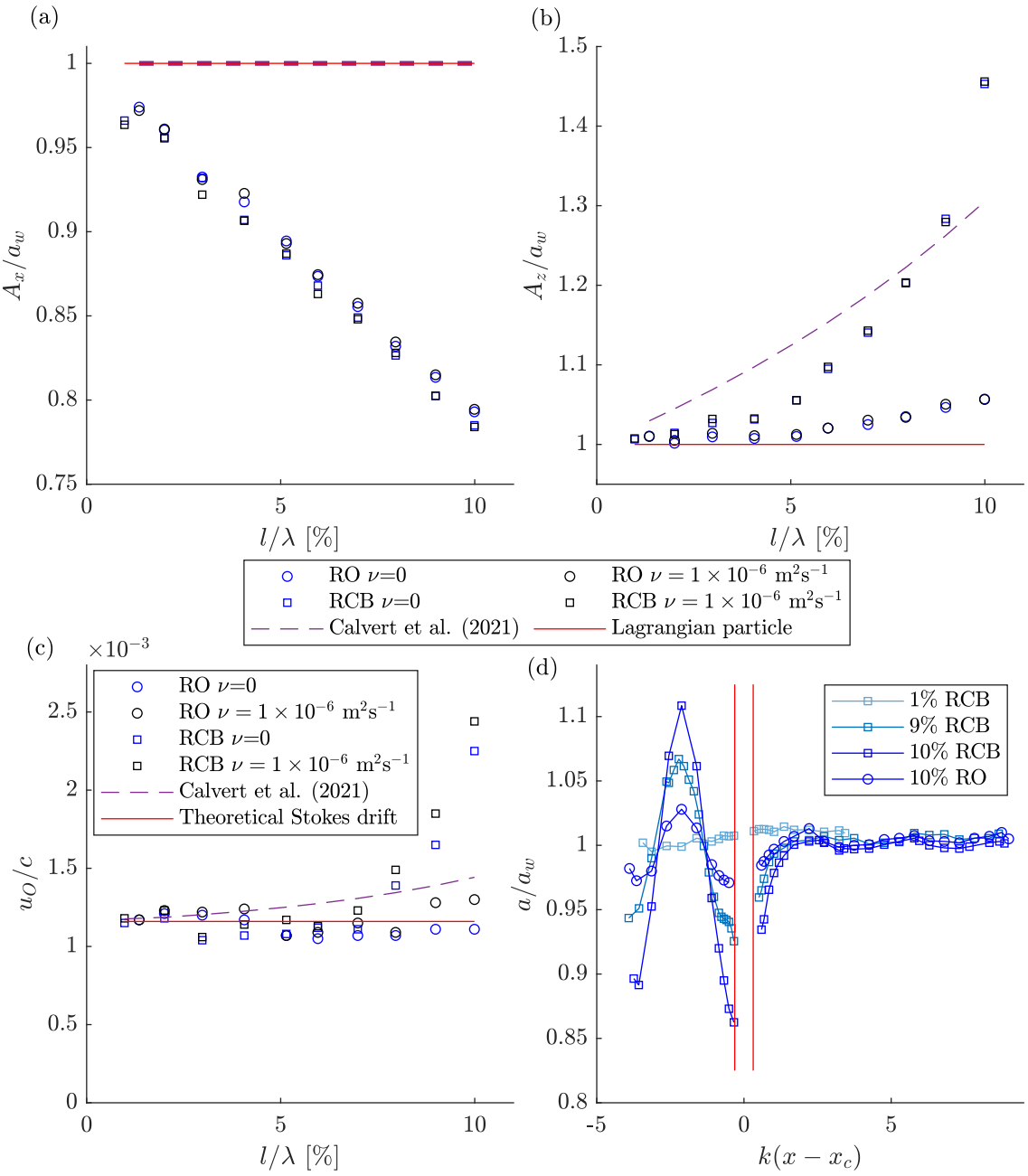


Figure 3.5: Effect of object size on object motion and drift (category I simulations): (a) horizontal oscillatory motion amplitude A_x, normalized by input wave amplitude a_w, as a function of relative object size; (b) vertical oscillatory motion amplitude A_z, normalized by wave amplitude a_w, as a function of relative object size; (c) celerity-normalized object drift u_O/c as a function of relative object size; (d) non-dimensional amplitude of the local surface elevation $a(x)/a_w$ as a function of horizontal distance (scaled by wavenumber) from the centre of mass x_c without viscosity ($\nu = 0$). The gap between the two vertical red lines in (d) represents the position of the object for $l/\lambda = 10\%$ and corresponds to its left and right sides, respectively. The percentage (%) in (d) represents the relative size of the object l/λ. The results for Calvert et al. (2021) in panels (a), (b) and (c) are their results for spheres with equivalent diameter to our round objects.

$l/\lambda = 10\%$ and round objects of relative size $l/\lambda = 10\%$.

We start by examining the oscillatory motion for the round-cornered box, shown in figure 3.5 (a) and (b). When the object is very small, the magnitudes of oscillatory motion in both directions are very close to the incident wave amplitude a_w, suggesting the object behaves as a Lagrangian particle. As object size increases, the horizontal oscillatory motion is reduced as an approximately linear function of relative size, while the vertical oscillatory motion increases nonlinearly at an increasing rate. For the object drift velocity in figure 3.5 (c), we observe that when the box is very small, its drift rate is equal to the Stokes drift, while, as the box becomes larger, the drift speed is enhanced significantly. The enhanced drift is minimal for round-cornered boxes (RCBs) with relative size less than approximately 7%, but becomes more evident for larger boxes. Significant increases in the drift for round-cornered boxes only become evident at greater relative size compared to increases in the vertical oscillatory motion. For completeness, we note the drift is slightly reduced compared to the theoretical Stokes drift for intermediate-size round-cornered boxes with a relative size of $3\% \leq l/\lambda \leq 7\%$ and round objects with $5\% \leq l/\lambda \leq 8\%$, The potential explaination of this decrease is given in section §3.6.2.

From the wave-field analysis in figure 3.5 (d), a standing-wave pattern emerges in the case of a large round-cornered box (with large submergence depth). On the upstream side, the time-averaged wave amplitudes show a pattern of partial nodes and anti-nodes with smaller and larger amplitudes locally compared to the incident undisturbed wave amplitude (and compared to the 1%-relative-size object, for which a standing wave pattern is not discernible). Wave amplitudes on the far downstream side for large objects are unaffected, while for locations near the object on the downstream side, smaller amplitudes are found. Differences in surface elevation between the two sides of the object become most evident for the larger round-cornered boxes. We note (numerical) wave gauges are set at a fixed spatial interval; thus there may be small errors in determining maxima and minima. The (partial) standing-wave pattern becomes difficult to discern for round-cornered boxes with relative size smaller than 7% (not presented here for brevity). All the above trends are similar whether viscosity is included or not; the drift of round-cornered boxes is enhanced further by viscous effects and even more so for larger objects, by up to 20%, as shown in figure 3.5 (c). For practical computational reasons, the

local wave amplitude is obtained by analysing the surface elevation in a stationary reference frame and not in the referencing frame moving with the object, in which the standing wave pattern most likely forms. As the object drift is always small relative to the phase speed (i.e., $u_O/c \leq 2.5 \times 10^{-3}$), we anticipate the standing wave patterns in both reference frames to be similar albeit likely smaller and more diffused in the stationary reference frame shown here.

Comparing the round object (RO) and the round-cornered box (RCB), both display a similar linear decrease in horizontal oscillatory motion with relative size (figure 3.5 (a)), whereas the vertical motion of round objects is only enhanced by a very small amount compared to round-cornered boxes (figure 3.5 (b)). Furthermore, for round objects (ROs), as depicted in the figure 3.5 (c), no obvious enhancement of the drift speed is found in the absence of viscosity even when the relative size is as large as 10%. In the presence of viscosity, a small amount of enhanced drift is observed as the round object becomes larger (relative size larger than 8%). The motion of round objects is thus distinctly different from that of round-cornered boxes, especially their vertical oscillatory motion and enhanced drift. To explain this, we note that the standing wave pattern in figure 3.5 (d) for the largest round object (10%) is even smaller than for the 8% relative size round-cornered box (not shown in the figure). The standing wave pattern is an indication of the presence of a diffracted wave field; the extent to which diffraction occurs depends on the streamlining of the object. In §3.6, the effect of shape is examined further.

We note that in the above simulations (category I), we have constrained the object's rotation. This is necessary, as in keeping the object density constant at $\rho = 500$ kg/m^3, we have considered a round-cornered box where height h exceeds length l (i.e., $h/l = 1.33$). This is hydrodynamically unstable, and would normally start to rotate upon small perturbations from its vertically upright position. In presenting the results here, we have thus assumed the interaction between the motions in the different degrees of freedom (translation and rotation) is small. In appendix 3.C, we keep the submergence depth and submerged shape of the round-cornered box the same as in table 3.3 but change its density to properly explore the effects of rotation. We show that allowing rotation does not affect the conclusions presented in this section. In the following sections, we will allow rotation.

l/λ (%)	10.0	10.0	10.0	10.0	10.0	10.0
h_d (m)	0.25	0.25	0.25	0.25	0.25	0.25
r (m)	0.03	0.06	0.08	0.10	0.12	0.15
r/h_d	0.12	0.24	0.32	0.40	0.48	0.60

Table 3.4: For category II simulations exploring the effect of object shape with fixed height (group 1): object dimensions for different shapes (l=0.37 m, h=0.32 m, $\rho = 781$ kg/m^3).

l/λ (%)	10.0	10.0	10.0	10.0
h_d (m)	0.25	0.22	0.20	0.18
h (m)	0.32	0.30	0.29	0.26
r (m)	0.06	0.06	0.06	0.06

Table 3.5: For category II simulations exploring the effect of submergence depth with fixed radius of the round corners (group 2): object dimensions for different submergence depths ($l = 0.37$ m, $\rho = 781$ kg/m^3).

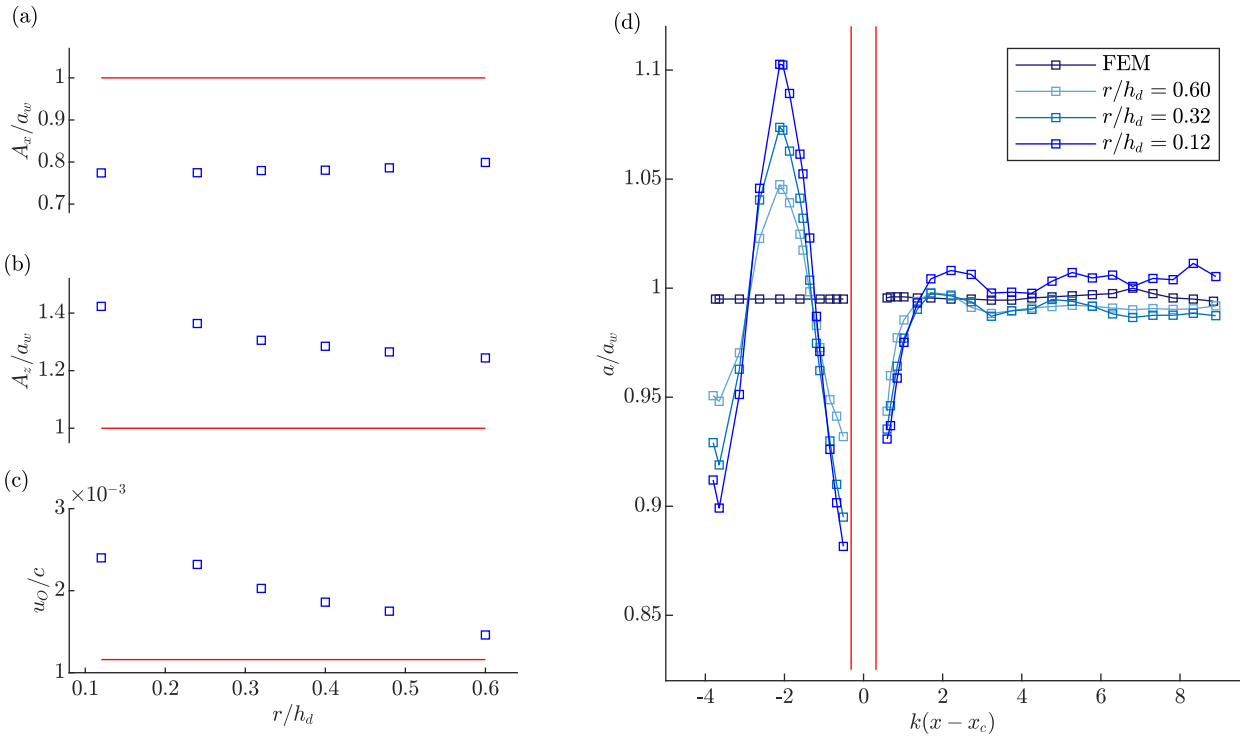


Figure 3.6: Effect of the shape of the submerged part of a round-cornered box as determined by the radius of the rounded corner r, scaled by submergence depth h_d, on object motion and drift (category II simulations, group 1): (a) and (b) non-dimensional amplitudes of oscillatory motion in the horizontal and vertical directions, respectively; (c) celerity-normalized object drift velocity; Blue square markers in (a), (b) and (c) represent the results for round-cornered boxes (RCBs). Red lines in (a) and (b) denote the oscillatory motions of a Lagrangian particle, these in (c) denote the theoretical Stokes drift. (d) non-dimensional amplitude of the local surface elevation $a(x)/a_w$ as a function of horizontal distance (scaled by wavenumber) from the centre of mass x_c. The gap between the two vertical red lines in (d) represents the position of the object and corresponds to its left and right sides, respectively. The line denoted by FEM in (d) corresponds to simulations of the incident wave field only.

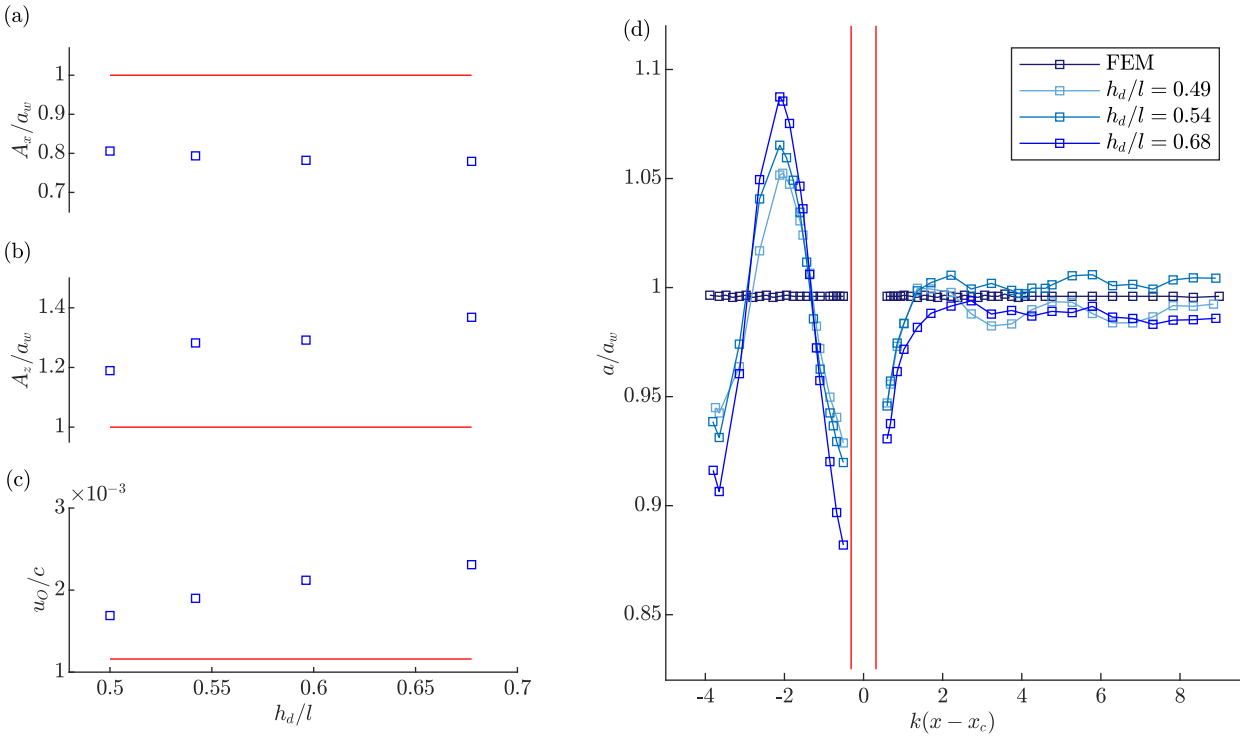


Figure 3.7: Effect of the submergence depth h_d of a round-cornered box on object motion and drift (category II, group 2): (a) and (b) non-dimensional amplitudes of oscillatory motion in the horizontal and vertical directions, respectively; (c) celerity-normalized object drift velocity; Blue square markers in (a), (b) and (c) represent the results for round-cornered boxes (RCBs). Red lines in (a) and (b) denote the oscillatory motions of a Lagrangian particle, these in (c) denote the theoretical Stokes drift. (d) non-dimensional amplitude of the local surface elevation $a(x)/a_w$ as a function of horizontal distance (scaled by wavenumber) from the centre of mass x_c. The gap between the two vertical red lines in (d) represents the position of the object and corresponds to its left and right sides, respectively. The line denoted by FEM in (d) corresponds to simulations of the incident wave field only.

3.5.2 Effect of shape and submergence depth (category II)

Motivated by the difference in drift enhancement between box-shaped and round objects of equivalent, relatively large size in category I above, we will proceed to examine how the shape and size of the submerged part of a round-cornered box affect the standing wave pattern and the drift enhancement (category II). Unlike in category I, the objects in category II are allowed to rotate but, to simplify the analysis, we do not include viscosity. In all cases, the object size and density are kept constant at a relative size of 10% and a density of $\rho = 781$ kg/m^3, respectively. Two groups of round-cornered boxes, one where each object has a different round-corner radius r (group 1) and the other where each object has a different height submergence depth h_d achieved through varying the height of the box h (group 2), are simulated. For group 1, the boxes have the same height, and we vary the radius of the round corners to change their submerged shape. Object dimensions for group 1 are given in table 3.4. For group 2, we vary the submergence depth of the box by varying its height, keeping the radius of the round corner constant. Object dimensions for group 2 are given in table 3.5.

For group 1, the amplitudes of the oscillatory part of the motion in both the horizontal and vertical directions are given as a function of normalized round-corner radius r/h_d in figure 3.6 (a) and (b), respectively. Amplitudes are obtained in the same way as for category I simulations. Figure 3.6 (c) presents the normalized time-averaged object drift speed u_O/c as a function of normalized round-corner radius r/h_d for group 1. Finally, figure 3.6 (d) depicts the spatial wave-amplitude distribution as a function of the wavenumber-normalized distance from the centre of mass of the object for group 1. Figure 3.7 gives analogous results for group 2.

We begin examining the influence of shape by returning to the results for category I. As shown in figure 3.5 (a), round-cornered boxes and round objects experience a similar linear decrease of the horizontal oscillatory motion amplitude with relative size. The amplitude of the vertical oscillatory motion of round objects increases much less with relative size compared to round-cornered boxes (figure 3.5 (b)). The difference in object drift becomes large when the relative size is larger than approximately 7% (figure 3.5 (c)). We note that increased drift is always accompanied by an increase in amplitude of the vertical motion.

We now turn to the simulations in category II, group 1, in which we vary the radius of the rounded corners. Figure 3.6 (c) shows that as the radius of the rounded corner becomes

larger, which corresponds to a more rounded shape, the drift speed decreases. Similarly, the amplitude of the vertical motion also decreases, as shown in figure 3.6 (b). The amplitude of the horizontal oscillatory motion increases by only a small amount with increasing radius (figure 3.6 (a)). Furthermore, the standing wave pattern becomes less apparent with increasing radius (figure 3.6 (d)). Accordingly, the wave-amplitude difference between the two sides of the object decreases. To sum up, figure 3.6 provides strong support for the idea that the increase in object drift compared to the Stokes drift is related to the standing wave pattern and is determined by how 'streamlined' the object is. We note that even for the round-cornered box with the largest rounded-cornered radius, the enhanced drift is still significant, which is due to its large submergence depth, as we will examine next.

For round-cornered boxes with different submergence depths (category II, group 2), it is evident from figure 3.7 that as the submergence depth increases, the object drift increases significantly, as does the amplitude of the oscillating vertical motion. The horizontal oscillatory motions increase by only a small amount with increasing submergence depth. Figure 3.7 (d) reveals that the increase in object drift is accompanied by an increase in the standing wave pattern. The largest wave amplitude on the upstream side and the relative difference in wave amplitudes between both sides of the object both increase as the submergence depth increases, further supporting our finding that the standing wave pattern drives enhanced drift.

Taking the above analysis of the effects of size, shape (of the submerged part of the object) and submergence depth together, we observe that object with similar size has little difference in their horizontal oscillatory motions, suggesting compared to the other two factors (i.e., shape and submergence), size is the dominating factor for the horizontal oscillatory motions whereas the vertical oscillatory motions are affected by a combination of size, shape and submergence. Larger size with more box-like shape, deeper submergence induces larger vertical oscillatory motions. In the above analysis, the role of the standing wave pattern generated by the object and the relative wave amplitude difference between the two sides of the object stands out. All these effects described above can be understood in terms of the ability of the object to 'hinder' the flow pattern associated with the incident wave field. The larger the submergence depth and the more box-like the submerged shape, the more the objects hinder the flow. Enhanced drift is always accompanied by a (small) reduction in horizontal oscillatory motion and a (large)

increase in vertical oscillatory motion.

3.5.3 Effect of wave steepness (category III)

Simulations in category I and II have all been conducted for low wave steepness $ka_w = 0.034$ ($a_w = 0.02$ m). In category III, we examine the dependence of drift on wave steepness. We select three different relative sizes ($l/\lambda = 5.1\%, 8.0\%, 10.0\%$; see table 3.C.1 in appendix 3.C for all object properties) and perform simulations with steepness in the range $ka_w = 0.02$ to $ka_w = 0.13$. Cases with and without viscosity are considered.

The dimensionless amplitudes of the horizontal oscillatory motion A_x/a_w and the vertical oscillatory motion A_z/a_w are shown as a function of wave steepness ka_w in figure 3.8 (a) and (b), respectively. The wave celerity-normalized object drift velocities of the objects of different sizes are shown as a function of wave steepness ka_w in figure 3.8 (c); the object drift is shown as a ratio of the Stokes drift, namely u_O/u_S, in figure 3.8 (d), noting $u_S \sim (ka_w)^2$. Finally, the local wave amplitude distribution of a round-cornered box with $l/\lambda = 10\%$ is shown as a function of horizontal distance from the centre of mass of the object in figure 3.8 (e) and (f) for three values of wave steepness. In (e), the wave amplitude is given in dimensional form as a difference between the local wave amplitude $a(x)$ and the input wave amplitude a_w. In (f), the local wave amplitude is scaled by its corresponding input wave amplitude, which is different for each steepness.

We commence our analysis with the oscillatory motions of the objects. For each box, the horizontal oscillatory motion amplitude, scaled by a_w, does not show any obvious variation with steepness (figure 3.8 (a)), while the vertical motion amplitude, scaled by a_w shows a small decrease as the wave steepness increases (figure 3.8 (b)). We note that this is consistent with the reduction in the heave response amplitude operator (RAO) with increasing wave height reported for wave energy devices of similar 2D shape (Palm et al., 2018). This is attributed therein to the induced drag and nonlinearity of the force the waves exert on the object. For the object drift, figure 3.8 (c) and (d) show that an object of relative size $l/\lambda = 5\%$ continues to follow the Stokes drift without notable enhancement (2%) despite the increase in wave steepness (for $\nu = 0$). As the object becomes large enough to induce a drift enhancement at low steepness (i.e., $l/\lambda = 8\%$ and 10%; cf. §3.5.1), the drift is further enhanced as the waves become steeper.

The amplification factors u_O/u_S of these large boxes initially decrease somewhat with increasing steepness for low values of steepness, but then reach constant values as steepness increases. This is consistent with what has been found in the experiments conducted by Huang et al. (2011); Huang and Law (2013); He et al. (2016) and Tanizawa et al. (2002). To be more specific, in the experiments of Huang et al. (2011) for 'small' floating objects ($l/\lambda = 13\%$-16%), these authors found that object drift is enhanced more as wave steepness increases and that the amplification factor u_O/u_S behaved in a similar fashion as presented here. Due to the large computational cost, we do not increase the relative size of our object beyond 10%.

Focusing on the standing wave pattern, identified in §3.5.1 and §3.5.2 as intimately related to drift enhancement, figure 3.8 (e) and (f) show the wave amplitude distribution for a round-corned box with $l/\lambda = 10\%$ for three different values of steepness ka_w. The absolute magnitude of the standing wave pattern increases with steepness, which is consistent with the increase in object drift shown for this object in figure 3.8 (c). However, the normalized wave amplitude distribution in figure 3.8 (f) shows a modest decrease in the amplitude of the wave pattern for the higher-steepness cases ($ka_w = 0.07$, 0.09), which is consistent with the behaviour of the amplification of object drift relative to Stokes drift in figure 3.8 (d).

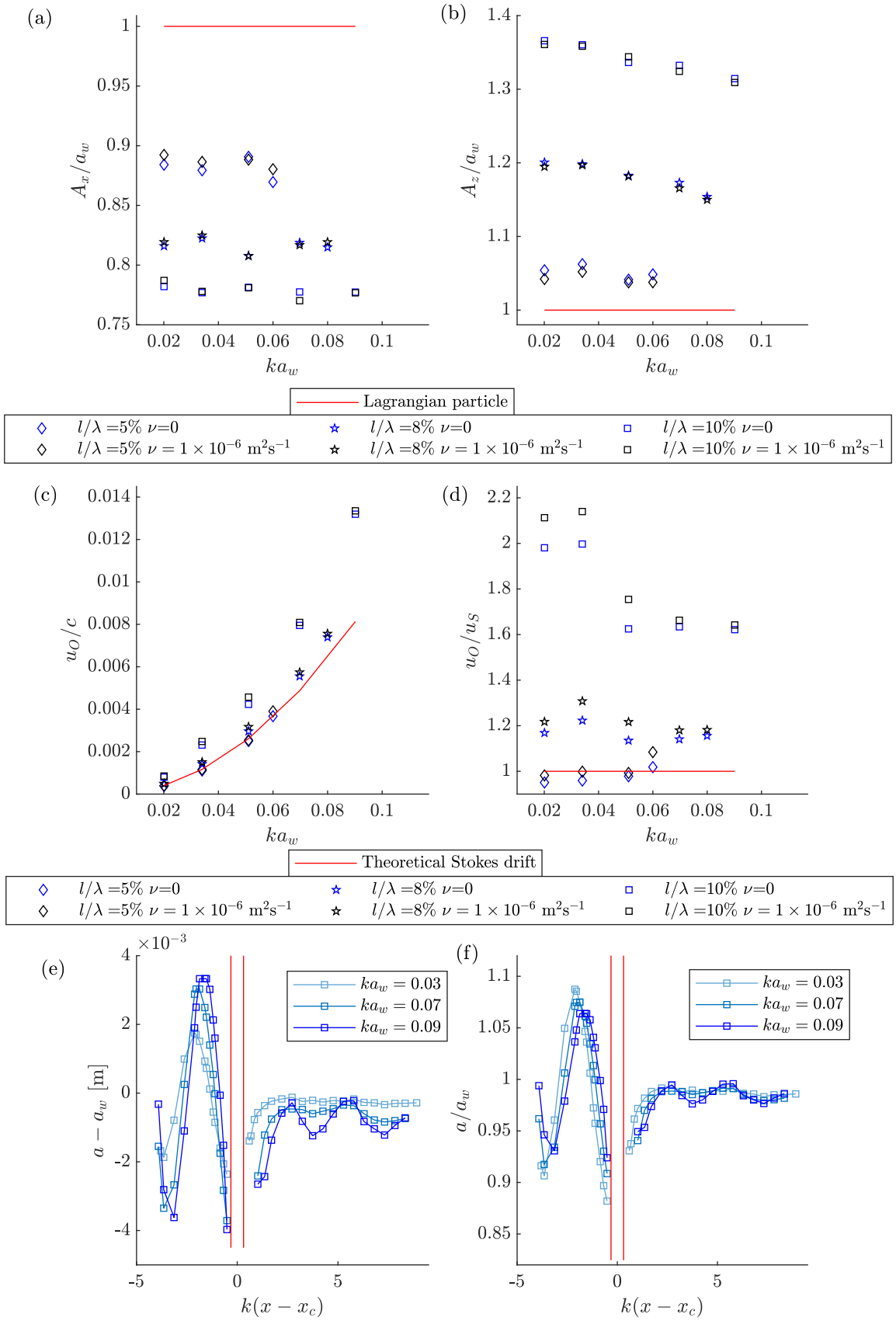

(a)
(b)
(c)
(d)
(e)
(f)
A_x/a_w
A_z/a_w
u_O/c
u_O/u_S
$a - a_w$ [m]
a/a_w
ka_w
$k(x - x_c)$
$\times 10^{-3}$
Lagrangian particle
Theoretical Stokes drift
l/λ =5% ν=0
l/λ =5% $\nu = 1 \times 10^{-6}$ m^{2}s^{-1}
l/λ =8% ν=0
l/λ =8% $\nu = 1 \times 10^{-6}$ m^{2}s^{-1}
l/λ =10% ν=0
l/λ =10% $\nu = 1 \times 10^{-6}$ m^{2}s^{-1}
$ka_w = 0.03$
$ka_w = 0.07$
$ka_w = 0.09$

Figure 3.8 *(previous page)*: Effect of wave steepness on object motion and drift (category III): (a) non-dimensional horizontal oscillatory motion amplitude; (b) non-dimensional vertical oscillatory motion amplitude; (c) celerity-normalized object drift velocity; (d) Stokes drift-normalized object drift velocity; (e) difference between the local wave amplitude distribution $a(x)$ and the input wave amplitude a_w for three different values of wave steepness for the object size of $l/\lambda = 10\%$; (f) normalized local wave amplitude distribution $a(x)/a_w$ for three different values of wave steepness for the object size of $l/\lambda = 10\%$. Diamond, star and square markers represent the results for round-cornered boxes (RCBs) of $l/\lambda = 5\%$, 8%, 10% relative sizes, respectively. Red lines in (a) and (b) denote input wave amplitudes, while in (c) and (d) they denote theoretical Stokes drift. The local wave amplitude distributions $a(x)$ in (e) and (f) are given as functions of horizontal distance (scaled by wavenumber) from the centre of mass x_c, and the gaps between the two vertical red lines in represent the position of the object ($l/\lambda = 10\%$) and correspond to its left and right sides, respectively.

3.5.4 Effects of viscosity (categories I & III)

Finally, we examine the role played by viscosity, re-examining the category I and III simulations. We do so by comparing results from our hybrid numerical model qaleFOAM that are based on the inviscid Euler equations ($\nu = 0$) and those that are based on the viscous Navier–Stokes equations ($\nu = 1 \times 10^{-6}$ m^{2}s^{-1}). We define and estimate Reynolds and Keulegan–Carpenter numbers in appendix 3.D, where we also present simulations using the Reynolds-averaged Navier–Stokes equations to examine the potential role of turbulence. These results show that the flow is laminar in our cases (at laboratory rather than field scale) with low Reynolds numbers and the inclusion of a turbulence model to ensure convergence is not necessary.

We begin by re-examining the simulations in category I (§3.5.1). As shown in figure 3.5 (a) and (b), the inclusion of viscosity induces negligible change to the oscillatory motion in the horizontal direction and a small increase in the vertical direction. This is more evident for round-cornered boxes. Turning to the object drift velocity (figure 3.5 (c)), we start by examining round objects because no obvious change to the standing wave pattern arises from the inclusion of viscosity (not shown). In the absence of viscosity no significant drift enhancement is found for round object of all sizes considered, whereas enhanced drift becomes evident for round objects larger than 8% when viscosity is considered.

Next, we consider round-cornered boxes, for which the standing wave pattern comes into play for large enough relative sizes. When the standing wave pattern is small, which is the case for objects with relative size smaller than 7%, the presence of viscosity contributes to drift

enhancement in a way consistent with the behaviour of round objects. As a round-cornered box becomes larger, the draft (submergence depth) of the box becomes larger and the standing wave pattern starts to drive drift enhancement. Viscosity works to promote enhanced drift and yields a larger drift increase compared to the case without viscosity included. For the largest round-cornered box, we observe a nearly 20% increase as a result of the inclusion of viscosity. We note the effect of the standing wave pattern and the effect of viscosity appear independent, with viscosity generally not affecting the standing wave pattern (not shown explicitly). From the simulations in category III, we observe from figure 3.8 that the inclusion of viscosity enhances the drift for all boxes. However, as a ratio of the Stokes drift, the enhanced drift speed reduces with wave steepness for low steepness, then reaches a constant value (figure 3.8 (d)).

The fact that drift increases with relative size when viscosity is considered (in the form of viscous drag) is consistent with the findings of Calvert et al. (2021), who do not consider diffraction of the wave field and who examine 3D spheres instead of the 2D round objects considered here. Calvert et al. (2021) propose two mechanisms to explain enhanced drift motion. First, they note that the linear motion (normal to the free surface) of a floating particle has a larger magnitude compared to that of a Lagrangian particle, leading to an increased drift. Second, the dynamic buoyancy force has a net effect when averaged over the wave cycle in a similar fashion to the slope-sliding term of Rumer et al. (1979). This net effect arises after averaging over the wave cycle because of a phase change that is introduced by the effect of a (viscous) drag force acting in the direction normal to the free surface. A comparison between our results for 2D round objects and their results for 3D spheres is made in figure 3.5 (a), (b) and (c). To evaluate the model of Calvert et al. (2021), we have taken the diameter of our (2D) round objects to be equal to the diameter of the spheres in Calvert et al. (2021). Due to the difference in geometry (2D vs. 3D), we emphasise that we do not expect quantitative agreement. As shown in figure 3.5 (a) and (b), Calvert et al. (2021) found that the horizontal linear motion remains unaffected by viscous drag, but the magnitude of vertical linear motion increases with relative size. We observe similar results for the vertical linear motion, although the vertical motion we observe is much smaller for the same relative size. Unlike Calvert et al. (2021), the horizontal linear motion that we predict is reduced. Figure 3.5 (c) shows a reasonable level of agreement for the drift between our results and Calvert et al. (2021) when the object is

small, but neither theory predicts significant drift enhancement for such small objects. For larger objects, we observe less enhanced drift than predicted by Calvert et al. (2021). The discrepancies in linear motion and drift may be due to the fact that the theoretical model in Calvert et al. (2021), based on the slope-sliding concept, does not consider two-way coupling between the waves and the object and assumes that the wave field is unaffected by the presence of the object, thus causing the object in Calvert et al. (2021) to lose less energy, as only viscous and no wave damping is considered therein. Wave damping could lead to reduced horizontal and vertical linear motions (Calvert et al. (2021) predict larger linear motion responses in both directions), which in turn results in less enhanced drift. Wave damping could also contribute to the phase difference and potentially enhance the second mechanism. Nevertheless, both mechanisms in Calvert et al. (2021) could play a role in explaining the phenomenon that the inclusion of viscosity for relatively large objects enhances the drift. For completeness, we note that we cannot rule out the occurrence of some boundary-layer streaming in the near-surface wave-driven boundary layer (see, e.g., Grue and Kolaas (2017)), which would also enhance drift and also only arises in the presence of viscosity, although this boundary layer only has a very short distance to develop (namely, only in the QALE-FEM domain). We examine the effects of viscosity in more detail in appendix 3.C.

3.5.5 Relationship between local standing wave pattern and the object drift

Thus far, we have investigated the effects of various factors on the drift behaviour of finite-size floating objects. All the results indicate that drift enhancement is closely related to the diffraction of the wave field. To gain a more quantitative understanding of this relationship, figure 3.9 shows the drift speed as a function of the maximum local wave amplitude $a_{\max}$ obtained from the standing wave pattern. All the results shown in this figure are based on the same input incident wave and thus identical theoretical Stokes drift. We note that the 'wave gauges' we have used to output information about the free surface elevation from the code are set at fixed intervals, making it challenging to precisely predict the local wave amplitude maxima. According to figure 3.9, there is a positive correlation between the local maximum amplitude $a_{\max}$ and the object drift, which is most clearly observable when the local maximum

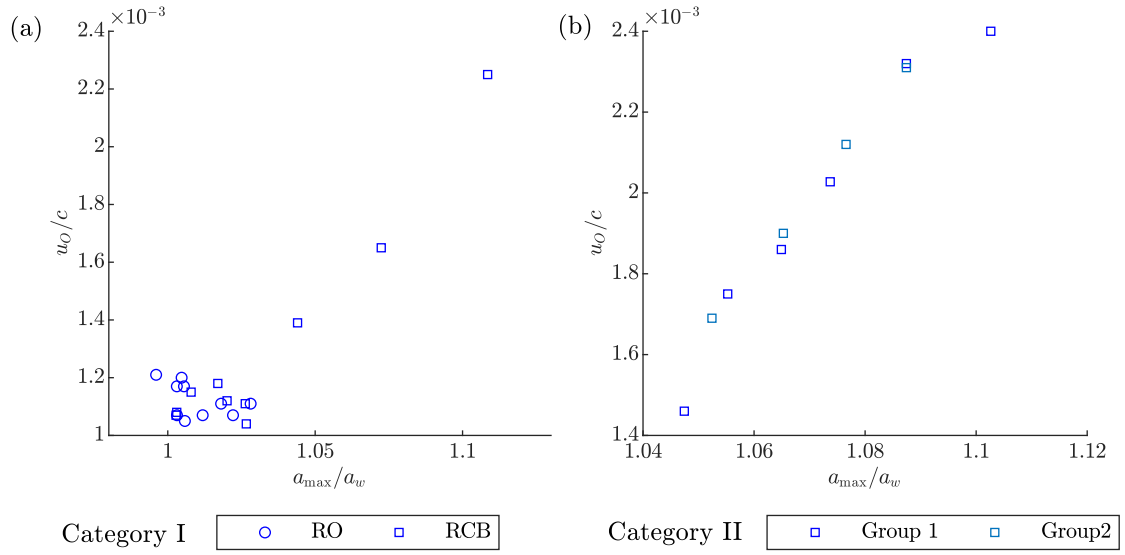


Figure 3.9: The celerity-normalized object drift u_O/c as a function of the local maximum wave amplitude normalized by the input wave amplitude $a_{\max}/a_w$: (a) the results for the round-cornered boxes and round objects of different sizes (category I simulations); (b) the results for the objects of $l/\lambda = 10\%$ with different round-corner radii and depths of submergence (category II simulations). All results shown are for the same input wave condition: $a_w = 0.02$ m and $u_S/c = 0.0012$.

wave amplitude $a_{\max}$ is relatively large (i.e., $a_{\max}/a_w \geq 1.05$). Figure 3.9 shows that the correlation between the maximum local wave amplitude (as a measure of how much diffraction takes place) and object drift is similar, regardless of differences in shape, submergence, or size of the object, as long as the object is large enough to diffract the wave field.

It is instructive to note that an increase in the magnitude of the vertical oscillatory motion is always accompanied by a more distinct standing wave pattern, as particularly evident in the case of large round-cornered boxes. This is because the formation of the standing wave pattern results from the disturbance to the fluid field caused by the presence of the object, which would be largest if the object were stationary (in which case we have only diffraction, no radiation). However, when the object is free to move, its motion serves as a response to the waves, mitigating the effects of diffraction. The radiated wave field arises due to the object's oscillation (as if it were in calm water, in the linear approximation), generating a wave field that weakens the standing wave pattern present in the combined diffracted and incident wave field.

3.6 Comparison between the hybrid numerical model and the diffraction-modified Stokes drift model

To develop the hypothesis developed in §3.5 that drift enhancement is a result of diffraction of the wave field by the object and gain a better understanding of the underlying mechanism (in the absence of the viscosity), we compare the predictions of the hybrid numerical model qaleFOAM presented in §3.5 with the diffraction-modified Stokes drift model introduced in §3.3. In particular, the diffraction-modified Stokes drift model can distinguish the contributions to the object drift of the incident, diffracted and radiated parts of the wave field. The objects considered are the same as for the hybrid numerical model, although we do not include rounded corners for the rectangular box in the diffraction-modified Stokes drift model (we set $r/h_d = 0.24$ in the simulations of the hybrid numerical model shown in this section). The grid sizes of all BEM simulations are chosen to be $\Delta x/h_d = \Delta z/h_d = 0.01$ for the rectangular box and $\Delta l/h_d = 0.01$ for the round object (following BEM model verification in appendix 3.A and a convergence study not shown here). We will examine oscillatory motion (§3.6.1) and object drift (§3.6.2) in turn.

3.6.1 Oscillatory motion

Amplitude of oscillatory motion

Figure 3.10 provides the non-dimensional amplitudes of oscillatory motion as a function of relative size for the different objects defined in table 3.3 predicted by both the BEM model and the qaleFOAM model for low wave steepness $ka_w = 0.034$. Specifically, for the BEM model, these take the form:

$$\xi_x = A_x \cos(\theta_x - \omega t) \quad \text{and} \quad \xi_z = A_z \cos(\theta_z - \omega t). \tag{3.10a,b}$$

Figure 3.10 demonstrates that the amplitude of motion between the two models is in agreement. The effects of size and shape on the oscillatory motions in the BEM model are consistent with those in the qaleFOAM model discussed in §3.5.1 and §3.5.2. The BEM and the qaleFOAM models agree well for the full range of steepnesses studied in this chapter ($ka_w = 0.02$-0.11)

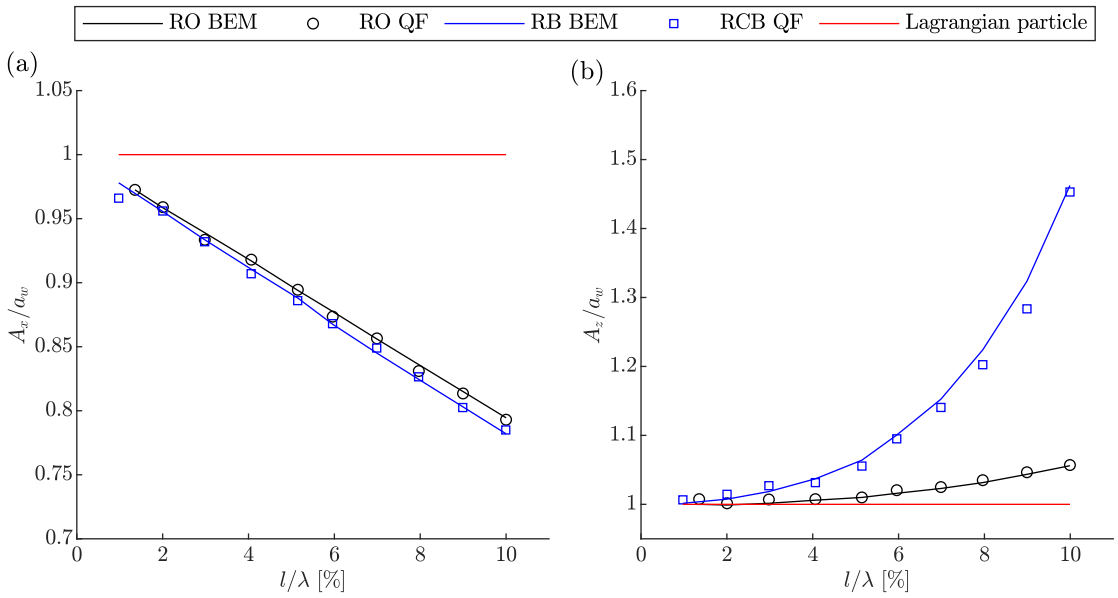


Figure 3.10: Comparison of amplitudes of oscillatory motion for objects of different sizes and shapes predicted by the qaleFOAM (QF) and BEM models for $ka_w = 0.034$: (a) horizontal oscillatory motion; (b) vertical oscillatory motion of objects. Motion amplitudes in (a) and (b) are normalized by input wave amplitude a_w, with the red lines then corresponding to the behaviour of a Lagrangian particle. Lines correspond to the results from BEM simulations, while markers are those from qaleFOAM (QF) simulations. Square markers represent results for boxes, rectangular boxes (RBs) for BEM simulations and round-cornered boxes (RCBs) for qaleFOAM simulations, and circle markers denote round object (ROs).

(not shown explicitly).

Phase of oscillatory motion

Having demonstrated the ability of the BEM model to capture the amplitude of the oscillatory motion, we will now examine its phase. The phases of the vertical and horizontal oscillatory motions predicted by the (linear) BEM model are defined in (3.10), and we will compare these to the phases of the linear incident wave field. For a linear incident wave of the form $\eta = a_w \cos(kx - \omega t + \theta_w)$, (linearized) horizontal and vertical components of the motion of a Lagrangian particle have the form:

$$\xi_{I,x}(t) = a_w \sin(\omega t - kx - \theta_w)_{x=0} = a_w \cos(\theta_w + \pi/2 - \omega t), \tag{3.11}$$

$$\xi_{I,z} = a_w \cos(\omega t - kx - \theta_w)_{x=0} = a_w \cos(\theta_w - \omega t), \tag{3.12}$$

which have been evaluated at the particle's initial location in the BEM model ($x = 0$). Figure 3.11 shows the phase difference between a finite-size object and a Lagrangian particle as a

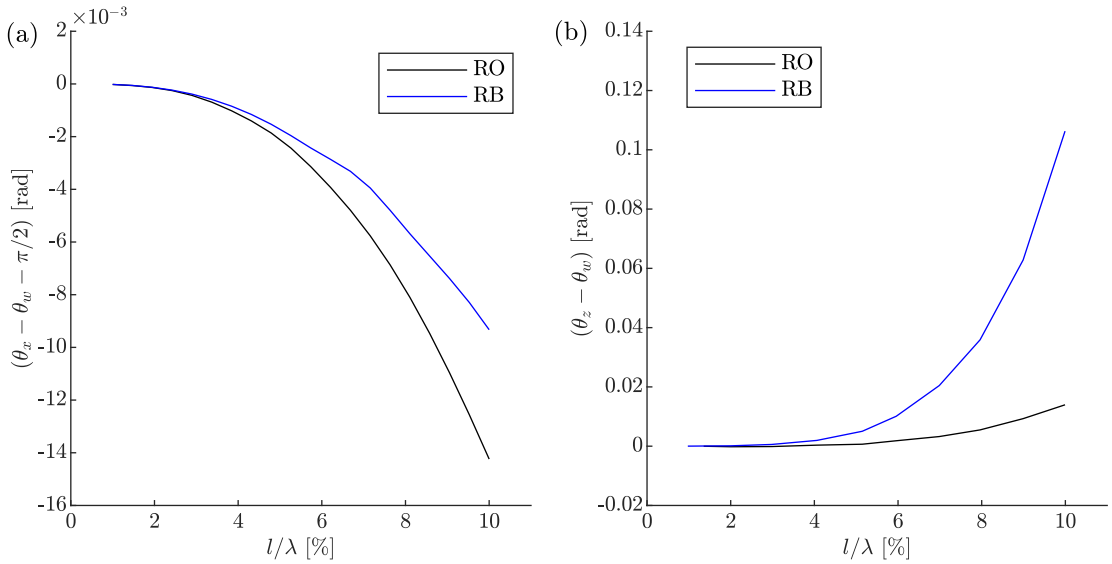


Figure 3.11: Phase difference of the oscillatory motion between a finite-size object and a Lagrangian particle as a function of relative object size from BEM simulations: (a) horizontal direction, (b) vertical direction. Blue lines correspond to rectangular boxes and black lines to round objects.

function of relative size of the object for both shapes for the horizontal and vertical oscillatory motions predicted by the BEM model, where horizontal and vertical phase difference is denoted by $\theta_x - \theta_w - \pi/2$ and $\theta_z - \theta_w$, respectively.

Figure 3.11 shows that when objects are very small, the phase difference is zero, confirming that the objects behave as Lagrangian particles. As the objects become larger, the magnitude of the phase differences of both horizontal and vertical motions become larger, and this relationship is nonlinear. Specifically, the larger the object is, the more phase lag it gains vertically while the more phase lead it shows horizontally. The magnitudes of the phase difference of the vertical motion are much larger than that of the horizontal motion, which are is negligibly small.

We note that rectangular boxes have larger phase lags vertically but a smaller phase leads horizontally compared to round objects. Furthermore, for objects with greater submergence depths, we find greater phase lags in the vertical and smaller phase leads in the horizontal. The phase differences are found to be independent of steepness. These results are not shown here explicitly in the interest of brevity.

3.6.2 Object drift

We will now compare predictions of object drift by the qaleFOAM model already examined in §3.5 to predictions of object drift based on the diffraction-modified Stokes drift model (i.e.,

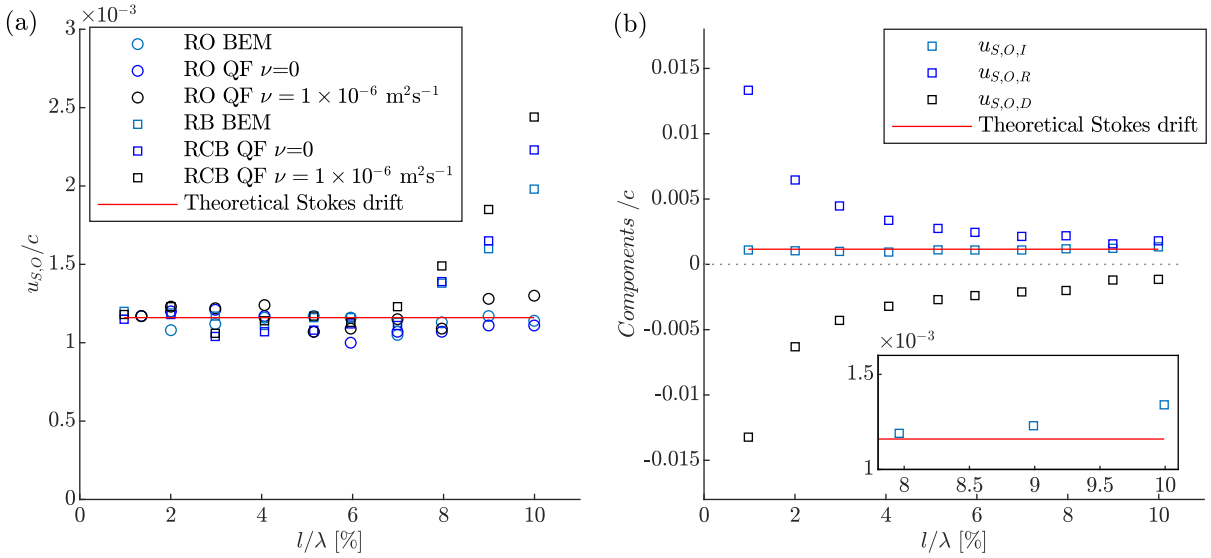


Figure 3.12: Diffraction-modified Stokes drift velocity $u_{S,O}$ as a function of object size: (a) comparison between BEM and qaleFOAM (QF) models with ($\nu = 1.00 \times 10^{-6}$m^2 s^{-1}) and without ($\nu = 0$) viscosity for round objects (ROs) and rectangular boxes (RBs, RCBs); (b) different components of the diffraction-modified Stokes drift velocity predicted by the diffraction-modified Stokes drift model, where $u_{S,O,I}$, $u_{S,O,R}$ and $u_{S,O,D}$ respectively represent the incident, radiation and diffraction components of the diffraction-modified Stokes drift velocity.

using (3.8)), i.e., an estimate of the drift accounting for the radiated and diffracted as well as the incident waves. We consider waves with a low input steepness of $ka_w = 0.034$, and the dimensions of the rectangular boxes and the round objects we consider are given in table 3.3 (and table 3.C.1 for boxes larger than $l/\lambda = 4\%$). Figure 3.12 makes the comparison between drift predictions by the qaleFOAM and the diffraction-modified Stokes drift model.

It is clear from figure 3.12 that the diffraction-modified Stokes drift model captures the main trend well, predicting a significant increase of object drift with increasing relative size for rectangular boxes. The diffraction-modified Stokes drift model and the qaleFOAM model without viscosity ($\nu = 0$) show good agreement except for the largest box with $l/\lambda = 10\%$, for which the diffraction-modified Stokes drift model underestimates the drift velocity compared with the prediction of the qaleFOAM model (for $\nu = 0$). This discrepancy can be attributed to two factors: the slight differences in shape between the boxes in the diffraction-modified Stokes drift model (rectangular box with sharp corners) and in the qaleFOAM model (rectangular box with round corners) and the approximate nature of the diffraction-modified Stokes drift model (cf. (3.3)), whose underlying assumptions become less valid as the object becomes larger.

To analyze the physical mechanism underlying the drift enhancement, we will decompose the object drift predicted by the diffraction-modified Stokes drift model (i.e., (3.8)) into con-

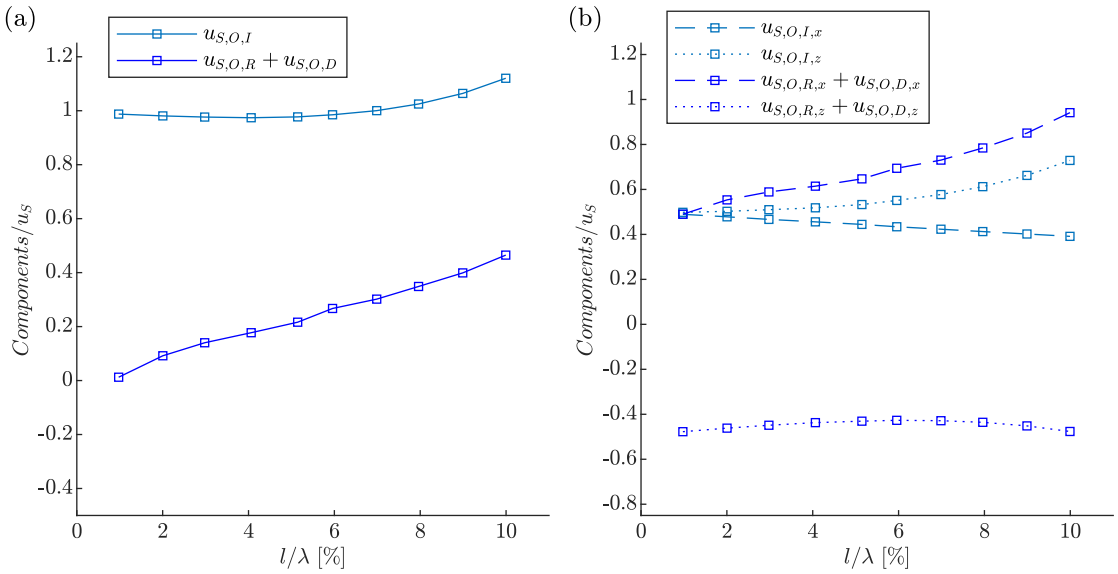


Figure 3.13: Decomposition of the diffraction-modified Stokes drift predicted by diffraction-modified Stokes drift model for rectangular boxes according to (3.13) and (3.14): (a) contributions of the incident ($u_{S,O,I}$) and the sum of the radiated and diffracted waves ($u_{S,O,R} + u_{S,O,D}$); and (b) further decomposition into contributions due to horizontal (x) and vertical (z) components of object motion. The diffraction-modified Stokes drift velocity components are normalized by the Stokes drift (of an infinitesimally small object).

tributions from the incident, radiated and diffracted waves:

$$u_{S,O} = u_{S,O,I} + u_{S,O,R} + u_{S,O,D}, \tag{3.13}$$

where

$$u_{S,O,I} = \frac{A_x}{2} k\omega A^I_{xx} \cos(\theta_x - \theta^I_{xx}) + \frac{A_z}{2} k\omega A^I_{xz} \cos(\theta_z - \theta^I_{xz}); \tag{3.14}$$

$$u_{S,O,R} = \frac{A_x}{2} k\omega A^R_{xx} \cos(\theta_x - \theta^R_{xx}) + \frac{A_z}{2} k\omega A^R_{xz} \cos(\theta_z - \theta^R_{xz}); \tag{3.15}$$

$$u_{S,O,D} = \frac{A_x}{2} k\omega A^D_{xx} \cos(\theta_x - \theta^D_{xx}) + \frac{A_z}{2} k\omega A^D_{xz} \cos(\theta_z - \theta^D_{xz}). \tag{3.16}$$

Each term (i.e., (3.14), (3.15) and (3.16)) includes contributions from the horizontal (first term) and vertical (second term) motion of the object. Figures 3.12 (b) and 3.13 show these contributions as a function of relative object size. We will start by examining the contribution of the incident wave field to the diffraction-modified Stokes drift, $u_{S,O,I}$. For very small objects, we have $A_x = a_w$, $\theta_x - \theta_w = \pi/2$, $A_z = a_w$ and $\theta_z - \theta_w = 0$ (cf. figures 3.10 and 3.11). Combined with $A^I_{xx} = a_w gk/\omega^2 = a_w$, $\theta_{I,x} - \theta_w = \pi/2$, $A^I_{xz} = a_w gk/\omega^2 = a_w$ and $\theta_{I,z} - \theta_w = 0$ (from (3.5))

for the deep-water incident wave field we consider, it is readily evident from (3.14) that

$$u_{S,O,I} = \frac{a_w}{2} k\omega a_w \cos(\pi/2 - \pi/2) + \frac{a_w}{2} k\omega a_w \cos(0 - 0) = {a_w}^2 \omega k = u_S. \tag{3.17}$$

Any contributions to the diffraction-modified Stokes drift from the radiated and the diffracted wave field for very small objects must therefore be equal and opposite (cf. (3.13)), which is consistent with what is presented in figure 3.12 (b).

As the object becomes larger, the amplitude of horizontal oscillatory motion A_x becomes smaller (figure 3.10(a)), its phase difference does not change significantly (figure 3.11 (a)), while the amplitude of vertical oscillatory motion A_z becomes larger (figure 3.10 (b)), but the phase difference of the vertical motion increases (figure 3.11 (a)), diminishing the effect of the enhanced amplitude of vertical motion (cf. $A_z \cos(\theta_{I,z} - \theta_w)$).

A careful reader may observe that the incident component of drift $u_{S,O,I}$ in figure 3.12 (b) and figure 3.13 (a) experiences a slight decrease before undergoing a more significant increase. To explain this, we note that as object size increases, the amplitude of vertical oscillatory motion increases (cf. figure 3.10 (b)) but its positive effect on drift is diminished by the increasing phase difference (cf. figure 3.11 (b)), while the amplitude of horizontal oscillatory motion decreases (cf. figure 3.10 (a)), acting to reduce drift. When the negative effects resulting from reduced horizontal oscillatory motion compete over the positive contribution of the enhanced vertical motion, the incident drift component $u_{S,O,I}$ is reduced. This is evident in figure 3.12 (b) and figure 3.13 (a) for objects with relative size between 3% and 7%.

Noting that A_x decreases with relative size in a linear fashion (figure 3.10(a)), whereas A_z increases nonlinearly at an increasing rate (figure 3.10(b)), figure 3.13 (a) and (b) show that the effect of the increased vertical oscillatory motion generally dominates and the contribution of the incident waves acts to increase the object drift for larger objects. However, the increased vertical oscillatory motion cannot explain the majority of the large drift enhancement observed for large objects.

Turning to the contributions of the radiated and diffracted waves to the diffraction-modified Stokes drift, $u_{S,O,R}$ and $u_{S,O,D}$, we observe from figure 3.12 (b) that both terms decrease rapidly with increasing relative size. Since these two terms have opposing signs, the fact that $u_{S,O,D}$ decreases more rapidly leads to a net positive contribution to the diffraction-modified Stokes

drift that increases with relative size, as illustrated in figure 3.13 (a). This explains most of the enhanced drift for large objects found in this chapter.

However, if the small reduction of the incident drift component $u_{S,O,I}$ for objects with intermediate size, described above, cannot be compensated for by the net positive contribution from the imbalance of diffraction and radiation components, the overall drift will be reduced. This helps to explain the slight reduction in drift compared to the theoretical Stokes drift for objects with a relative size of $2\% \leq l/\lambda \leq 6\%$ in figure 3.12 (a).

From figure 3.13 (b) it is further evident that the horizontal object motion is responsible for the increase in $u_{S,O,R}$ and $u_{S,O,D}$ and thus the total diffraction-modified Stokes drift for large objects. Note that the motions evaluated in section §3.5 are linear oscillatory motions, while the object motion evaluated in figure 3.13 is the drift motion. According to (3.14)-(3.16), the drift components are dependent not only on oscillatory motions (amplitudes and phases) but also on derivatives of the velocity field. Only their combined effect determines the drift. Physically, such large objects are less able to follow the horizontal motion the waves would induce for a Lagrangian particle (cf. figure 3.10 (a)) and are therefore transported at a faster speed.

It may seem somewhat counter-intuitive that the smallest object has the largest diffraction/radiation drift components (i.e. $u_{S,O,R}$ and $u_{S,O,D}$) and that the absolute values of these components decrease as the object size increases, as shown in figure 3.12 (b). Contrary to what is shown in figure 3.12, from a physical point of view, when the object is very small, it behaves like a fluid particle and generates no diffraction. However, it is argued that each drift velocity component defined here results from the interaction of object's oscillatory motion and velocity field, both of which are influenced by a combination of incident, diffracted and radiated problems. What really matters here is the combined contribution of the diffraction and radiation components, as shown in figure 3.13 (a), as they do not contribute to drift independently.

For round objects, the decrease in $u_{S,O,I}$ is not balanced by a sufficiently large increase in the sum of $u_{S,O,R}$ and $u_{S,O,D}$, and these objects do not experience an increase in diffraction-modified Stokes drift for large size (in the absence of viscosity). For increased submergence depth, the effects discussed above for a rectangular box are only enhanced. Furthermore, the diffraction-modified Stokes drift model (cf. (3.3)) and the qaleFOAM model agree well for the

full range of steepnesses studied in this chapter ($ka_w = 0.02$-0.11). These results are not shown here explicitly in the interest of brevity.

3.7 Conclusions

In this chapter, we have investigated the fluid mechanics which can lead to enhancements in the drift of floating objects under the influence of gravity waves beyond that of the well understood Stokes drift. We restrict our analysis to unidirectional waves on deep water and where the object is less than 10% the size of the wavelength. Based on numerical modelling we have identified two mechanisms that can explain increased drift compared to the Stokes drift: a mechanism that relies on viscosity and a mechanism that is related to the diffraction of the wave field by the object and the standing wave pattern that arises. Both these mechanisms come into play when the size of the object is larger than a few percent of the wavelength. When the object is smaller than this, the inertial (i.e., non-Lagrangian) behaviour of the object becomes less evident and the difference in velocity between the object and the surrounding fluid can be ignored. There is no obvious increase in the amplitude of the vertical motion, and the drift motion becomes that of a Lagrangian particle. As the object becomes larger, the amplitude of the motion normal to the free surface increases, which creates a drag force because of the difference between the object motion and the fluid surrounding it. This effect can cause enhanced horizontal drift (Calvert et al., 2021). In addition, as the object size becomes larger, the draft of the object (submergence depth) becomes larger, and the submerged part of the object acts to impede the fluid motion associated with the waves and thereby changes the waves themselves. That is, the object diffracts the wave field. Dependent on how large the submerged part of the object is and on its shape, the impeding effect is different, and thus the drift is enhanced to a different degree. The larger the submergence depth is and the closer the shape of the object is to a box (i.e., not streamlined), the stronger is the impeding effect, yielding a larger increase in horizontal drift.It deserves noting that the standing wave pattern (and thus the impeding effect) implies an exchange of momentum between the object and waves. A detailed analysis of the force and momentum balance is not explored and well understood and should be investigated in the future work.

We consider objects of up to 10% of the wavelength and for the largest of these drift

enhancement over that of a Lagrangian particle can be as large 92% of the Stokes drift for simulations without viscosity or 113% with viscosity. Most of the increased drift results from diffraction for round-cornered boxes with viscosity typically contributing a further 20%. For round objects, diffraction only has a small effect, and the much smaller enhanced drift arises because of the effects of viscosity.

To enable quantitative predictions to be made about the contribution of diffraction to drift, we have derived a 'diffraction-modified' Stokes drift akin to Stokes (1847), but accounting for the combination of the incident, diffracted and radiated wave fields rather than simply the first of these. To calculate the necessary diffracted and radiated fields a linear boundary element method (BEM) model based on potential-flow theory is used. Two effects become clear. First, the increased vertical oscillatory motion of the object causes a greater contribution from the incident wave field to the diffraction-modified Stokes drift. Second, the combination of diffracted and radiated waves makes an additional contribution to the diffraction-modified Stokes drift that is not present when the object is small. Although we have not analysed the force and momentum balance resulting in the object's (enhanced) drift motion, we foresee this will give valuable insight into the mechanism and recommend it as future work.

Various authors have found evidence for enhanced drift in different circumstances. Calvert et al. (2021) (based on previous work by Rumer et al. (1979), Shen and Ackley (1991) and Huang et al. (2016)) explored the influence of viscosity described above using a theoretical model that considers viscous forces but ignores the diffraction of the wave field caused by the presence of the object (required for the second mechanism). Future work should quantitatively compare the findings of the present work on the effect of viscosity to the predictions of Calvert et al. (2021), taking account of Reynolds number and wave steepness, but most importantly for the same geometry, that is, by extending the 3D model of Calvert et al. (2021) to 2D or our 2D numerical simulations to 3D. According to the experiments and theoretical analysis by Longuet-Higgins (1953, 1960); Grue and Kolaas (2017), the presence of viscosity should also be accompanied by an additional mechanism for (Eulerian-mean) wave-induced drift, namely boundary-layer streaming. In principle, boundary-layer streaming of the free surface is included in the viscous simulations performed in this chapter but it is not explicitly investigated and likely only small, as the boundary layer only has a short distance to develop in the Navier–Stokes part of the

hybrid numerical model. As boundary-layer streaming is associated with strong vertical shear, its differential effect on objects of different submergence depths is foreseeable and should be investigated for inertial objects in future work.

Enhanced object drift due to diffraction has probably been observed in previous experiments, although it has not been identified as such. Harms (1987) showed using experiments that for ice floes (box-shaped) with large submergence depths the drift velocity increased with the draft of the object, keeping size constant (for relative sizes smaller than approximately 25%). Enhanced drift was also found for larger submergence depth in experiments conducted by Huang et al. (2011), and a similar trend of the drift scaled by Stokes drift as a function of wave steepness can be identified in their results. In the experiments carried out by He et al. (2016) for regular waves in finite depth, drift enhancement is seen to increase with wave steepness for boxes with $l/\lambda = 9\%$ and 10%. Future experiments should focus explicitly on identifying the standing wave pattern associated with diffraction and should explore the roles of both length and width (i.e., 3D effects) of objects relative to the wavelength.

To clarify, the term 'diffraction' in DMS (Diffraction-modified Stokes drift) indicates that the effects we observe are in the diffraction regime. According to the theory, the diffraction regime involves a combination of and interactions between incident, radiated and diffracted problems.

Appendices

3.A Mathematical formulation and verification of the BEM model

In the BEM model, we deal with the problem based on linearized potential-flow theory, which assumes the fluid is homogeneous, incompressible, inviscid and the flow is irrotational. The flow is described by a velocity potential Φ, which, under the linear approximation, can be further divided into an incident potential Φ_I, a diffraction potential Φ_D and a radiation potential Φ_R (cf. (3.1)), where the incident potential neglects the influence caused by the presence of the object, the diffraction potential considers the disturbance induced by the presence of the object on the incident wave field and ignores the oscillatory motion of the object, and the radiation potential describes the wave field forced by the oscillatory motion of the object in still water. The incident potential is given in (3.2).

3.A.1 Radiation potential

Based on potential-flow theory (e.g., Newman (2018), specifically, sections 6.15-6.19), the radiation potential ϕ_R can be further decomposed into components representing radiation of waves due to horizontal, vertical and rolling object motions:

$$\phi_R(x,z) = \sum_{j=1}^{3} -\iota\omega A_j \hat{\phi}_j(x,z) \tag{3.18}$$

in which A_j (for $j = x, z, \alpha$) represent the amplitudes of the corresponding three modes of motion of the object, and $\hat{\phi}_j$ ($j = x, z, \alpha$) represents the radiation velocity potential due to unit body motion in mode j. Three motion modes are included: horizontal ($j = x$), vertical ($j = z$),

and rolling motion ($j = \alpha$, where α is defined as the angle of rotation around the y-axis in the (x,z)-plane). The potential $\hat{\phi_j}$ is governed by Laplace's equation $[L]$ and subject to linearized free surface boundary C_F condition $[F]$, body surface C_B condition $[B]$, bottom C_D condition $[D]$ as well as far-field radiation C_R condition $[R]$, shown as:

$$
\begin{aligned}
&[L] \qquad \frac{\partial^2 \hat{\phi_j}}{\partial x^2} + \frac{\partial^2 \hat{\phi_j}}{\partial z^2} = 0, \\
&[F] \qquad \frac{\partial \hat{\phi_j}}{\partial z} - \frac{\omega^2}{g}\hat{\phi_j} = 0 \qquad \text{for } z = 0, C_F, \\
&[B] \qquad \frac{\partial \hat{\phi_j}}{\partial N} = N_j \qquad \text{for } C_B, \\
&[D] \qquad \frac{\partial \hat{\phi_j}}{\partial z} = 0 \qquad \text{for } z = -d, C_D, \\
&[R] \quad \lim_{x \to \pm\infty} \left(\frac{\partial \hat{\phi_j}}{\partial x} \mp ik\hat{\phi_j} \right) = 0 \qquad \text{for } C_R,
\end{aligned}
\tag{3.19}
$$

in which C_B refers to boundaries of C_1, C_2 and C_3 in figure 3.3 (a) and C_r in figure 3.3 (b), N is the unit normal vector of the object surface, and N_j represents the projection of the unit normal vector of the relevant boundary in the jth direction.

In numerical simulations, we truncate the domain at $x = \pm L_{BEM}/2$ for both two horizontal sides (shown in figure 3.3) and rewrite the radiation condition in a uniform expression for both ends as:

$$
\frac{\partial \hat{\phi_j}}{\partial N} = ik\hat{\phi_j} \tag{3.20}
$$

3.A.2 Diffraction potential

The governing equation and boundary conditions of the diffraction potential ϕ_D are:

$$\begin{aligned}
&[L] \quad \tfrac{\partial^2 \phi_D}{\partial x^2} + \tfrac{\partial^2 \phi_D}{\partial z^2} = 0, \\
&[F] \quad \tfrac{\partial \phi_D}{\partial z} - \tfrac{\omega^2}{g}\phi_D = 0 \qquad \text{for } z = 0, C_F, \\
&[B] \quad \tfrac{\partial \phi_D}{\partial N} = -\tfrac{\partial \phi_I}{\partial N} \qquad \text{for } C_B, \\
&[D] \quad \tfrac{\partial \phi_D}{\partial z} = 0 \qquad \text{for } z = -d, C_D, \\
&[R] \quad \tfrac{\partial \phi_D}{\partial N} = ik\phi_D \qquad \text{for } C_R.
\end{aligned} \tag{3.21}$$

From (3.21) and (3.19), it can be seen that the description of the diffraction potential is very similar to that of the radiation potential; the only difference is in the body surface condition.

3.A.3 Equations of motion

The equations of motion of the object are given by:

$$\mathbf{Ma} = \mathbf{F}_R + \mathbf{F}_C + \mathbf{F}_K + \mathbf{F}_D \tag{3.22}$$

in which $\mathbf{M}$ is the general mass matrix, $\mathbf{a}$ is the acceleration, $\mathbf{F}_R$, $\mathbf{F}_C$, $\mathbf{F}_K$, $\mathbf{F}_D$ are the radiation, restoring, incident and diffraction forces, respectively. The radiation forces $F_{R,kj}$ can be expressed as:

$$F_{R,kj} = -\mathrm{Re}\{(-\omega^2 \mu_{kj} - \iota\omega\lambda_{kj})A_j e^{-\iota\omega t}\}, \tag{3.23}$$

where λ_{kj}, μ_{kj} are the added mass coefficient and damping coefficient, respectively. They can be calculated by:

$$\mu_{kj} = \mathrm{Re}\left(\rho_f \int_{C_B} \hat{\phi}_j N_k \mathrm{d}l\right), \tag{3.24}$$

$$\lambda_{kj} = \omega \mathrm{Im}\left(\rho_f \int_{C_B} \hat{\phi}_j N_k \mathrm{d}l\right), \tag{3.25}$$

where Re and Im represent the real and imaginary parts of the complex number, and ρ_f is the fluid density, N_k represents the projection of the unit normal vector of the boundary in the kth direction. The restoring forces $F_{C,k}$ can be calculated by:

$$F_{C,k} = \mathrm{Re}\{-C_{kj} \cdot A_j e^{-\iota\omega t}\}, \tag{3.26}$$

where C_{kj} is the matrix of restoring force coefficient. Einstein notation is used here to imply the summation over a set of $j = 1, 2, 3$. The incident wave forces (Froude–Krylov) F_k^I can be calculated by:

$$F_k^I = \mathrm{Re}\{f_k^I e^{-\iota\omega t}\} = \mathrm{Re}\{\rho_f \iota\omega \int_{C_B} \phi_I N_k \mathrm{d}l e^{-\iota\omega t}\} \tag{3.27}$$

The diffraction wave forces F_k^D of the kth mode in the BEM model can be calculated in two ways:

$$F_k^D = \mathrm{Re}\{f_k^D e^{-\iota\omega t}\} = \mathrm{Re}\{\rho_f \iota\omega \int_{C_B} \phi_D N_k \mathrm{d}l e^{-\iota\omega t}\}, \tag{3.28}$$

$$F_k^D = \mathrm{Re}\{f_k^D e^{-\iota\omega t}\} = \mathrm{Re}\{-\rho_f \iota\omega \int_{C_B} \hat{\phi}_k \frac{\partial \phi_I}{\partial N} \mathrm{d}l e^{-\iota\omega t}\}, \tag{3.29}$$

where (3.28) calculates the diffraction force by directly integrating the diffraction potential, while (3.29) calculates the diffraction force using the Haskind formula. If we substitute (3.23), (3.26), (3.27), (3.28) into (3.22) and take the time factor $e^{-\iota\omega t}$ out, we obtain the equations of motions in the frequency domain for k-th motion mode ($k = 1, 2, 3$):

$$\sum_{j=1}^{3} \left[-\omega^2 \left(m_{kj} + \mu_{kj}\right) - \iota\omega\lambda_{kj} + C_{kj}\right] A_j = f_k^I + f_k^d. \tag{3.30}$$

The equations of motion for the object contain the (added) mass, hydrodynamic damping and restoring forces on its left side and forces due to the incident and diffracted wave field on the right side. We thus take the object's inertia and wave-body interaction into account.

3.A.4 Two-dimensional Green's function method

The potentials $\hat{\phi}_j$ and ϕ_D are harmonic functions and are governed by the Laplace equation. Assuming $P(x, z)$ is a field point in the fluid domain and $Q(x', z')$ is the source point in the field, we choose a Green's function that satisfies $\nabla^2 G(P, Q) = \delta(P, Q)$, then according to Green's second formula, the value of the potential $\hat{\phi}_j$ and ϕ_D can be determined uniquely by giving its value and normal derivative over all boundaries (Newman, 2018). We have:

$$\alpha(P)\hat{\phi}_j(P) = -\int_C \left[\hat{\phi}_j(Q)\frac{\partial G(P,Q)}{\partial N} - G\frac{\partial \hat{\phi}_j(Q)}{\partial N}\right]\mathrm{d}l, \tag{3.31}$$

$$\alpha(P)\phi_D(P) = -\int_C \left[\phi_D(Q)\frac{\partial G(P,Q)}{\partial N} - G\frac{\partial \phi_D(Q)}{\partial N}\right]\mathrm{d}l, \tag{3.32}$$

in which C represents the boundaries of the fluid domain, including free surface boundaries C_F, body surface boundaries C_B, far-field radiation boundaries C_R and bottom boundaries C_D. For smooth boundary, $\alpha(P)$ is valued as:

$$\alpha(P) = \begin{cases} 2\pi & P \in \Omega \\ \pi & P \in S \\ 0 & P \notin S \cup \Omega \end{cases} \tag{3.33}$$

where Ω represents the region inside of the fluid domain, and S denotes the boundary of the fluid domain. Here, the simple Green's function $G(P, Q) = \ln\frac{1}{r(P,Q)}$ is used. As $\ln\frac{1}{r(P,Q)}$ is the general solution of the governing equation and does not satisfy any boundary conditions, this requires the source to be distributed over all boundaries.

3.A.5 Second derivatives of the velocity potential

Calculation of the diffraction-modified Stokes drift based on (3.8) requires the evaluation of second derivatives of velocity potentials in (3.6) and (3.7). Due to the singularity of the Green's function method employed here, direct numerical evaluation of these second derivatives based on finite differences is challenging as it may cause a loss of accuracy (Zhang et al., 2010; Chen et al., 2018). We follow Zhang et al. (2010) and use the so-called desingularized source distribution method. Different from the standard source distribution method (Newman,

2018), the desingularized method enforces the boundary conditions are satisfied exactly on the boundary (denoted by P) but distributes the source points Q slightly outside the boundary, so that the singularities on the boundaries are removed (see also Raven (1988) and Kim and Kim (2007) for more details). We set the distance of the source points to the boundaries to be 1-2 times the grid size in the direction normal to the boundary. Second derivatives at point P are thus calculated as:

$$\frac{\partial^2\phi(P)}{\partial x^2} = \int_{C_l'} \sigma(Q)\frac{\partial^2 G(P,Q)}{\partial x^2}\mathrm{d}l; \quad \frac{\partial^2\phi(P)}{\partial x\partial z} = \int_{C_l'} \sigma(Q)\frac{\partial^2 G(P,Q)}{\partial x\partial z}\mathrm{d}l, \tag{3.34a,b}$$

in which C_l' denotes the boundaries where the source points Q are located, obtained by moving a certain distance from the original fluid boundaries (i.e., C_1, C_2 and C_3 in figure 3.3 (a)) according to the desingularized source distribution method. In (3.34), $\sigma(Q)$ is the source strength at source point Q. Based on (3.34), we can obtain the second derivatives in (3.8) once the source strength $\sigma(Q)$ is known. The source strength $\sigma(Q)$ is solved following the standard source distribution method. Derivatives of the incident potential are directly calculated from (3.2).

It is worth noting that, theoretically, based on (3.34), the diffraction-modified Stokes drift could be evaluated on the surface of the body or at the object's centre of mass. For large objects, we use the second derivatives obtained by (3.34) evaluated at the object's centre of mass. However, when the size of the object is very small, the second derivatives evaluated at the centre of mass or at the boundaries of the object become very sensitive to small changes in position in the direction normal to the boundary due to the use of the desingularized source distribution method. Instead, we make use of the boundary conditions on the object boundary (C_1, C_2, C_3 or C_r) to calculate second derivatives.

To improve the accuracy of second derivatives evaluated on object boundaries in the BEM model (i.e., in (3.6) and (3.7)) when the object is small, we take advantage of the boundary conditions, which are themselves given in the form of normal derivatives on the boundary. For the rectangular box defined in figure 3.3 (a), there are three object boundaries: C_1, C_2 and C_3. We will examine the general principle of our method using C_2 as an example. The boundary

conditions on C_2 for the radiation and the diffraction problem are:

$$\frac{\partial \hat{\phi}_j}{\partial z} = N_j = [0, 1, -x] \quad \text{for} \quad j = x, z, \alpha \quad \text{on} \quad C_2; \tag{3.35}$$

$$\frac{\partial \phi_D}{\partial z} = -\frac{\partial \phi_I}{\partial z} \quad \text{on} \quad C_2, \tag{3.36}$$

where N_j represents the projection of the unit normal vector of the relevant boundary in the jth-direction. For the object boundary C_2 (see figure 3.3 (a)) the normal vector is in the vertical direction and the normal derivative of its velocity potential in the form of a Green's function is continuous in the x-direction but not continuous in the z-direction. We can therefore evaluate horizontal derivatives directly along the boundary and we have:

$$\frac{\partial^2 \hat{\phi}_j}{\partial x \partial z} = [0, 0, -1]; \tag{3.37}$$

$$\frac{\partial^2 \phi_D}{\partial x \partial z} = -\frac{\partial^2 \phi_I}{\partial x \partial z}. \tag{3.38}$$

The second derivative $\partial^2 \phi_R / \partial x \partial z$ in (3.6) can now be calculated directly based on (3.37) and (3.18). The second derivatives $\partial^2 \phi_D / \partial x \partial z$ in (3.7) can be calculated directly based on (3.38). The second derivatives $\partial^2 \hat{\phi}_j / \partial x^2$, $\partial^2 \phi_D / \partial x^2$ can be calculated numerically directly from the potential as the latter is continuous over the boundary C_2 in the horizontal direction. Finally, to obtain a single value to be used to estimate the diffraction-modified Stokes drift, we evaluate the second derivative at the centre of the boundary C_2.

3.A.6 Verification of the BEM model

To verify the BEM model we use in this chapter, we evaluate the radiation and diffraction solutions for three specific examples involving rectangular objects in regular waves and compare these numerical solutions to the theoretical solutions of Zheng et al. (2004). In their theoretical model, the added mass coefficient μ_{kj} and radiation damping λ_{kj} are calculated based on (3.24) and (3.25) based on an analytical solution for $\hat{\phi}_j$. The wave excitation forces in their paper are:

$$f_k = f_k^I + f_k^D = \rho_f \imath \omega \int_{C_B} (\phi_I + \phi_D) N_j \mathrm{d}l, \tag{3.39}$$

In example 1, the object's size and density are chosen so that $d/h_d = 3$ and $l/h_d = 1$. The (truncation) length of the domain $L_{BEM}/2 = 10h_d$, and the grid size is chosen to be $\Delta x/h_d = \Delta z/h_d = 0.01$. Figure 3.A.1 compares the normalized added mass and hydrodynamic damping coefficients μ and λ predicted by our BEM model to their theoretical counterparts by Zheng et al. (2004). Good agreement is achieved for both added mass and hydrodynamic damping coefficients for a broad range of water depths kd, including the deep-water values we examine in the chapter.

For example 2 and 3, we consider objects with $d/h_d = 2$, $l/h_d = 2$ and $d/h_d = 2$, $l/h_d = 6$, respectively, and we compare the wave-induced forces predicted by our BEM model to their theoretical counterparts by Zheng et al. (2004). We choose the (truncation) domain length to be $L_{BEM}/2 = 15l$ and $\Delta x/h_d = \Delta z/h_d = 0.01$ for both cases. The diffraction wave forces F_j^D of the jth mode in the BEM model can be calculated in two ways based on equations (3.28) and (3.29). Given the accuracy with which our BEM model solves the radiation problem, as verified in example 1 (figure 3.A.1), consistency between the two approaches (i.e., (3.28) and (3.29)) confirms the diffraction potential is solved correctly. The results of this comparison and the comparison to the theoretical solutions of Zheng et al. (2004) are given in figure 3.A.2 for examples 2 and 3. The BEM model performs well in predicting the wave forces for a range of water depths kd, and the two different approaches agree well for both examples, further verifying the model.

3.B Convergence of the hybrid numerical model (qale-FOAM)

Our convergence tests focus on the Navier–Stokes domain, as corresponding tests for the Qale-FEM domain used to simulate the incident wave field have been performed extensively and are well documented in the literature (e.g., Ma and Yan (2009); Li et al. (2018)). To ensure optimal relaxation zone lengths, we have conducted a series of simulations with different lengths and draw similar conclusions to Li et al. (2018) and Yan et al. (2019), namely that for the high-wave steepness cases, 1.5 wavelengths are required, while a single wavelength is sufficient for the low-wave steepness cases. In the interest of brevity, these results are not shown

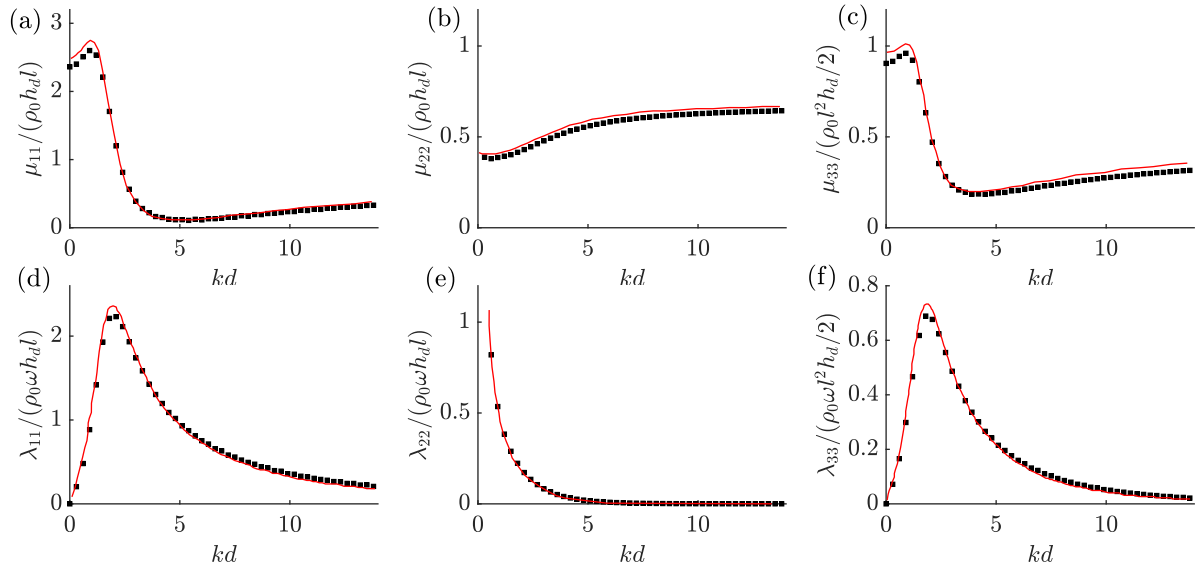


Figure 3.A.1: Non-dimensional added mass (μ_{ii}) and damping (λ_{ii}) coefficients for example 1 ($d/h_d = 3$, $l/h_d = 1$) of the BEM model verification. The black squares are the predictions by the BEM model, the red lines correspond to the theoretical solutions of Zheng et al. (2004) based on (3.24) and (3.25), ρ_0 is the density of water, and d the water depth.

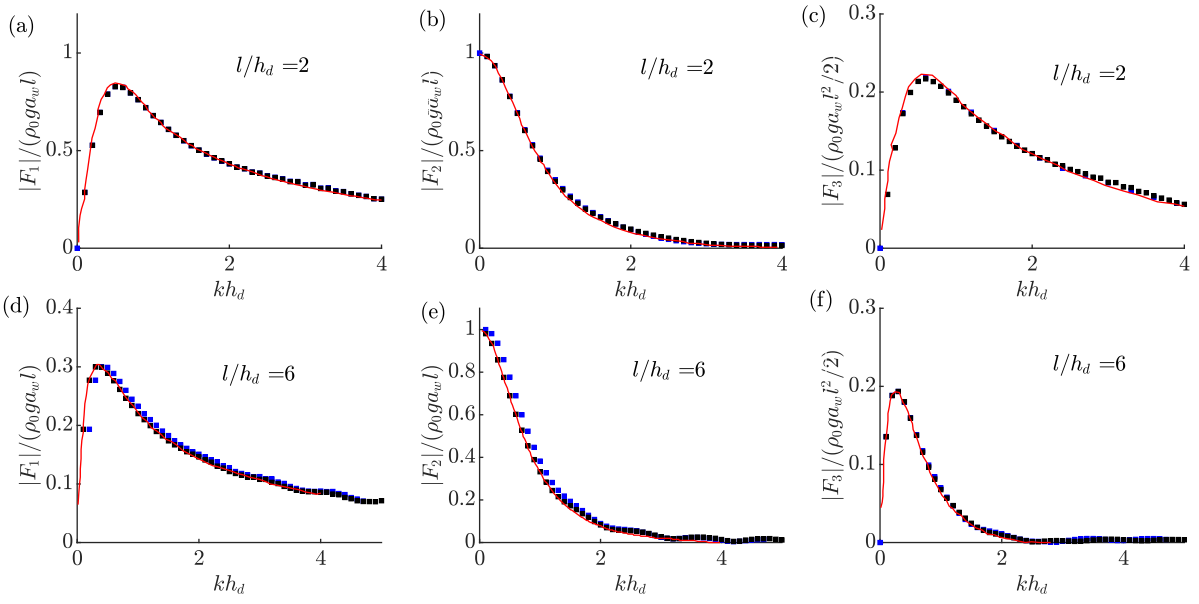


Figure 3.A.2: Non-dimensional wave-induced forces for example 2 ($d/h_d = 2$, $l/h_d = 2$) and example 3 ($d/h_d = 2$, $l/h_d = 6$) of the BEM model verification. The black and blue squares are the predictions by the BEM model using (3.28) and (3.29), respectively. The red lines correspond to the theoretical solutions of Zheng et al. (2004) based on (3.39).

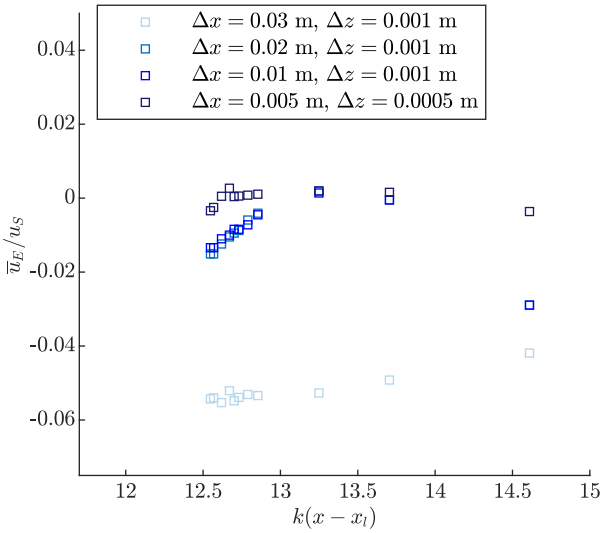


Figure 3.B.1: Eulerian-mean velocity scaled by the theoretical Stokes drift u_S a small distance below the wave trough $a_w = 20.0$ mm ($z = -25.0$ mm) for different spatial resolutions as a function of horizontal position; x_l indicates the location of the left boundary of the Navier–Stokes domain.

here.

We note that in previous studies the surface elevation is typically considered in a convergence test, whereas in our simulations the focus is on the velocity field. Our targets for the convergence tests are surface elevation (wave amplitude), Eulerian-mean velocity and (Lagrangian-mean) drift rates. Here, we report results for the lower-frequency waves (from table 3.1) of the lowest steepness $ka_w = 0.034$ and the highest steepness $ka_w = 0.126$ examined in §3.4.1. In each case, four sets of grids have been tested, which are defined by their spatial resolution, and the three target quantities are examined and compared.

For the lowest-steepness case ($ka_w = 0.034$), figure 3.B.1 shows the spatial Eulerian-mean (time-averaged) velocity distribution covering the region where our object is placed. The Eulerian-mean velocity $\overline{u}_E$ is obtained by time averaging the Eulerian velocity after a quasi-steady state has been achieved, in which the drift speed is constant. The figure demonstrates that, as the spatial resolution becomes higher, the Eulerian-mean velocity becomes very small (at most 1% of the Stokes drift for the highest steepness), which confirms the (near) absence of Eulerian currents in our numerical wave tank, so that the Lagrangian velocity becomes equal to the Stokes drift (as already shown in §3.4.1).

Tables 3.B.1 and 3.B.2 outline the values of our three target quantities obtained for four sets of grids for the lowest-steepness ($ka_w = 0.034$) and the highest-steepness ($ka_w = 0.126$)

Δx (m)	$\lambda/\Delta x$	Δz (m)	$a_{\text{in}}/\Delta z$	N_c	a_w/a_{in}	$\overline{u}_L/u_S$	$\overline{u}_E/u_S$
0.03	123	0.001	20	99015	1.035	0.953	-0.0134
0.02	185	0.001	20	148350	1.030	1.008	-0.0151
0.01	369	0.001	20	320407	1.020	1.004	-0.0054
0.005	739	0.0005	40	338446	1.010	1.000	-0.0034

Table 3.B.1: Values of the three target quantities of the convergence tests: wave amplitude a_w, Eulerian-mean velocity $\overline{u}_E$ and drift rate of a Lagrangian particle $\overline{u}_L$. Results are shown for four different spatial resolutions for the low-wave steepness case, where Δx and Δz represent the grid size in x- and z-directions, respectively, N_c is the total number of cells in the Navier–Stokes domain, and a_{in} is the input wave amplitude.

Δx (m)	$\lambda/\Delta x$	Δz (m)	$a_{\text{in}}/\Delta z$	N_c	a_w/a_{in}	$\overline{u}_L/u_S$	$\overline{u}_E/u_S$
0.02	185	0.0019	39	139416	0.997	0.972	-0.0148
0.01	369	0.0019	39	278832	1.003	0.965	-0.0221
0.005	739	0.0019	39	557664	1.001	0.986	-0.0126
0.005	739	0.00095	78	753024	1.000	0.989	-0.0101

Table 3.B.2: Values of the three target quantities of the convergence tests: wave amplitude a_w, Eulerian-mean velocity $\overline{u}_E$ and drift rate of a Lagrangian particle $\overline{u}_L$. Results are shown for four different spatial resolutions for the high-wave steepness case, where Δx and Δz represent the grid size in x- and z-directions, respectively, N_c is the total number of cells in the Navier–Stokes domain, and a_{in} is the input wave amplitude.

cases, respectively. Results are given for wave amplitudes, Eulerian-mean and Lagrangian-mean velocities after a quasi-steady state has been achieved at the location $x = 22.5$ m, $z = -25.0$ mm for $ka_w = 0.034, a_w = 20.0$ mm and $x = 25.2$ m, $z = -85.0$ mm for $ka_w = 0.126, a_w = 74.0$ mm. The Lagrangian-mean velocities are obtained in the same way as in §3.4.1. We find that as the wave steepness is increased, a finer spatial resolution is required for sufficient convergence. Eulerian-mean flows remain small even for the highest steepness case (at most 1% of the Stokes drift).

l/λ (%)	5.1	6.0	7.0	8.0	9.0	10.0
l (m)	0.19	0.22	0.26	0.29	0.33	0.37
h_d (m)	0.13	0.15	0.18	0.20	0.23	0.25
h (m)	0.16	0.19	0.22	0.25	0.29	0.32
r (m)	0.03	0.036	0.043	0.048	0.054	0.06

Table 3.C.1: Object dimensions of round-cornered boxes of different sizes with $\rho = 781$ kg/m^3.

3.C Effects of object rotation and density

The boxes in §3.5.1 (table 3.3) were constrained to prevent rotation during the simulations as these boxes ($\rho = 500$ kg/m^3, $h/l = 1.33$) are hydrodynamically unstable. To examine the implications of this assumption and to investigate the effects of object density and rotation, we simulate the drift of a new set of boxes that are hydrodynamically stable. We keep the submergence depth and submerged shape of the new set of round-cornered boxes the same as for the previous set but change the height and the density of the boxes. Dimensions of the new set of boxes are given in table 3.C.1. The density of the new boxes is $\rho = 781$ kg/m^3. For this density, we do not consider relative sizes smaller than $l/\lambda = 5\%$ to ensure the freeboard of the object (i.e., $h - h_d$) is larger than the incident wave amplitude, thus avoiding green-water/plunging impact of the wave onto the object. For this new set of round-corned boxes, we consider three scenarios: without rotation (i.e., with the rotational degree of freedom constrained as in §3.5.1) and without viscosity; with rotation but without viscosity; and with rotation and with viscosity. The corresponding object drift velocities are given in figure 3.C.1 (a). Figure 3.C.1 (b) provides a comparison of object drift velocities between the round-cornered boxes with $\rho = 500$ kg/m^3 (defined in table 3.3 and considered in §3.5.1) and the new set of round-cornered boxes with $\rho = 781$ kg/m^3 (defined in table 3.C.1) without rotation and without viscosity.

It is clear from figure 3.C.1 that restraining the rotational degree of freedom causes only a very small change to the object drift. Object rotation also does not significantly change the role that the viscosity plays in altering the drift of the objects. Furthermore, figure 3.C.1 (b) shows that as long as the submergence depth and submerged shape of the objects are unchanged, the density of the object only has a very minor effect on the object drift.

3.D Effects of viscosity and turbulence

3.D.1 Reynolds and Keulegan–Carpenter numbers

The problem we consider is one of flow around a two-dimensional bluff body (a round-cornered box) or a circular object that is freely floating in a surface wave field without a current. We use the characteristic length of the object l and the velocity difference between

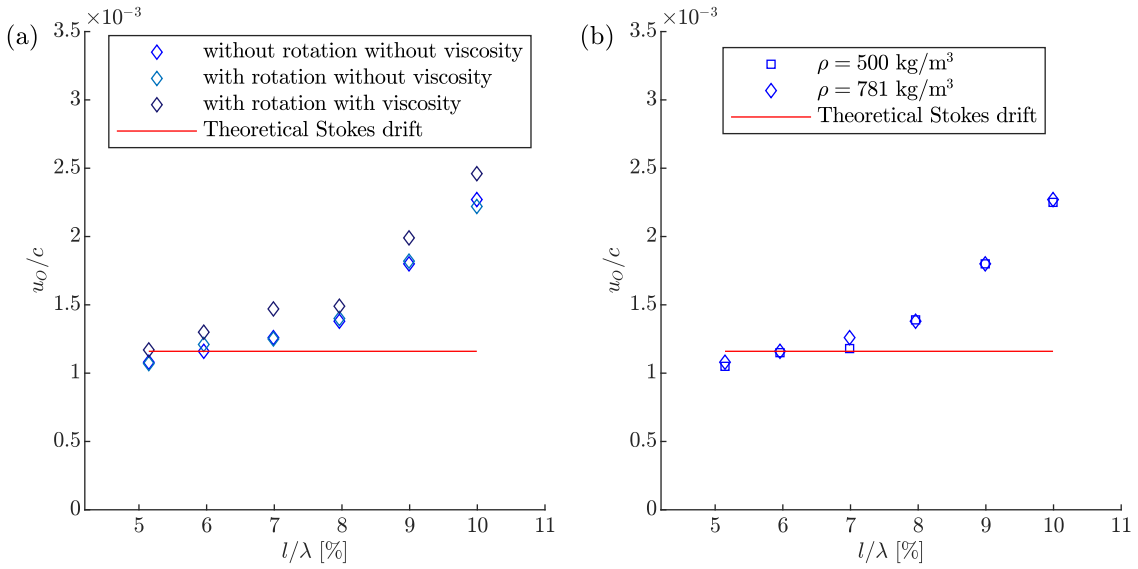


Figure 3.C.1: Effects of rotation and density on object drift: (a) celerity-normalized drift velocity as a function of relative size of the objects in table 3.C.1 for three different scenarios; (b) celerity-normalized drift as a function of relative size for objects of density $\rho = 500$ kg/m^3 (cf. table 3.3) and $\rho = 781$ kg/m^3 (cf. table 3.C.1) without rotation and without viscosity. The red lines correspond to the theoretical Stokes drift.

RCB							RO						
l/λ (%)	l (m)	Re_x	$\Delta_{\min}/2$ (m)	y_d (m)	K_c	N_c	l/λ (%)	l (m)	Re_x	$\Delta_{\min}/2$ (m)	y_d (m)	K_c	N_c
1.0	0.037	6	3.40×10^{-4}	4.52×10^{-2}	0.27	353532	1.4	0.05	21	3.10×10^{-4}	1.93×10^{-2}	0.26	394896
2.0	0.07	231	4.00×10^{-4}	3.24×10^{-3}	0.24	548966	2.0	0.07	57	3.82×10^{-4}	1.15×10^{-2}	0.22	519520
3.0	0.11	470	3.90×10^{-4}	2.54×10^{-3}	0.24	553392	3.0	0.11	15	3.82×10^{-4}	5.51×10^{-2}	0.24	585602
4.0	0.15	763	3.80×10^{-4}	2.24×10^{-3}	0.24	606056	4.0	0.15	187	3.80×10^{-4}	7.95×10^{-3}	0.22	661740
5.1	0.19	1175	3.80×10^{-4}	1.93×10^{-3}	0.25	640220	5.1	0.19	184	3.50×10^{-4}	1.02×10^{-2}	0.21	656068
6.0	0.22	1750	3.50×10^{-4}	1.56×10^{-3}	0.26	742164	6.0	0.22	185	3.50×10^{-4}	1.18×10^{-2}	0.22	934922
7.0	0.26	2311	3.40×10^{-4}	1.42×10^{-3}	0.28	712020	7.0	0.26	308	3.50×10^{-4}	8.71×10^{-3}	0.22	985334
8.0	0.29	2831	3.50×10^{-4}	1.35×10^{-3}	0.30	854260	8.0	0.29	274	3.50×10^{-4}	1.11×10^{-2}	0.22	1021932
9.0	0.33	3376	3.40×10^{-4}	1.30×10^{-3}	0.33	854260	9.0	0.33	332	3.39×10^{-4}	1.05×10^{-2}	0.22	1062074
10.0	0.37	3851	3.20×10^{-4}	1.28×10^{-3}	0.36	910226	10.0	0.37	334	3.37×10^{-4}	1.16×10^{-2}	0.22	1124168

Table 3.D.1: For category I simulations exploring the effect of size, Reynolds numbers, smallest mesh sizes near the boundary $\Delta_{\min}$, estimates of normal-wall distance y_d, and total numbers of cells in the mesh N_c, and Keulegan–Carpenter numbers K_c for round-cornered boxes (RCBs) and round objects (ROs).

$l/\lambda = 5\%$					$l/\lambda = 8\%$					$l/\lambda = 10\%$				
ka_w	Re_x	$\Delta_{\min}/2$ (m)	y_d (m)	K_c	ka_w	Re_x	$\Delta_{\min}/2$ (m)	y_d (m)	K_c	ka_w	Re_x	$\Delta_{\min}/2$ (m)	y_d (m)	K_c
0.020	770	2.00×10^{-4}	2.82×10^{-3}	0.14	0.020	2198	3.45×10^{-4}	1.91×10^{-3}	0.18	0.020	2383	3.50×10^{-4}	1.98×10^{-3}	0.36
0.034	1209	3.80×10^{-4}	1.88×10^{-3}	0.24	0.034	3874	3.50×10^{-4}	1.15×10^{-3}	0.30	0.034	3747	3.20×10^{-4}	1.32×10^{-3}	0.60
0.051	1857	3.00×10^{-4}	1.28×10^{-3}	0.35	0.051	5116	5.00×10^{-4}	8.95×10^{-4}	0.44	0.051	5763	5.00×10^{-4}	8.94×10^{-4}	0.89
0.060	1970	5.00×10^{-4}	1.21×10^{-3}	0.41	0.070	7499	2.50×10^{-4}	6.34×10^{-4}	0.58	0.070	7219	3.50×10^{-4}	7.30×10^{-4}	1.18
					0.080	8764	4.00×10^{-4}	5.51×10^{-4}	0.65	0.090	9840	4.50×10^{-4}	5.52×10^{-4}	1.49

Table 3.D.2: For category III simulations exploring the effect of steepness, Reynolds numbers, smallest mesh sizes near the boundary $\Delta_{\min}$, estimates of normal-wall distance y_d, and total numbers of cells in the mesh N_c, and Keulegan–Carpenter numbers K_c for round-cornered boxes (RCBs) and round objects (ROs).

the object and the fluid to define a Reynolds number: $\mathrm{Re}_x = |u_{o,x} - u_x| l/\nu$, where $u_{o,x}$ and u_x represent the magnitude of the horizontal velocity of the object and the fluid, respectively, and $l = D$ for round objects. The magnitude of the horizontal velocity of the object $u_{o,x}$ is obtained after a quasi-steady state has been achieved, in which the object oscillates harmonically and drifts at a constant speed. We estimate the magnitude of the horizontal fluid velocity as $u_x = a_w\omega \exp(-kh_d)$ for boxes and $u_x = \int_{-D/2}^{D/2} a_w\omega \exp\left(-k\sqrt{r^2 - x^2}\right) \mathrm{d}x/D$ for round objects. The Reynolds numbers for all simulations in category I (see §3.5.1) and category III (see §3.5.3) are given in tables 3.D.1 and 3.D.2, respectively. These tables also report the grid size near the moving object boundary: $\Delta_{\min} = \Delta x_{\min} = \Delta z_{\min}$ (the aspect ratio of the mesh near the object is 1). Because OpenFOAM uses collocated grids, which means all of the flow variables are calculated and stored at the cell centroids and these variables vary linearly within a cell, we report $\Delta_{\min}/2$. In order to evaluate whether the mesh density in the vicinity of the boundary is sufficient, we estimate the normal wall distance y_d. We estimate y_d from $y_d = \nu y^+/u_*$, where the shear velocity is estimated as $u_* = \sqrt{(0.058/2)\mathrm{Re}^{-0.2}\,|u_{x,o} - u_{x,f}|^2}$, and the non-dimensional wall distance y^+ is set to 1 (Schlichting and Kestin, 1961). By comparing y_d to $\Delta_{\min}/2$, which is much smaller, we can conclude from tables 3.D.1 and 3.D.2 that the mesh used in our simulations is fine enough to capture the detailed boundary-layer flows around the object. To determine the relative importance of drag and inertial forces and thereby determine the likelihood of boundary-layer separation, we also estimate the Keulegan–Carpenter number: $K_c = |u_{o,z} - u_z| T/l$, $T = 2\pi/\omega$ is the wave period, and we use the size of the object as the characteristic length scale. In our problem, separation can occur in both the horizontal and the vertical boundary layers and we thus estimate the Keulegan–Carpenter number in both directions. We find the Keulegan–Carpenter number in the vertical directions to always be larger and we therefore report this number in tables 3.D.1 and 3.D.2. We estimate the

	k	ν_t	ω	$\overline{y}^+$	u_O/c	A_x/a_w	A_z/a_w
BC1	fixedValue	calculated	fixedValue	0.5	0.0026	0.80	1.32
BC2	kLowReWallFunction	nutLowReWallFunction	omegaWallFunction	0.5	0.0026	0.80	1.32
Laminar					0.0025	0.79	1.37

Table 3.D.3: Near-wall treatment and effect of including a turbulence model for a round-cornered box with $l/\lambda = 10\%$ and $ka_w = 0.034$ for two different boundary conditions (BC1 and BC2) in the URANS simulation. Here, k is the turbulent kinetic energy (its initial value on both BCs is set to a uniform value of $k = 1.00 \times 10^{-12}$ m^2/s ^{2}), ν_t is the turbulent viscosity (its initial value on both BCs is set to a uniform value of $\nu_t = 0$ m^2/s), ω is the specific turbulence dissipation rate (its initial value is calculated as $\omega = 60\nu/(0.075y^2)$, where y is the normal distance from the boundary to the first cell center), $\overline{y}^+$ is the time-averaged mean value of y^+ on the object boundary.

	$l/\lambda = 8\%$, $ka_w = 0.08$				$l/\lambda = 10\%$, $ka_w = 0.09$			
	$\overline{y}^+$	u_O/c	A_x/a_w	A_z/a_w	$\overline{y}^+$	u_O/c	A_x/a_w	A_z/a_w
BC1	0.85	0.0085	0.88	0.98	0.62	0.0136	0.80	1.22
BC2	0.85	0.0085	0.88	0.98	0.62	0.0137	0.80	1.22
Laminar		0.0078	0.82	1.15		0.0134	0.78	1.30

Table 3.D.4: Effect of including a turbulence model for round-cornered boxes with $l/\lambda = 8\%$, $ka_w = 0.08$ and $l/\lambda = 10\%$, $ka_w = 0.09$ (category III). The boundary conditions BC1 and BC2 are those in table 3.D.3, $\overline{y}^+$ is the time-averaged mean value of y^+ on the object boundary.

magnitude of the vertical fluid velocity as $u_z = a_w\omega \exp(-kh_d)$ for both boxes and round objects. The Keulegan–Carpenter number K_c can be interpreted as the ratio of the magnitude of the oscillatory motion of fluid particles to the length of the object. When the K_c number is small, fluid moves only a small distance along the object's boundaries without flow separation, and inertial or diffraction forces will be dominant. For large K_c, the fluid particle travels a large distance relative to the size of the object, leading to flow separation and vortex formation. When $K_c < 3$, the flow is inertia dominated, and the effects of boundary layer separation and vorticity are small (e.g., Sumer et al. (2006); Yoon et al. (2016); Mohseni et al. (2018)). All of our simulations are in this regime (cf. tables 3.D.1 and 3.D.2). Furthermore, we do not observe vortex formation and boundary-layer separation in the streamlines and in the velocity and vorticity (using the Q-criterion) fields.

3.D.2 Turbulent simulations

Our maximum Reynolds numbers in tables 3.D.1 and 3.D.2 Re > 3000; these numbers are in the sub-critical Reynold-number regime for typical flow around a cylinder, which suggests the boundary layer is laminar but the wake becomes turbulent (Sumer et al., 2006). Although

our analysis shows that there is no distinct wake in our simulations, given the Reynolds number of the problem, the flow around the object may become turbulent. To investigate whether the effects of turbulence need to be taken into account (following Yu and Li (2013); Li et al. (2018)), we implement a URANS model (unsteady Reynolds-averaged Navier–Stokes) by introducing an SST k-ω turbulence model. We consider the cases with the largest Reynolds number in category I (the round-cornered box with $l/\lambda = 10\%$, $ka_w = 0.034$) and category III (the round-cornered boxes with $l/\lambda = 8\%$, $ka_w = 0.08$ and $l/\lambda = 10\%$, $ka_w = 0.09$). The results are given in tables 3.D.3 and 3.D.4. Our mesh is fine near the object boundary, as an accurate prediction of viscous forces (wall shear stress) on the object is important. Therefore, in terms of the near-wall treatment, we choose a wall-resolving approach and compare these results with a low-Reynolds-number wall function approach. The boundary conditions for the object boundary are given in table 3.D.3.

The mesh used for simulations with and without the turbulence model (for both boundary conditions) is the same. It is clear from table 3.D.3 that there is no difference between the two boundary condition (BC) settings, which also confirms that our mesh is fine enough for a wall-resolving approach. Tables 3.D.3 and 3.D.4 shows that, compared with the results of the laminar model, a URANS model predicts a similar albeit very slightly lower value of the object drift (u_O/c) along with a similar albeit very slightly larger horizontal motion (A_x/a_w) and a similar albeit slightly smaller vertical motion (A_z/a_w). Sensitivity to the initial value of the specific turbulence dissipation rate ω is small.

Chapter 4

Laboratory study of the enhanced wave-induced drift of large rectangular floating objects

4.1 Abstract

Surface gravity waves induce a drift on objects floating on the water's surface. This study presents laboratory experiments investigating the drift of large two-dimensional floating objects on deep-water, unidirectional, regular waves, with wave steepness ranging from 0.04 to 0.31 ($0.04 < ka_w < 0.31$). The objects were carefully designed to have a rectangular cross-section with a constant aspect ratio; their size varied from 2.6% to 27% of the incident wavelength. We observed Lagrangian behaviour for small objects. Small and large objects exhibited fundamentally different drift behaviour at high compared to low wave steepness, with a regime shift observed at a certain size and wave steepness. The scaling of object drift with steepness depends on the relative size of the object. For small objects, drift scales with steepness squared, whereas drift becomes a linear function of steepness as object size increases. For objects that are relatively large but smaller than 13-16% of a wavelength (low to high steepness), we provide experimental evidence supporting the mechanisms of drift enhancement recently identified by Xiao et al. (2024) and termed the 'diffraction-modified Stokes drift'. This enhanced drift behaviour, compared to the theoretical Stokes drift for infinitely small fluid parcels, is attributed to changes in the objects' oscillatory motion and local wave amplitude distribution (standing

wave pattern) due to the presence of the object. In the case of larger objects (large enough to experience enhanced drift), similar to Harms (1987), we relate the critical size at which drift is maximised to their vertical bobbing motion. We determine the domain of validity for both Stokes drift and the diffraction-modified Stokes drift model of Xiao et al. (2024) in terms of relative size and wave steepness and propose an empirical parameterisation based on our experimental data.

4.2 Introduction

The assessment of mass transport in the ocean plays a crucial role in determining the migration of sediments, pollutants (Iwasaki et al., 2017; Dobler et al., 2019), tracking buoys (Nath, 1978; DeBok and Roehrig, 1981; Wilson, 1982; Tanizawa et al., 2001), ice floes (Arikainen, 1972; Perrie and Hu, 1997; Meylan et al., 2015), as well as trajectory forecasting for search and rescue operations (Röhrs et al., 2012; Breivik et al., 2013). The recent surge in interest in this topic is driven by the alarming increase in plastic pollution, which requires effective management and clean-up, beginning with an improved understanding of their global transport patterns (Law et al., 2010; Eriksen et al., 2014; Van Sebille et al., 2015; Law, 2017; Van Sebille et al., 2020). In this study, we investigate the drift motion induced by surface gravity waves.

The orbit of a fluid particle in waves is not fully closed over a wave cycle, resulting in a net drift in the direction of wave propagation known as Stokes drift (Stokes, 1847). To study the transport of floating objects, several studies have superimposed the Stokes drift onto the Eulerian current field obtained from ocean general circulation models or observations (see Van Sebille et al. (2020) for a review). There are three reasons why this approach may not result in a correct prediction of the drift of floating objects in the real ocean. First, this approach ignores the modification of the Eulerian-mean flow by the surface waves: on the rotating Earth, the Stokes–Coriolis force drives an Eulerian-mean. This so-called Ekman–Stokes flow needs to be added to the Stokes drift to properly estimate the wave-induced Lagrangian-mean flow, which is the flow responsible for transporting objects floating on the ocean surface (Higgins et al., 2020). On the time and spatial scales associated with typical laboratory experiments, this Ekman–Stokes flow does, of course, not arise. Second, it has been shown that the drift at the surface of a breaking wave is much larger than the prediction of classical Stokes drift

for non-breaking waves (Deike et al., 2017b), as confirmed in experiments (Lenain et al., 2019; Sinnis et al., 2021), and breaking may make a significant contribution to the Lagrangian drift of realistic wave fields (Pizzo et al., 2019). In the context of irregular waves, Eeltink et al. (2023) have recently proposed a stochastic differential equation that uses a Brownian motion to capture the non-breaking drift-diffusion effect associated with a random non-breaking sea state and a compound-Poisson process to capture the rapid jumps in particle position that take place during wave breaking. Third, unlike an idealised fluid particle (that is, a perfect Lagrangian tracer), floating marine objects exhibit significant variations in size, which can lead to non-Lagrangian drift behaviour (Nath, 1978; Santamaria et al., 2013; Calvert et al., 2021; DiBenedetto et al., 2022). This non-Lagrangian drift behaviour is the subject of the present chapter.

Studies that have examined the drift of non-Lagrangian particles or 'objects' can be classified into those that ignore the disturbance of the wave field by the object and those that take this disturbance into account. Typically, the effect of the object on the wave field can be neglected when the relative size of the object (characterised by l/λ, the ratio of the object's characteristic dimension l to the incident wavelength λ) is smaller than 0.2 (Isaacson, 1979). It deserves mentioning that this threshold value of 0.2 is evaluated for the linear motions of the object, regarding the drift, a second-order term, this threshold might not hold water. Nevertheless, based on this threshold and assumptions, theoretical models that apply forces derived from the wave field onto a moving object, assuming the wave field is unaffected by the presence of the object itself (e.g., through Morison's equation (Morison et al., 1950)) are thus commonly used to study the drift motion of small objects (Rumer et al., 1979; Shen and Ackley, 1991; Shen and Zhong, 2001; Grotmaack and Meylan, 2006; Huang et al., 2016).

Beginning with studies that have ignored the disturbance of the wave field by the object and focusing on fully submerged particles, Eames (2008) and Santamaria et al. (2013) used the Maxey–Riley equations (Maxey and Riley, 1983) to examine how far slightly positively or negatively buoyant objects are transported by regular waves as they either rise to the free surface or sink. Santamaria et al. (2013) predicted that positively buoyant objects in deep-water waves experience an increase in drift owing to their inertia (see DiBenedetto et al. (2022) for an extension to finite depth). Also considering fully submerged objects, DiBenedetto and Ouellette

(2018) showed that non-spherical objects have a preferential orientation under waves, confirming this result numerically (DiBenedetto and Ouellette, 2018) and experimentally (DiBenedetto et al., 2019), but not examining the effect of the object's inertia or its modified drift. Even without direct modification of the drift, the orientation changes the drag on slightly negatively buoyant objects, which results in objects of different shapes being transported different distances before 'raining out' (DiBenedetto et al., 2018). Taking a similar approach, Pujara and Thiffeault (2023) have shown that wave action reduces the vertical dispersion of particles but increases horizontal dispersion.

Turning to floating objects, but still ignoring the disturbance of the wave field they cause, Calvert et al. (2021) used a perturbation expansion in wave steepness to derive a closed-form solution for the enhanced drift of a floating sphere, extending the models of Rumer et al. (1979) and Huang et al. (2016). Calvert et al. (2021) attributed the enhanced drift to two physical mechanisms: the increased vertical oscillatory (linear) motion of the floating sphere and the (viscous) drag-induced phase difference between the motion of the inertial sphere and that of an idealised Lagrangian particle, giving rise to a net horizontal component of the buoyancy force when averaged over a wave cycle. The first to consider the effect of diffraction of the wave-induced drift of floating objects, Xiao et al. (2024) used a (2D) hybrid numerical solver, which deals with both viscosity and wave-body interaction, to predict significant drift enhancement of large (5-10% of the wavelength) floating rectangular boxes. The drift enhancement was explained in small part by the effect of viscosity (as in Calvert et al. (2021)) but in large part by the standing wave pattern generated by the presence of the (oscillating and drifting) object in the wave field. To explain their numerical results, Xiao et al. (2024) derived a 'diffraction-modified Stokes drift' akin to Stokes (1847), but based on the combination of incident, diffracted and radiated wave fields, which are based on potential-flow theory and obtained using the boundary element method (BEM). This 'diffraction-modified Stokes drift' could explain both qualitatively and quantitatively the increase in drift predicted by the hybrid numerical model.

Experimental investigations of the wave-induced motion and drift of floating objects have been conducted for nearly half a century. Table 4.2.1 provides a summary of relevant experimental studies, including the present chapter. This table shows that the drift of an object depends on its relative size. The drift of very small objects is equal to the theoretical Stokes

drift. However, as the objects become larger, enhanced drift is observed (we refer to drift as 'enhanced' in this thesis when it is larger than the theoretical Stokes drift). Nath (1978) reported Lagrangian drift behaviour for small discs and spheres on regular waves but found enhanced drift for larger objects with deep drafts (such as spar-type buoy drifters) in low wave steepness. Measurements by Murray et al. (1983) suggested that the maximum horizontal drift attained by floating spheres differs substantially from that of a water particle only when $l/\lambda > 12.5\%$. Similar conclusions were drawn by Alsina et al. (2020) regarding the drift of floating spherical particles with l/λ ranging from 0.1% to 1.4%, which were not enhanced. Calvert et al. (2021) suggested that the drift of a sphere increases with its relative size, and enhanced drift was found for objects as small as $l/\lambda = 6\%$. Le Boulluec et al. (2008) found that, regardless of shape, the drift velocity increases with relative size of the object l/λ, considering a range of relative size from 6% to 50%.

Drift behaviour is also influenced by the incident wave steepness. Tanizawa et al. (2001) reported Lagrangian drift behaviour for a spherical buoy with a relative size of $l/\lambda = 6\%$ at low wave steepness, while enhanced drift was observed for all objects with $l/\lambda > 10\%$ across various wave steepnesses. They proposed that, for small objects, drift is proportional to the square of the wave steepness, and as the object size increases, drift gradually becomes linearly proportional to the wave steepness. Huang et al. (2011) also found enhanced drift behaviour for objects with l/λ ranging from 12.8% to 15.8%, and the magnitude of this drift enhancement increased with wave steepness.

All the studies mentioned above are three dimensional (3D), meaning that while the wave conditions may be unidirectional, the objects do not span the entire wave crest. Few studies specifically focus on truly two-dimensional (2D) systems, despite their importance in identifying key physical processes relevant to certain applications, such as ice floes (Arikainen, 1972; EI-Tahan et al., 1983; Wadhams, 1983; Harms, 1987). This scarcity of 2D studies can be attributed to the greater experimental difficulty in designing objects that are truly 2D and capable of moving freely in a wave tank, especially for very small objects. Additionally, lateral variations in surface elevation for unidirectional waves pose challenges. Previous 2D studies have typically used models that occupy the full width of the flume, with a small gap between the walls and models to ensure free movement. Harms (1987) conducted systematic laboratory measurements

on the drift of ice floes, which exhibit significant variations in size. He proposed an empirical formula for wave-induced drift based on the ratio of wave period to the object's natural roll period, wave steepness, and the length of the floe. His formula suggests that the object's drift changes with its relative size, and there is a critical size, the value of which depends on the object's aspect ratio (typically around $l/\lambda = 50\%$ for an object with $h/l = 0.08$, where h is its height and l its length, and density $\rho = 920$ kg/m^3). When the object is smaller than the critical size, the drift increases approximately linearly with its relative size. On the other hand, when the object is larger than the critical size, the drift decreases substantially and nonlinearly with further increases in relative size. The value of this critical size does not vary significantly with wave steepness. For objects with different aspect ratios (but the same density), when the relative size is smaller than the critical size for all objects, the drift increases as the submergence increases with increasing h/l. This finding is consistent with the measurements in Huang and Law (2013), which focused on relatively large objects with $l/\lambda > 60\%$. Tanizawa et al. (2001) and He et al. (2016) also observed enhanced drift for intermediate sizes (l/λ ranging from 10% to 60%), and the relationship between drift velocity and wave steepness shifted from a quadratic to a linear relationship. Specifically, He et al. (2016) found that the ratio of the magnitudes of the quadratic components to the linear components shifted from 10 to 0 for objects ranging from $l/\lambda = 9\%$ to 30 %.

While documenting the dependence of enhanced drift on different parameters, the literature surveyed above has not examined the mechanism(s) explaining the drift enhancement or the relationships between drift velocity and the oscillatory motion of objects, nor has it examined the surface elevation in the vicinity of the object. Furthermore, to the best of the authors' knowledge, the drift behaviour of objects with relative sizes ranging from $l/\lambda < 6\%$ to $l/\lambda = 27\%$ has not been examined in 2D experiments previously. In an effort to address these gaps and explore object sizes ranging from very small to intermediate size, near or crossing the critical size reported by Harms (1987)), we conduct 2D laboratory experiments investigating the drift behaviour of objects with relative sizes in the range $l/\lambda = 2.6$-27% in regular deep-water waves. To ensure two-dimensionality in our experiments, we utilise carefully designed objects equipped with low-friction bearings. In doing so, the purpose of the chapter is to identify the mechanism(s) for drift enhancement in two dimensions and to provide experimental evidence

2D:	Third dimension	l/λ [%]	h/l	Shape	ρ [kg/m^3]	kd	ka_w	Wave type
Harms (1987)	6 mm gap	5.8-106.5	0.01-0.68	rectangular box	920	>1.7	0.06-0.30	R
Tanizawa et al. (2001)	10 cm gap	12.7-63.6	0.56	rectangular box	887	0.8-5	0.03-0.20	R&IR
Huang and Law (2013)	5 cm gap	61.0-308.0	0.01-0.05	rectangular box	720	2.6-12.9	0.04-0.32	R
He et al. (2016)	2 cm gap	9.2-30.4	0.67	rectangular box	500	0.7-2.5	0.04-0.30	R
Present chapter	plastic bearings	2.6-27.1	0.67	rectangular box, sphere	636	2.8-4.1	0.03-0.32	R
3D:								
Nath (1978)	-	0.2-176.5	0.17,0.23,1	sphere, disk and deep-draft buoy	>=500	1.1-14.1	> 0.02	R
Murray et al. (1983)	-	11-53	-	cylinder, sphere and cube	900	2.6-12.3	0.02-0.06	R&WG
Tanizawa et al. (2001)	-	3.0-60.8	1.00	spherical buoy	> 500	> 2.8	0.06-0.4	R&IR
Le Boulluec et al. (2008)	-	10.0-100.0	0.24-0.50	rectangular container and cylinder	175-954	> 4.0	-	R&IR
Huang et al. (2011)	-	12.8-15.8	0.15, 0.23	square, circular and elliptical plates	960	3.2-4.0	0.04-0.15	R
Meylan et al. (2015)	-	8.0-80.0	0.04	thin plastic disk	891	1.0-10.1	> 0.006	R
Alsina et al. (2020)	-	0.1-1.4	1.00	spherical particles	760-1340	0.3-3.0	0.06-0.22	R
Calvert et al. (2021)	-	1.9-5.1	1.00	sphere	508-809	3.1	0.1	WG

Table 4.2.1: Summary of previous laboratory studies of wave-induced drift of freely-floating objects on waves. Some values not explicitly provided in the cited papers were obtained from digitized figures or estimated using the linear dispersion relationship. In 2D experiments, the 'third dimension' shows the approach used to ensure the experiment's 2D nature. l represents the length of the object in the direction of wave propagation, λ the wavelength, h the height of the object, ρ the density of the object, k the wavenumber, d the water depth, and a the wave amplitude. The wave types R, IR, and WG correspond to regular waves, irregular waves, and wave groups, respectively.

and support for the mechanism of diffraction-modified Stokes drift proposed by Xiao et al. (2024).

The outline of the chapter is as follows: in §4.3 we present our experimental method, followed by a brief introduction to the theoretical model of Xiao et al. (2024) and the empirical parameterisation of Harms (1987) in §4.4. We present our experimental results in §4.5 and compare these to the theoretical model of Xiao et al. (2024) and the empirical parameterisation of Harms (1987). Finally, we draw conclusions in §4.6.

4.3 Experimental method

4.3.1 Wave flume and camera setup

Experiments were conducted in the Wave and Current Flume at the University of Oxford, UK. The flume is 10 m long, 1.1 m wide, and 1 m deep with working water depth of 0.85

m. Figure 4.3.1 provides a diagram of the experimental setup. Waves were generated using three hinged flap-type wavemakers, located at one end of the flume. At the other end, a wave-absorbing beach was positioned. It is important to note that the flume is not fully closed and includes pumps and a pipe system for fluid recirculation underneath the flume that is used to create a current. Although a current was not actively generated in the present experiments, the presence of the pipe system allows fluid recirculation during wave generation, which may influence the Eulerian current in the flume. To measure wave properties, seven resistance-type wave gauges were distributed along the flume, sampling the surface elevation at a rate of 128 Hz. The gauges were mounted on a steel frame in five rows. The distances of the rows from the wavemaker were as follows: 2.14 m, 4.59 m, 6.02 m, 6.32 m, and 6.59 m. Within the rows located at distances of 6.02 m and 6.32 m, two pairs of gauges were placed to assess any lateral variation in the wave field. For each pair of gauges, one was positioned at $y = 0.0$ m (the middle of the flume), while the other was located at $y = 0.275$ m, away from the middle position.

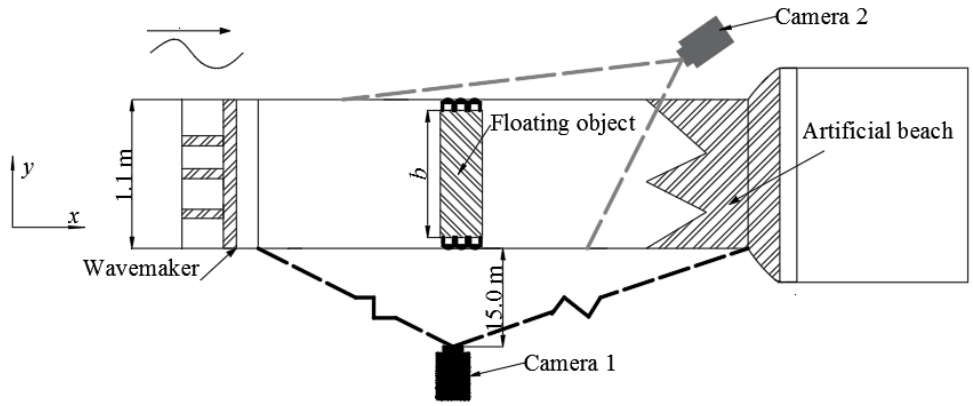
Two E2-4K Ultra-HD Cinematic Cameras (Z-CAM-E1503) equipped with Panasonic 12-60 mm digital interchangeable lens were used to measure the movement of the floating objects at 50 frames per second (fps), as depicted in figure 4.3.1. Side Camera 1 was positioned at the same height as the still-water level, located 12 m away from the flume. In this configuration, the camera's field of view encompassed the entire length of the flume, and it was horizontally orientated normally to the region of interest including the water surface. Its calibrated camera images were used to measure the drift and oscillatory motion of the floating objects (introduced below) in the (x, z)-plane. Top-side Camera 2 was mounted 0.65 m above the still-water level, facing down the wave flume towards the wavemakers. In this setup, the camera's field of view covered approximately 4 m of the flume length. Camera 2 was specifically used to measure the drift of small yellow spheres in the (x, y)-plane, as these spheres were not visible from the side of the flume due to their size. To ensure proper illumination and consistent lighting conditions for all experiments, three LG-600SC daylight dimmable LED lights (not shown in figure 4.3.1) were strategically placed along the length of the flume. These lights illuminated the ends of the objects, which were painted yellow. This illumination scheme also facilitated consistent lighting conditions for subsequent image processing. Optical distortion and pixel scale quantification were achieved by capturing calibration images of a 13 by 10 chequerboard with 50 mm square

size using the cameras.

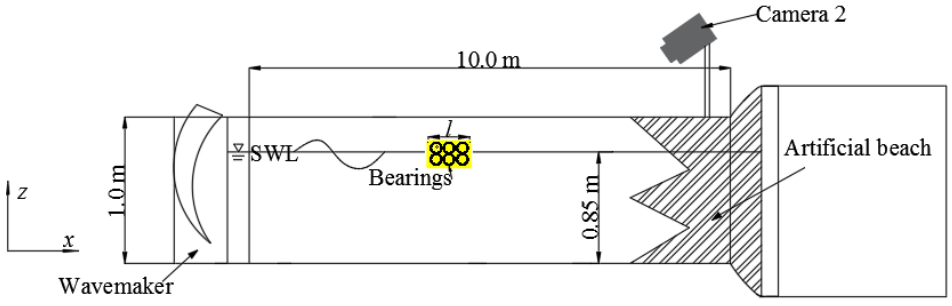
The parameters describing the waves used in our experiments are presented in table 4.3.1. Initially, we conducted experiments with wave gauges installed in the flume, without any objects, to measure the undisturbed wave field. These experiments also allowed us to quantify any unabsorbed reflections and lateral variation of the wave field within the flume. The lateral variation for a single frequency was calculated by determining the relative difference in amplitude measured by the gauges. A reflection analysis based on the methods described in Goda and Suzuki (1976) and MANSARD (1980) was performed. As shown in table 4.3.1, the lateral variation was found to be low, and the wave reflection coefficients were predominantly below 5%, with a maximum value of 10%. For experiments involving the measurement of object motion, the wave gauges were removed. At the beginning of each experiment, the objects were positioned 1.5 m away from the wavemakers. Waves were then continuously generated until the objects reached a position 1 m from the beach. The camera and wavemakers were triggered manually. In cases where large drift speeds were expected (i.e., for large objects in steep waves), the experiments were repeated 2-3 times to ensure a minimum duration of 35 wave periods of data after the drift has reached a quasi-steady state. Following each experiment, a 10-min wait time was observed to allow the flume to settle. To assess the repeatability of our experiments, we conducted additional experiments for four out of the twelve values of input wave steepness ($ka_w = 0.06$, 0.10, 0.20, and 0.32) for each frequency and each object. For these experiments, we performed 5 repeats, which are analysed in appendix 4.B.

4.3.2 Floating objects

To ensure that our experiments were as close to 2D as possible, we carefully designed the width b of our floating objects to match that of the flume. To minimize friction between objects and the walls, and to reduce the potential for rotation about the z-axis, we installed bearings (Xiros polymer ball transfer unit BB-515-B180-POM) at each end of the objects. Without a certain amount of restraint, smaller objects are prone to twisting caused by small lateral perturbations in the wave-induced forces. The bearings were specifically chosen for their low friction properties. The dimensions of the objects are provided in table 4.3.2, and diagrams showing their dimensions are given in figures 4.3.1 and 4.3.2, which also depict the layout of the



(a) Plan view.



(b) Side view (camera 1 is not shown).

Figure 4.3.1: Schematic layout of the wave flume and experimental setup, indicating the positions of the two cameras, the coordinate system, and the dimensions of the floating object.

f (Hz)	a_w (m)	k	$\epsilon = ka_w$	kd	λ (m)	Δa_w [%]	R [%]
0.90	0.012-0.094	3.28	0.04-0.31	2.79	1.91	1.27	4.19
1.00	0.010-0.079	4.03	0.04-0.32	3.43	1.56	1.80	4.03
1.05	0.009-0.072	4.44	0.04-0.32	3.78	1.41	2.23	6.91
1.10	0.007-0.064	4.87	0.03-0.31	4.14	1.29	2.58	5.33

Table 4.3.1: Experimental matrix showing the different wave parameters. We have examined a total of 48 wave conditions, combining 4 different frequencies, each with 12 different wave steepness values ranging from 0.04 to 0.32. The wave steepness interval was 0.02 for ka values between 0.04 and 0.2, and 0.04 for ka values between 0.2 and 0.31. The table includes the following parameters: f (wave frequency), a_w (measured wave amplitude), k (wavenumber), ϵ (wave steepness), d (water depth), and λ (wavelength). The term Δa_w represents the lateral variation of the wave amplitude calculated by measuring the wave amplitude using two pairs of gauges positioned at $x = 6.02$ m, $y = 0.0$ m; $x = 6.02$ m, $y = 0.275$ m; $x = 6.32$ m, $y = 0.0$ m; and $x = 6.32$ m, $y = 0.275$ m. The average value across all wave steepness values is reported. $R = a_I/a_R$ refers to the reflection coefficient, which corresponds to the ratio of the incident wave amplitude a_I to the reflected wave amplitude a_R.

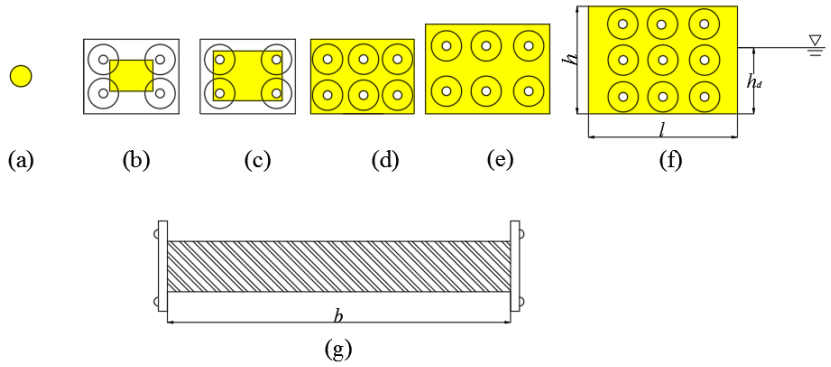
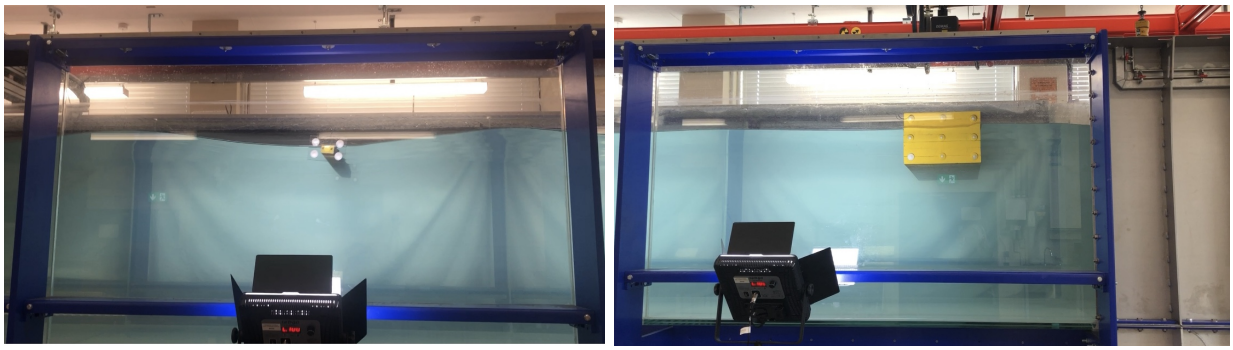


Figure 4.3.2: Shapes, bearing layouts, and dimensions of the objects used: (a) Object 0: small yellow polypropylene balls with a diameter of 2 cm and a density of $\rho = 920$ kg/m^3), serving as Lagrangian tracers. (b) Object 1: including flange. (c) Object 2: including flange. (d) Object 3: structure with 6 bearings. (e) Object 4: structure with 6 bearings. (f) Object 5: structure with 9 bearings. (g) Top view of the objects with flanges (Objects 1&2). The flanges are made of perspex sheet and have a width of 0.15 m, a height of 0.1 m, and thickness of 0.006 m.

Object numbers	b (m)	l (m)	h (m)	h_d (m)	Number of bearings
0	0.02	0.02	0.02	-	-
1	1.066	0.050	0.033	0.021	9
2	1.066	0.100	0.066	0.042	6
3	1.076	0.161	0.106	0.067	6
4	1.076	0.201	0.131	0.084	4
5	1.076	0.350	0.235	0.149	4

Table 4.3.2: Object dimensions. Object 0 spherical ball, functioning as a current drogue. The number of bearings indicates the number installed at each end of the object. Objects 1-5 are solid and were constructed from teak wood. The density of these objects is $\rho = 6.36 \times 10^2$ kg/m^3.

bearings that are fixed to each of the object's ends (see appendix 4.A for additional details). The smallest objects with length l less than 0.16 m (objects 1 and 2), were fitted with 6 mm thick perspex flanges on their ends to provide enough surface area to mount 4 bearings and to prevent the objects from rotating about the z-axis. To increase the range of relative object sizes l/λ, alongside varying the size of objects themselves, we also varied the wavelength of the incident waves (see table 4.3.3). Figure 4.3.3 provides a side and a top view of the smallest and largest objects in the flume. We also carried out reference experiments, in which we used small floating balls with a relative size of $l/\lambda = 1\%$. Previous studies have shown that these behave as Lagrangian tracers (Harms, 1987; Alsina et al., 2020; Calvert et al., 2021). Thus, they may be used to measure unenhanced drift and determine the strength of Eulerian-mean currents at the surface.



(a) Side view of small (left) and large (right) objects.



(b) Top view of small (left) and large (right) objects.

Figure 4.3.3: Side and top view of two objects in the wave flume. (a) On the left is the small object with $l = 0.05$ m, and on the right is the large object with $l = 0.35$ m. (b) On the left is the small object with $l = 0.05$ m and on the right is the large object with $l = 0.35$ m.

Object number	0	1	1	1	1	2	3	4	3	4	5	5	5	5
f (Hz)	0.9	0.9	1.0	1.05	1.1	0.9	0.9	0.9	1.1	1.1	0.9	1.0	1.05	1.1
l (m)	0.02	0.050	0.05	0.05	0.05	0.100	0.161	0.201	0.161	0.201	0.350	0.350	0.350	0.350
λ (m)	1.91	1.91	1.56	1.41	1.29	1.91	1.91	1.91	1.29	1.29	1.91	1.56	1.41	1.29
l/λ [%]	1.1	2.6	3.2	3.6	3.9	5.2	8.4	10.5	12.5	15.6	18.3	22.4	24.8	27.1

Table 4.3.3: Matrix of relative object size l/λ. For each relative object size, experiments with 12 different values of incident wave steepness were performed.

4.3.3 Data acquisition

Our goals are to examine the wave-induced drift of floating objects, investigate the effects of relative size and wave steepness, and understand the underlying mechanisms of drift enhancement by analyzing the objects' oscillatory motions and local surface elevation amplitude distribution in their vicinity. To achieve this, we first measured the wave amplitude for each wave condition in the flume using the mean value obtained from all seven wave gauges. This measured wave amplitude is used to calculate wave steepness and, subsequently, the theoretical Stokes drift. Next, we extracted the objects' trajectories and the local surface elevation from the calibrated camera images. Image-processing techniques were used to calibrate the images, perform object tracking, and obtain the horizontal and vertical trajectories of the objects (only the horizontal trajectory for the small yellow balls). We used edge detection and curve line extraction methods to obtain the free surface elevation.

Image processing and object tracking

The small yellow balls were tracked using the CSRT algorithm in OpenCV in Python using images from Camera 2, allowing us to obtain their (x, y)-locations in pixel space. Care was taken to identify potential issues such as sphere collision and loss of tracking. The 2D objects were tracked from the side of the flume using images from camera 1. As the objects passed the vertical upright members of the wave flume structure, the camera's view of the objects was partially or entirely obscured depending on object size. This loss of sight meant that it was not possible to use the CSRT tracker for tracking objects from the side of the flume. Instead, the objects, which were painted yellow, were identified using an HSV mask in the HSV Color space with OpenCV for each frame, followed by temporal advancement of the frame to get the time history of object motion. To remove background noise, unwanted stationary yellow elements were removed from the frame in a preliminary step. After applying the HSV mask, we extracted the contours of rectangular boxes with fixed sizes for each object. From these contours, we identified the position of the object's center and calculated its roll angle in pixel space (we define the rotation of our objects around y-axis as its roll motion). This method, in which we enforced that the tracked objects have a constant shape and size, meant it was possible to maintain tracking of the objects when they were partially obscured. Once the object

trajectories were identified in pixel space, they were undistorted and transformed into physical space. The calibrated Camera 1 had an overall mean reprojection error of approximately 0.09 pixels (0.2 mm), while Camera 2 had a mean reprojection error of 0.46 pixels (0.6 mm). Examples of the horizontal trajectories are provided in figure 4.3.4 (a).

Edge detection to measure the free surface elevation

It was not possible to operate wave gauges while the objects were in the flume, as they would obstruct the floating objects. To estimate the instantaneous free surface elevation while objects were in the flume, we used the images recorded by camera 1. Surface elevation was extracted using edge-detection techniques. We set up virtual wave gauges that travelled with the objects, to obtain measurements of surface elevation on fixed positions relative to the objects. Specifically, we first determined the location of the objects for each frame and then established a group of virtual gauges with pre-set x- coordinates. The distance between the virtual gauges and the objects was kept constant. We set up 60 gauges with their relative position, $x - x_c$, ranging from -1.1λ to 1.1λ, in which x represents the location of the wave gauges and x_c the location of the centre of the object. To perform edge detection, we found that standard algorithms such as Canny edge detection and threshold approaches did not yield satisfactory results for our study in this chapter. Therefore, we utilised the Holistically-Nested Edge Detection (HED) algorithm, which employs a deep neural network capable of learning rich hierarchical edge maps (see Xie and Tu (2015) for more details). We used a pre-trained HED Caffe model to leverage the benefits of the HED algorithm (see Xie (2015)). It is worth noting that while HED preserves boundaries in the image better than other methods, it produces more blurry boundaries than Canny edge detection. To enhance the sharpness of the edges, we applied the Zhang-Suen thinning algorithm using the 'ximgproc.thinning' function in OpenCV. By skeletonising the image, we obtained the surface elevation at the pre-set locations of the virtual wave gauges. Throughout the experiment, the positions of the objects and virtual wave gauges were updated with each frame as time progressed. Figure 4.3.4 (b) provides examples of the time history of several virtual gauges, illustrating the variations in surface elevation.

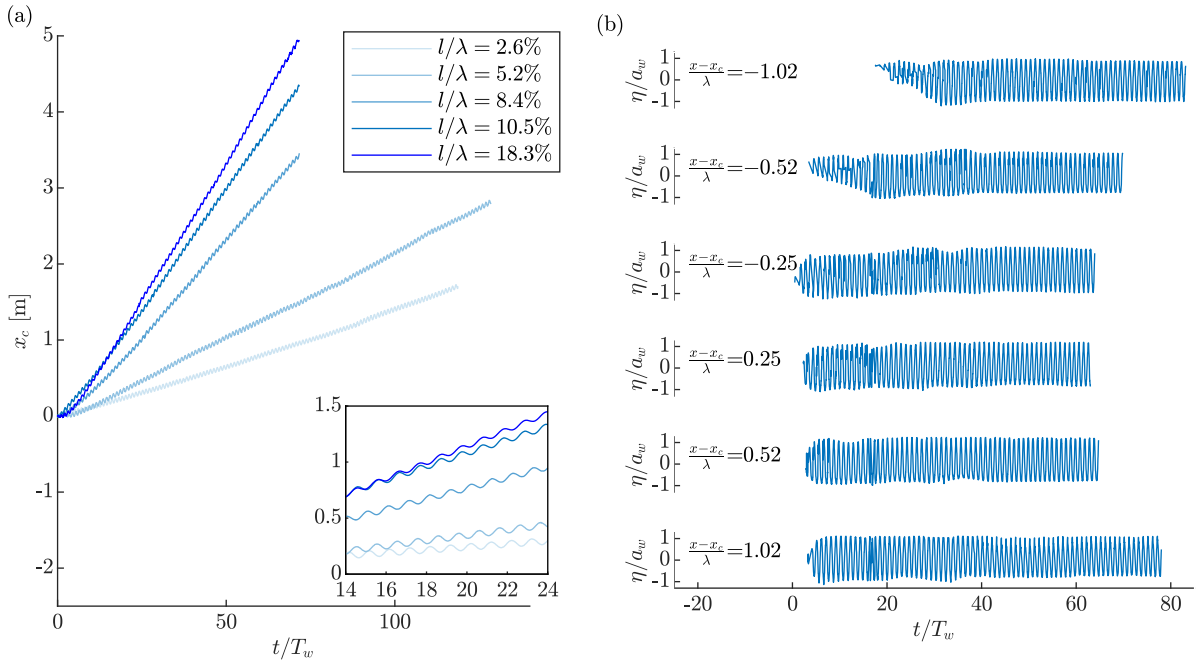


Figure 4.3.4: Example time history of objects' horizontal trajectories and surface elevation in regular waves with $f = 0.9$ Hz. (a) Horizontal trajectories of objects with different relative sizes for $ka_w = 0.10$, where x_c is the horizontal position of the objects' centre, and T_w denotes the wave period. (b) Local surface elevation of virtual gauges at various locations for $ka_w = 0.20$, where x is the horizontal position of the virtual gauges, and η is the local wave elevation. During the extraction process of the surface elevation for virtual wave gauges, the data is removed when the gauges are obscured by the flume's structural members or leave the pixel space (that is, when the position of the wave gauges is beyond the scope of the camera). Extraction begins when the object reaches $x_c = 2.3$ m and ends when it reaches $x_c = 8.2$ m, away from the wave maker.

Data post-processing

We aim to analyse the drift velocity, oscillatory linear motion in both the horizontal and vertical directions, as well as the magnitudes of local free surface elevations using the data obtained in §4.3.3 and §4.3.3. The time-average drift and horizontal oscillatory motions are derived from the horizontal trajectories of the objects. Since it takes time for the object to accelerate and reach a steady state, we eliminate the initial transient from the data. The horizontal motion is then filtered by using low- and high-pass frequency filters to separate the sub-harmonic ($f/f_p \leq 0.4$) motion and linear motions ($0.4 < f/f_p \leq 1.7$), thus removing higher-order motion. The drift velocity is examined by performing a linear regression of the sub-harmonic motion with time. The amplitude of horizontal oscillatory motion (corresponding to the x-direction) is determined by performing zero-up-crossing analysis on the signal and calculating the mean magnitude over the full time duration. The analysis of vertical oscillatory motions and local wave amplitude distribution of the surface elevation follows a procedure similar to that of horizontal motions. Each trajectory and time history of the surface elevation undergoes a manual inspection as part of the quality-control process.

4.4 Existing theoretical and empirical models used for comparison

In this section, we outline the two models for drift enhancement (compared to the Stokes drift) that we will use to compare with our experimental results in §4.5. The Stokes drift in finite water depth can be calculated by:

$$u_S = c(a_w k)^2 \frac{\cosh\left(2k\left(d+z\right)\right)}{2\sinh^2\left(kd\right)}, \tag{4.1}$$

where $c = \omega/k$ is the wave celerity, $\omega = 2\pi f$ the angular frequency, z the vertical coordinate of the fluid particle. For deep water ($kd \gg 1$), (4.1) becomes $u_S = c(a_w k)^2 e^{2kz}$. For the floating objects that we study, we evaluate the Stokes drift at $z = 0$.

The only two models that we believe are suitable for comparison with our experimental results for large objects are the diffraction-modified Stokes drift model recently developed in

Xiao et al. (2024) and the empirical formulas for drift enhancement proposed by Harms (1987). We will summarize the key equations of both models in turn.

4.4.1 The diffraction-modified Stokes drift of Xiao et al. (2024)

Xiao et al. (2024) showed that diffraction of the wave field affects wave-induced drift and cannot be neglected even for objects of $l/\lambda < 10\%$. They proposed a diffraction-modified Stokes drift akin to Stokes (1847) but considering the combination of the incident, diffracted and radiated wave fields. Here, we follow Xiao et al. (2024) and use a simplified Boundary Element Method (BEM) model based on potential-flow theory to solve for the linear wave field. The total linear wave field is decomposed into its incident, diffracted, and radiated parts. If we describe the flow by a linear velocity potential Φ, it can be written as:

$$\Phi(x,z,t) = \Phi_I(x,z,t) + \Phi_D(x,z,t) + \Phi_R(x,z,t), \tag{4.2}$$

where Φ_I, Φ_D and Φ_R are incident, diffraction and radiation potentials, respectively, then the diffraction-modified Stokes drift $u_{S,O}$ can be calculated by a second-order accurate expansion that is analogous to Stokes (1847), as shown by Xiao et al. (2024) :

$$u_{S,O} = \overline{\xi_x \frac{\partial^2 \Phi}{\partial x^2} + \xi_z \frac{\partial^2 \Phi}{\partial x \partial z}} = \overline{\xi_x \left(\frac{\partial^2 \Phi_I}{\partial x^2} + \frac{\partial^2 \Phi_R}{\partial x^2} + \frac{\partial^2 \Phi_D}{\partial x^2} \right) + \xi_z \left(\frac{\partial^2 \Phi_I}{\partial x \partial z} + \frac{\partial^2 \Phi_R}{\partial x \partial z} + \frac{\partial^2 \Phi_D}{\partial x \partial z} \right)}, \tag{4.3}$$

where $\xi_x = \mathrm{Re}\{A_x e^{-\iota\omega t}\}$ and $\xi_z = \mathrm{Re}\{A_z e^{-\iota\omega t}\}$ are the linear horizontal and vertical harmonic oscillatory motions of the object, and the overline denotes averaging over a wave period. To evaluate (4.3), the linear oscillatory motions, the three potentials, and their derivatives are all calculated using a standard BEM model, as described in detail in Xiao et al. (2024).

4.4.2 The empirical model of Harms (1987)

In addition to the theoretical model of Xiao et al. (2024), we also compare the data with the empirical formulas proposed by Harms (1987) based on their extensive set of laboratory

Object number	$T_{O,R,BEM}$ (s)	$T_{O,R,H87}$ (s)	$T_{O,H,BEM}$ (s)
1	0.61	0.35	0.40
2	0.88	0.49	0.56
3	1.08	0.63	0.72
4	1.15	0.71	0.81
5	1.67	0.94	1.05

Table 4.4.1: Estimated natural periods of object heave and roll motion. Object numbers 1-5 correspond to the objects specified in table 4.3.2. The periods $T_{O,R,BEM}$ and $T_{O,H,BEM}$ are the estimated natural periods of roll and heave motions for the objects calculated from the BEM simulations; $T_{O,R,H87}$ denotes the natural roll period given by (4.5) from Harms (1987).

experiments for 2D objects. According to Harms (1987), object drift can be estimated by:

$$u_{S,O} = \begin{cases} 0.87\sqrt{gl}\frac{2a_w}{\lambda}\left(\frac{T_w}{T_{O,R}}\right)^{2.81+\log\frac{2a_w}{\lambda}} & \frac{T_w}{T_{O,R}} \leq 1.15, \\ 1.15\sqrt{gl}\frac{2a_w}{\lambda}\left(\frac{T_w}{T_{O,R}}\right)^{0.87+\log\frac{2a_w}{\lambda}} & \frac{T_w}{T_{O,R}} > 1.15, \end{cases} \tag{4.4}$$

where T_w is the wave period, $T_{O,R}$ is the natural period of the roll motion of the object. Harms (1987) presented a simplified formula to calculate the natural roll frequency:

$$\frac{T_{O,R,H87}}{T_0} = 1.03\sqrt{1 + 0.156\left(\frac{\rho_w}{\rho}\right)\left(\frac{l}{h}\right)}, \tag{4.5}$$

where $T_0 = 2\pi\sqrt{(\rho/\rho_w)(h/g)}$, ρ_w and ρ denote the densities of water and of the object, respectively, and g is the gravitational acceleration.

Equation (4.5) was shown to only provide a good estimate of natural roll periods for aspect ratios $l/h > 3$ (Harms, 1987), whereas our objects all had an aspect ratio of $l/h = 1.5$. To estimate the natural roll period for each object, we conducted numerical simulations using the BEM model and identified the local peak value of the roll-mode response in waves of different frequencies. These responses were calculated for a range of frequencies from $f = 0.01$ to 4 Hz (corresponding to relative size l/λ ranging from nearly 0 to 0.5, which covers the range of relative sizes considered in our study in this chapter) with 0.01 Hz increments. We also identified the frequency corresponding to the peak value of the heave motion within this frequency range. The estimated values of the natural roll and heave period, $T_{O,R,BEM}$ and $T_{O,H,BEM}$, for each object, along with the results calculated using (4.5), $T_{O,R,H87}$, are listed in table 4.4.1. From the table, we can observe that the predictions of the natural period by the BEM model are significantly larger than that from the simplified approach of Harms (1987). This is because

l/λ (%)	2.6	5.2	8.4	10.5	12.5	15.6	18.3	22.4	24.8	27.1
Object number	1	2	3	4	3	4	5	5	5	5
T_w (s)	1.11	1.11	1.11	1.11	0.91	0.91	1.11	1.00	0.95	0.91
$T_w/T_{O,R,BEM}$	1.83	1.27	1.03	0.97	0.85	0.79	0.67	0.60	0.57	0.55
$T_w/T_{O,H,BEM}$	2.74	1.97	1.54	1.37	1.26	1.12	1.06	0.95	0.90	0.86

Table 4.4.2: Estimates of the ratio of natural heave and roll period for objects with different relative sizes to incident wave periods (see table 4.3.3 for object dimensions and table 4.4.1 for values of the natural period).

(4.5) provided by Harms (1987) is an estimate of the natural roll period in waves, which is obtained from the slender-object limit ($l/h \gg 1$) and does not apply into the objects here.

To validate our approach to calculating the roll period, we compared our estimate with the value obtained for a floating cuboid in the study by He et al. (2016). The cuboid in their study had dimensions $b = 0.42$ m, $l = 0.3$ m, $h = 0.2$ m, and $h_d = 0.1$ m, with a density of $\rho = 500$ kg/m^3. For this geometry, our estimate of the roll period is $T_{O,R,BEM} = 1.85$ s, whereas a value of $T_{O,R,H87} = 0.79$ s is obtained from (4.5). The period derived from the experiments of He et al. (2016) is 1.6 s. We note that the free-damped oscillation decay test used in He et al. (2016) will be affected by viscosity, whereas our (potential-flow) estimate only accounts for radiation damping. Nevertheless, we can conclude that our BEM-based estimates provide reasonable estimates of the natural roll period, and we use these estimates instead of $T_{O,R,H87}$ given by (4.5) to evaluate object drift predicted by Harms (1987) according to (4.4). We note that the empirical parameterisation (4.4) suggests that the drift peaks when $T_w/T_{O,R} = 1.15$. Values of $T_w/T_{O,R}$ we use for all of the objects considered in our study in this chapter, alongside values of $T_w/T_{O,H}$ are listed in table 4.4.2.

4.5 Results and analysis

In this section, we present the results of our laboratory experiments, focusing on the linear oscillatory motion, drift velocities, and the local wave amplitude distributions of the wave field surrounding the objects. We compare the results of our laboratory experiment with the models in §4.4 and analyse the effects of object size and wave steepness in turn. Before analysing our results for drift, we must take into account the Eulerian-mean background current. Appendix 4.B provides a comprehensive assessment of the repeatability of our experiments.

4.5.1 Eulerian-mean background current

After estimating the Lagrangian-mean drift of objects $\overline{u}_{L,O}$ based on the data acquired in §4.3.3, we can calculate what we define as the 'Stokes object drift' $u_{S,O}$. The Stokes object drift is defined analogously to the Stokes drift (cf. Bühler (2014)) as $u_{S,O} \equiv \overline{u}_{L,O} - \overline{u}_E$, in which $\overline{u}_E$ is the Eulerian-mean velocity. In flumes, $\overline{u}_E$ usually takes the form of a return current. To examine the Eulerian-mean velocity in our flume, we use small ($D = 0.02$ m), yellow, spherical balls with a density close to that of water ($\rho_p = 920$ kg/m^3) as current drogues, which are expected to behave as accurate Lagrangian tracers based on their size and density (cf. Nath (1978); Harms (1987); Alsina et al. (2020); Eeltink et al. (2023)). Figure 4.5.1 (a) shows the Lagrangian drift of the small yellow balls and of the smallest 2D object ($l = 0.05$ m) as a function of wave steepness. The drift of the balls, which are 3D, and the small 2D object are similar, indicating that the 2D objects with a relative size of $l/\lambda = 2.6\%$ exhibit predominantly Lagrangian drift behaviour and follow the Stokes drift when the Eulerian-mean velocity is removed. We also compare the measured Eulerian-mean drift obtained from the experiments with theoretical values in figure 4.5.1 (b), which we calculate by assuming the Eulerian-mean return current is depth uniform and balances the forward volume flux associated with the Stokes drift:

$$\overline{u}_E = -\frac{\int_{-d}^{0} u_s(z)\mathrm{d}z}{h} = -\frac{1}{h}\int_{-d}^{0} \frac{c(ak)^2 \cosh 2k(d+z)}{2\sinh^2(kd)}\mathrm{d}z. \tag{4.6}$$

Surprisingly (see van den Bremer and Breivik (2018) and Monismith (2020) for context), the Eulerian-mean velocity in the flume can be predicted very well by (4.6) (for an incident wave frequency with $f = 0.9$ Hz).

Analytical estimates of the return current of regular waves are sensitive to the exact assumptions used and the boundary conditions within a given flume, as such the predicted and measured values often differ (van den Bremer and Breivik, 2018). Our estimate is averaged with depth (based on depth uniform assumption), the result is expected to be subjected to variation in the Eulerian-mean current with depth, which may affect the results for larger objects with larger submergence. The extent to which the Eulerian-mean current is affected by object size (submergence) is further discussed in the conclusion. Nevertheless, we consider deep water conditions and thus the ratio of object submergence to the water depth is very small. Our observations indicate that the theoretically estimated Eulerian-mean flow agrees with calculations

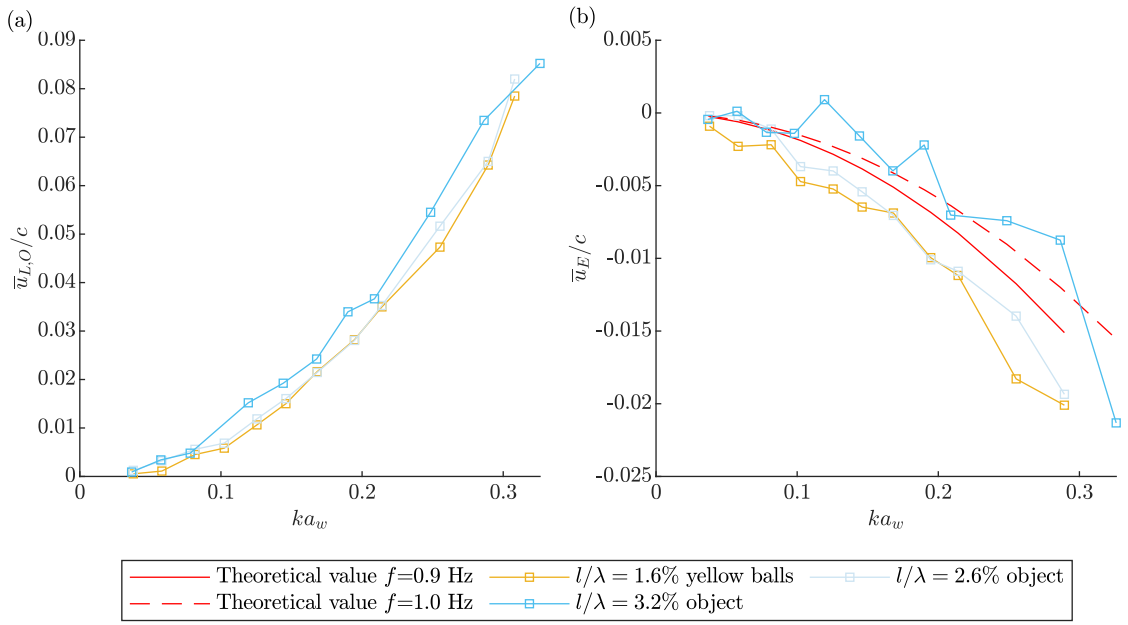


Figure 4.5.1: Lagrangian drift of small objects and the Eulerian-mean velocity on the surface as a function of wave steepness in waves with frequencies of $f = 0.9$ Hz and $f = 1.0$ Hz. (a) Lagrangian drift, normalised by wave celerity c, of the 3D small yellow balls ($l = D = 0.02$ m) with $l/\lambda = 1.6\%$ and the smallest 2D objects with $l/\lambda = 2.6\%$ and $l/\lambda = 3.2\%$. (b) Comparison of wave-celerity normalised Eulerian-mean velocity derived from experiments and theory (4.6). The values of $\overline{u}_E$ for $l/\lambda = 2.6\%$ and $l/\lambda = 1.6\%$ are obtained by $\overline{u}_E = \overline{u}_{L,O} - u_{O,S} = \overline{u}_{L,O} - u_S$, in which $\overline{u}_{L,O}$ is the Lagrangian drift of the corresponding objects that is directly measured in the wave flume and u_S is the theoretical Stokes drift (4.1), which is equal to the Stokes object drift for such small objects.

derived from reference experiments with the yellow balls.

Given this good agreement we use the theoretical values of Eulerian-mean velocity (4.6) to evaluate the Stokes object drift $u_{S,O}$ from the measured Lagrangian-mean object drift for all objects. The expression for the Stokes object drift is then given by:

$$u_{S,O} = \overline{u}_{L,O} - \overline{u}_E = \overline{u}_{L,O} + \frac{1}{h}\int_{-d}^{0} \frac{c(ak)^2 \cosh 2k(d+z)}{2\sinh^2(kd)} \mathrm{d}z. \tag{4.7}$$

4.5.2 Effect of object size and wave steepness

To examine the effects of relative object size and wave steepness, we will first look at the oscillatory motion and then the Stokes object drift followed by the local wave amplitude distribution. The linear oscillatory motions in both the horizontal and vertical directions are given in figure 4.5.2 as a function of wave steepness and in figure 4.5.3 as a function of relative

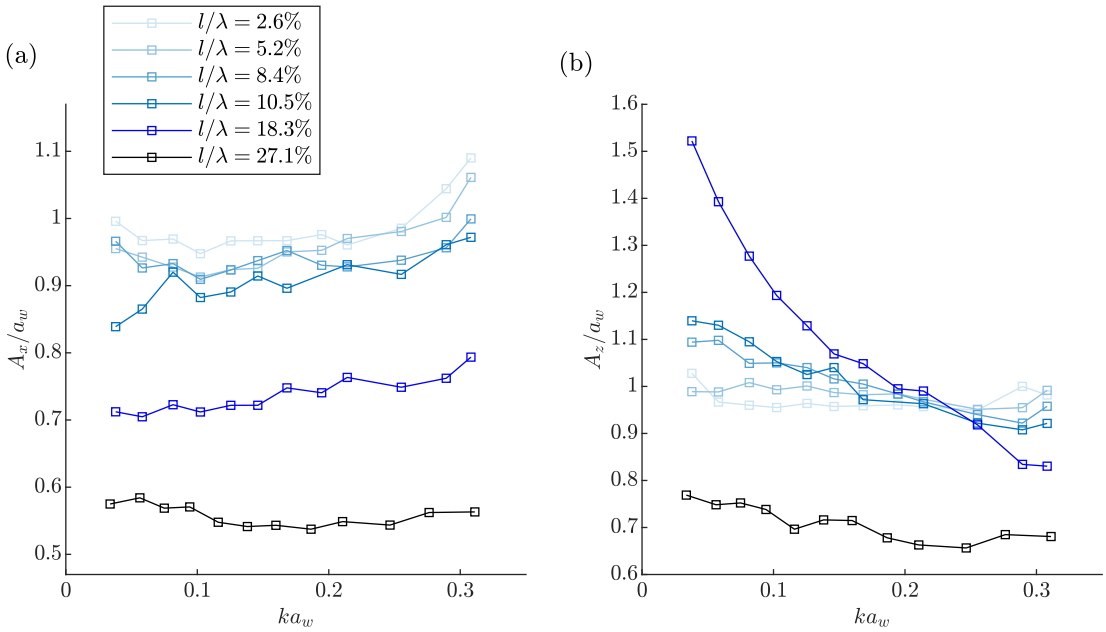


Figure 4.5.2: Linear oscillatory motion amplitudes as a function of wave steepness for objects of different relative size. (a) Magnitude of horizontal motion normalised by wave amplitude. (b) Magnitude of vertical motion normalised by wave amplitude.

size. The motions are normalised by the corresponding wave amplitudes a_w measured using wave gauges in the wave flume without objects. The Stokes object drift obtained using (4.7) is reported in figure 4.5.4 as a function of wave steepness and relative size. For clarity, we do not plot all the measured data in each figure (that is, we do not present the data for $l/\lambda = 12.5\%$, 15.6%, 22.4% and 24.8% in figure 4.5.4 (a), but include this data in figure 4.5.4 (b)). By time averaging the time history of the local surface elevations of all moving virtual wave gauges (as described in §4.3.3), we obtain the local wave amplitude distribution $a(x)$ as a function of the relative distance between the gauges and the object's centre. Figure 4.5.5 plots the normalised local wave amplitude distribution $a(x)/a_w$ for objects of different relative sizes when $ka_w = 0.21$ and figure 4.5.6 plots this distribution for an object of $l/\lambda = 18.3\%$ for different values of wave steepness.

Oscillatory motion

We start by looking at the horizontal oscillatory motion. As shown in figure 4.5.2 (a) and figure 4.5.3 (a), when the objects are small, with a relative size of $l/\lambda \lesssim 5\%$, the magnitude of the horizontal motions is very close to the incident wave amplitude a_w, implying behaviour is essentially Lagrangian. The amplitude of horizontal motion decreases at an approximately

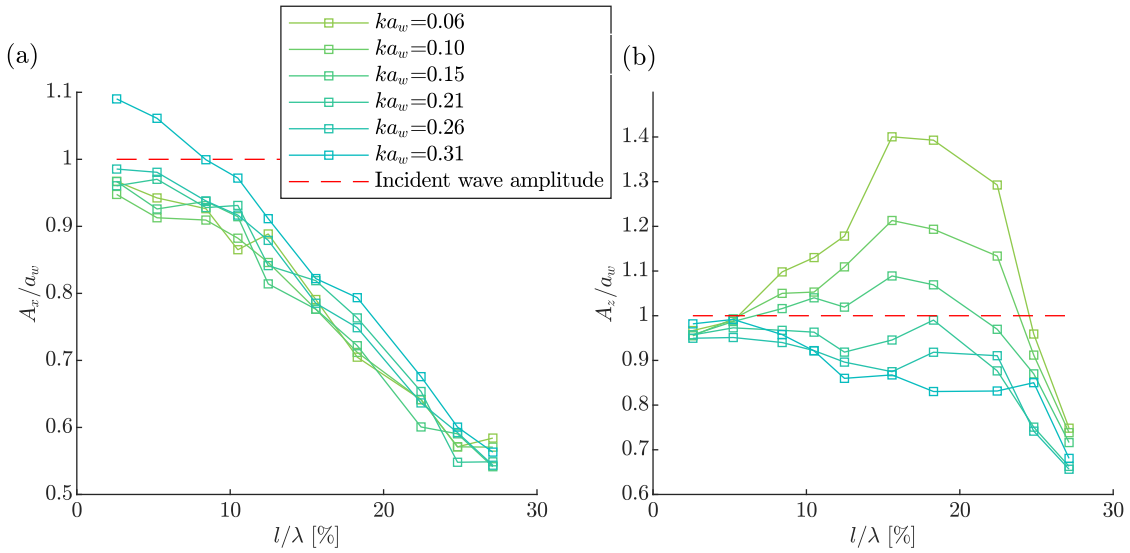


Figure 4.5.3: Linear oscillatory motion amplitudes as a function of the relative size of the objects for different wave steepness. (a) Magnitude of horizontal motion normalised by wave amplitude. (b) Magnitude of vertical motion normalised by wave amplitude.

linear rate as the relative object size increases. This trend applies to all objects in the size range we considered and is independent of wave steepness. For fixed relative size, the non-dimensional motion does not vary significantly with wave steepness ($ka_w \lesssim 0.25$). For the highest wave steepness, $ka_w = 0.31$, the non-dimensional horizontal motion is slightly larger than for lower values of wave steepness, and this difference is greatest for smaller objects $l/\lambda \lesssim 15.6\%$.

The vertical motion of the objects exhibits a more complex behaviour, as shown in figure 4.5.2 (b) and figure 4.5.3 (b). When the objects are very small, they behave like Lagrangian particles. However, as the object size increases, the non-dimensional vertical motion becomes dependent on both wave steepness and relative object size. Considering the dependence on relative size first, at low wave steepness, $ka_w \lesssim 0.15$, the vertical motion increases with relative object size when $l/\lambda \lesssim 15.6\%$, but decreases with size when $l/\lambda \gtrsim 18.3\%$. At high wave steepness, $ka_w \gtrsim 0.20$, the vertical motion always decreases with relative size, with a more pronounced decrease for larger objects, $l/\lambda \gtrsim 22.4\%$. The behaviour of vertical motion as a function of wave steepness also varies depending on the object size. When the object is either very small, $l/\lambda \lesssim 5.2\%$ or very large, $l/\lambda = 27.2\%$, its non-dimensional vertical motion remains independent of wave steepness. However, for objects with intermediate sizes with $8.4\% \lesssim l/\lambda \lesssim 24.8\%$, their non-dimensional vertical motion decreases with increasing wave steepness. This

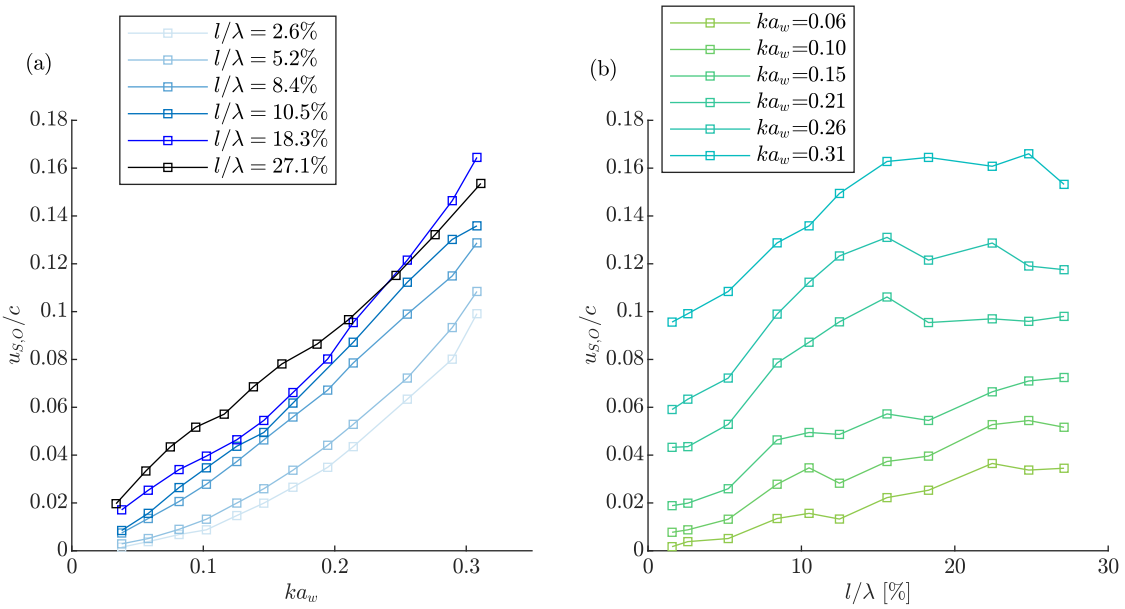


Figure 4.5.4: Celerity-normalised Stokes object drift velocity (a) as a function of wave steepness for different relative object sizes and (b) as a function of relative size for different wave steepness.

decreasing trend is most pronounced for objects with a relative size of $l/\lambda = 15.6\%$, 18.3%, 22.4%. We believe that this behaviour may be attributed to the effect of a resonance.

Stokes object drift

The Stokes object drift, normalised by wave celerity, shown in figure 4.5.4 (a) and (b), exhibits a clear dependence on both object size and wave steepness. In general, for low wave steepness, $ka_w \lesssim 0.15$, the Stokes object drift increases with relative size for all the object sizes covered here (i.e., $2.6\% \leq l/\lambda \leq 27.2\%$). However, for relatively high wave steepness, $ka_w \gtrsim 0.17$, the drift shows a different trend. It increases with object size for $l/\lambda \lesssim 15.6$ but exhibits a decreasing trend for $l/\lambda \gtrsim 15.6$. Changes in the functional dependence of the Stokes object drift on the wave steepness are also evident. Drift always increases with increasing wave steepness. For small objects (i.e., $l/\lambda = 2.6\%$), this increase appears to be quadratic, whereas for larger objects the relationship between drift and steepness appears to be closer to linear — we will consider this in more detail in §4.C. It is noted that there are only several points in figure 4.5.4 indicating different regimes before and after the turning point of the wave steepness, which might appear overstated. However, it is argued that the scaling effect of object drift changes from quadratic to linear function of the wave steepness as the object size increases, suggesting a regime shift at a certain wave steepness, after which object drift does not monotonically

increase with its size.

Local wave amplitude distribution

The local wave amplitude distribution in the vicinity of the moving objects is shown in figure 4.5.5; a standing wave pattern forms that is clearest for relatively large objects, $l/\lambda = 10.5\%$ and 18.3%. The local amplitude of the surface elevation is normalised by the wave amplitude in the absence of the object, a_w. For small objects, $l/\lambda = 2.6\%$, the local time-averaged wave amplitude does not vary significantly with distance to the object's centre. It remains relatively constant at a value of $a(x)/a_w = 1.1$, which is slightly higher than the theoretical value of 1. This slight discrepancy may be attributed to measurement errors in the camera data. Similarly to observations in Xiao et al. (2024), as object size increases, a standing wave pattern becomes apparent. On the upstream side, the time-averaged wave amplitudes show a pattern of smaller and larger amplitudes compared to the incident wave field (or compared to the case of a very small object) at different distances from the object's centre. The standing wave pattern thus identified is more evident as the object becomes larger. On the downstream side, smaller amplitudes are observed for all locations, and there is a discernible difference in the magnitude of the surface elevation between the two sides of the object for large enough objects.

In figure 4.5.6, we show how the standing wave pattern varies with steepness for relatively large objects (large enough to generate a clear standing wave pattern). The standing wave pattern is plotted as $a(x) - a_w$ in figure 4.5.6 (a) and as $a(x)/a_w$ in figure 4.5.6 (b), for an object of size $l/\lambda = 18.3\%$. The pattern is clearer when plotted as an absolute value (that is, as $a(x) - a_w$) as incident wave steepness increases from $ka_w = 0.10$ to $ka_w = 0.21$, while the pattern is less evident when plotted as a normalised value (that is, as $a(x)/a_w$) as steepness increases.

Despite obvious general qualitative agreement, there are two ways the standing wave pattern found here is different from the one identified in Xiao et al. (2024): (1) the phase difference between the standing wave patterns formed by objects of different sizes and (2) the sign of the difference in amplitude between the two sides of the object. First, Xiao et al. (2024) found that the local maxima and minima in the amplitude distribution occurred at similar relative distances for objects of different sizes, which is not the case here (cf. figure 4.5.5).

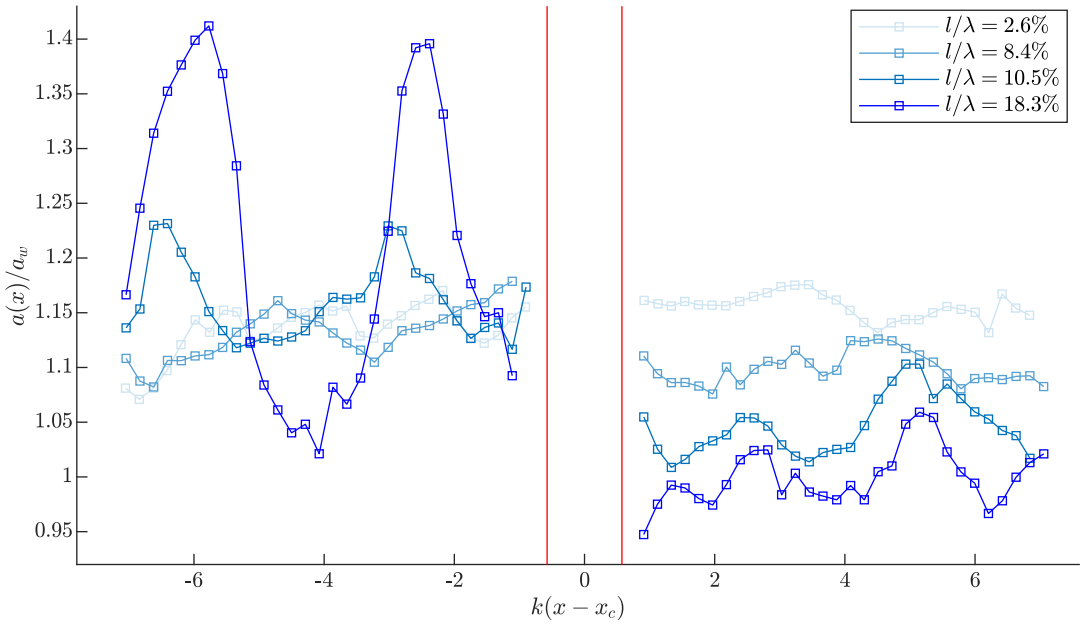


Figure 4.5.5: Non-dimensional amplitude of the local surface elevation amplitude distribution, $a(x)/a_w$, as a function of horizontal distance (scaled by wavenumber) from the centre of mass of the object, $k(x - x_c)$, for objects of different relative sizes with incident wave steepness $ka_w = 0.21$, and frequency $f = 0.9$ Hz. The red lines represent the left and right sides of the largest object with a relative size of $l/\lambda = 18.3\%$.

Second, in Xiao et al. (2024), the local surface elevation amplitude on the upstream side of the object is smaller than on the downstream side, while our experiment shows the opposite. The discrepancies are likely due to our (virtual) gauges moving with the objects (i.e., the distance between the gauges and the object is constant), while the gauges in Xiao et al. (2024) were fixed in a stationary reference frame, causing a phase shift and a non-stationary standing wave pattern. We also consider objects much larger than those analysed in Xiao et al. (2024). In their method, it is very difficult to obtain a time history of the wave amplitude distribution in close proximity to the object.

4.5.3 Comparison with existing theoretical and empirical models

In this section, we set out to assess the range, in terms of relative object size and wave steepness, over which the classical Stokes drift (given by 4.1), the diffraction-modified Stokes drift of Xiao et al. (2024) (given by 4.3) and the empirical formulas of Harms (1987) (given by 4.4) are valid.

The experimentally measured Stokes object drift scaled by the theoretical Stokes drift as

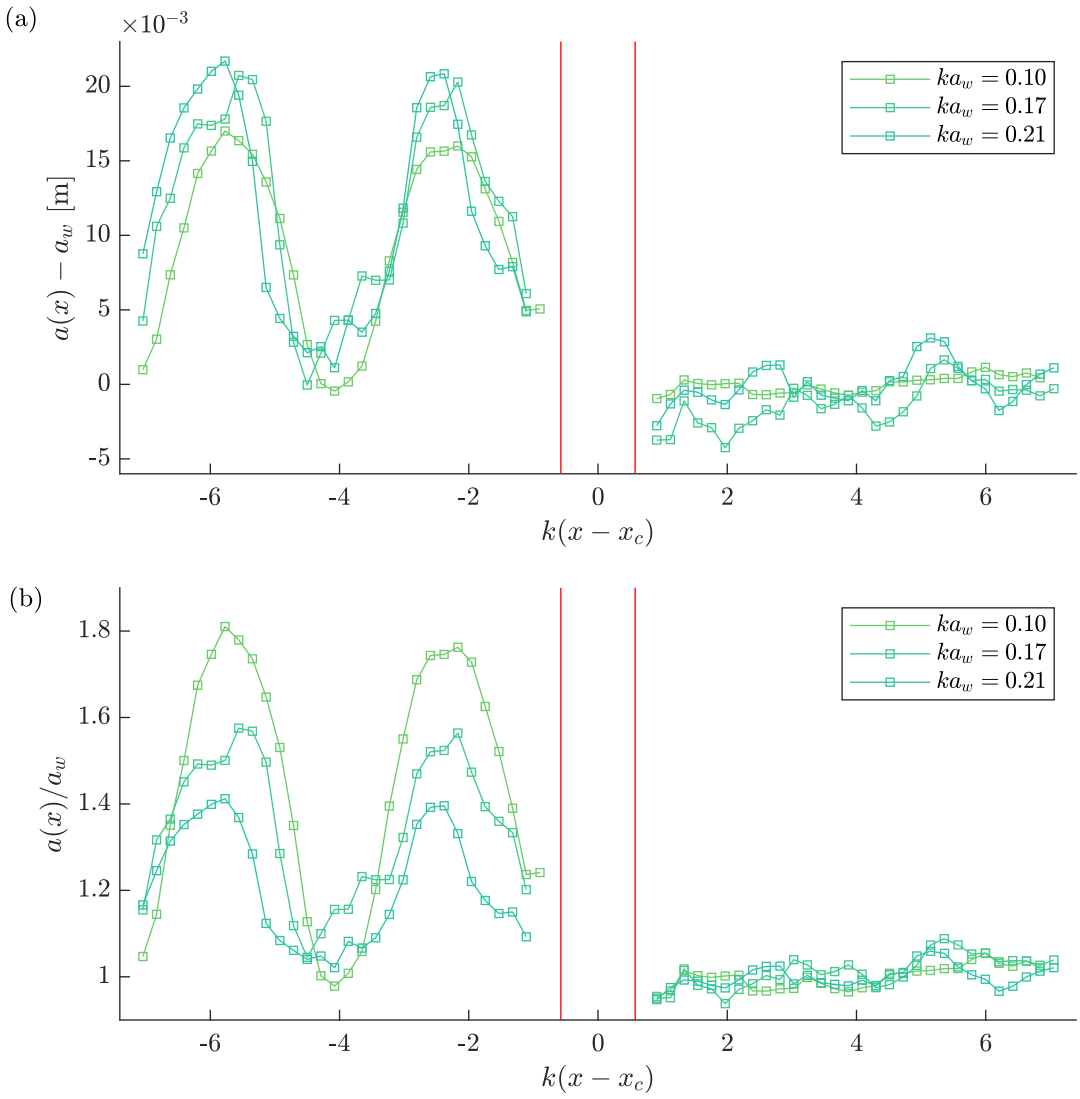


Figure 4.5.6: Local surface elevation amplitude distribution, $a(x)$, as a function of horizontal distance (scaled by wavenumber) from the centre of mass, $k(x - x_c)$, for the largest object with a relative size of $l/\lambda = 18.3\%$ at a frequency of $f = 0.9$ Hz. (a) Difference between the local surface elevation amplitude and the incident wave amplitude, $a(x) - a_w$, for three different wave steepnesses. (b) Ratio of local surface elevation and incident wave amplitudes, $a(x)/a_w$, for three different wave steepnesses. The red lines represent the left and right sides of the object.

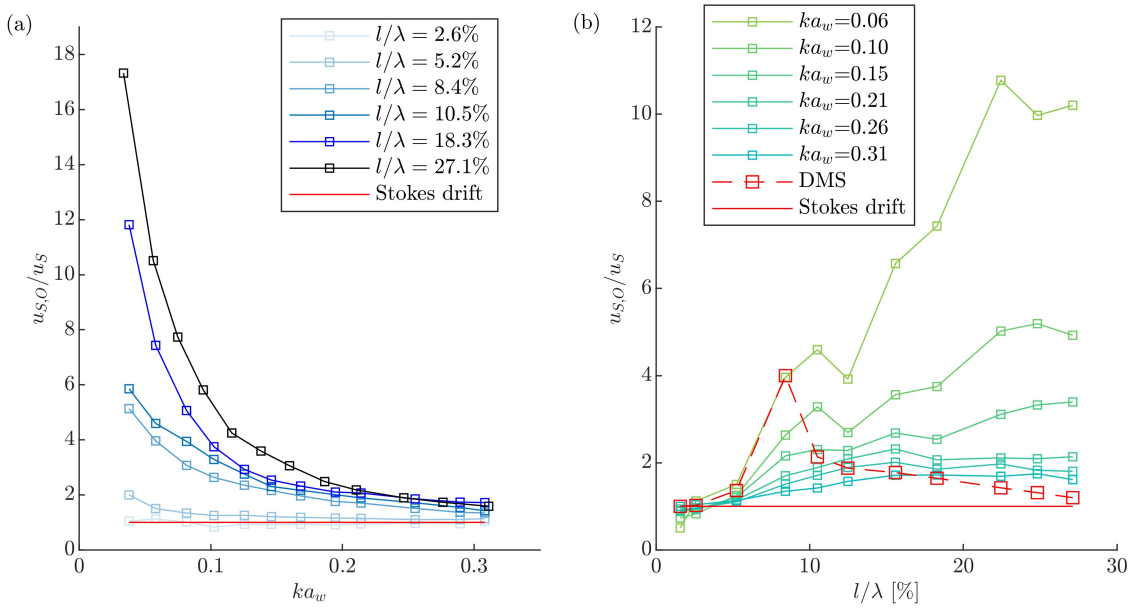


Figure 4.5.7: Stokes drift-normalised Stokes object drift (a) as a function of wave steepness for different relative object sizes and (b) as a function of relative size for different values of wave steepness. An idealised Lagrangian particle with zero enhanced drift would have $u_{S,O}/u_S = 1$. The red dashed line with red square labelled DMS represents the diffraction-modified Stokes drift given by (4.3). As the diffraction-modified Stokes drift for a certain object size does not change with wave steepness (we use a linear 'BEM' model to solve (4.3), and (4.3) is a second-order accurate quantity), it is shown as a single line in panel (b).

a function of wave steepness and relative object size are presented in figure 4.5.7 (a) and (b), respectively. As shown in panel (a), small objects $l/\lambda \leq 2.6\%$ follow the theoretical Stokes drift. As the object size increases, the amplification factor $u_{S,O}/u_S$ increases, suggesting a larger drift enhancement. This is true for all values of wave steepness but is especially evident for smaller values of wave steepness. For objects of a certain size, the amplification factor decreases drastically as wave steepness increases in the low to intermediate wave steepness range, reaching its peak value at the lowest wave steepness. As the wave steepness increases further, the amplification factor either becomes constant or decreases slowly with steepness. A decreasing trend with wave steepness is more distinct for larger objects and was also observed in measurements by Huang et al. (2011), although they do not explicitly discuss this.

Comparison between the experimentally measured Stokes object drift and the diffraction-modified Stokes drift normalised by theoretical Stokes drift is made in figure 4.5.7(b). In addition, a comparison between the measured Stokes object drift, the diffraction-modified Stokes drift proposed by Xiao et al. (2024) and the empirical formula of Harms (1987) is made in figure 4.5.8 by examining the drift normalised by wave celerity c as a function of relative size

for different values of wave steepness. The figures show that for small objects, the diffraction-modified Stokes drift accurately predicts Stokes object drift for various values of steepness, but this agreement breaks down for relatively large objects, for which the expansion that underlies (4.3) is no longer valid. As shown in both figure 4.5.7 (b) and figure 4.5.8, the diffraction-modified Stokes drift is capable of giving a good prediction beyond the range of the classical Stokes drift.

As the diffraction-modified Stokes drift (4.3) is calculated based on the linear oscillatory motion of the object, figure 4.5.9 compares the amplitudes of the horizontal and vertical components of motion between experiments and the linear BEM that underlies (4.3) (see Xiao et al. (2024) for details) as a function of relative size for different values of wave steepness. The linear BEM model performs well in predicting the horizontal oscillatory motions for all objects and wave steepnesses but fails to accurately predict the vertical motions of larger objects where the assumption of linearity underlying the BEM model probably fails.

Despite the difference in density between the objects used here ($\rho = 636.2$ kg/m^3) and by Harms (1987) ($\rho = 0.92$ kg/m^3), the empirical formula by Harms (1987) still works well for small wave steepness and all object sizes considered here. However, the formula by Harms (1987) underestimates the drift significantly for all sizes when the wave steepness is relatively large ($ka_w \geq 0.16$).

The empirical formula of Harms (1987) is a discontinuous function of $T_w/T_{O,R}$, with one parametric fit for short-period waves, $T_w/T_{O,R} \leq 1.15$ (corresponding to objects of large relative size) and another for long-period waves, $T_w/T_{O,R} > 1.15$ (corresponding to objects of small relative size). The transition from short-wave to long-wave drift behaviour occurs when $T_w/T_{O,R} = 1.15$. According to (4.4), Stokes object drift is fundamentally different in long and short waves. When the object is small, that is, in the long-wave regime, the drift increases monotonically with relative size, while when the object is large, that is, in the short-wave regime (i.e., when $l/\lambda \geq 50\%$) drift decreases continuously with relative size. The drift peaks at the transition point between the two regimes.

Finally, in figures 4.5.10 and 4.5.11, we present the domains over which the different models we have discussed agree with the experimental data in this chapter. When an object is very small $l/\lambda \lesssim 3.2\%$, it follows the theoretical Stokes drift for the full range of wave steepness

considered. As object size increases, up to $l/\lambda = 8.4$ %- 23.6% depending on steepness, drift behaviour is enhanced compared to the theoretical Stokes drift, and the diffraction-modified Stokes drift gives a relative error of less than 20% when compared with experimental data. The diffraction-modified Stokes drift predicts drift enhancement as a result of increased vertical motion (relative to the incident wave field) and the difference between the diffracted and radiated wave fields. The range of object sizes for which the diffraction-modified Stokes drift result of Xiao et al. (2024) is valid depends on the wave steepness (see figure 4.5.7). As the wave steepness increases, its drift enhancement amplification (relative to the theoretical Stokes drift) decreases to a smaller number compared to the same ratio in low wave steepness. As the relative object size is increased further, the assumptions underlying the diffraction-modified Stokes drift derivation in Xiao et al. (2024) break down, and the theory becomes ineffective. The empirical formula by Harms (1987) for large object sizes is then more accurate provided the steepness is low. To investigate the correlation between object drift and both relative size and wave steepness, we perform the polynomials regression analysis based on our experimental data. The detailed analysis including our own parameterisation is given in Appendix 4.C.

4.6 Conclusion

This chapter has presented an experimental study of the drift of large rectangular 2D objects under the action of waves. It is experimentally difficult to examine the drift of 2D objects (as objects may spin under the influence of lateral variation and become jammed). To overcome these difficulties, we have designed objects that float freely on the water's surface, while occupying the full width of the wave flume used, meaning our experiments are as close to 2D as possible. To achieve this, the objects are equipped with low-friction bearings and 'flange' structures to support these bearings for small objects.

We have considered rectangular objects with sizes up to 27% of the length of the incident waves. Very small objects (less than 3% of the wavelength) essentially behave as Lagrangian tracers, and their drift is well captured by the classical Stokes drift of Stokes (1847). However, for larger objects, we found drift much greater than that predicted by the classical Stokes drift; we observed drift velocities up to 17 times larger than the Stokes drift in the extreme case (for the largest object in the smallest steepness waves considered).

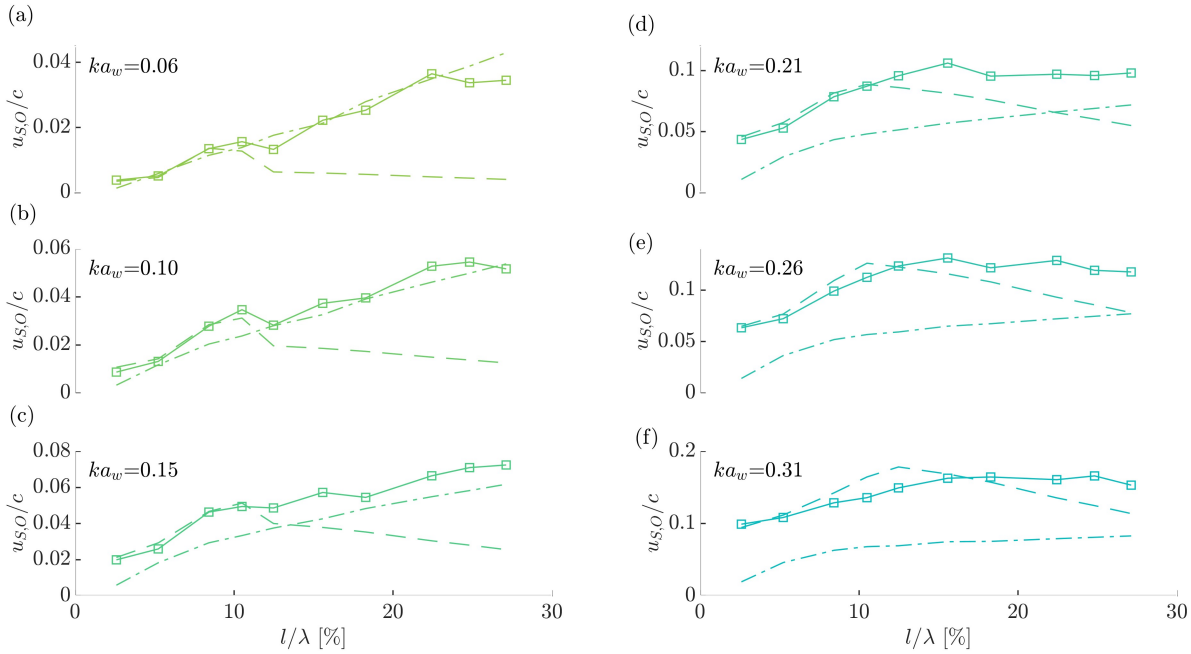


Figure 4.5.8: Comparison of the Stokes object drift from experiments with the diffraction-modified Stokes drift (4.3) proposed by Xiao et al. (2024) and the empirical formula (4.4) of Harms (1987) as a function of relative object size for different values of wave steepness. The drift is normalised by wave celerity. Markers connected by continuous lines correspond to the results from experiments, dashed lines (of the same colour, corresponding to the colour in figure 4.5.7 (b)) to the diffraction-modified Stokes drift, and dash-dotted lines (of the same colour) to the empirical formula of Harms (1987).

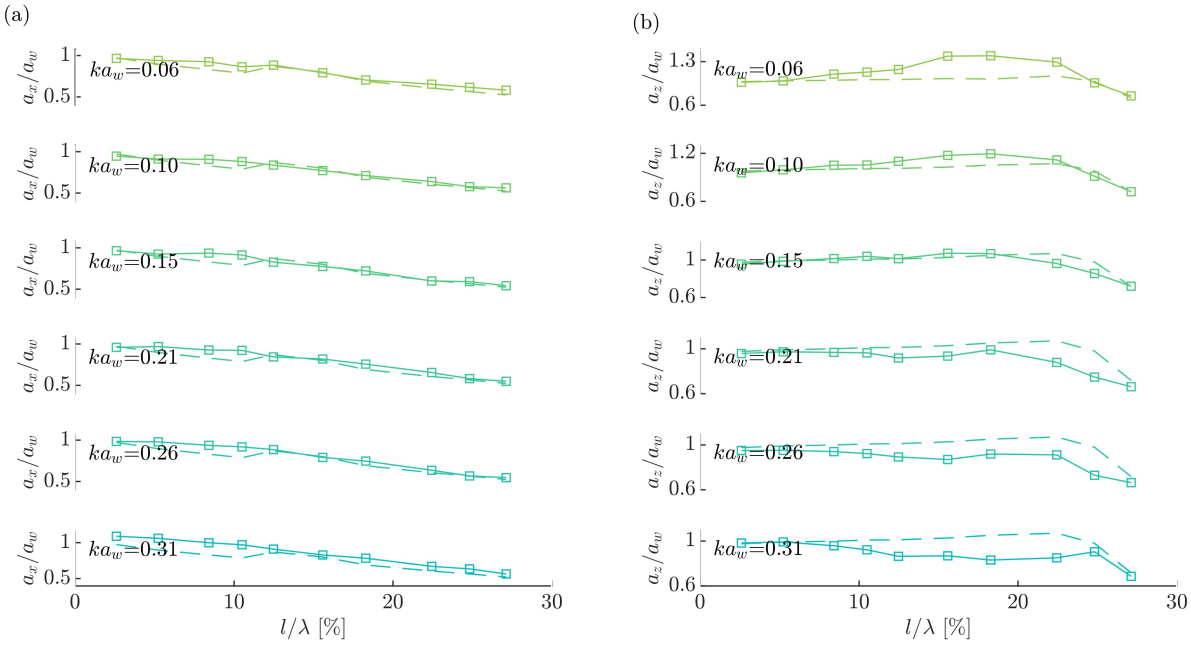


Figure 4.5.9: Comparison of the amplitudes of oscillatory motion for objects of different sizes and in different wave steepness from experiments to results predicted by a linear BEM model. (a) Horizontal oscillatory motion. (b) Vertical oscillatory motion. The motion amplitudes in (a) and (b) are normalised by the incident wave amplitude a_w. Markers connected by continuous lines correspond to the results from experiments, while dashed lines of the same colour are those from BEM simulations.

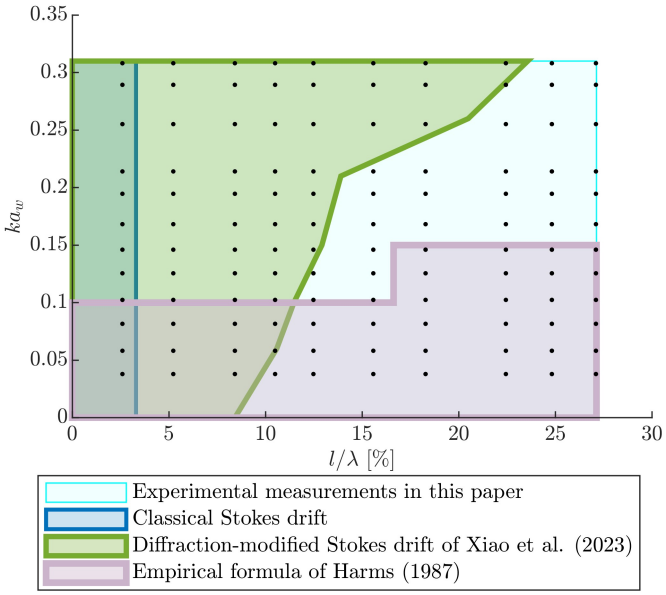


Figure 4.5.10: Domains of validity of the three different models for Stokes object drift within the parameter space covered by experiments in this chapter: the classical Stokes drift for idealised Lagrangian particles (4.1), the diffraction-modified Stokes drift (4.3), and the empirical formula of Harms (1987) (4.4). The black dot represents the experimental data points.

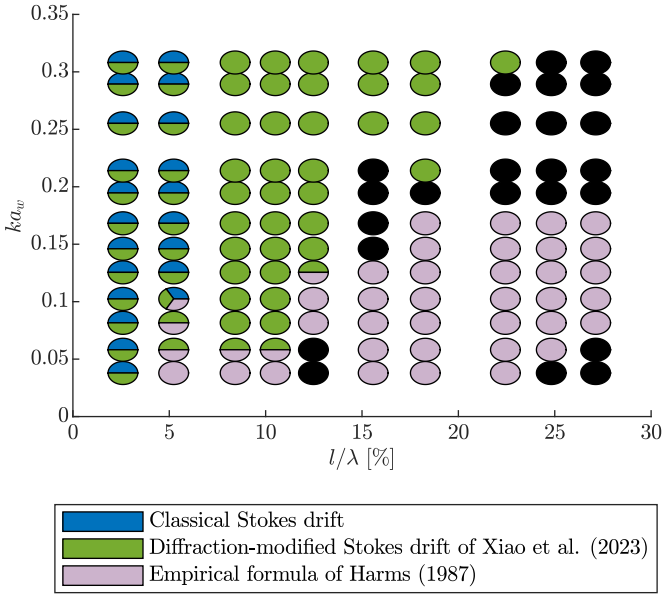


Figure 4.5.11: Domain of validity of the three models compared to the experiments in this chapter. Each circle represents an experiment, with the colour of the filled circle denoting the model(s) that has an error of less than 20% compared to the experiment. The black circle corresponds to an experiment for which none of the three models is able to predict the drift observed in experiments with an error of less than 20%. Blue and green denote the classical Stokes drift and the diffraction-modified Stokes drift, respectively. Purple denotes the empirical formula of Harms (1987) (4.4). A combination of colours within a circle suggests multiple models have an error of less than 20% compared to experiments.

In trying to understand the behaviour of larger objects, an important transition occurs when the ratio of the incident wave period to the natural frequency of heave is of order 1 ($T_w/T_{O,H} = \mathcal{O}(1)$), as previously observed by Harms (1987). Around this point, the vertical oscillatory motion peaks, and the drift behaviour changes from increasing with relative size to decreasing with relative size. For objects that are large enough to diffract the wave field and whose natural period of oscillation is significantly smaller than that of the incident waves, the enhanced drift appears to be primarily caused by the disturbance to the wave field the object causes. Xiao et al. (2024) proposed a diffraction-modified Stokes drift, which appears to capture the drift behaviour well in this regime. Once the object becomes too large ($\sim l/\lambda > 10\%$), the small-parameter assumption underlying the diffraction-modified Stokes drift starts to break down. The domain of validity of the diffraction-modified Stokes drift extends to larger objects for steeper waves, which we attribute to the fact that the drift enhancement amplification $u_{O,S}/u_S$ is greatly reduced (more linear) for high wave steepness, which, somewhat counter-intuitively, extends the range the underlying linear BEM model is valid.

The transition behaviour is related to the behaviour of the objects' natural heave motion. For objects whose natural period of motion is much smaller than the period of the incoming waves, the oscillatory motion of the object change monotonically (vertically increased and horizontally decreased) . The drift increases with object size. The drift enhancement for such objects is attributed by Xiao et al. (2024) to increases in their heave motion and a positive imbalance between the effects of the diffracted and radiated wave fields. For objects whose periods are much larger than those of the incoming waves, the oscillatory motions are greatly reduced (e.g., $l/\lambda = 27.1\%$), and their drift increases with relative size at a slow rate or becomes constant.

The dependence of drift behaviour on wave steepness is found not to be purely quadratic (as predicted by Stokes (1847)) but a mixture of linear and quadratic and changing with relative size. In addition, if the waves are too steep, the linearised BEM model we use to predict diffraction, and thus the diffraction-modified Stokes drift of Xiao et al. (2024), breaks down, and a higher-order model would be needed to predict the diffracted and radiated wave field. The empirical formula of Harms (1987) does well for larger object sizes and small steepness but breaks down for larger steepness. Based on our experimental data, we proposed a new

parameterization that predicts the wave-induced drift as a function of relative size (the ratio of object size to the wavelength) and wave steepness, including linear and quadratic terms.

To improve reliability and accuracy in future experiments, several considerations are recommended: i) Longer flume: a longer flume is needed to accommodate larger object sizes, as larger objects have greater drift velocity and require more distance to travel. ii) Larger sample size with smaller intervals: it is ideal to fix the wave frequency and vary the object size with smaller intervals to ensure enough data points. The current study varies both wave frequency and object size, but focusing the variation of the object size along will improve data consistency. iii) Accurate tank measurements: precise measurement of the tank, especially its width, are critical for designing the object. Consistent width along the tank ensures smooth movement with minimal friction. Variations in width can be detrimental, particularly for smaller objects. Accurate measurements should be conducted initially to minimize iterations in manufacturing the object's size. iv) Controlled lighting. Lighting effect camera capture and data extraction. Due to the influence of the daylight, which cannot be completely blocked by curtains in the current lab, it is recommended to conduct experiments in a location with minimal daylight interference. v) Vorticity observations. Significant vorticity is observed in the tank, especially with larger objects. The effect of vorticity on drift, discussed in Chapter 5, is significant. It is recommended to collect more videos with a larger field of view to allow further study of vorticity effects.

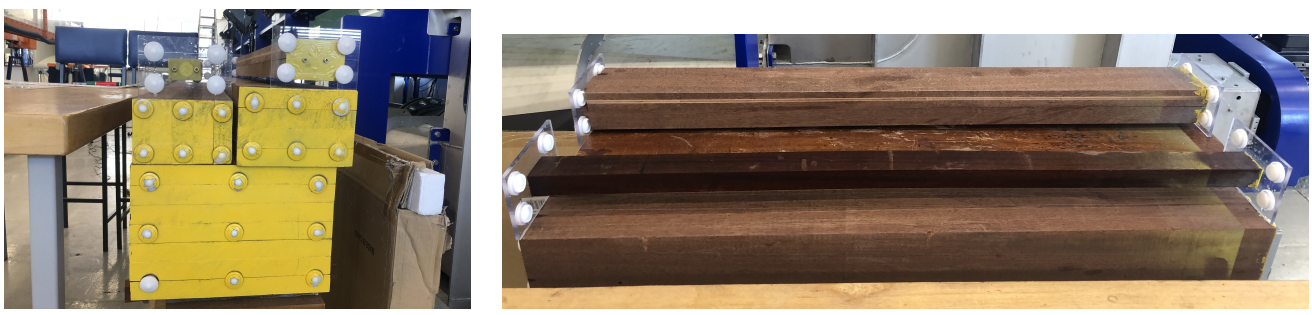
Appendices

4.A Photographs of objects with bearings

Figure 4.A.1 provides side and front views of the objects outside of the water. It shows the yellow-painted ends of the objects, where the bearings are installed.

4.B Measurement error and repeatability

To assess the repeatability of the experiments we present and the precision of the approaches we use to acquire measurements, we performed repeated experiments for four wave steepnesses (ka_w = 0.06, 0.10, 0.20 and 0.32) for each object size l/λ. We conducted 5 repeats for these experiments and present the results in figure 4.B.1, where we show normalised linear oscillatory motions and drift as a function of relative size for different wave steepness. For drift, our experiments demonstrate very small variability for low wave steepness and small objects; variability is larger for high wave steepness and larger objects. We attribute this to two factors. Firstly, the way we conducted the experiment plays a role. For very small objects in low wave steepness,



(a) (b)

Figure 4.A.1: 2D type objects. Left panel (a) is the side view of five objects (painted yellow) installed with bearings. Objects 1, 2, 3, 4, and 5 are shown from left to right, top to bottom. Objects 1 and 2 are designed with 'flange' structure shown in figure 4.3.2. The right panel (b) is the front view of objects.

we limited the object to drift a shorter section of the flume (only the middle two sections, 4 m) instead of allowing it to drift along the entire length. This is because these objects travel very slowly. The objects are thus not subject to any potential variation in conditions along the length of the flume, leading to less variability. On the other hand, for larger objects in high wave steepness, which travel more quickly, for one experiment, we needed to perform 2-3 runs to ensure that we acquired sufficient data for at least 35 wave periods (after reaching a quasi-steady state). This introduces more variability in the measurements. The second factor that contributes to the variability is the repeatability of the waves in the flume, as shown below in figure 4.B.2. The variability of the oscillatory motion appears larger due to the normalization process, where the standard deviation is amplified. Unlike the drift, the relatively large variability of the oscillatory motions occurs primarily in cases with small objects and intermediate wave steepness. Apart from the wave repeatability and ways to conduct the experiment, this is also due to the fact that the larger the object is, the easier it is to capture its bobbing motion using the camera.

We assess the repeatability of the waves in the absence of the object here, to better understand the nature of the uncertainty we observe above. The wave gauges set up are the same as in §4.3.1. We chose four wave steepnesses (ka_w = 0.06, 0.10, 0.20 and 0.32) for each frequency in table 4.3.1. We conducted 5 repeats for each experiment. The mean values of wave amplitude for each wave gauge are calculated, and we use the average value of all 7 gauges as our wave amplitude for one repeat. The measured data is given in figure 4.B.2. The main variability occurs at high wave steepness, and at intermediate wave steepness for a frequency of $f = 1.1$ Hz. This variability is most likely caused by reflections that are not absorbed by the beach. We conclude wave gauge measurements are a small cause of error. We calculate drift velocity by performing a linear regression on the measured trajectories once a steady state is reached. To evaluate how well this works for our measured object trajectories and estimate the uncertainty in the gradient (drift velocity, $\overline{u}_{L,O}$), we report the measurement errors, including the coefficients of determination in table 4.B.1. The quantity $1 - R^2$ increases monotonically with wave steepness. This is expected, as larger wave steepness leads to larger horizontal oscillatory motions of the object, causing deviations from a constant gradient and increasing the uncertainty in the fit. The relative uncertainties for the parameters are all very small with a

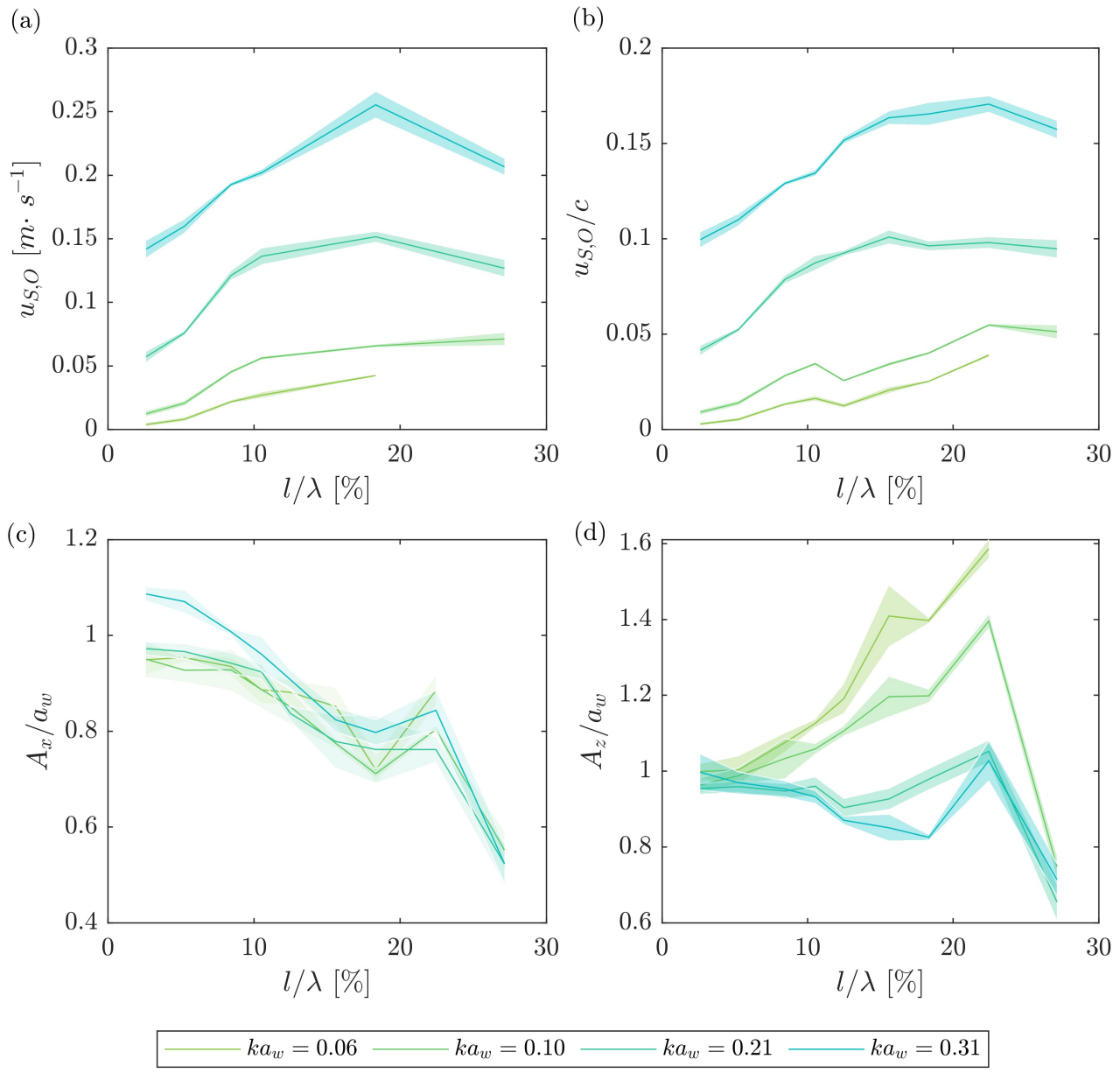


Figure 4.B.1: Uncertainty envelopes as a function of relative size for different wave steepness; (a) Stokes object drift, this data is shown without normalization, and we only plot data for objects with relative sizes of $l/\lambda = 2.6\%$, 5.2%, 8.4%, 10.5%, 18.3% and 27.1%; (b) Celerity-normalised Stokes object drift velocity; (c) Wave-amplitude-normalised magnitude of horizontal motion; (d) Wave-amplitude-normalised magnitude of vertical motion. Mean values, denoted by lines, are obtained using 5 repeat experiments. The error bars, shown as shaded areas, correspond to two standard deviations either side of the mean. The transparency of (c) has been adjusted to make it clearer for overlapping parts.

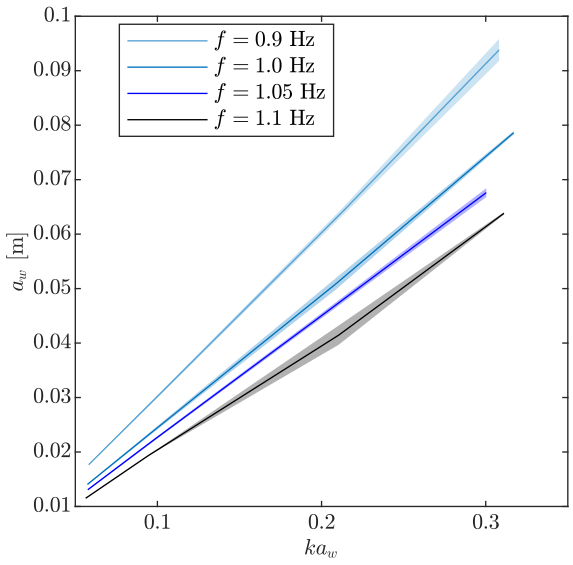


Figure 4.B.2: Uncertainty envelopes of wave amplitude as a function of wave steepness for different wave frequencies. Mean values, denoted by lines, are obtained using 5 repeated experiments. The error bars, shown as shaded areas, correspond to two standard deviations either side of the mean.

maximum value of 1.5%.

4.C A new empirical parametrisation for enhanced Stokes object drift

To quantitatively describe the effects of relative size l/λ and wave steepness $\epsilon = ka_w$ in our experimental observations, we perform the following polynomial regression for the wave

	$l/\lambda = 2.6\%$		$l/\lambda = 12.5\%$		$l/\lambda = 22.4\%$	
ka_w	1-R^2	$\sigma/\overline{u}_{L,O}$	1-R^2	$\sigma/\overline{u}_{L,O}$	1-R^2	$\sigma/\overline{u}_{L,O}$
0.06	0.012	0.0083	0.011	0.0015	0.009	0.0029
0.10	0.023	0.0054	0.015	0.0011	0.014	0.0094
0.21	0.046	0.0056	0.029	0.0140	0.025	0.0067
0.31	0.074	0.0130	0.043	0.0042	0.040	0.0151

Table 4.B.1: Measurement error of the Lagrangian object drift $\overline{u}_{L,O}$ during fitting of the horizontal trajectory for objects with different sizes and in varying wave steepness. We chose three different sizes of objects to report here: $l/\lambda = 2.6\%$ for object 1 in wave $f = 0.9$ Hz; $l/\lambda = 12.5\%$ for object 3 in wave $f = 1.1$ Hz; $l/\lambda = 22.4\%$ for object 5 in wave $f = 1.0$ Hz. $1 - R^2$ refers to the goodness of fit with R^2 the uncertainty in the prediction of the fitted polynomial. σ refers to the standard deviation (uncertainty of the coefficients) of the linear coefficient determination in the fit, and thus $\sigma/\overline{u}_{L,O}$ represents the standard deviation of the fitted linear coefficient.

	$p_{00}[\times 10^{-2}]$	$p_{10}[\times 10^{-2}]$	p_{01}	$p_{20}[\times 10^{-2}]$	$p_{11}[\times 10^{-2}]$	p_{02}	R^2
All terms retained	-3.10 ± 0.40	0.46 ± 0.04	0.14 ± 0.04	-0.01 ± 0.00	0.40 ± 0.09	0.80 ± 0.09	0.98
$p_{00}=0$	-	0.26 ± 0.03	-0.07 ± 0.03	-0.00 ± 0.00	0.79 ± 0.09	1.19 ± 0.10	0.97
$p_{00}=0$, $p_{20}=0$	-	0.08 ± 0.02	0.03 ± 0.03	-	0.60 ± 0.10	1.00 ± 0.10	0.96

Table 4.C.1: Coefficients of the regression of wave-celerity normalised Stokes object drift $u_{S,O}/c$ on wave steepness $\epsilon = ka_w$ given by (4.8). The error bounds represent $\pm$ one standard deviation of the coefficients, and R^2 is the coefficient of determination.

celerity-normalised Stokes object drift $u_{S,O}/c$:

$$u_{S,O}/c = p_{00} + p_{10}\left(\frac{l}{\lambda}\right) + p_{01}\epsilon + p_{20}\left(\frac{l}{\lambda}\right)^2 + p_{11}\left(\frac{l}{\lambda}\right)\epsilon + p_{02}\epsilon^2. \tag{4.8}$$

where p_{00}, p_{10}, p_{01}, p_{11}, and p_{02} are the coefficients to be determined.

We consider cases with all terms retained as well as those with several terms set to zero. Table 4.C.1 shows the coefficient values obtained from the regression with 95% confidence bounds. To ensure independence between the covariates, which were varied independently in our experimental matrix, we have also estimated the population Pearson correlation between relative size l/λ and wave steepness ϵ, finding very small sample correlation coefficient $O(10^{-18})$. There is clear evidence that the Stokes object drift is dependent on both linear and quadratic terms in wave steepness (ϵ and ϵ^2); the coefficient on the quadratic term is the most significant followed by the linear term. Ideally, if both the wave steepness and relative size of the object are 0, the drift should be zero, so we set $p_{00} = 0$. The fact that this (setting $p_{00} = 0$) significantly changes the regression coefficients suggests that the simplified combination of linear and a quadratic terms has limitations. The quadratic term in l/λ is insignificant, and we set it to zero ($p_{02} = 0$). We thus propose the simplified relationship:

$$u_{S,O}/c = 0.0008\left(\frac{l}{\lambda}\right) + 0.03\epsilon + 0.0060\left(\frac{l}{\lambda}\right)\epsilon + 1.0\epsilon^2. \tag{4.9}$$

This simplified model provides a reasonably accurate representation of the wave celerity-normalised Stokes object drift in terms of relative size and wave steepness, with the most significant contributions coming from the linear and quadratic terms of wave steepness.

Chapter 5

Vorticity and turbulent effects on mean drift of bluff bodies

5.1 Abstract

Under the influence of surface gravity waves, a floating object experiences a drift in addition to its oscillatory motion. Due to its inertia, both the object's oscillatory motion and its drift will experience a deviation from that of a fluid particle, with the drift of the object typically exceeding the Stokes drift of a fluid particle. This study uses two-dimensional numerical simulations to examine the drift of floating objects in unidirectional, regular, deep-water waves. We investigate the effects of vorticity and turbulence induced by different shapes of objects. We consider two corner shapes: sharp and round. We investigate object sizes ranging from 1% to 10% of the wavelength. Three types of (two dimensional) numerical simulations are performed to explore the roles played by viscosity and turbulence: simulations based on the Reynolds-averaged Navier–Stokes equations (RANS), viscid simulations using the Navier–Stokes equations, and inviscid simulations solving the Euler equations. The Reynolds numbers of this study range from 6.0 to 8.0×10^4 and Keulegan–Carpenter (KC) numbers range from 0.22 to 0.87. Objects smaller than 4% of the wavelength are predicted to have a drift equal to the Stokes drift for both corner shapes. As size increases, objects with sharp corners exhibit greater drift enhancement compared to round-cornered objects of equivalent size (we report a 454% increase for a sharp-cornered box and 134% increase compared to the Stokes drift for a round-cornered object, both with an object size of 10% of the wavelength). In addition to

differences in diffraction patterns and phase differences in the linear motion between objects of two different shapes, a new mechanism for drift enhancement, which is caused by the vorticity generated by the sharp corners, has been identified. The vorticity that arises due to the sharp corners is asymmetrically distributed between the two sides of the object, leading to a non-symmetric dynamic pressure field and thereby mean horizontal forces in the direction of wave propagation. The influence of viscosity and turbulence on drift is explored. Viscosity is found to play a dual role. On the one hand, it induces a phase difference in the linear motion and thus increases the drift. On the other hand, viscosity reduces vorticity and thereby decreases the drift enhancement. Finally, we define an unsteadiness ratio of object drift to examine the effect of non-zero acceleration, revealing a correlation between unsteadiness and drift enhancement.

5.2 Introduction

Flow around a bluff body is a topic that has attracted considerable interest and has been extensively explored in various engineering applications over many decades. Bluff-bodied structures, including skyscrapers, bridges, wind turbines and (floating) ocean platforms etc., are surrounded by highly unsteady flow fields, characterised by phenomena such as flow separation, shear-layer instability, and vortex shedding and reattachment. These phenomena not only impact the aerodynamic/hydrodynamic characteristics of the structure but also affect the forces and motions experienced by them. Pioneering work on the flow around square cylinders (i.e., a three-dimensional geometric shape that has a square base and top, and its side faces are rectangles) was conducted by Roshko (1952); Lyn et al. (1995); Wiliamson (1996), who investigated vortex shedding and the properties of the turbulent flow. More recently, researchers such as Yoon et al. (2010); Yen and Yang (2011); Chen and Xia (2017) performed numerical and experimental studies to explore different flow patterns, including flow separation, vortex formation and reattachment, across various Reynolds numbers and their effects on flow-induced forces.

Much effort has been made to investigate the influence of different cross-sectional shapes and corner radii on flow features and flow-induced loads. Delany and Sorensen (1953) carried out an experimental study for different cross-sectional shapes, including rectangular, elliptical, and diamond shapes, with different corner radii, and explored the corresponding variation in drag

coefficients for different Reynolds numbers. For Reynolds numbers of 10^5, the drag coefficient remains essentially constant or decreases with an increase of the corner radius. Bearman et al. (1984) presented experimental measurements using U-tube water tunnel and investigated the effects of corner radius on hydrodynamic forces and loads on bluff bodies with Reynolds numbers ranging from 200 to 2×10^4 and Keulegan–Carpenter (KC) numbers ranging from 1 to 100. They reported that sharp-cornered bodies experience flow separation at lower KC values compared to of circular shapes, and the drag coefficient is reduced with increasing corner rounding, especially at relatively high KC numbers. This reduction is more evident in oscillatory flow than in steady flow and is highly sensitive to the corner radius.

Tamura et al. (1998) used a CFD (Computational Fluid Dynamic) model without incorporating a turbulence model to investigate the relationship between flow structure, vortex formation, and unsteady pressure. They explored various corner shapes (e.g., sharp corners, chamfered corners, and round corners) and compared their numerical simulations with experimental measurements. Tamura et al. (1998) found that slight changes in corner shape could drastically modify the pressure distribution on the rectangular cylinder (i.e., a three-dimensional geometric shape that has a rectangular base and top, and its side faces are rectangles) surface and affect drag. The effect of corner modification on forces on the object in different turbulent flows was investigated further in experiments by Tamura and Miyagi (1999). They explained that decreased drag arose due to rounding of the corners as a result of different separation patterns and extents of reattachment. Hu et al. (2006) put their focus on the near-wake structure and experimentally investigated the influence of different corner radii. They found that an increase in the corner radius leads to a decrease in vortex-shedding strength and vortex-relevant circulation. Sharp-cornered structures exhibit a lower quasi-periodic vortex-shedding frequency than other objects. Moreover, Hu et al. (2006) emphasized that the leading-edge corner radius is most important, as it determines to a great extent the behaviour of streamlines, separation angle, pressure on the base of the object, and near-wake structure.

Liang et al. (2016) used Detached Eddy Simulation to simulate the vortex-induced motions of four square cylinders in uniform flow and compared the results with experiments. The cross-sectional shapes of their cylinders were all diamonds with small round-corner radii. They found that the flow characteristics around the downstream cylinders are strongly affected by

the vortices induced by the upstream cylinders.

Despite extensive research on bluff bodies in steady or unsteady flows described above, none of the above studies considered the presence of a free surface. However, for problems involving structures such as hydrofoils, offshore platforms, wave energy converters, and other surface-piercing objects, the presence of a free surface introduces additional complexity, such as the generation of waves and their interaction with boundary layers, vortices and bubbles. The effects of the free surface and the surface waves generated for surface-piercing cylinders have been studied by several authors (Inoue et al., 1993; Kawamura et al., 2002; Lin and Li, 2003). These authors found that the strength and frequency of vortex shedding are reduced, while a different instability mechanism with more random fluctuations of higher frequency dominates in the region near the surface. Kandasamy et al. (2005) employed Reynolds-averaged Navier–Stokes (RANS) simulations with complementary experiments to investigate the unsteady flow pattern of free surface wave-induced separation for two different Froude numbers. They found that the formation of shear-layer vortices is also impeded by the presence of the free surface. However, it is important to note that the water surface in those studies is initially calm without waves, and waves are only induced by the motion of the object as the fluid flows past the object.

In the ocean environment, structures often encounter both a mean flow and free surface waves. Wave run-up around surface-piercing cylinders has been extensively explored both numerically and experimentally (Stansberg and Nielsen, 2001; Stansberg and Kristiansen, 2005; Stansberg et al., 2005; Danmeier et al., 2008; Huang et al., 2008; Bøckmann et al., 2014). Recently, Yoon et al. (2016); Mohseni et al. (2018) have conducted unsteady RANS simulations of wave run-up on surface-piercing cylinders in regular waves of different wavelengths and wave steepnesses. They found that, compared to wave steepness, wavelength (relative to object size) is the major factor influencing wave-induced loads. Longer waves are more prone to developing vortex shedding, and the size of the vortices is highly related to the KC number. Moreover, the difference in the velocity direction between the crest and the trough disturbs the regular structure of the vortex shedding, especially in low-KC cases. Moradi et al. (2015) simulated wave-induced fluid-flow resonance in narrow gaps between two fixed surface-piercing bodies over a variety of incident wave frequencies and evaluated the effects of geometry properties (e.g., different corner shapes) of the object on gap-resonance characteristic. They showed that

changes in corner shape significantly affect the wave elevation in the gap during resonance by altering the amount of water trapped in the gap. For sharp-cornered objects, the wave height during resonance reduces significantly due to large-scale vortex structure and kinetic energy dissipation.

Vortical structures observed in simulations using the VOF-RANS model of Palm et al. (2016) are similar across different wave periods, and no wake was found. According to Palm et al. (2018), vorticity generated in the flow modifies the driving wave pressure distribution and can cause separation, resulting in a reduction of wave force amplitude. Palm et al. (2018) found that for geometries with sharp edges (e.g., sharp-cornered objects), regions of sharp pressure gradients induce drag that is dominated by geometrically induced vorticity, while viscosity plays a less important role.

Despite extensive research on the effects of vorticity and turbulence on surface-piercing objects that are either fixed or moored in flows with waves, relatively little work has been done for freely floating objects, which typically undergo net drift in the direction of wave propagation. For an idealized fluid parcel in a flow without Eulerian mean current, this drift is equal to Stokes drift (Stokes, 1847). Since Stokes first described this drift, now 177 years ago, it has been widely explored in experimental and theoretical studies (see van den Bremer and Breivik (2018) for a review). However, as Stokes drift is derived for an idealized fluid particle based on ideal fluid and irrotational flow assumptions, it may not accurately predict the drift of a freely floating object in the real ocean. Ignoring the Earth's rotation, which becomes relevant only for large spatial and temporal scales, there are four main factors affecting the drift. First, wave breaking has been shown to increase drift at the wave surface compared to non-breaking waves and may alter Lagrangian transport in realistic wave fields (Deike et al., 2017b; Sinnis et al., 2021; Eeltink et al., 2023). Second, the presence of viscosity may lead to additional drift due to velocity streaming within the boundary layer beneath the water surface (Longuet-Higgins, 1953; Grue and Kolaas, 2017; van den Bremer et al., 2019). Vorticity from the boundary layers may be transported or diffused into the interior of the fluid, affecting the transport of particles (Longuet-Higgins, 1953). Third, inertial objects of non-negligible size exhibit non-Lagrangian drift behaviour (Calvert et al., 2021; DiBenedetto et al., 2022). Drift enhancement for inertial objects has been found for objects with sizes larger than several percent of the wavelenghth

and such enhancement can vary depending on the objects' shape (Calvert et al., 2021). Fourth, diffraction effects caused by the presence of objects can induce drift enhancement for relatively larger objects. Xiao et al. (2024) introduced a diffraction-modified Stokes drift to predict the enhanced drift resulting from object diffraction. They observed that the drift enhancement is closely linked to a standing wave pattern generated by wave diffraction. Previous chapters have explored the effects of size, shape, wave steepness and viscosity on an objects's drift. However, the object's shape was chosen there to avoid the generation of vorticity due to sharp gradients of the geometry, that is, sharp corners.

This chapter aims to investigate the effects of vorticity and turbulence induced by the geometry of the object along with the effects of viscosity on the forces and mean drift velocity of freely floating objects of different sizes and for different wave steepnesses. The geometry of the object is varied by considering different corner shapes. Velocity and pressure fields, as well as vortex structures, are analysed. We use the two-dimensional hybrid numerical model, QaleFOAM (Li et al., 2018; Yan et al., 2019; Gong et al., 2020), and conduct three types of simulations for each case: RANS simulations, viscid simulations, and inviscid simulations to investigate the effects of viscosity and turbulence. The KC numbers in this study are over a small range with a small value. We report significant differences in the mean drift of relatively large objects with sharp corners compared to round-cornered objects.

5.3 Numerical model

The hybrid numerical model QaleFOAM is employed in this chapter; it is based on a domain-decomposition method and couples a fully nonlinear potential-flow solver with a two-phase incompressible Navier–Stokes (NS) solver. The region of interest, typically near the object and referred to as the NS domain, encompasses small-scale complex physics and is modelled using the two-phase incompressible InterDyMFoam solver available within OpenFOAM. This solver employs the Volume of Fluid (VOF) method to discern the interface between two fluids. Conversely, the larger region, termed the Qale-FEM domain, is used to simulate wave propagation and evolution and employs the Qale-FEM (Quasi Arbitrary Lagrangian-Eulerian Finite Element Method) potential-flow solver. One-way coupling scheme is adopted, in which the QaleFEM solver provides wave solutions to the InterDyMFoam solver at the coupling inter-

Boundary \ Variable	α	p	$\mathbf{u}$
Inlet	Coupled	$fixedFluxPressure$	Coupled
Outlet	Coupled	$fixedFluxPressure$	Coupled
Bottom	$zeroGradient$	$zeroGradient$	$slip$
Atmosphere	$inletOutlet$	$totalPressure$	$pressureInletOutletVelocity$
Body surface	$zeroGradient$	$fixedFluxPressure$	$movingWallVelocity/noSlip/slip$

Table 5.3.1: Setup of boundary conditions for different variables in our numerical simulations. α is the volume phase fraction, p represents the pressure and $\mathbf{u}$ denotes the velocity field. The conditions in italics are the standard conditions available in the OpenFOAM platform and the 'Coupled' conditions represent the boundary conditions that are coupled with the QaleFEM solver. The boundary conditions, as described in the OpenFOAM official user guide and manual, are as follows: '$inletOutlet$' serves as a generic outflow condition, allowing for specified inflow when there is return flow; '$totalPressure$' establishes a total pressure condition; '$fixedFluxPressure$' sets the pressure gradient to a provided value such that the flux on the boundary matches the specified velocity boundary condition; '$pressureInletOutletVelocity$' is a velocity inlet/outlet boundary condition applied to pressure boundaries where pressure is specified. For outflow, a zero-gradient condition is applied based on the flux, while for inflow, the velocity is determined from the patch-face normal component of the internal-cell value; '$slip$' refers to a no-flow, free-slip condition ($slip$); '$noSlip$' restrains velocity to zero at walls; '$movingWallVelocity$' provides a velocity value for moving walls; For the body surface, we use three different types of velocity boundary conditions for different types of simulations: $movingWallVelocity$ is used for the moving object cases (for both viscous and inviscid simulations), $noSlip$ is used for the stationary object cases in the viscous simulation, and $slip$ is used for inviscid simulation of the stationary object cases.

faces but does not feed any solutions back. Wave generation and absorption are implemented within the QaleFOAM solver with wave absorbers deployed at the interfaces of the two models to manage reflected and radiated waves. Given the two-dimensional nature of the calculations, the front and back boundaries of the NS model are turned off. For further details of the QaleFOAM solver, readers are referred to Li et al. (2018); Yan et al. (2019); Gong et al. (2020) and related references therein.

In the InterDyMFoam solver, there are inlet, outlet, bottom, atmosphere, and body surface boundaries over which we need to define the boundary conditions (BC) for the variables we compute: volume phase fraction α, pressure p and velocity $\mathbf{u} = (u, w)$. The detailed boundary condition types are given in table 5.3.1, where a no-flow, free-slip condition ($slip$) is used for the bottom, as we study waves in deep water. Following Moradi et al. (2015), we use the divergence scheme $GaussMUSCL$ for the advection term in the momentum equation. The discretization schemes that we use in our model are listed in table 5.3.2. The $PIMPLE$ algorithm is used

Terms	Symbol	Setup in OpenFOAM	Schemes
Temporal	$\partial/\partial t$	ddtSchemes	$CrankNicolson0.9$
Gradient terms	∇	gradSchemes	$cellMDLimitedGausslinear1$
Momentum advection term	$\nabla \cdot (\rho\phi\mathbf{u})$	div(rhoPhi,U)	$GaussMUSCL$
Phase fraction-related terms	$\nabla \cdot (\phi\alpha)$	div(phi,alpha)	$GaussvanLeer$
	$\nabla \cdot (\phi_{rb}\alpha)$	div(phirb,alpha)	$Gaussinterface Compression/Gausslinear$
Turbulence modelling-related terms	$\nabla \cdot (\phi k)$	div(phi,k)	$GausslinearUpwindlimitedGrad$
	$\nabla \cdot (\phi\omega)$	div(phi,omega)	$GausslinearUpwindlimitedGrad$
Viscosity term	$\nabla \cdot \mu_{eff}\nabla\mathbf{u}$	div((muEff*dev(T(grad(U)))))	$Gausslinear$
Diffusive terms	$\nabla \cdot (\nabla)$	laplacianSchemes	$Gausslinearcorrected$

Table 5.3.2: Discretization schemes used in our numerical simulations, where $t, \mathbf{u}$ refers to time and velocity, respectively; μ_{eff} is the effective dynamic viscosity, which encompasses both the molecular dynamic viscosity and the turbulent viscosity. ϕ refers to the mass flux; for incompressible fluid, it is replaced by velocity. α is the volume fraction and α_{rb} is related to an artificial compression term. Turbulent modelling-related terms refer to the convection terms of turbulent kinetic energy (TKE) k_e and the specific rate of dissipation ω in RANS modelling. The column 'Setup in OpenFOAM' corresponding to the terms used in $fvSchemes$ (a setup file name) in OpenFOAM simulation cases. The schemes in italics are standard schemes available in OpenFOAM.

for velocity-pressure coupling. We use an adjustable time step controlled by the maximum Courant number $\mathrm{Co} = \frac{\Delta t|\mathbf{u}|}{\Delta x}$, in which $|\mathbf{u}|$ refers to the absolute velocity in the flow, and Δt and Δx are the time and space resolutions, respectively. The maximum Courant number is given by $\mathrm{Co} = 0.25$. The effect of surface tension is ignored in all our simulations.

This chapter involves three types of simulations: RANS simulations, viscid simulations and inviscid simulations. In the Reynolds averaged Navier–Stokes (RANs) simulations, following Yu and Li (2013); Li et al. (2018), we use k–ω SST turbulence model. Due to the importance of accurately predicting forces for evaluating drift, we use a wall-resolving treatment for near-wall regions. As required by the wall-resolving treatment, the boundary conditions on the body surface are set as follows: the kinetic turbulent energy k is initialized with a very small value 1.0×10^{-12} with the boundary condition set as the $fixedValue$ type; the turbulent viscosity ν_t is $calculated$ with an initial value 0 and the turbulent specific dissipation rate ω is initialized using a $fixedValue$ condition with a value calculated by $\omega = \frac{60\nu}{0.075y^2}$, in which y is the distance to the first cell centre normal to the wall. We have conducted sensitivity tests of different boundary conditions for wall conditions (including of low-Reynolds number wall functions and of high-low Reynolds number blended wall functions) with various initial values. However, these tests have shown little impact on the results, as our near-wall mesh is sufficiently fine, ensuring that the non-dimensional wall distance $y^+ < 1$ and the first-layer wall cell is always located in the viscous sublayer. Viscid simulations solve the incompressible Navier–Stokes equations without

any turbulence model. Inviscid simulations are based on incompressible Euler equations, which are compared with viscous results (RANS and viscid Navier–Stokes simulations) to identify and quantify the effects of viscosity. Although inviscid simulations do not include viscosity, they support flow rotation (i.e., vorticity). Despite their inability to model boundary layer separation effects due to the absence of near-wall shear stress, Euler equations are widely used to study the vorticity generated in regions with high pressure and velocity gradients such as those induced by high wall curvature (Spalart, 1998; Yang et al., 2007; Palm et al., 2018). This geometrically induced vorticity is inherently triggered by the numerical viscosity from the discretisation.

In the present chapter, we investigate the flow dynamics around a 2D bluff body on water surface with incoming waves in the absence of current. We have two types of objects: stationary objects and moving objects. To better characterize our problem, we introduce the particle Reynolds number (Re), which is different from the Reynolds number of the flow itself, and Keulegan–Carpenter (KC) number separately for each type of object. For moving objects, we follow Xiao et al. (2024) and define a particle Reynolds number by using the characteristic length of the object, denoted as l (equal to the length of the object), and the horizontal velocity difference between the object and the fluid: particle $\mathrm{Re}_x = |u_{o,x} - u_{f,x}|l/\nu$. Here, $u_{o,x}$ and $u_{f,x}$ denote the magnitudes of the horizontal velocities of the object and the fluid, respectively, and ν is the kinematic viscosity of the fluid. We estimate $u_{f,x} = a_w\omega e^{(-kh_d)}$ and $u_{o,x} = A_x\omega$, where a_w is the wave amplitude, ω is the wave angular frequency, k is the wave number, h_d is the submergence (draft) of the object and A_x is the magnitude of the horizontal oscillatory motion of the object. The KC number is defined as KC$= |u_{o,z} - u_{f,z}|T_w/h_d$, where $u_{o,z}$ and $u_{f,z}$ denote the magnitude of the vertical velocity of the object and the fluid, respectively, and $T_w = 2\pi/\omega$ is the wave period. We estimate $u_{f,z} = a_w\omega e^{(-kh_d)}$ and $u_{o,z} = A_z\omega$, where A_z is the magnitude of the vertical oscillatory motion of the object. For stationary object, the particle Reynolds and KC numbers are obtained by setting $u_{o,x} = 0$ and $u_{o,z} = 0$, since the object is stationary. The Reynolds number measures the ratio of inertial forces to viscous forces, with laminar flow dominating at low Reynolds numbers and turbulent flow at high Reynolds numbers, which thereby helps predict the flow patterns and vortex structures. On the other hand, the KC number describes the relative importance of drag forces compared to inertial forces. A small

KC number suggests inertia dominates, while a large KC number indicates the drag forces that are more important. The KC number can be interpreted as the ratio of the travel distance of fluid particles to the length of the object, thus indicating the likelihood of boundary-layer separation.

5.4 Convergence study for stationary objects

A convergence study and grid dependency analysis are conducted for both the InterDyMFoam solver and QaleFEM solver, but only the results of the InterDyMFoam NS solver are presented in this chapter, as discretization error is typically the main source of errors in CFD solvers. The meshing in the NS domain is constructed using blockMesh and snappyhexMesh with refinement near the object and the free surface. The aspect ratio of the mesh near the object is set to 1. Near the surface, the addlayer in snappyHexmesh is typically set to 6 or 10, and the surface refinement level is set to 2. RefinewallLayer is used in some cases to further refine the mesh near the wall. The convergence study is carried out for the stationary object with the largest objects of size $l/\lambda = 10\%$, subjected to waves with the low wave steepness $ka_w = 0.034$ as well as the highest wave steepness $ka_w = 0.09$ where k is the wave number and a_w is the wave amplitude. We include low wave steepness because it represents the main wave steepness in our later explorations. When the object is stationary, the relative velocity between the object and the flow is larger and the flow is more turbulent than for the moving objects (both particle Reynolds number Re and Keulegan–Carpenter number KC are therefore higher). That is to say, for stationary cases, it is more challenging to achieve convergence.

We use three sets of solutions: Mesh 1 (M1, most refined), Mesh 2 (M2, moderately refined) and Mesh 3 (M3, coarse) for the RANS simulation, while viscid simulations use only Mesh 1. Table 5.4.1 and 5.4.2 summarize the specific parameters associated with each mesh, along with the corresponding simulation results. The horizontal mesh resolution Δx is given in a range to reflect its gradual refinement closer to the object. The mesh in the region extending $2l$ ($\pm l$) (where l is the length of the object) from the object is uniform, with the smallest horizontal resolution indicated in the table. The non-dimensional wall distance y^+ over the object's surface is used to evaluate the near-wall mesh refinement. Convergence is evaluated based on the magnitude of surface elevations at points located $0.0155l$ from the object's front

Simulation	Mesh	N_c	$\lambda/\Delta x$	$l/\Delta x$	$a_w/\Delta z$	$\Delta_{\min}$ (m)	$\overline{y}^+$	Front (a/a_w)	Back (a/a_w)	F'_x	F'_z
Viscid	M1	1.15M	185-7385	738	40	1.06×10^{-4}	0.37	1.74	0.59	2.02	1.00
RANS	M1	1.15M	185-7385	738	40	1.06×10^{-4}	0.35	1.75	0.57	2.03	1.03
	M2	0.69M	185-3693	369	20	2.11×10^{-4}	0.74	1.76	0.57	2.08	1.05
	M3	0.35M	185-1846	185	10	9.48×10^{-4}	2.77	1.92	0.55	2.24	1.11

Table 5.4.1: Convergence test for low wave steepness ($ka_w = 0.034$), conducted at particle $\mathrm{Re} = 1.97 \times 10^4$, $\mathrm{KC} = 0.33$. The mesh refinement is reduced in the order M1, M2, M3 with M3 being the most coarse mesh. N_c is the total number of cells in the mesh with the unit 'M' representing million. λ and l represent the wavelength and size of the object, respectively. Δx and Δz indicate the horizontal and vertical mesh sizes, while $\Delta_{\min}$ represents the smallest mesh size near the object surface. $\overline{y}^+$ is the time-averaged value of the average y^+ over the body surface. a represents the local wave amplitude of the sampled location. The sample location of 'Front' and 'Back' are chosen from the distance $0.0155l$ away from the front and back side of the object. F_x and F_z are the magnitudes of the oscillatory parts of the horizontal and vertical forces, which are made non-dimensional as $F'_x = F_x/(\rho g a_w l^2/4)$ and $F'_z = F_z/(\rho g a_w l^2/4)$, respectively.

and back, as well as the forces in both directions. The magnitudes of these physical quantities are determined by averaging the signals over time after $t = 21T_w$ (where T_w represents the wave period), corresponding to the time that a quasi-steady state is achieved. The first and second harmonic amplitudes of the quantities are computed using the Fast Fourier Transform (FFT) of the respective signals. Following the methodologies outlined by Stern et al. (2001); Mohseni et al. (2018), the convergence study analysis is carried out focusing on the first harmonic quantities. The convergence condition is indicated by the convergence ratio $R = \dot{\varepsilon}_{21}/\dot{\varepsilon}_{32}$, in which $\dot{\varepsilon}_{ij} = \varphi_i - \varphi_j$ denotes changes to the solutions between Mesh i and Mesh j, with φ being the simulation result for any physical quantity of interest. For three sets of mesh, monotonic convergence is achieved when $R \in (0, 1)$ (which is true in our cases), allowing for error estimation and uncertainty assessment through generalized Richardson Extrapolation (RE) (Liu et al., 2020). If we define the refine ratio of the i-th mesh to j-th mesh as $\dot{r}_{ij} = \Delta_i/\Delta_j$, in which $\Delta = \Delta x = \Delta z$ is the mesh resolution on the free surface, then in both wave steepness cases, $\dot{r}_{21} = \dot{r}_{32} = 2$. The order of accuracy $\dot{m}$ for a constant refinement mesh ratio could be obtained by (Roache, 1994):

$$\dot{m} = \frac{\ln(\dot{\varepsilon}_{32}/\dot{\varepsilon}_{21})}{\ln(\dot{r})}. \tag{5.1}$$

Additionally, for a standard three-grid convergence study with an error estimated from RE, the Grid Convergence Index (GCI) approach is used with a safety factor F_S to indicate the

Simulation	Mesh	N_c	$\lambda/\Delta x$	$l/\Delta x$	$a_w/\Delta z$	$\Delta_{\min}$ (m)	$\overline{y}^+$	Front (a/a_w)	Back (a/a_w)	F'_x	F'_z
Viscid	M1	1.04M	185-7385	738	106	1.05×10^{-4}	0.87	1.74	0.61	1.96	1.06
RANS	M1	1.04M	185-7385	738	106	1.05×10^{-4}	0.87	1.70	0.60	1.97	1.04
	M2	0.69M	185-3693	369	53	2.11×10^{-4}	1.81	1.71	0.60	1.97	1.04
	M3	0.35M	185-1846	185	27	4.47×10^{-4}	3.51	1.72	0.62	1.98	1.03

Table 5.4.2: Convergence test for the highest wave steepness ($ka_w = 0.09$) conducted at particle Re = 8.0^4, KC = 0.87. Mesh refinement is reduced in the order M1, M2, M3 with M3 being the most coarse mesh. N_c is the total number of cells in the mesh with the unit 'M' representing a million. λ and l are the wavelength and size of the object, respectively. Δx and Δz is the horizontal and vertical mesh sizes, while Δ_{min} represents the smallest mesh size near the object surface. $\overline{y}^+$ denotes the time-averaged value of the average y^+ over the body surface. a represents the local wave amplitude of the sampled location. The sample location of 'Front' and 'Back' are chosen from the distance $0.0155l$ away from the front and back side of the object. F_x and F_z are the magnitudes of oscillatory parts of the horizontal and vertical forces, which are made non-dimensional as $F'_x = F_x/(\rho g a_w l^2/4)$ and $F'_z = F_z/(\rho g a_w l^2/4)$, respectively.

Parameter	Front (a/a_w)	Back (a/a_w)	F'_{px}	F'_{pz}	F'_{vx}	F'_{vz}
M1	1.75	0.57	2.04	1.02	2.16×10^{-3}	2.02×10^{-3}
M2	1.76	0.57	2.09	1.03	2.16×10^{-3}	1.97×10^{-3}
M3	1.92	0.55	2.24	1.08	2.44×10^{-3}	1.47×10^{-3}
$\dot{\varepsilon}_{21}$	0.01	-2.33×10^{-4}	0.05	0.01	5.01×10^{-6}	-4.82×10^{-5}
$\dot{\varepsilon}_{32}$	0.16	-0.02	0.15	0.05	2.73×10^{-4}	-5.02×10^{-4}
R	0.06	0.01	0.33	0.29	0.02	0.10
$\dot{m}$	4.18	6.46	1.62	1.81	5.77	3.38
GCI_{21} [%]	1.09	0.03	6.24	1.65	6.26×10^{-4}	6.02×10^{-3}
GCI_{32} [%]	19.67	2.57	19.19	5.75	3.41×10^{-2}	6.27×10^{-2}

Table 5.4.3: Convergence statistics of normalized first-harmonic components of target quantities for low wave steepness $ka_w = 0.034$ with particle Re = 3.01×10^4, KC = 0.34. F_{px} and F_{pz} are the magnitudes of the first-harmonics parts of the pressure forces in horizontal and vertical directions, respectively, and F_{vx} and F_{vz} are the magnitudes of the first-harmonics parts of the viscous forces in horizontal and vertical directions, respectively. All these forces shown with its non-dimensional form at the table are normalized by $F' = F/(\rho g a_w l^2/4)$.

uncertainty of the error estimate:

$$\mathrm{GCI}_{ij} = F_S \frac{|\varepsilon_{ij}|}{\dot{r}_{ij} - 1}. \tag{5.2}$$

The results from this convergence analysis are detailed in tables 5.4.3 and 5.4.4, where $F_S = 1.25$ for a minimum of three grids (Roache, 1994).

It is evident that for both the low- and high- wave steepness cases, overall, satisfactory convergence has been achieved for the quantities of interest, with minimal changes to the solution observed, particularly between Mesh 1 and Mesh 2. Analysis of the first-harmonic

Parameter	Front (a/a_w)	Back (a/a_w)	F'_{px}	F'_{pz}	F'_{vx}	F'_{vz}
M1	1.73	0.53	1.99	0.96	2.26×10^{-3}	2.46×10^{-3}
M2	1.73	0.53	2.00	0.96	2.13×10^{-3}	2.32×10^{-3}
M3	1.75	0.55	2.00	0.96	1.79×10^{-3}	1.72×10^{-3}
$\dot{\varepsilon}_{21}$	3.42×10^{-3}	3.84×10^{-3}	3.95×10^{-4}	-1.77×10^{-4}	-1.29×10^{-4}	-1.36×10^{-4}
$\dot{\varepsilon}_{32}$	1.40×10^{-2}	1.78×10^{-2}	2.19×10^{-3}	-4.81×10^{-3}	-3.40×10^{-4}	-6.02×10^{-4}
R	0.24	0.22	0.18	0.04	0.38	0.23
$\dot{m}$	2.04	2.21	2.47	4.77	1.40	2.15
GCI_{21} [%]	4.27×10^{-3}	4.81×10^{-3}	0.05	0.02	0.02	0.02
GCI_{32} [%]	0.02	0.02	0.27	0.60	0.04	0.08

Table 5.4.4: Convergence statistics of normalized 1st harmonic components of target quantities for low wave steepness $ka_w = 0.09$ with particle Re $= 8.0 \times 10^4$, KC $= 0.9$. F_{px} and F_{pz} are the magnitudes of the first-harmonics parts of the pressure forces in horizontal and vertical directions, respectively, and F_{vx} and F_{vz} are the magnitudes of the first-harmonics parts of the viscous forces in horizontal and vertical directions, respectively. All these forces shown with its non-dimensional form at the table are normalized by $F' = F/(\rho g a_w l^2/4)$.

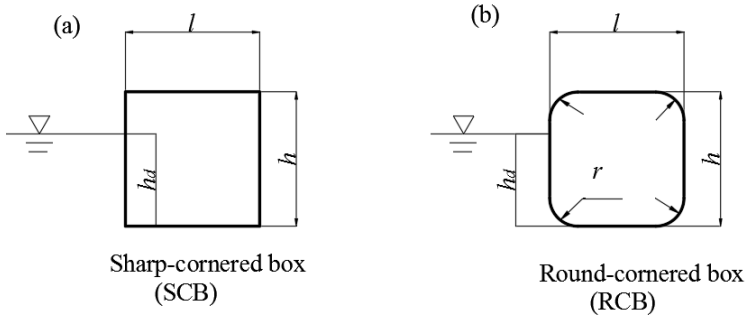


Figure 5.5.1: Shapes and dimensions of the objects with two different corner types: (a) Sharp-cornered boxes (SCBs) and round-cornered boxes (RCBs).

component reveals a small convergence ratio accompanied by a relatively high order of accuracy and small GCI, indicating the simulated value is approaching the asymptotic range (Stern et al., 2001; Mohseni et al., 2018). Notably, for Mesh 1 and Mesh2, the time-averaged y^+ averaged over the body surface is below 1. Mesh 1 (the most refined mesh) is selected as the final mesh for all subsequent simulations.

5.5 Validation and verification for small moving objects

Validation and verification of the QaleFOAM model are conducted by examing the drift of very small moving objects, focusing on viscid and inviscid simulations under low wave steepness conditions. The drift of infinitely small objects, i.e. fluid parcels, as well as the drift of very small objects with round corners and spherical shapes were shown to be predicted correctly

Simulation	Mesh	l/λ	$\lambda/\Delta x$	$l/\Delta x$	$a_w/\Delta z$	N_c	a/a_w	u_O/u_S	F'_x	F'_z
Inviscid	M1	0.97	185-7385	72	40	0.38M	1.00	1.002	0.095	0.100
	M2	0.97	185-3692	36	20	0.24M	1.01	0.995	0.097	0.101
Viscid	M1	0.97	185-7385	72	40	0.38M	1.01	1.010	0.106	0.107
	M2	0.97	185-3692	36	20	0.24M	1.00	1.000	0.098	0.101

Table 5.5.1: Results and mesh sensitivity study of a very small sharp-cornered box in low wave steepness $ka_w = 0.034$. For inviscid simulations, the kinematic viscosity in the simulation is set as $\nu = 0$ and for viscid simulations, $\nu = 1 \times 10^{-6}$ m$^2 \cdot$ s^{-1}. The level of mesh refinement is reduced from M1 to M2, with M1 being the mesh used for later simulations. a is the wave amplitude in the far downstream of the tank, which is a good indicator of a clean wave field with minimal radiated and diffracted disturbance to the waves. u_O is the time-averaged horizontal drift velocity of the object. F_x and F_z are the magnitudes of the oscillatory parts of horizontal and vertical forces, which are made non-dimensional as $F'_x = F_x/(\rho g a_w l^2/4)$ and $F'_z = F_z/(\rho g a_w l^2/4)$.

by the QaleFOAM model in Xiao et al. (2024); only simulations involving sharp-cornered boxes are presented here for brevity. Experiments and theoretical models (Nath, 1978; van den Bremer et al., 2019; Calvert et al., 2021), show that when objects are very small, they behave as perfect Lagrangian tracer, rendering viscosity insignificant due to the very small relative velocity between the object and the surrounding fluid. Consequently, RANS simulations for the small objects is with a very small particle Reynolds number ($|u_o - u_f| \to 0$), indicating laminar flow regime around the object though the flow itself could be turbulent. We have conducted RANS simulations but to find very similar results with viscid simulations. For brevity, the results of RANS simulations are no longer presented here. The leading-order theoretical expression for the Stokes drift u_S is:

$$u_S = {a_w}^2 \omega k e^{2kz}, \tag{5.3}$$

The objects with different corner shapes and their dimensional specifications are illustrated in figure 5.5.1. In this section, we focus on a small sharp-cornered box with dimensions $l = 0.036$ m and $h_d = 0.025$ m. The results from viscid and inviscid simulations are given in table 5.5.1. The wave conditions are $\lambda = 3.69$ m,$a = 0.02$ m and $ka_w = 0.034$. Regarding the calculation of the (time-average) drift velocity, two methods are considered: processing the horizontal velocity using the Fast Fourier Transform (FFT) and applying a low-pass filter to obtain its subharmonic part (filtering out frequencies larger than 0.4 times the wave frequency) or applying a best linear fit over the horizontal trajectory to derive the mean velocity (Huang et al., 2011). Both methods yield similar results. We chose the latter approach as it allows potential future comparison with

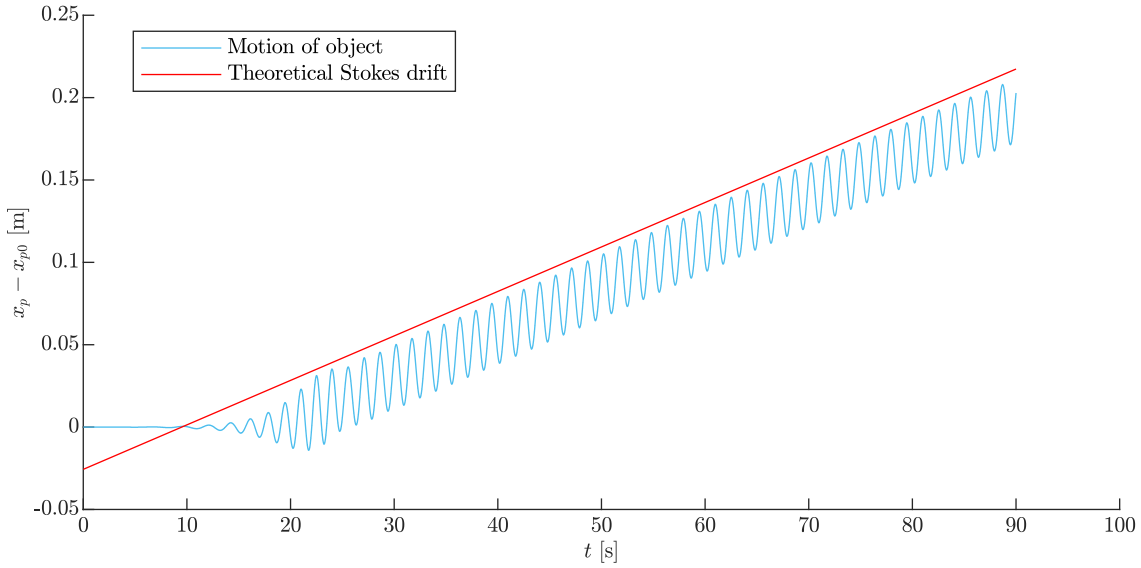


Figure 5.5.2: Time history of the horizontal motion of the small object in low-wave steepness waves ($ka_w = 0.034$) for inviscid simulations. x_p is the time-dependent horizontal position of centre of mass of the object and x_{p0} is the initial horizontal position of its centre of mass.

experimental data, where only the trajectory data is available.

Following Xiao et al. (2024), the time-averaged drift velocity of the object, denoted as u_O, is obtained by applying a best linear fit to the signal after reaching a quasi-steady state. Figure 5.5.2 provides an example of the drift trajectory obtained in the inviscid simulation, demonstrating the achievement of a quasi-steady state around $t = 21T = 32$ s, leaving a duration of $39T$ for estimation of the time-averaged velocity. The wave amplitude a at a location far downstream near the outlet is calculated by averaging its wave amplitude over $39T$ after $t = 30s$, as are the magnitudes of the oscillatory parts of forces F'_x and F'_z in both directions.

Figure 5.5.2 shows that except for the oscillatory motion, the object experiences a nearly constant mean drift that remains stable over $39T$ after $t = 32$ s. The observed drift follows the theoretical Stokes drift, thus confirming the accuracy of the inviscid simulation. The data in table 5.5.1 corroborates this finding, indicating that for the inviscid simulation, the mean drift velocity closely aligns with the theoretical Stokes drift. Moreover, in the viscid simulations incorporating viscosity, the small object follows Lagrangian drift behavior, validating the efficacy of the viscid simulation model. In addition, table 5.5.1 shows that the quantities of interest exhibit minimal sensitivity to the mesh resolution. It is important to note that verification and validation of the model, including the convergence test and the validation of the small

SCB & RCB	$l/\lambda(\%)$	1.0	2.0	3.0	4.0	5.0	6.0	7.0	8.0	9.0	10.0
	l (m)	0.037	0.07	0.11	0.15	0.19	0.22	0.26	0.29	0.33	0.37
	h_d (m)	0.025	0.05	0.075	0.10	0.13	0.15	0.18	0.20	0.23	0.25
	h (m)	0.055	0.08	0.105	0.13	0.16	0.19	0.22	0.26	0.29	0.32
SCB	r (m)	0	0	0	0	0	0	0	0	0	0
RCB		0.006	0.012	0.018	0.024	0.03	0.036	0.043	0.048	0.054	0.06

Table 5.6.1: Object dimensions of sharp-cornered boxes and round-cornered boxes with a constant density of $\rho = 781$ kg/m^3 and aspect ratio $h_d/l = 0.67$.

objects, only cover partly the validation process. Ideally, the comparisons of the trajectories of large objects to the experiment should be conducted in the future to further validate the CFD simulations presented here. Also, the comparison of the vorticity structures and patterns that we observe (reported in section §5.6.1) with the relevant data/results should be conducted for comprehensive validation.

5.6 Results

To explore the effects of vorticity and turbulence induced by the geometry of the object (i.e., different corner shapes) on the drift behavior of floating objects of different sizes, we consider objects with two different shapes (cf. figure 5.5.1). For each shape, we vary the size of the objects systematically. The wave condition employed for moving objects is $a = 0.02$ m, $\epsilon = ka_w = 0.034$ (ϵ is the wave steepness), $\lambda = 3.69$ m. To present our results, we introduce two dimensionless parameters that describe shape and size: the relative object size defined as l/λ and the relative radius of the corners of the round-cornered box defined as r/h_d. Throughout our simulations, the relative size of the objects spans from 1% to 10% in 1%-point steps, while the relative radius of the corners of the round-cornered box remains constant at $r/h_d = 0.24$. Detailed dimensional parameters are provided in table 5.6.1. We maintain a fixed box density of $\rho = 781$ kg/m^3 and aspect ratio $h_d/l = 0.67$. However, to avoid green-water impact, it is essential to ensure the freeboard of the object exceeds the local wave amplitude. Yet, if we maintain the density and aspect ratio of the object, for a relative size smaller than 5%, its freeboard is less than 0.03, which is the minimum value to avoid green water if we consider the incident wave amplitude is $a_w = 0.02$ m plus locally enlarged wave amplitude. Therefore, we must set the freeboard of those objects to be at least 0.03 m, which creates a further problem. Boxes with such dimension make it difficult to maintain stability (they are not

l/λ	1.0	2.0	3.0	4.0	5.0	6.0	7.0	8.0	9.0	10.0
Viscid	0.22	0.26	0.34	0.38	0.42	0.46	0.48	0.51	0.58	0.63
RANS	0.21	0.29	0.23	0.45	0.42	0.44	0.47	0.51	0.55	0.59

Table 5.6.2: Mean values of y^+ for viscid and RANS simulations of sharp-cornered boxes. The mean value is obtained by averaging the time-averaged (over the whole simulation duration) y^+ value over the surface.

hydro-dynamically stable), we thus constrain their rotation. However, considering the constant ratio of submergence depth to size (h_d/l), we anticipate that this constraint (of rotation) only leads to minor changes to the drift, if any (Xiao et al., 2024).

For each size of the sharp-cornered box, three types of simulations are conducted: RANS, viscid, and inviscid simulations. However, for the round-cornered box, only viscid and inviscid simulations are considered here. This is based on the findings by Xiao et al. (2024), which shows a high level of similarity between the results from the RANS and viscid model for round-corned boxes. Abbreviations are used in the graphs below to denote different types of simulations: 'SCB-RANS' for RANS simulations of sharp-cornered boxes, 'SCB-viscid' for viscid simulations of sharp-cornered boxes, 'SCB-inviscid' for inviscid simulations for sharp-cornered boxes, and similarly for round cornered boxes with 'RCB'. The simulations with 'RCB' results are those conducted in Chapter 3, and are revisited here for further analysis.

To better explain the difference in the flow field, pressure distribution, and resultant forces, which result in a difference in drift velocity, simulations for stationary objects were performed. This analysis was specifically carried out for the largest objects (i.e., $l/\lambda = 10\%$). Simulations of stationary objects allow a clearer definition of the relative velocity between the fluid and the objects and have a more distinct flow field and vorticity, facilitating analysis and understanding. The M1 mesh discussed in §5.4 and §5.5 is utilized consistently across all simulations below.

We will start our analysis with the motions and drift behaviours of moving objects in section §5.6.1, followed by the examination of the flow field, pressure distribution and forces for the stationary objects in section §5.6.2.

5.6.1 Analysis of moving objects

We first address the drift of moving objects. To ensure that the mesh resolution across all cases is sufficiently fine to accommodate a wall-resolved turbulent model, it is essential to

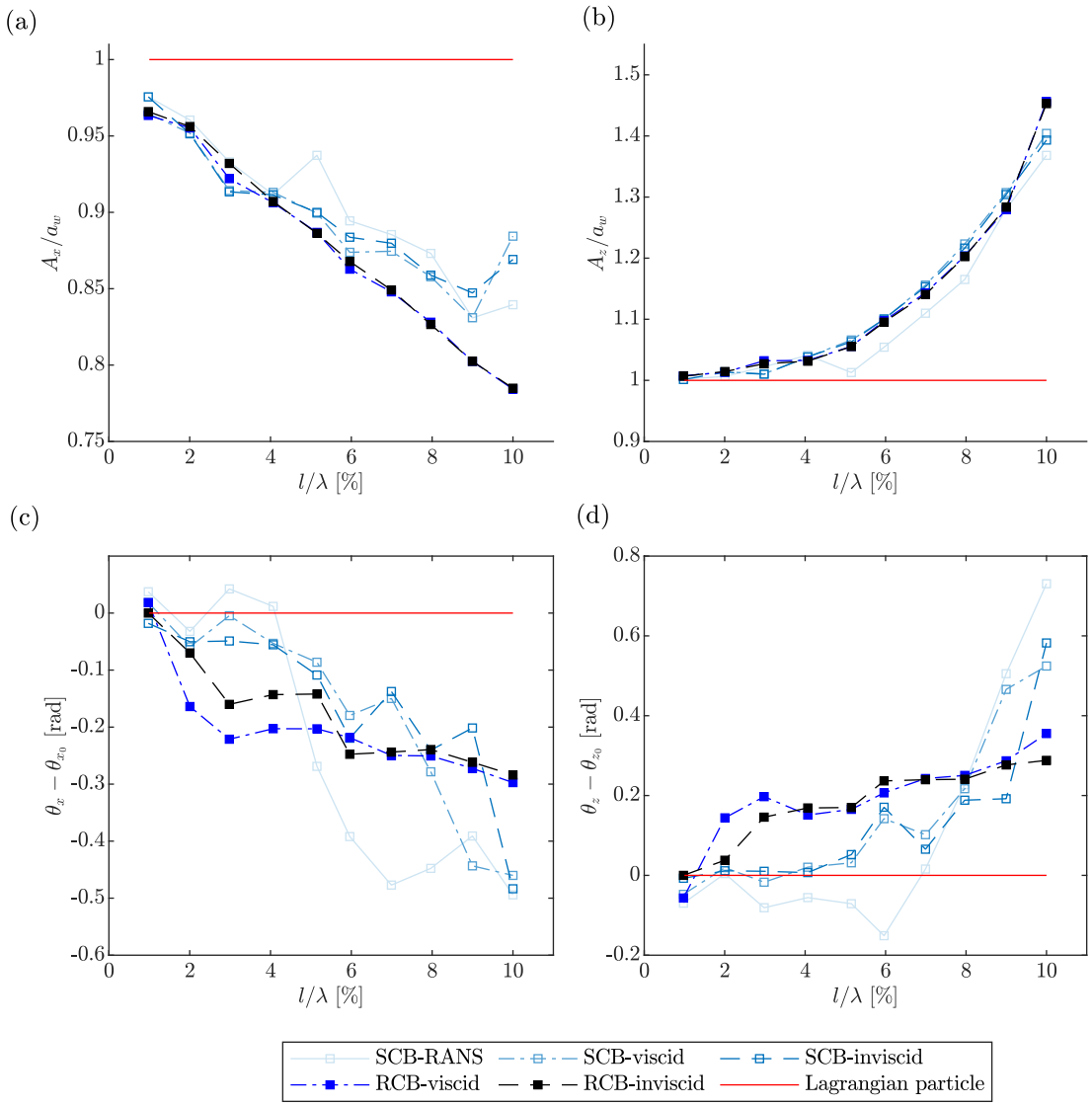


Figure 5.6.1: Oscillatory Motion of objects with different corner shapes in different types of simulations in both horizontal and vertical directions: (a) and (b) oscillatory motion amplitudes (normalized by input wave amplitude a_w) as a function of relative object size in horizontal and vertical direction, respectively; (c) and (d) phase differences in both directions of the oscillatory motions between a finite-size object θ_x, θ_z and a Lagrangian particle θ_{x0}, θ_{z0}. The red line denotes the results of an ideal Lagrangian particle.

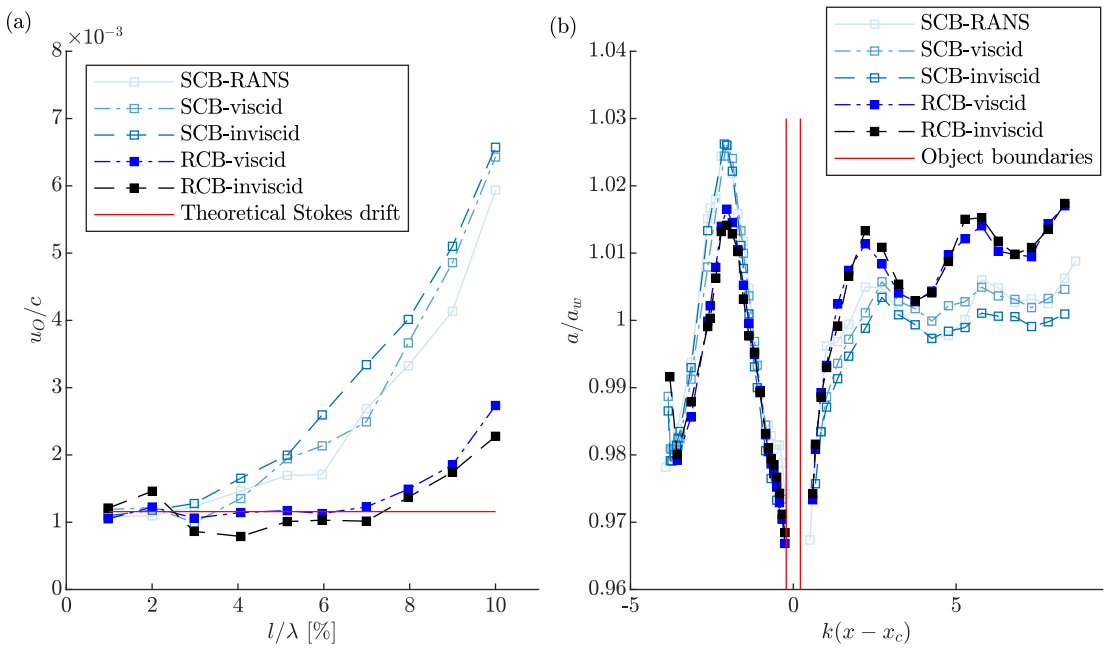


Figure 5.6.2: Different types of simulations for objects with different corner shapes: (a) celerity-normalized drift velocity u_O/c as a function of relative object size; (b) amplitude of local wave surface elevation $a(x)$ (normalized by incoming wave amplitude a_w) as a function of horizontal distance (scaled by wavenumber) from the centre of mass x_c (i.e., standing wave pattern) for an object with relative size $l/\lambda = 7\%$. The object boundaries represent the left and right sides of the objects.

maintain an average y^+ value below 1. Table 5.6.2 lists the average y^+ values for simulations of sharp-cornered boxes (both RANS and viscid simulations). The mean y^+ value is obtained by first averaging the values across the entire object surface in space and then throughout the simulation in time. As demonstrated in table 5.6.2, the mean y^+ values for all cases remain below 1. The particle Reynolds number and Keulegan–Carpenter numbers for both types of objects are given in table 5.6.3. As suggested in the table, the particle Reynolds number falls within the range of $5 < \mathrm{Re}_x < 3 \times 10^5$ and the KC numbers fall into a small range and satisfy $0 < \mathrm{KC} < 0.4$. Because there is limited literature on flow regimes around square cylinders in oscillatory flow with a free surface (cf. Tong et al. (2017)), we use the flow regimes around a circular cylinder in steady current to identify current flow regime. Most of our simulations fall within the subcritical region where $300 < \mathrm{Re} < 3 \times 10^5$. This suggests laminar boundary layer separation with a turbulent wake. Regarding the KC number, according to Sumer et al. (2006); Yoon et al. (2016); Mohseni et al. (2018), when $\mathrm{KC} < 3$, the flow is inertia-dominated and the effects of boundary layer separation and vorticity are small. Although vortex formation and a wake structure are observed around the object in our simulations of sharp-cornered boxes, no

	l/λ (%)	1.0	2.0	3.0	4.0	5.0	6.0	7.0	8.0	9.0	10.0
SCB	Re_x	1.80×10^{1}	2.02×10^{2}	3.06×10^{2}	8.52×10^{2}	1.41×10^{3}	1.78×10^{3}	2.78×10^{3}	3.51×10^{3}	4.04×10^{3}	6.96×10^{3}
	KC	0.24	0.24	0.22	0.24	0.26	0.27	0.30	0.32	0.35	0.38
RCB	Re_x	6.0	2.31×10^{2}	4.70×10^{2}	7.63×10^{2}	1.18×10^{3}	1.75×10^{3}	2.31×10^{3}	2.83×10^{3}	3.38×10^{3}	3.85×10^{3}
	KC	0.27	0.24	0.24	0.24	0.25	0.26	0.28	0.30	0.33	0.36

Table 5.6.3: Reynolds and Keulegan–Carpenter numbers of moving objects for both round-cornered and sharp-cornered bpxes.

distinct flow separation has been found to occur.

Object motion and drift

The simulation results are shown in figures 5.6.1 and 5.6.2. Figure 5.6.1 shows the linear oscillatory motions, encompassing both motion amplitudes and phases in both horizontal and vertical directions. The amplitudes and phases of these oscillatory motions are determined by evaluating the phase and magnitude of the linear components only, filtering out sub- and super-harmonics components after the quasi-steady state has been achieved. Figure 5.6.2 (a) illustrates the celerity-normalized drift velocity for all simulation types. Across all cases, a time of $t_s = 21T$ is employed to define the quasi-steady state, where T is the wave period. Figure 5.6.2 (b) displays the standing wave pattern as defined in Xiao et al. (2024) for different simulation types and for sharp-cornered and round-cornered boxes with a relative size of $l/\lambda = 7\%$. The standing wave pattern depicts the local wave amplitude at different locations around the object. The local wave amplitude is obtained by time averaging the magnitude of the surface elevation at specific locations after achieving a quasi-steady state. The surface wave elevation is measured using virtual wave probes in the earth-fixed coordinates system.

Oscillatory linear motions: To examine the effects of corner shape on object motions, we analyze the amplitudes of oscillatory motions as depicted in figure 5.6.1 (a). Consistent with findings by Xiao et al. (2024), it is observed that as the object size increases, the amplitudes of horizontal oscillatory motion decrease, while those of vertical oscillatory motion increase. Notably, for relatively large objects, sharp-cornered boxes demonstrate a slightly smaller reduction in horizontal motion amplitude compared to round-cornered boxes. However, the amplitudes of vertical motion for both types of objects are very similar for all relative sizes studied. For sharp-cornered boxes, a comparison between the 'SCB-viscid' and 'SCB-inviscid' reveals that the inclusion of viscosity induces negligible differences in both horizontal and vertical motion amplitudes.

In figure 5.6.1 (c) and (d), a phase lead in the horizontal direction and a phase lag in the vertical direction are observed, qualitatively consistent with the findings of Xiao et al. (2024). Comparison between the two types of objects reveals that when the object size is small, the sharp corners of the objects exhibit less phase difference in both directions, while larger phase differences are observed for large objects. Furthermore, comparing 'RCB-viscid' and 'RCB-inviscid' shows that the inclusion of viscosity causes a slightly greater phase lead in the horizontal direction and a greater phase lag in the vertical direction for round-cornered boxes. Conversely, for sharp-cornered boxes, the inclusion of viscosity (that is 'SCB-viscid' vs. 'SCB-inviscid') does not significantly affect the phase differences in both directions. However, in contrast to 'SCB-viscid' and 'SCB-inviscid', the 'SCB-RANS' simulations exhibit a non-monotonic trend as the object size increases. This can be explained by the fact that the inclusion of the turbulent viscosity alters the object motion phase in a slightly different way as the object becomes larger.

Overall, the linear motion and phases of the objects in both directions do not exhibit significant differences between objects with different corner shapes and between the different types of simulations.

Object drift and standing wave pattern: we move on to examine drift velocity in figure 5.6.2 (a). For both types of objects, small objects have a drift equal to the Stokes drift, while larger objects exhibit enhanced drift compared to the theoretical Stokes drift, and such drift enhancement increases with object size, as observed and reported by Xiao et al. (2024). However, a notable difference is observed between sharp-cornered and round-cornered boxes. The enhanced drift for round-cornered boxes becomes distinct when the object is $l/\lambda \geq 8\%$, whereas the drift enhancement for sharp-cornered boxes is noticeable for objects as small as $l/\lambda = 4\%$. Moreover, the drift enhancement for sharp-cornered boxes is larger. The inclusion of viscosity increases the drift enhancement for round-cornered boxes, while decreasing the drift enhancement for sharp-cornered boxes, suggesting an additional role played by viscosity in the case of sharp-cornered boxes due to their different corner shapes. The inclusion of turbulent viscosity further reduces the drift enhancement for sharp-cornered boxes.

In figure 5.6.2 (b), the standing wave patterns for the different types of simulations and objects are reported. The inclusion of viscosity (kinematic or turbulent) does not have an

obvious influence on the standing wave pattern. However, sharp-cornered boxes experience a more distinct standing wave pattern with a larger local maximum on the upstream side and a smaller local minimum on the downstream side. According to Xiao et al. (2024), the standing wave pattern is intimately related to diffraction, which results in drift enhancement. The more capable the object is to 'impede' the wave field (i.e., the less streamlined the object is), the more its drift will be enhanced. Therefore, the difference in drift enhancement between two types of objects can partly be explained by the different standing wave patterns.

Given that a standing wave pattern with a local maximum of $a/a_w = 1.12$ in Xiao et al. (2024) results in a 92% increase in drift, the amplitude difference between the standing wave patterns (with a local maximum $a/a_w = 1.026$ for sharp-cornered box vs. $a/a_w = 1.017$ for round-cornered boxes) between the two types of objects is not sufficient to explain the 176% increase in drift of sharp-cornered boxes relative to round-cornered boxes with a relative size of $l/\lambda = 7\%$. The phase difference of linear motion in figure 5.6.1 may induce some differences in drift enhancement between two types of objects, if any, according to Calvert et al. (2021); Xiao et al. (2024), but there must be another explanation.

Drift unsteadiness

Motivated by the difference in drift enhancement between the two types of objects, we revisit the object's trajectory to examine the drift velocity. In section §5.6.1, we investigate the drift by removing data before the start of the quasi-steady state t_s and performing a linear fit to its horizontal trajectory. Here, we begin by testing the sensitivity of the drift evaluated at different t_s values, using RANS simulations of sharp-cornered boxes, as shown in figure 5.6.3 (a). The drift velocity shows little dependence on t_s for smaller objects, while varying more for larger objects. This dependence could arise because larger objects have a greater mass and require more time to achieve steady state. Nevertheless, the variations in drift velocity are considered small relative to the drift and drift enhancement. Hence, it is reasonable to conclude that $t_s = 21T$ is an appropriate value for both types of objects and the steady state not having been reached therefore cannot account for the difference in drift enhancement between the types.

Next, we explore the linear fit approach. A sample trajectory for $l/\lambda = 10\%$ obtained from RANS simulation is presented in figure 5.6.3 (b). Upon closer examination, it becomes

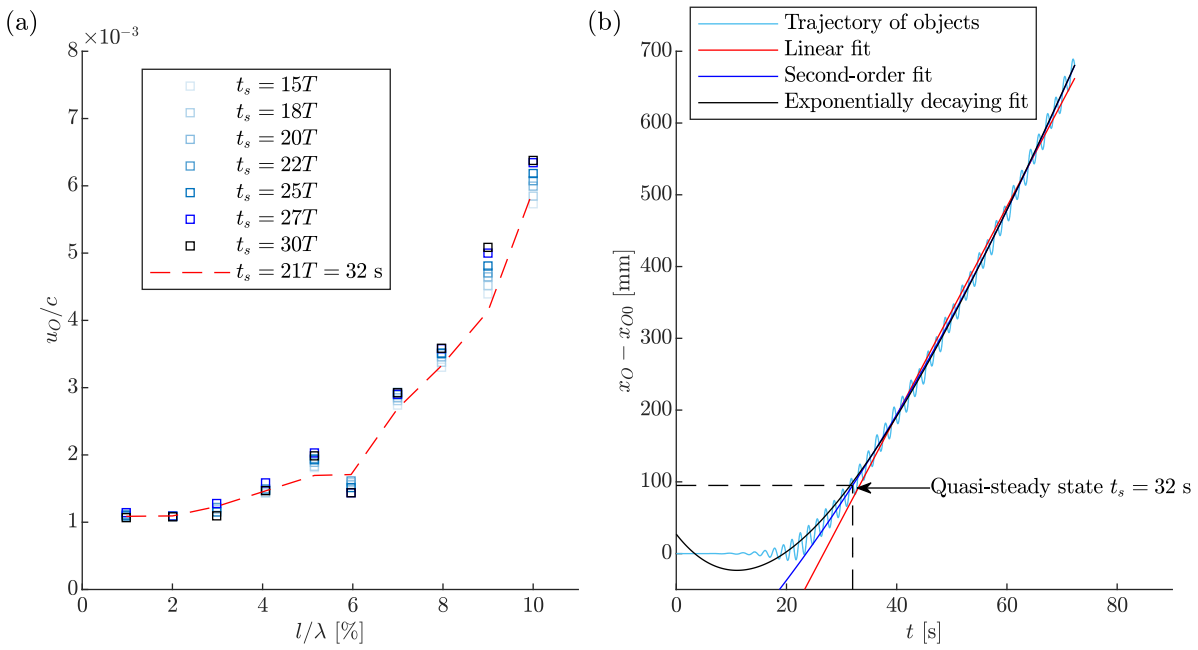


Figure 5.6.3: Examining unsteadiness of the drift velocity of sharp-cornered objects: (a) dependence of drift velocity on the assumed start of the quasi-steady state t_s as a function of object relative size for the RANS simulations. For each relative size, seven different values of t_s are shown, ranging from 23 s to 45 s (i.e., $15T$ to 30 T). The red lines are the drift from figure 5.6.2 (a) using $t_s = 21T$; (b) an illustrative example showcasing different types of fits of the horizontal trajectory of the RANS simulation results for $l/\lambda = 10\%$. Here, x_O denotes the horizontal position of the object at time t, with $x_{O,0}$ representing the initial position at $t = 0$ s. The red line denotes the linear fit: $x_{O,LF}(t) = 14.5t - 388.4$, the approach used in section §5.6.1; the blue line corresponds to the second-order fit: $x_{O,SF} = 0.067t^2 + 7.5t + 214.3$, while the exponentially decaying fit is represented by $x_{O,EF} = 740.1e^{-0.0385t} + 18.64t + 710$. The Stokes drift in this case is $u_S = 2.78$ mm/s. Both linear and second-order fits use the trajectory data after $t_s = 32$ s, whereas the exponential decay fit uses all the trajectory data including those before $t \leq 32$ s.

apparent that the trajectory may contain other components of behaviour besides the oscillatory component and the constant drift. To examine this further, we perform three types of fits to the object drift trajectory in our data: a linear fit (LF), a second-order fit (SF) and an exponentially decaying fit (EF). The fitting functions are as follows:

$$x_{O,LF}(t) = u_{O,LF}t + d_{LF}, \tag{5.4}$$

$$x_{O,SF}(t) = s_{O,SF}t^2 + u_{O,SF}t + d_{SF}, \tag{5.5}$$

$$x_{O,EF}(t) = e_{O,EF}e^{-b_{O,EF}t} + u_{O,EF}t + d_{EF}. \tag{5.6}$$

All of the fits are performed after filtering out the linear oscillatory part of the motion, retaining

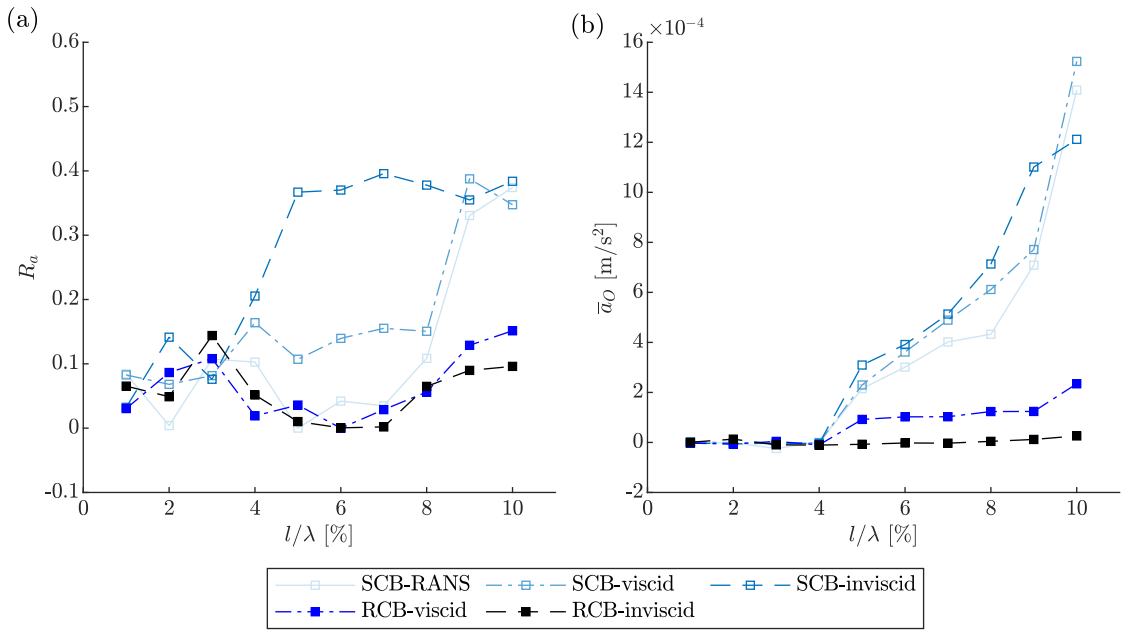


Figure 5.6.4: Different types of simulation results of (a) unsteadiness ratio R_a (b) mean acceleration ($\overline{a}_O$) as a function of relative size for objects with different corner shapes.

only the drift. The linear fit assumes that the object moves steadily with a constant drift. On the other hand, the second-order fit describes an accelerating motion, incorporating both linear and quadratic terms in time. In contrast, the exponential decay fit characterizes the drift motion as a combination of a constant linear drift speed and a transient component that decays exponentially with time. It is evident from figure 5.6.3 (b) that the linear fit does not provide the best fit for the trajectory, particularly for later times.

To quantify the level of unsteadiness in object motion, we introduce the ratio

$$R_a = |1 - \frac{u_{O,SF}}{u_{O,LF}}|, \tag{5.7}$$

which measures the relative magnitude of the linear speed in the second-order fit to the (constant) linear speed in the linear fit. The more R_a deviates from 0, the more unsteady the object drift is (typically, $u_{O,SF}/u_{O,LF}$ is smaller than 1, and the larger the ratio R_a is, the more unsteady the drift is). The value of the ratio for both types of objects and simulations is illustrated in figure 5.6.4 (a). Additionally, the acceleration $\overline{a}_O$ represents the mean (time-averaged) value of the acceleration obtained from the motion in the horizontal direction in our simulations, which is evaluated with the oscillatory part not included. The values of $\overline{a}_O$ for all simulations are given in figure 5.6.4 (b).

From figure 5.6.4 (a), it is clear that the unsteadiness ratios of both types of objects and simulations are very close to 0 for smaller objects. For round-cornered objects of $l/\lambda \geq 7\%$, there is a some unsteadiness, whereas for sharp-cornered objects with relative size $l/\lambda \geq 4\%$, the unsteadiness ratio becomes notably smaller compared to round-cornered boxes. The comparison between the unsteadiness for different types of simulations for sharp-cornered box shows that the 'SCB-inviscid' simulation is the most unsteady followed by 'SCB-viscid' and 'SCB-RANS' simulations, respectively. The same trend is observed for the drift velocity observations, where the 'SCB-inviscid' simulation experiences the largest drift enhancement, followed by 'SCB-viscid' and 'SCB-RANS' simulations. This might be because the inclusion of (turbulent) viscosity helps to suppress the unsteadiness of the drift, showing less drift enhancement. Complementary to this, figure 5.6.4 (b) shows that the average acceleration of sharp-cornered boxes is significantly larger than that of round-cornered boxes. For round-cornered boxes, the average acceleration of 'RCB-inviscid' is close to 0, and the inclusion of viscosity slightly increases the accelerations. However, for sharp-cornered boxes, the acceleration in the inviscid simulations is the largest, and the inclusion of (turbulent) viscosity reduces the accelerations. Analysis of figure 5.6.4 suggests that compared to round-cornered boxes, sharp-cornered boxes with equivalent size experience more unsteadiness (acceleration) at a relatively small size on the time scale of the simulations (around $60T$). The unsteadiness could be attributed to two effects: a fundamental unsteadiness and instability induced by the sharp gradients of geometry that will not decay over time, or an initial transient due to the stationary conditions (initial) of the object at the start of the simulations. To examine the dependence of unsteadiness on the time scale and confirm the underlying reasons for unsteadiness, we revisit the experimental data from Chapter 4, as shown in figure 5.6.5. It is worth noting that the objects used in the laboratory experiments in Chapter 4 are boxes with sharp corners and vorticity is observed visually for large objects. We use two different time durations, namely a shorter duration $T_d = 35T$ and a longer time duration $T_d = 1 \times 10^2 T$-$1 \times 10^4 T$ to evaluate the unsteadiness of object drift. The shorter duration is consistent with the time duration used in our numerical simulations, while the longer time duration corresponds to the duration of the experiments in Chapter 4. It can be observed that for high wave steepness, the unsteadiness ratio shows little dependence on time duration and remains close to 0, suggesting the absence of an accelerating pattern. However,

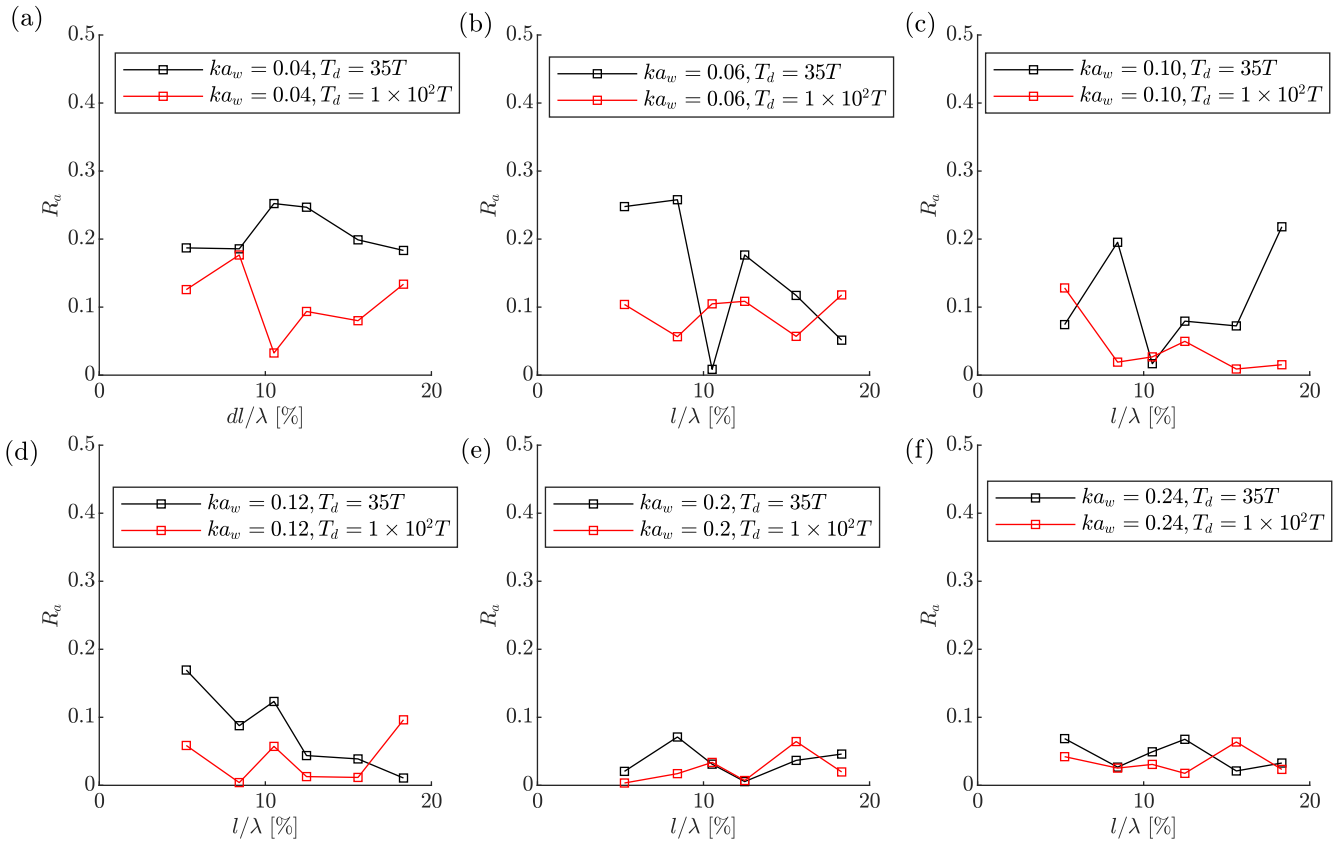


Figure 5.6.5: Unsteadiness ratio of drift in the laboratory experiment conducted in Chapter 4 as a function of relative object size for different wave steepness ranging from $ka_w = 0.04$ to $ka_w = 0.24$. The unsteadiness ratio experiment data is evaluated for both shorter and longer time duration T_d. $T_d = 1 \times 10^2 T$ given is the minimum time duration in the experiments evaluated for the largest objects in high wave steepness, while for small objects of $l/\lambda \leq 12\%$, the overall evaluation duration can be up to $10^4 T$.

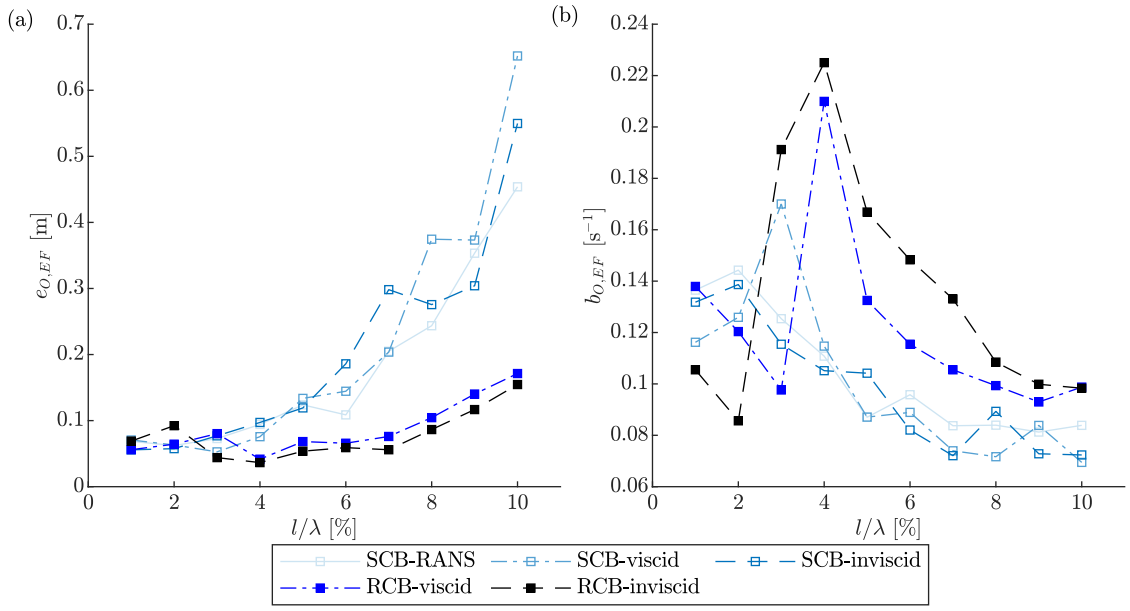


Figure 5.6.6: Parameters of decaying component of the exponential-decay fit based on (5.6) as a function of relative size for objects with different corner shapes in different types of simulations: (a) magnitude of the decaying term $e_{O.EF}$, (b) decay rate $b_{O.EF}$.

for lower wave steepness, the unsteadiness for the longer duration consistently remains close to 0, regardless of object sizes and wave steepness, whereas this is not observed for the shorter duration. Particular attention is paid to the case $ka_w = 0.04$, as this is the wave steepness closest to our numerical simulations. For objects smaller than $l/\lambda = 10\%$, the unsteadiness ratio for shorter duration tends to be smaller, suggesting that in low wave steepness scenarios, initial transients that ultimately decay may play a role in short-duration simulations ($T_d = 35T$).

Building on the above analysis of the unsteadiness of experiments, we return to our numerical simulations and perform exponentially decaying fits using (5.6). Instead of allowing for acceleration, we aim to divide the data into two components: one with a constant drift and the other decaying with time. It is found that exponential decay fitting yields better results, as shown in figure 5.6.3 (b). As the parameters of the constant speed are similar to the drift speed shown in figure 5.6.2 (a), only the terms of the exponentially decaying components $e_{O,EF}$ and $b_{O,EF}$ are presented in figure 5.6.6. The parameter $e_{O,EF}$ determines the magnitude of the exponentially decaying component, and $b_{O.EF}$ denotes its decay rate. The exponential-decay fit is obtained from the entire time history, including $t \leq t_s$.

We examine the two parameters in turn, commencing with $e_{O,EF}$. The exponentially decaying component increases with object size, potentially explained by the fact that as the object size grows larger, it gains more mass and thus exhibits greater inertia. The comparison between the two types of object reveals that sharp-cornered boxes contain larger exponentially decaying components, and the size of this component is influenced by the simulation type. For round-cornered boxes, the inclusion of viscosity enlarges the decaying component, while for sharp-cornered boxes, the inclusion of (turbulent) viscosity generally reduces it. Maximum values of the decay rate $b_{O,EF}$ are reached for object sizes around $l/\lambda = 4\%$. The sharp-cornered boxes have a smaller decay rate than the round-cornered boxes. Moreover, the inclusion of (turbulent) viscosity also influences the decay rate. This analysis further supports the notion that the initial transient (at least, partially) contributes to the unsteadiness observed in figure 5.6.4. However, this analysis does not provide a definitive answer for large duration simulations.

We now turn our attention to exploring how this unsteadiness correlates with the corner shape of objects. We begin by examining the flow field analysis, examining the vorticity field and the corresponding pressure field at different time intervals. It is important to note that

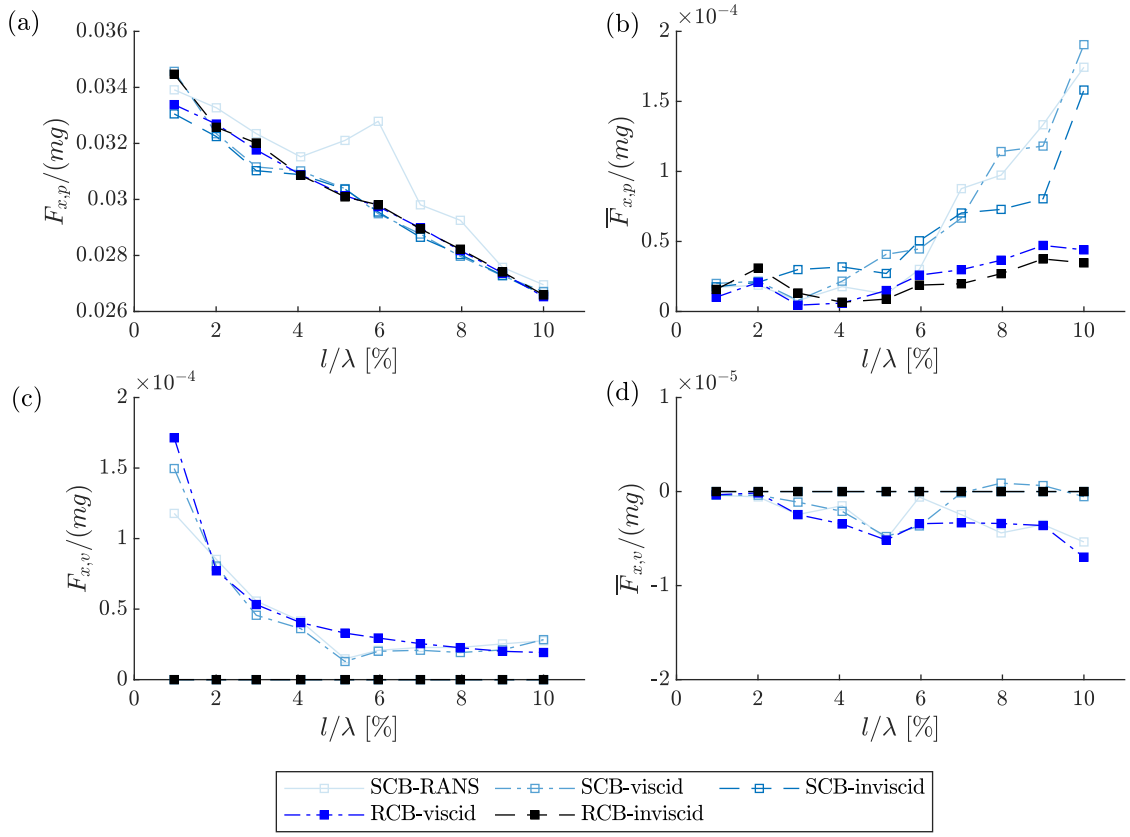


Figure 5.6.7: Horizontal forces on the object as a function of relative size for objects with different corner shapes in different types of simulations. (a) magnitudes of the oscillatory part of the pressure forces. (b) mean values of pressure forces over the simulated time duration after $t_s = 21T$. (c) magnitudes of the oscillatory part of viscous forces (b) mean value of the viscous forces over the simulated time duration after $t_s = 21T$. The forces are all normalized by the gravitational force mg, where m is the mass of the object and $g = 9.81$ m/s^2. For 'SCB-inviscid' and 'RCB-inviscid', viscous forces are all 0, as viscosity is not included in these simulations.

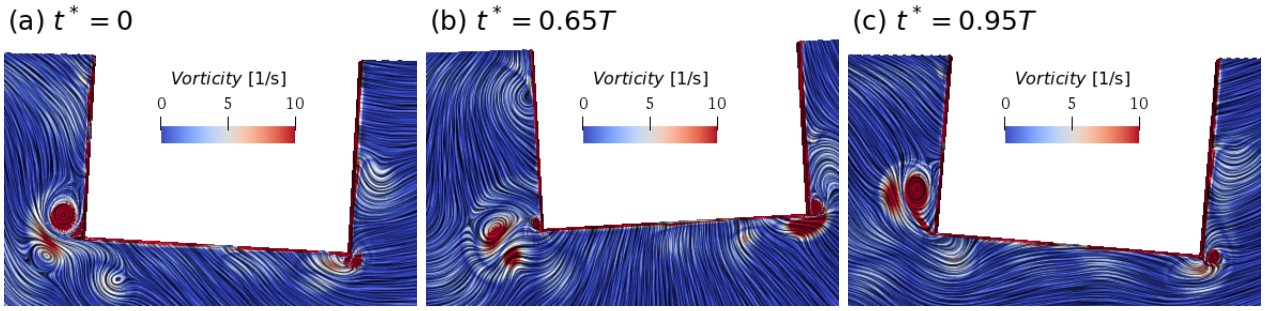


Figure 5.6.8: Vorticity magnitude field (the curl of the velocity field) across one wave period for the RANS simulations of a moving sharp-cornered box ($l/\lambda = 10\%$) for $ka_w = 0.034$. Time starts at $t^* = t - 40$s (after $t_s = 32$s) for initial time $t^* = 0$s, as denoted in the figures. Only the submerged part is shown, achieved by only displaying phase fraction values $\alpha \geq 0.5$.

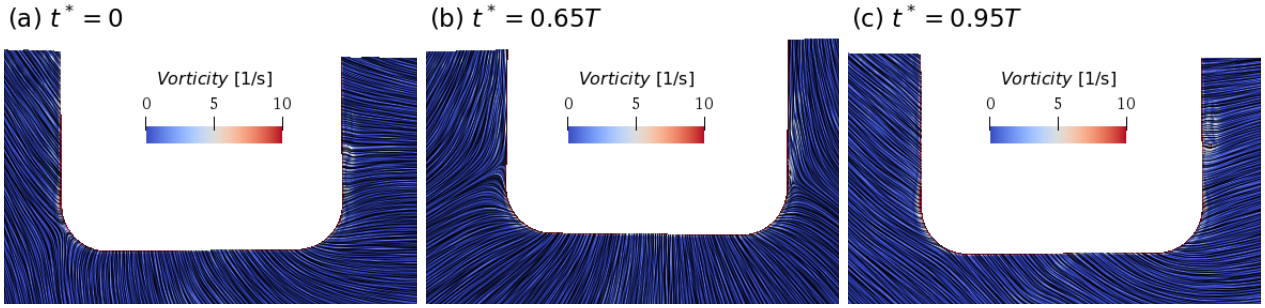


Figure 5.6.9: Vorticity magnitude field (the curl of the velocity field) across one wave period for the viscid simulations of a moving round-cornered box ($l/\lambda = 10\%$) for $ka_w = 0.034$. Time starts at $t^* = t - 40$s (after $t_s = 32$s) for initial time $t^* = 0$s, as denoted in the figures. Only the submerged part is shown, achieved by only displaying phase fraction value $\alpha \geq 0.5$.

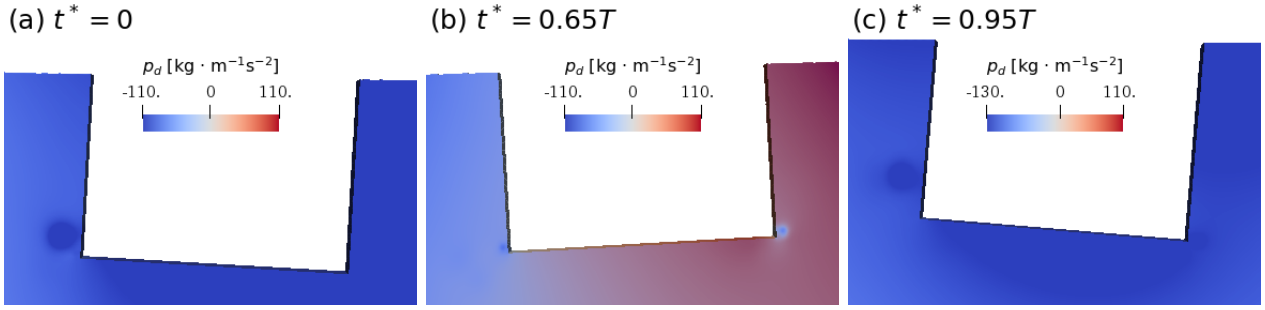


Figure 5.6.10: Dynamic pressure field (p_d) across one wave period for the RANS simulations of a moving sharp-cornered box ($l/\lambda = 10\%$) for $ka_w = 0.034$. Time starts at $t^* = t - 40$s (after $t_s = 32$s) for initial time $t^* = 0$s, as denoted in the figures. Only the submerged part is shown, achieved by only displaying phase fraction value $\alpha \geq 0.5$.

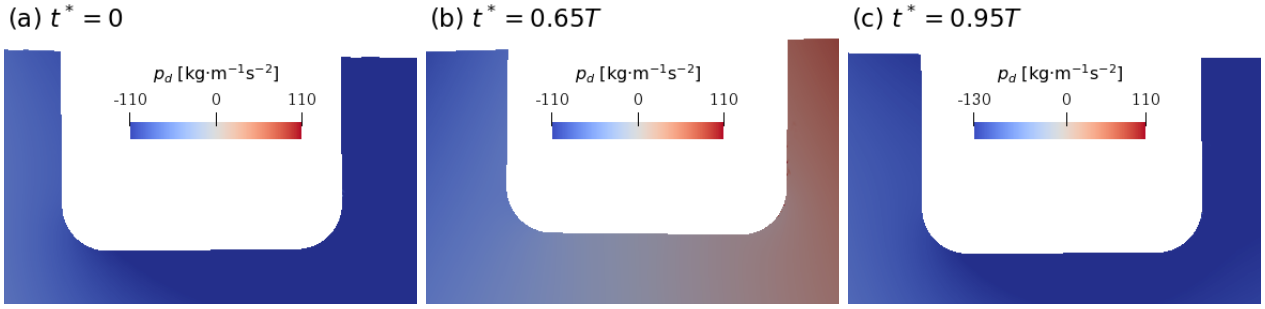


Figure 5.6.11: Dynamic pressure field (p_d) across one wave period for the viscid simulations of a moving round-cornered box ($l/\lambda = 10\%$) for $ka_w = 0.034$. Time starts at $t^* = t - 40$s (after $t_s = 32$s) for initial time $t^* = 0$s, as denoted in the figures. Only the submerged part is shown, achieved by only displaying phase fraction value $\alpha \geq 0.5$.

due to the complexities involved in tracking the pressure history of moving objects, we opted not to analyze the time history of the pressure distributions.

We plot the vorticity and dynamic pressure fields for both sharp-cornered and round-cornered objects in figures 5.6.8 – 5.6.11. Vorticity is prominently observed in simulations of sharp-cornered boxes, as shown in figure 5.6.8, whereas it is notably absent in simulations involving round-cornered boxes, as shown in figure 5.6.9. The presence of vorticity, attributed to the sharp corner, induces changes in the dynamic pressure field around the box, as evidenced by the comparison between figure 5.6.10 and figure 5.6.11. Notably, vorticity and flow separation occur unevenly and asymmetrically around the front and rear regions of the sharp-cornered box, as shown in figure 5.6.8.

Having examined the vorticity and dynamic pressure fields, we proceed to investigate how these factors influence the motions of the object by exploring the different force components experienced by the object. Apart from the gravity and the static pressure force, (both partially and fully) submerged objects exposed to fluid typically experience dynamic pressure and viscous forces. In this analysis, we focus on the horizontal direction. Figure 5.6.7 presents the magnitudes and time-averaged values of the dynamic pressure and viscous force components for objects of different sizes and corner shapes and for the different simulation types. Notably, the figure illustrates that pressure forces outweigh viscous forces by two orders of magnitude.

The comparison between two types of objects and the different types of simulations reveals that compared to round-cornered boxes, the magnitude of pressure and viscous forces for sharp-cornered boxes are slightly smaller but the differences are not significant. The inclusion of viscosity does not exert a pronounced influence on the magnitudes of these forces for both types of objects. An exception is observed in the RANS modeling of sharp-cornered boxes, where there appears to be a smaller magnitude of the oscillatory component of the pressure forces compared to other types of simulations, consistent with the oscillatory motions depicted in figure 5.6.1. However, comparison of mean values reveals significant differences between the two types of objects and different types of simulations. The sharp-cornered boxes experiences larger mean values of pressure forces than the round-cornered boxes. Relating the mean value of the pressure force to the acceleration in figure 5.6.4 (b), we observe consistent trends. Compared to the round-cornered boxes, the larger dynamic pressure forces on the sharp-cornered boxes are

ka_w	Location	Left region					Bottom region				Right region			
		l_1	l_2	l_3	l_4	l_5	b_1	b_2	b_3	b_4	r_1	r_2	r_3	r_4
0.03		$(x-x_c)/l \in [-0.65, -0.52]$					$(x-x_c)/l \in [-0.46, 0.54]$				$(x-x_c)/l \in [0.52, 0.57]$			
	z/h_d	-0.12	-0.6	-0.72	-0.8	-0.98	-1.04	-1.1	-1.16	-1.2	-0.8	-0.84	-0.92	-0.96
0.07		$(x-x_c)/l \in [-0.76, -0.52]$					$(x-x_c)/l \in [-0.46, 0.54]$				$(x-x_c)/l \in [0.52, 0.65]$			
	z/h_d	-0.26	-0.52	-0.6	-0.8	-0.98	-1.04	-1.16	-1.2	-1.32	-0.26	-0.6	-0.72	-0.98
0.09		$(x-x_c)/l \in [-0.76, -0.52]$					$(x-x_c)/l \in [-0.46, 0.54]$				$(x-x_c)/l \in [0.52, 0.65]$			
	z/h_d	-0.26	-0.52	-0.6	-0.8	-0.98	-1.04	-1.16	-1.2	-1.32	-0.26	-0.6	-0.72	-0.98

Table 5.6.4: Detailed coordinates of sampling points in the fluid field shown in figure 5.6.12 for different wave steepness values for stationary objects. The variables x and z represent the horizontal and vertical coordinates of the points, respectively, while x_c is the horizontal coordinates of the centre of object. Variables l and h_d denote the length and draft of the objects, respectively. Consequently, the horizontal locations of lines AB and CD are $x - x_c = -0.5l$ and $x - x_c = 0.5l$, respectively. The vertical locations of lines $A'D'$ and BC are $z/h_d = 0$ and $z/h_d = -1$, respectively. For $ka_w = 0.034$, the sampling points cover the region of $-0.65l \leq x - x_c \leq 0.57l$ and $-0.12h_d \leq z \leq -1.2h_d$. For higher wave steepness values $ka_w = 0.07, 0.09$, the region expands to $-0.76l \leq x - x_c \leq 0.65l$ and $-0.26h_d \leq z \leq -1.32h_d$.

likely to be induced by the asymmetry in the vorticity field, which results in net drift forces that accelerate the object forward. The inclusion of (turbulent) viscosity plays a role in suppressing or influencing the generation and development of vorticity, subsequently affecting the forces and consequently its drift behaviour. Regarding the mean value of the viscous forces, round-cornered boxes experience the highest values, followed by the RANS and viscid simulations of sharp-cornered boxes, suggesting sharp-cornered boxes experiences relatively lower mean viscous force due to the alterations in the fluid field.

To better understand the pattern of vorticity generation over time, especially under oscillatory input energy, it is crucial to explore the relationship between corner shape, vorticity generation, dynamic pressure fields, and resultant forces. However, analyzing this relationship for moving objects is challenging due to the constantly changing relative positions between the object and the fluid field, as they oscillate and drift. We therefore conduct additional analysis focusing on stationary objects.

5.6.2 Analysis of stationary objects

We conducted simulations of stationary boxes with two corner types, sharp and round, at the largest size, $l/\lambda = 10\%$ for three different wave steepness values: $ka_w = 0.034, 0.07, 0.09$. For sharp-cornered boxes, we conduct RANS, viscid and inviscid simulations, while for round-cornered boxes, only viscid simulations are performed for comparison. As the object is sta-

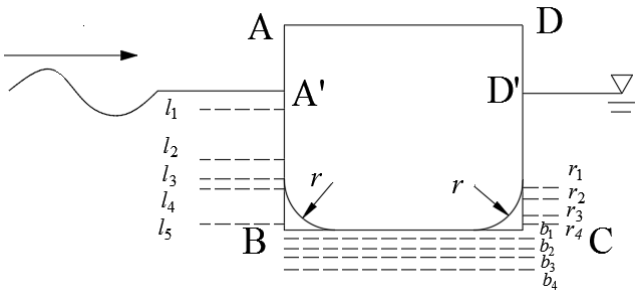


Figure 5.6.12: Diagram of the stationary box with both types of corner shapes and the locations of sampling points in the fluid field around the box for stationary object simulations. In the diagram, A and D represent two endpoints at the top of the box while A' and D' denote the points of intersection of the box with the still water level. The sampling points are categorized based on their location regions and then vertical positions (denoted by lines such as l_1). Several points are positioned at the same vertical locations. Typically, for the left and right sides of the region, 5 to 6 points are located on each line while for the bottom region, 8 to 10 points are distributed on each line.

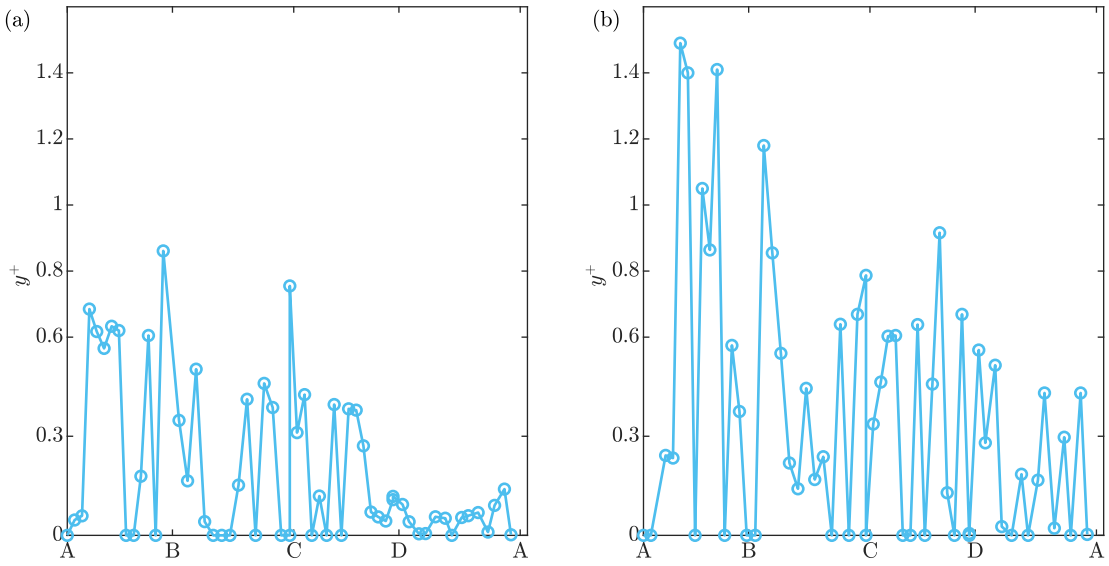


Figure 5.6.13: Time-averaged y^+ distribution over the edges of the stationary object for two values of wave steepnesses for the RANS simulations of a sharp-cornered box. (a) $ka_w = 0.034$,(b) $ka_w = 0.09$.

ka_w	l/λ (%)	Re_x ($\times 10^4$)	KC
0.03	10.0	1.97	0.33
0.07	10.0	6.18	0.67
0.09	10.0	7.99	0.87

Table 5.6.5: Particle Reynolds and Keulegan–Carpenter numbers for stationary objects for different wave steepness. The values of Reynolds and Keulegan–Carpenter numbers are the identical for sharp-cornered and round-cornered boxes.

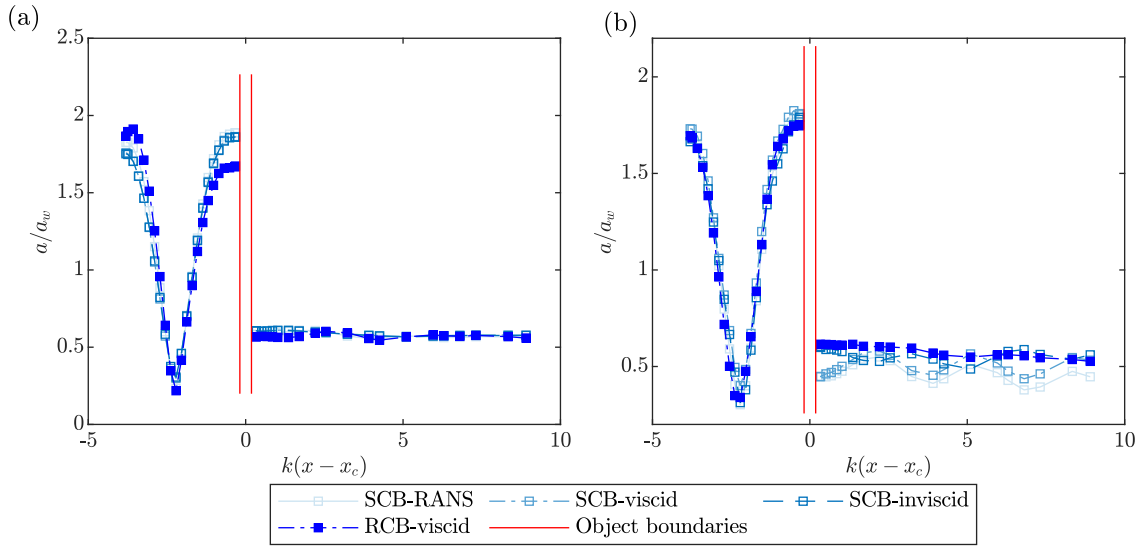


Figure 5.6.14: Standing wave pattern: amplitude of local wave surface elevation $a(x)$ as a function of horizontal distance from the centre of mass x_c for a stationary object of relative size $l/\lambda = 10\%$ with two different corner shapes. (a) different types of simulation in low wave steepness $ka_w = 0.034$, (b) different types of simulation in high wave steepness $ka_w = 0.09$. The local wave amplitude $a(x)$ is normalized by incoming wave amplitude a_w and the horizontal distance is scaled by the wavenumber. The object boundaries represent the left and right sides of the object.

tionary,it is straightforward to set sampling points around the object to collect time-history data for analysis. The sampling points are categorized into two types: points on the object boundaries and points in the surrounding fluid field. For the points on the object boundaries, we evenly distributed 10 points along each edge. Regarding the points in the surrounding fluid field, these are located in the left (front), bottom and right(rear) regions surrounding the objects, as shown in figure 5.6.12. The detailed coordinates of these points are provided in table 5.6.4. The distribution of points is designed to cover the main regions where the vorticity and flow separation occur. It is noteworthy that as the vorticity generation is not symmetrical on the upstream and downstream sides, we also distribute the sampling points asymmetrically. Specifically, for the left region, our sampling points span $0.13l$, while for the right side, only $0.05l$ is considered. Figure 5.6.13 gives the y^+ distribution over the object boundaries for the lowest and highest wave steepness values in the RANS simulations. It demonstrates that the current mesh used ensures that most of the mean value of y^+ across all boundaries remains smaller than 1 except for very small parts on AB for the highest wave steepness are larger than 1 where the region is either on the air phase or near the free surface. Suffice to say, the mesh used is sufficient for the wall-resolving models. The corresponding particle Reynolds numbers

and Keulegan–Carpenter (KC) numbers are given in table 5.6.5. Compared to the moving object, both particle Reynolds numbers and Keulegan–Carpenter numbers for stationary objects fall within the same flow regimes but have slightly larger values, leading to larger regions where vortex and wake structures are observed.

We conducted a wave-field analysis to examine wave diffraction effects on the stationary objects. The results are shown in figure 5.6.14 for $ka_w = 0.034$ and $ka_w = 0.09$. For low wave steepness, in line with the observations in section §5.6.1, the sharp-cornered boxes induce a larger standing wave pattern compared to the round-cornered boxes, with no significant variation across different simulation types. For high wave steepness, however, the difference between the two types of objects diminishes noticeably. Furthermore, it is observed that the normalized wave pattern in high wave steepness (maximum $a/a_w = 1.8$) is smaller than that for low wave steepness (maximum $a/a_w = 2.0$). This finding aligns with the conclusions drawn by Xiao et al. (2024), indicating that as the wave steepness increases, the standing wave pattern normalized by wave amplitude decreases, resulting in smaller drift amplification factor.

Vorticity and dynamic pressure field

Next, we examine the fluid and vorticity fields over one wave cycle. Figure 5.6.15 presents the vorticity magnitude field over one wave period for the RANS simulations of a stationary object with sharp corners when $t^* = t - 40$s (which is larger than $t_s = 32$s). We can see that the vorticity is asymmetrically generated around the two corners. The front (left) region experiences larger vorticity, covering a large extensive area compared to the rear region. Additionally, the vorticity pattern appears to be periodic, as evident when comparing panel (a) with panel (f) at $t = 0$ and $t = 0.98T$, respectively. In contrast, figure 5.6.16 gives the corresponding vorticity field for round-cornered boxes. The streamlines are smooth with a clean field containing little vorticity, consistent with our findings for moving objects. Spectral analysis of the turbulent kinetic energy for the sampling points in the fluid field is conducted in appendix §5.A.

The corresponding dynamic pressure fields for boxes with sharp-cornered and round-cornered boxes are given in figures 5.6.17 and 5.6.18, respectively. A noticeable difference can be observed in the pressure gradient/distributions at the locations where the vorticity is generated, leading to different pressure forces after integration over the boundaries. We note that similar analyses

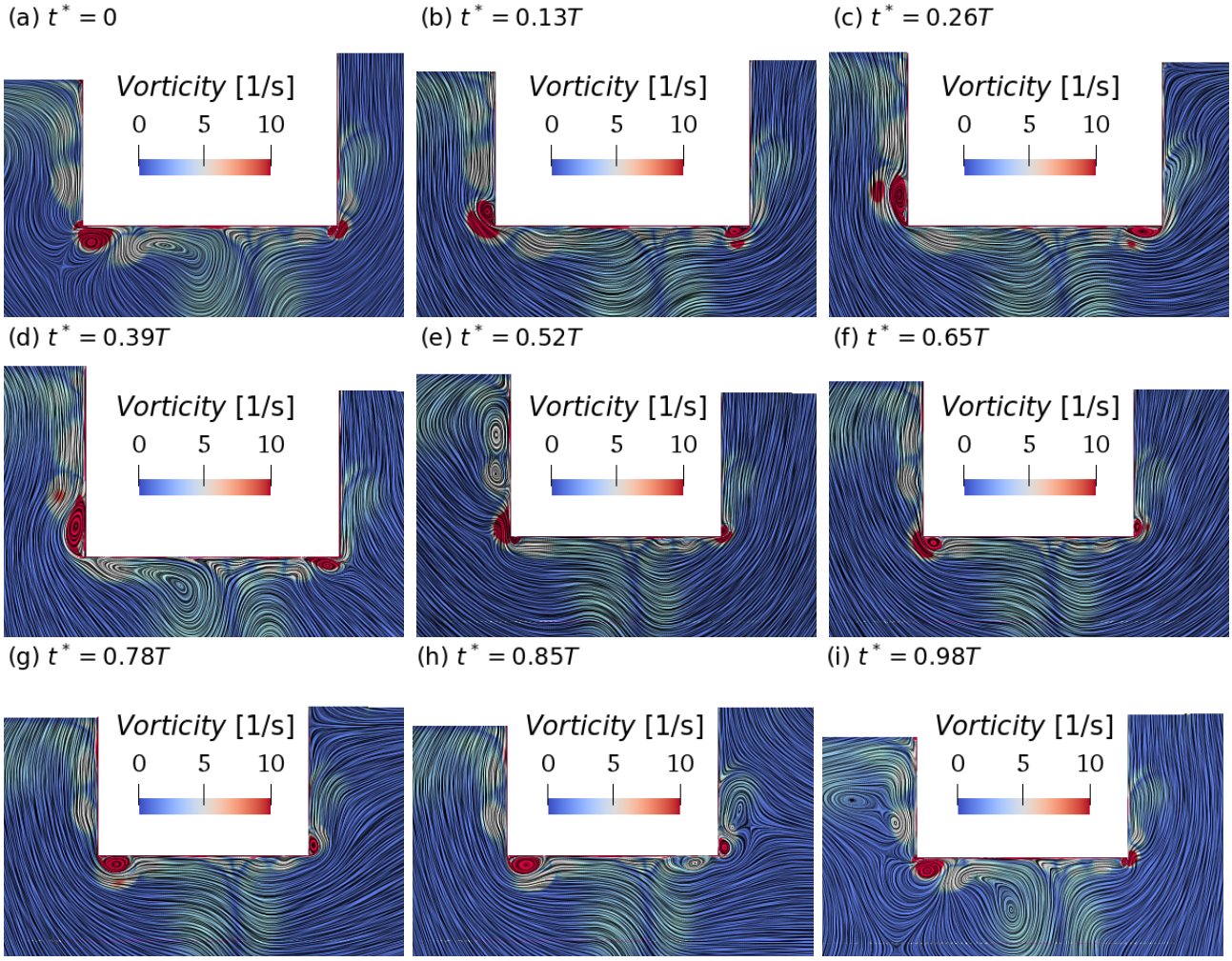


Figure 5.6.15: Vorticity magnitude field (the curl of the velocity field) across one wave period for the RANS simulations of a stationary sharp-cornered box with $l/\lambda = 10\%$ for $ka_w = 0.034$.

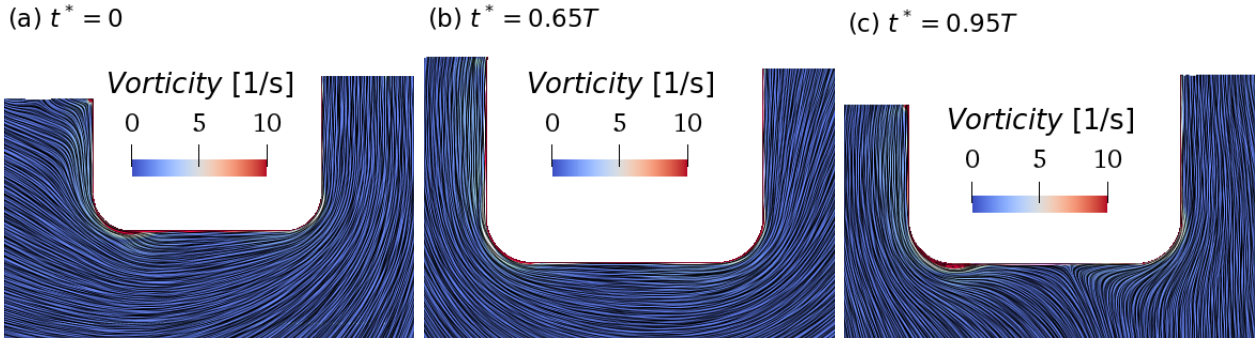


Figure 5.6.16: Vorticity magnitude field (the curl of the velocity field) across one wave period for viscid simulations of a stationary round-cornered box with $l/\lambda = 10\%$ when $ka_w = 0.034$. Time starts at $t^* = t - 40$s (after $t_s = 32$s) for initial time $t^* = 0$s, as denoted in the figures. Only the submerged part is shown, achieved by only displaying phase fraction value $\alpha \geq 0.5$.

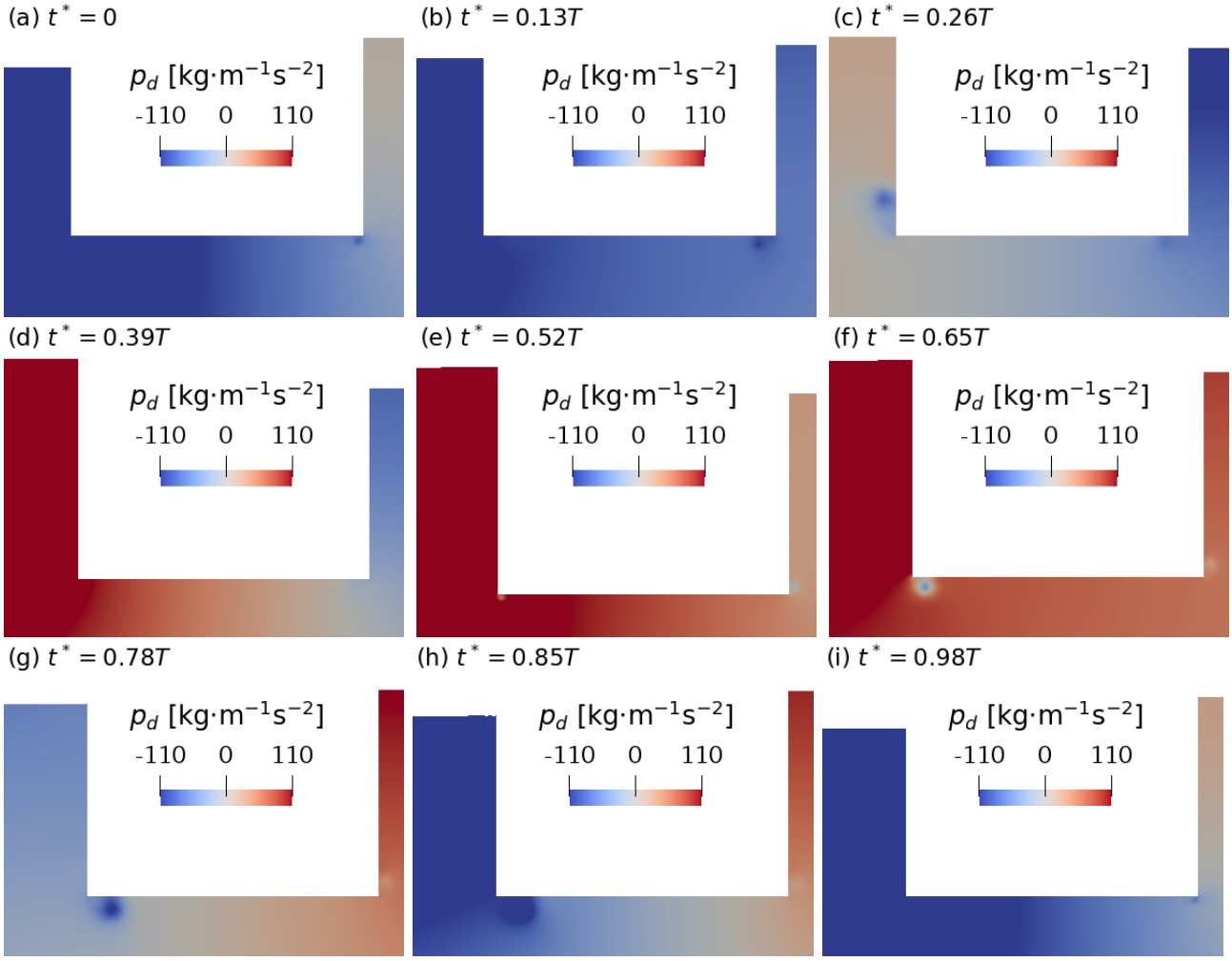


Figure 5.6.17: Dynamic pressure field p_d across one wave period for RANS simulations of a stationary sharp-cornered box with $l/\lambda = 10\%$ when $ka_w = 0.034$. Time starts at $t^* = t - 40$s (after $t_s = 32$s) for initial time $t^* = 0$s, as denoted in the figures. Only the submerged part is shown, achieved by only displaying phase fraction value $\alpha \geq 0.5$.

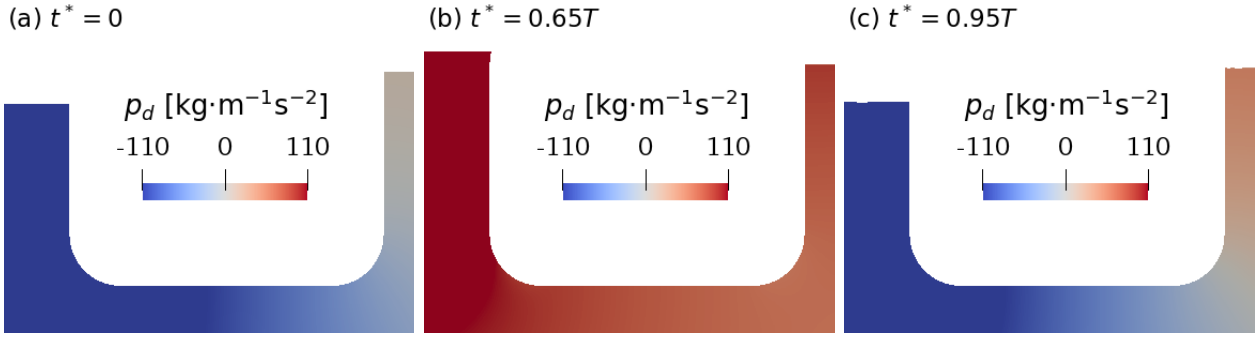


Figure 5.6.18: Dynamic pressure field p_d across one wave period for viscid simulations of a stationary round-cornered box with $l/\lambda = 10\%$ when $ka_w = 0.034$. Time starts at $t^* = t - 40$s (after $t_s = 32$s) for initial time $t^* = 0$s, as denoted in the figures. Only the submerged part is shown, achieved by only displaying phase fraction value $\alpha \geq 0.5$.

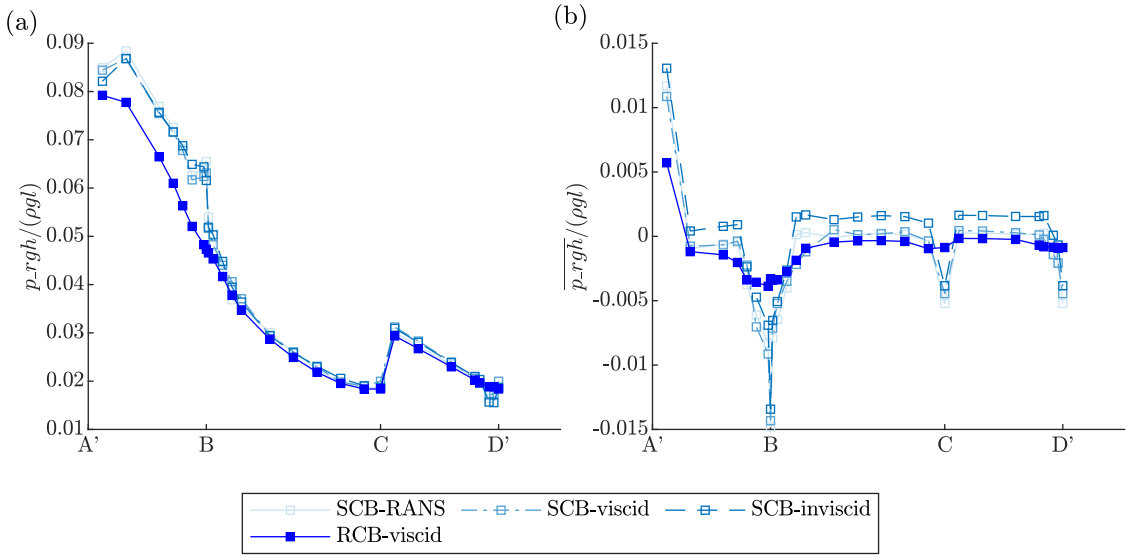


Figure 5.6.19: Dynamic pressure p_rgh (scaled by ρgl) distributions over the object boundaries for objects with $l/\lambda = 10\%$ and two different corner shapes for $ka_w = 0.034$. (a) dynamic pressure magnitude (p_rgh), normalized by ρgl, for different types of simulations. (b) mean values of dynamic pressure $\overline{p_rgh}$, normalized by ρgl, for different types of simulations.

are conducted for viscid and inviscid simulations of the sharp-cornered box, revealing larger vorticity magnitude and broader vorticity generation areas in inviscid simulations compared to RANS and viscid simulations. This subsequently induces different dynamic pressure fields and pressure forces. The inclusion of viscosity helps to suppress the generation of vorticity and reduce its magnitude. However, these results are not presented here for brevity. The trends observed are consistent for higher wave steepness, albeit with larger vorticity magnitudes in larger areas.

To further support and quantify these observations, we analyze dynamic pressure over the object boundaries. The magnitude and time-averaged value of the dynamic pressure for low wave steepness, serving as a representative case, are given in figure 5.6.19 where the magnitude (of the oscillatory part) and the mean value are both evaluated after t_s. The figure shows that the primary difference between the two types of objects occurs on the front edges.

Force analysis

Thus far, we have looked at how the vorticity generated due to the sharp corner alters the dynamic pressure distributions. The analysis proceeds to examine the relationship between dynamic pressure distributions and object motions over time through analysis of the forces, as shown in figure 5.6.20. Here, both magnitudes and mean values of the pressure and viscous

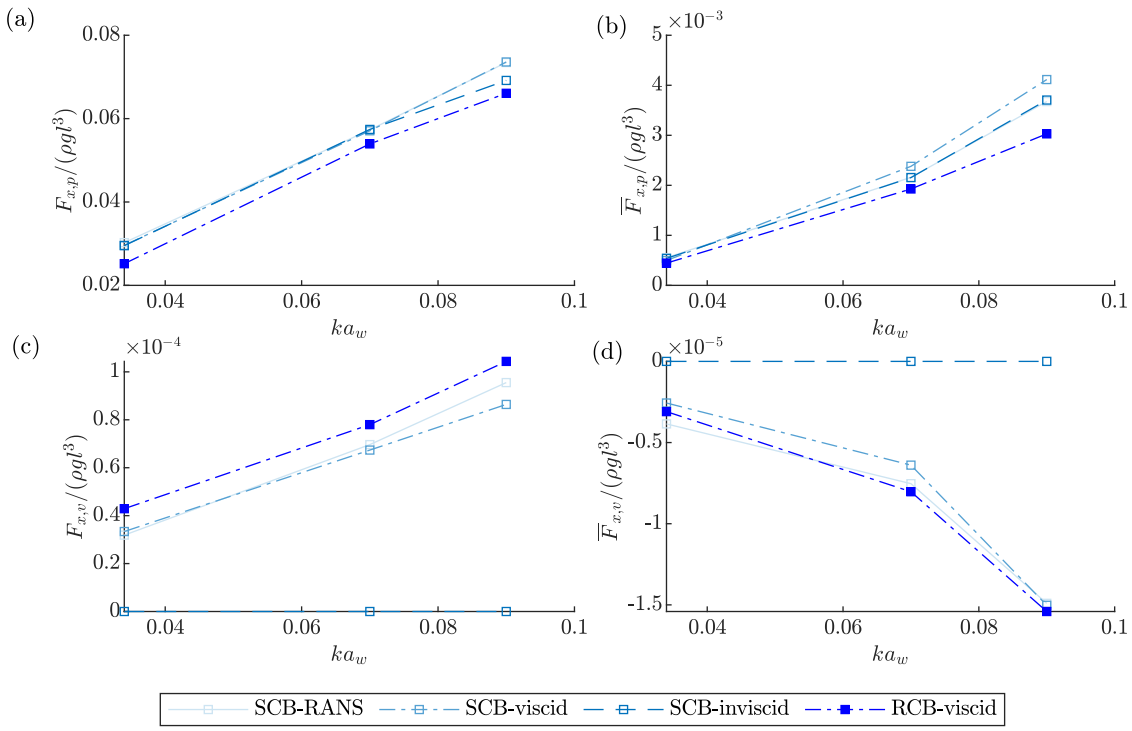


Figure 5.6.20: Non-dimensional horizontal forces as a function of wave steepness for objects with different corner shapes in different types of simulations: (a) magnitudes of the oscillatory part of pressure forces $F_{x,p}$, normalized by $\rho g l^3$; (b) mean values of pressure forces $\overline{F}_{x,p}$, normalized by $\rho g l^3$, over the simulated time duration after $t_s = 21T$; (c) magnitudes of the oscillatory part of viscous forces $F_{x,v}$, normalized by $\rho g l^3$; (d) mean values of viscous forces $\overline{F}_{x,v}$, normalized by $\rho g l^3$, over the simulated time duration after $t_s = 21T$. Notably, for 'SCB-inviscid', viscous forces are all 0 owing to the absence of viscosity in these simulations.

forces are compared. It is shown that sharp-cornered boxes exhibit larger oscillatory magnitudes and mean values of pressure forces relative to round-cornered boxes, aligning with the observations from figure 5.6.19. Conversely, the forces for round-cornered boxes have larger viscous magnitudes and absolute mean values compared to their sharp-cornered counterparts. Comparing with those for moving objects in figure 5.6.7, we see consistent results that sharp-cornered boxes experience larger mean values for both pressure forces and viscous forces, as well as larger magnitudes of viscous oscillatory forces. This consistency suggests that the larger mean values of the forces experienced by the sharp-cornered box in section §5.6.1 is directly related to the accelerations of the object drift, manifesting as enhanced drift. However, for moving objects, there is no pronounced difference between the two types of objects regarding the magnitude of oscillatory pressure forces. This discrepancy may be attributed to the object's drift motion, which alleviates the impedance and disturbance caused by the objects to the fluid field, thereby mitigating the differences between the two types of objects.

5.7 Conclusion

This chapter has investigated the influence of corner shape on the drift behaviour of bluff-bodied objects (rectangular boxes) floating on unidirectional, deep-water surface gravity waves. Two different corner shapes are considered: sharp corners and round corners with a corner radius of up to 24% of the object's draft. Three types of models are used: RANS simulation (including turbulent and kinematic viscosity), viscid simulation (only incorporating kinematic viscosity) and inviscid simulations (without viscosity). We restrict our analysis to objects with sizes less than 10% of the wavelength. The particle Reynolds and Keulegan–Carpenter numbers are in the range of $6 < \mathrm{Re}_x < 8 \times 10^4$ and $0 < \mathrm{KC} < 0.9$, suggesting turbulent wake (with laminar boundary layer separation) and a small amount of flow separation. We observe vortex formation in the simulations of sharp-cornered boxes which is absent for round-cornered boxes. We observe significantly larger drift enhancement (compared to the theoretical Stokes drift) for objects with sharp corners and show that the drift of these objects becomes unsteady. In addition to previously identified mechanisms of drift enhancement that arise from (viscous) drag (Calvert et al., 2021) and diffraction of the wave field (Xiao et al., 2024), which together explain only part of the drift enhancement found here, we identify another mechanism related to vortex formation that contributes to the drift enhancement of objects with sharp corners.

Consistent with the findings of Calvert et al. (2021); Xiao et al. (2024), we observe that drift enhancement for boxes with both shapes of corners is only relevant for objects larger than a few percent of the wavelength. For smaller objects ($l/\lambda \leq 3\%$ in this study), the non-Lagrangian behaviour is less evident and the drift speed of the objects is equal to the Stokes drift. However, as size increases, a difference in velocity between the object and its surrounding fluid emerges due to the object's inertia, leading to enhanced drift compared to a Lagrangian tracer. Importantly, objects with sharp corners experience much greater drift enhancement than objects of equivalent size with round corners. For instance, compared to a Lagrangian tracer, there is a 454% increase in drift for a sharp-cornered box and a 134% increase for a round-cornered box when $l/\lambda = 10\%$. Furthermore, sharp-cornered boxes experience enhanced drift from relatively smaller sizes ($l/\lambda \geq 4\%$) compared to round-cornered boxes ($l/\lambda \geq 7\%$). The presence of vorticity due to the sharp corners results in changes to the dynamic pressure field and subsequently affects the forces exerted on the object. Larger magnitudes of

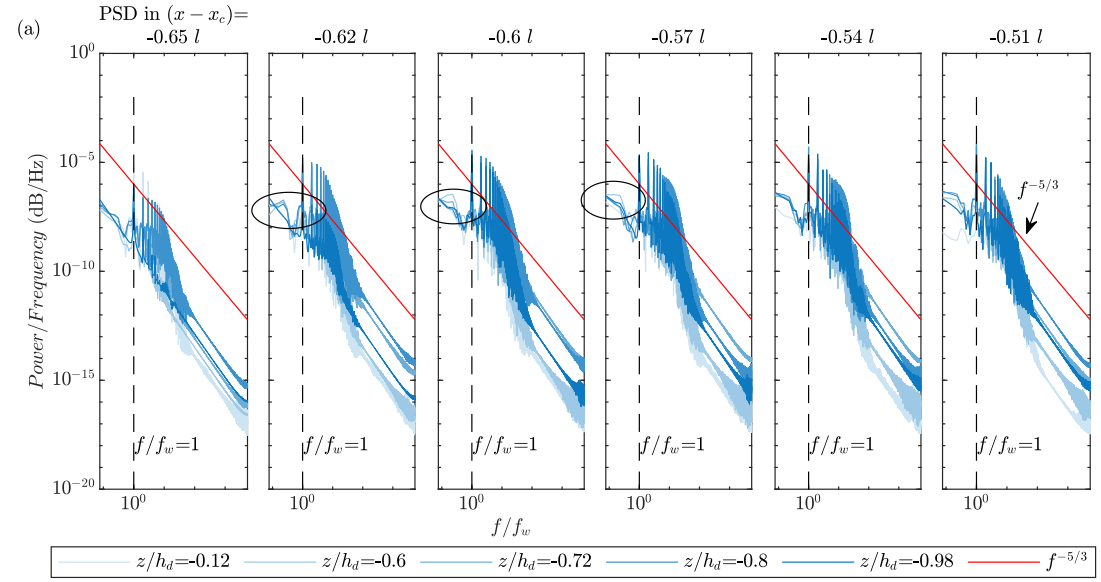
vorticity and vorticity-containing regions on the upstream side of sharp-cornered boxes lead to larger magnitudes of the oscillatory forces (more observable for stationary objects) and mean (time-averaged) forces. Viscosity plays a dual role in object drift. First, viscosity induces a phase difference between the object and the surrounding fluid, which acts to enhance drift, as described by Calvert et al. (2021); this occurs for objects with both sharp and round corners. Second, viscosity suppresses vorticity generation, reducing its magnitude and restraining its development for sharp-cornered boxes, thus mitigating drift enhancement.

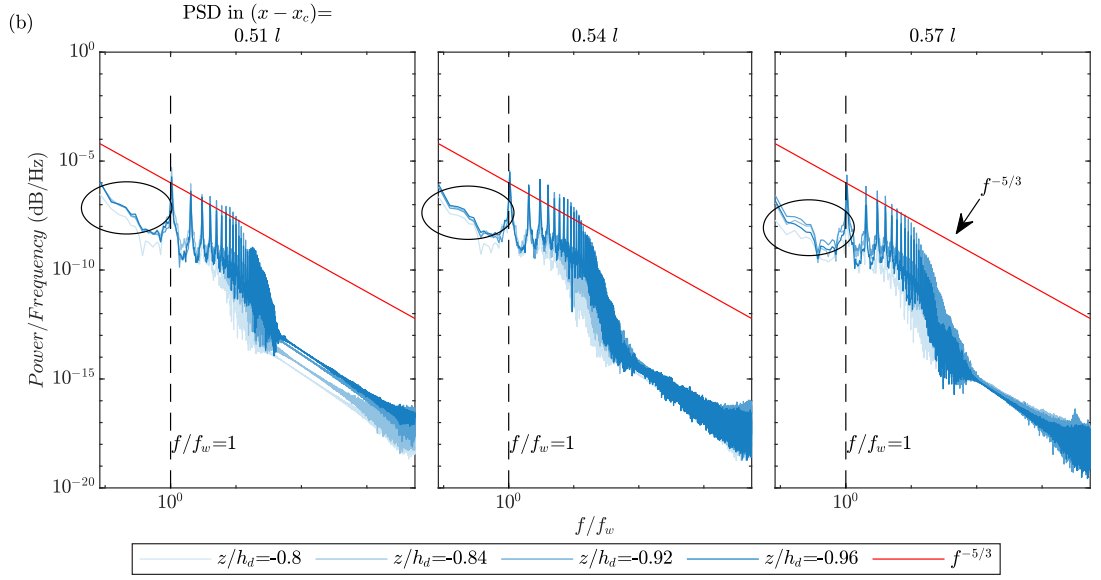
Finally, we examine the potential unsteadiness of the drift of objects. Our analysis reveals that the unsteadiness of the drift of objects with sharp corners is larger than that of round-cornered objects. Evaluating the unsteadiness over different durations using experimental data from chapter 4 suggests that, for low wave steepness, the duration of numerical simulations may not be sufficient for the transient term to disappear (or for the object to reach a quasi-steady state), indicating that at least part of the unsteadiness will diminish with time and may be the result of an initial transient. However, considering that vorticity is periodically generated by the periodic incoming waves, it is likely that the unsteadiness of drift is fundamental and persists over time. Determining which of the two hypotheses is correct requires longer duration experiments and numerical simulations, and these are recommended as future work.

Appendices

5.A Spectral analysis of turbulent kinetic energy

To analyze the turbulent statistics in the fluid field around the object, we conduct a spectral analysis of the turbulent kinetic energy k_e based on the time history collected at the sampling points in the fluid field defined in table 5.6.4. The power spectral density of k at left (front), bottom and right (rear) regions is presented in figure 5.A.1. We selectively chose sampling points within regions where vorticity is pronounced, resulting in uneven distributions at the upstream and downstream regions. For the left region, where vorticity is generated and covers $0.13l$, turbulent energy k_e is observed to follow Kolmogorov's 5/3 law. As points move closer to the object, the power spectral density of k_e increases, indicating a more turbulent fluid field. Notably, at $x = -0.65l$, turbulent energy is only observed at locations $z = -0.72h_d$ and $z = -0.8h_d$, while points closer to the object exhibit more turbulent energy distribution. For points located at $x - x_c = -0.52l$, that is just $0.015l$ from edge AD (the left edge of the object), the turbulent region spans the entire sampling region $-0.12h_d \leq z \leq 1$. Compared to the upstream side, the downstream side contains less turbulent energy, with the turbulent region spanning a smaller horizontal and vertical extent.


(a)
PSD in $(x - x_c)$=
-0.65 l
-0.62 l
-0.6 l
-0.57 l
-0.54 l
-0.51 l
Power/Frequency (dB/Hz)
f/f_w
$f^{-5/3}$
f/f_w=1
z/h_d=-0.12
z/h_d=-0.6
z/h_d=-0.72
z/h_d=-0.8
z/h_d=-0.98
$f^{-5/3}$


(b)
PSD in $(x - x_c)$=
0.51 l
0.54 l
0.57 l
Power/Frequency (dB/Hz)
f/f_w
$f^{-5/3}$
f/f_w=1
z/h_d=-0.8
z/h_d=-0.84
z/h_d=-0.92
z/h_d=-0.96
$f^{-5/3}$

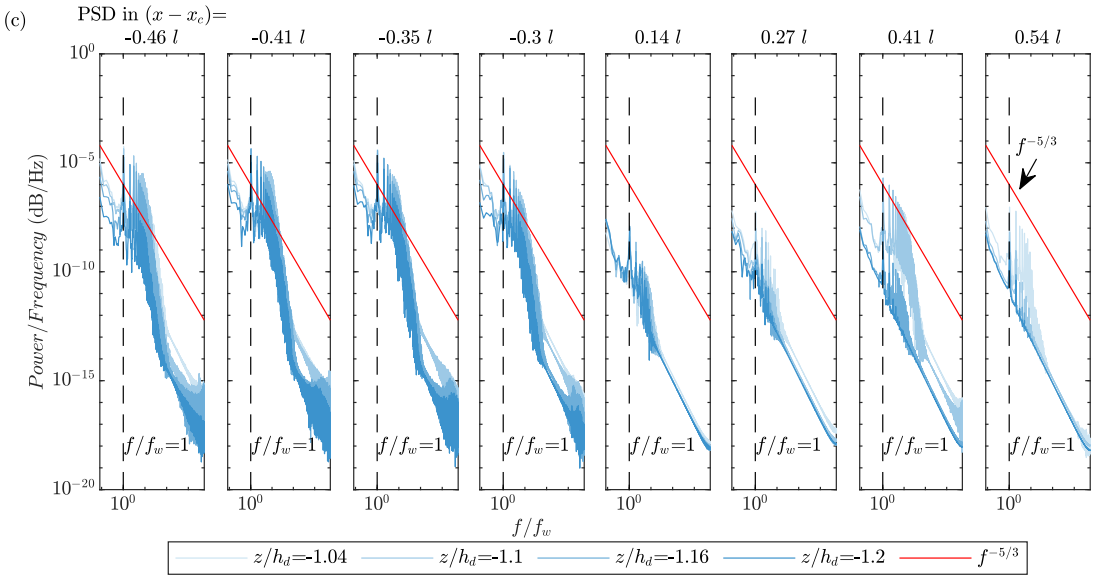

(c)
PSD in $(x - x_c)$=
-0.46 l
-0.41 l
-0.35 l
-0.3 l
0.14 l
0.27 l
0.41 l
0.54 l
Power/Frequency (dB/Hz)
f/f_w
$f^{-5/3}$
f/f_w=1
z/h_d=-1.04
z/h_d=-1.1
z/h_d=-1.16
z/h_d=-1.2
$f^{-5/3}$

Figure 5.A.1 *(previous page)*: Power spectral density (PSD) of turbulent kinetic energy (TKE) k_e at sampling points in the fluid field around the object for RANS simulations of stationary objects ($l/\lambda = 10\%$) with sharp corners when $ka = 0.034$. (a) left (front region) (b) rear (right) region (c) bottom region. The red lines represent the theoretical lines of Kolmogorov's 5/3 law in the inertial subrange. The left and right boundaries of the object are located at $x - x_c = -0.5l$ and $x - x_c = 0.5l$, respectively. The bottom boundaries are located at $z/h_d = 1$, $x - x_c = [-0.5l, 0.5l]$.

To be more specific, the region in the downstream side spans from $0.05l$ horizontally and $0.2h_d$ vertically (vs. $0.13l$ horizontally and $0.88h_d$ vertically for the upstream side). In the bottom region, points on the left side accumulate more turbulent energy and have a larger vertical span compared to the right side region. In addition to the turbulent energy peak at the frequencies $f/f_w \geq 1.0$ Hz, there is a large amount of turbulent energy for $f/f_w \leq 1.0$ Hz. There is an area for $f/f_w \leq 1.0$ Hz that gains local increase as frequency increases (outlined by ellipse in the corresponding figures) in the left region of which the pattern is not observed in the right region. Because those frequencies are lower than the frequency of objects' linear motion (equal to the incident wave frequency), it induces more sub-harmonic disturbance for the object's drift, which might help to explain the unsteadiness and time-decaying components found in section §5.6.1.

Chapter 6

Conclusions and recommendations

6.1 Summary

Effective plastic management and cleaning necessitates a better understanding of the physical processes that govern mass transport and dispersion. This thesis has examined the wave-induced drift by regular waves using theoretical, numerical, and experimental approaches. The exploration is conducted within a specific parameter space focusing on object sizes within the range of $1\% \leq l/\lambda \leq 30\%$ (where l is the object size and λ denotes the wavelength) and wave steepness values ranging from $0.03 \leq ka_w \leq 0.3$. The research seeks to answer the following four key questions, which are stated in the introduction Chapter and repeated here: (1) What role does the size play in influencing objects' drift in comparison to an infinitely small fluid particle? (2) How does the shape impact the object's drift behaviour? (3) In what manner does the drift of an object change with variations in wave steepness? (4) To what extent do viscosity and vorticity contribute to the alteration of object drift? The reference and baseline for all measurements and analysis is established by considering an object of a very small size (relative size l/λ down to 1%). At this scale, the object behaves as a perfect Lagrangian tracer and follows 'standard' Stokes drift. The validity and reliability of numerical, theoretical models and experimental designs are confirmed against this baseline. The key findings derived from this thesis study on object drift are summarised below.

In Chapter 3, an in-depth exploration is conducted to analyze the effects of size, shape, submergence depth, and wave steepness on the drift of floating objects in regular deep water waves. We consider unidirectional waves and a problem in two dimensions. Modelling has

been carried out using a hybrid numerical model called qaleFOAM that encompasses viscous effects and the ability to capture wave-body interaction dynamics. The qaleFOAM model couples a fully nonlinear potential model with a two-phase Navier–Stokes (NS) model. This hybrid numerical model is validated by considering both the wave field and the oscillatory motion and drift of very small objects. The drifts of fluid parcels and very small objects agree perfectly with the theoretical Stokes drift. Of great importance is the accurate simulation of the velocity fields of the waves to such an extent that drift rates can be estimated accurately. Drift motions in a (numerical) wave tank are very sensitive to wave-averaged (or sub-harmonic) velocities, which must be controlled with special care. In our simulations, these Eulerian-mean wave-averaged velocities are negligibly small. Simulations are carried out with and without viscosity for various objects of different sizes, shapes (a rectangular box and a round object) and submergence depths across a variety of wave steepness. The dependence of object drift rates on these factors is investigated. The role played by viscosity in different scenarios has been investigated. To complement the numerical models, a linear BEM model is employed to model the wave-body interaction without the inclusion of viscosity, and the results of this model are compared with those by the qaleFOAM model. Notably, the linear BEM model is used to derive an estimate of what we term the 'Diffraction-modified Stokes drift' in a fashion akin to the Stokes drift (Stokes, 1847), which can be decomposed into contributions from the incident, diffracted and radiated wave fields and from horizontal and vertical components of the object's motion.

Based on numerical modeling, we distinguish two mechanisms that can explain enhanced drift, compared to standard Stokes drift: viscosity and diffraction effects. Both these mechanisms come into play as the size of the object increases. When the object is small, its inertial behaviour is not evident, leading to a minimal difference in velocity between the object and the surrounding fluid. Consequently, the drift motion becomes Lagrangian with no obvious deviation from the incident wave amplitude in the magnitudes of the oscillatory linear motions in both horizontal and vertical directions. However, as the object size increases, an enhanced motion in the normal direction to the free surface emerges, altering the motion orbit and inducing a drag force due to the difference between the object's motion and the surrounding fluid. This phenomenon results in enhanced horizontal drift (Calvert et al., 2021). Moreover, as the

object size increases, the draft (submergence) becomes larger, and the box-shaped (less streamlined) submerged part of the object acts as an impediment to fluid motion (induced by wave propagation) and thereby the waves themselves. The relative difference in surface elevation between the two sides of the object induces a drift increase. The impeding effect varies based on the size and shape of the submerged part, thereby inducing drift enhancement to a different degree. Larger submergence and less streamlined objects intensify the impeding effect, yielding more significant surface elevation differences and horizontal forces, consequently a greater increase in horizontal drift. Furthermore, in the presence of viscosity, the drift experiences further enhancement.

Additionally, we employ the linear BEM model to characterize the wave elevation distribution and linear motions. The results by the BEM model are compared with those of the QaleFOAM model. The second mechanism found by the QaleFOAM has been re-investigated and supported by the BEM model. Moreover, the BEM model is applied to predict the drift of the object by decomposing it into three parts: incident part, radiation part, and diffraction part. We identified two ways the factors of size, shape, submergence, and wave steepness affect those components, providing further explanations of the differential drift behaviours. On one hand, the difference in linear motions and phases between the object and the theoretical waves alters the incident part and thus induces the deviation from theoretical Stokes drift. On the other hand, the balanced relationship between the radiation and diffraction contributions determines the extra contribution to the overall drift.

In Chapter 4, we present the findings of an experimental study of drifts of essentially 2D objects under unidirectional deep-water surface gravity regular waves. The measurements provide experimental evidence for the diffraction-based mechanism identified in Chapter 3 in low and intermediate wave steepness. Based on the data, we identified several patterns that characterize the drift behaviour for various relative sizes and wave steepness. In addition, we relate the critical size in Harms (1987) to heave motion instead of roll motion to explain the behaviour changes in different relative sizes.

We restrict our analysis to objects ranging from 2.6% to 27.1% of the size of the wavelength, with wave steepness values ranging from $0.04< ka_w <0.31$. By showing the drift of a 2D type of object of l/λ=2.6% agrees with the 3D small balls of l/λ=1.05%, we have demonstrated the

Lagrangian behaviour of the smallest of our 2D objects. Our observations reveal an enhanced drift for larger objects across all investigated wave steepness values. This enhancement is found to be a function of the object's relative size and wave steepness. Particularly, we identified a critical size regarding the object's relative size. When the object is smaller than the identified critical size, drift enhancement increases with size for all wave steepness. However, when the object surpasses the critical size, the pattern of drift enhancement with the wave steepness becomes non-monotonous. For low wave steepness, the enhancement continues to increase with size, while for high wave steepness, a decreasing trend is observed. This phenomenon is intricately linked to the way the drift increases with wave steepness.

In the case of very small objects, drift increases as an approximately quadratic function of wave steepness (cf. (4.1)), and as the object becomes larger, the drift exhibits a more linear increase (cf. Tanizawa et al. (2001); He et al. (2016)). Near the critical size, this trend undergoes a breakdown, and there is a local peak for the linear correlations and a local trough for the quadratic components. The presence of a similar critical size phenomenon is further examined for vertical oscillatory motions. However, this is not the case for horizontal motions which exhibit a monotonic reduction with relative size. This transition size phenomenon is found to be intimately related to the natural heave and roll frequency (surge motion does not have such frequency as it has no 'stiffness'). We also reported a standing wave pattern for larger objects compared with the wave field for very small objects, which gives experimental evidence for the mechanism identified in Chapter 3.

To assess the effectiveness of the theoretical model derived in Chapter 3 across different relative sizes and wave steepness, and to evaluate the applicability range of corresponding theories, we conduct a comparison with the experimental data. The comparison involves three models: the theoretical Stokes drift (Stokes, 1847), diffraction-modified Stokes drift (presented in Chapter 3), and empirical formula proposed by Harms (1987). A pattern emerges in assessing the drift enhancement amplification to the Stokes drift (i.e. $u_{S,O}/u_S$ where $u_{S,O}$ refers to the Stokes object drift predicted by the diffraction-modified Stokes drift model). The amplification factor reaches its maximum at the smallest wave steepness and subsequently experiences a rapid decrease as the wave steepness increases up to a certain point. Beyond this point, the amplification factor tends to stabilize or experience a slight reduction for higher wave steepness.

This observed pattern holds for objects of different sizes. Notably, the wave steepness values at which this critical behaviour occurs vary with the relative size of the object. For a given wave steepness, as the relative size increases, the amplification factor increases and peaks at a certain size value before exhibiting gradual changes with sizes. This peak point value differs for low and high wave steepness. This explains the distinct enhanced behaviours of the drift with the relative size in low and high wave steepness.

Comparisons with the diffraction-modified Stokes drift reveal the model's robust prediction for relatively small objects but a breakdown in accuracy for larger objects. This effective limit regarding the size is more pronounced for larger objects in high-wave steepness scenarios, owing to the linear nature (i.e. $u_{S,O}/u_S$ predicted by the model remains constant for a specific size) and the milder amplification changes associated with higher wave steepness which vary less with object size. The empirical formula by Harms (1987) relates the drift to its natural roll frequency and predicts the drift. However, we propose relating the critical size to the heave motion instead of the roll motion. Based on the comparison, we introduce a range in relative size and wave steepness that encapsulates the effective limit for the theoretical models.

The effect of corner shapes on drift is explored in Chapter 5 by conducting numerical simulations based on the QaleFOAM model. Two different corner shapes, sharp and round, are investigated across a variety of object sizes ranging from 1% to 10% of the wavelength. Given the emergence of vorticity in sharp-cornered simulations, three types of simulations are performed to explore the effects of viscosity and turbulence: turbulent modeling, laminar modelling and Euler inviscid modeling. A significantly larger enhanced drift is observed in sharp-cornered objects compared to their round-cornered counterparts for large objects. In addition to the factors of phase difference in linear motions and induced diffraction patterns, a primary factor associated with the vorticity pattern is identified as the main contributor to the drift difference between two groups of objects. To gain more insights and explore further, a detailed examination of the vorticity pattern and forces is conducted for stationary objects with a relative size of $l/\lambda = 10\%$ across different wave steepnesses. The effects of viscosity and turbulent viscosity are explored through comparisons between results from different types of simulations.

A convergence study has been conducted firstly for the stationary object simulations across

three sets of meshes in different wave steepness. The convergence statistics are analyzed, and convergence is achieved by employing the generalized Richardson Extrapolation to estimate the errors and uncertainties. Then, for moving objects, the model is validated by predicting Stokes drift for a sharp-cornered object of 1% of the wavelength. The corresponding convergence test is carried out by two sets of meshes, assessing the convergence of several key quantities including drift.

Linear oscillatory motions, encompassing both magnitude and phase, are analyzed and compared for both groups–those with sharp corners and those with round corners. It is shown that for small object, the deviation in magnitude and phase of both groups from those of a Lagrangian particle is minimal and becomes more evident as the object size increases. Consistent with the findings in Xiao et al. (2024), larger objects, in comparison to Lagrangian particles and very small objects, experience a reduced magnitude and phase lag horizontally but an enhanced magnitude and phase lead vertically. Generally, in contrast to round-cornered objects, the group with sharp corners experiences a slightly lesser reduction in horizontal motion magnitude and a smaller phase difference in both directions. The presence of viscosity and turbulent viscosity causes minimal influence on the linear motions.

The drift velocities of the two groups are compared across various sizes. Initially, small objects in both groups follow the Stokes drift. However, as the object size increases, the sharp-cornered group exhibits a notably greater drift enhancement compared to the round-cornered counterparts. The presence of viscosity and turbulent viscosity appears to reduce this drift enhancement. According to Xiao et al. (2024), a smaller phase difference (between that of an object and a Lagrangian tracer) and a larger motion magnitude contribute to drift enhancement. Additionally, wave field analyses of both groups reveal that when the object size is relatively large, the sharp-cornered boxes generate larger standing wave patterns which also contributes to the drift increase. Nevertheless, these two factors only explain a fraction of the substantial difference in drift enhancement between the two groups.

To further explain the difference in drift enhancement, we reevaluate the drift trajectories of the objects. Three different types of regression data fitting including linear fit, second-order fit, and exponential decay fit have been conducted. A drift unsteadiness ratio is defined based on the linear fit and second-order fit. It is found that the sharp-cornered group possesses a

smaller unsteadiness ratio representing higher unsteadiness, and this ratio, alongside the mean (time-averaged) acceleration of drift, is intimately related to the drift enhancement. Based on the experiment data, the unsteadiness in low wave steepness appears to correlate with the time duration of drift evaluation. Furthermore, the exponential decay fit of the drift suggests that objects with sharp corners exhibit a slower decay rate compared to round-cornered boxes. These observations suggest the presence of a transient component in the drift of the sharp-cornered boxes contributing to the evaluated drift enhancement.

Analysis of the fluid field reveals the presence of vorticity in sharp-corner simulations which is absent in round-corner simulations. A dominant factor associated with this vorticity has then been identified. Combined with the analysis of stationary objects, it is evident that the presence of vorticity alters the dynamic pressure distributions over and around the objects, consequently influencing the forces exerted on them. The asymmetrical generation of vorticity causes a non-zero mean force in the direction of wave propagation, resulting in positive mean accelerations in horizontal directions and ultimately, drift enhancement.

6.2 Research impact

The experimental observations, analytical solutions and numerical simulations of wave-induced drift in this thesis have affirmed the Lagrangian behaviour of very small objects in a 2D context. The numerical model marks the first effort to explore the drift of small objects with a complex flow model accommodating the effects of wave-body interactions, viscosity, vorticity and turbulence. The carefully designed 2D experiment is the first effort to validate the Stokes drift in 2D objects.

Plastic debris exhibits an extremely broad size and shape distribution, resulting in a diverse range of system drift behaviours. Varied drift behaviours arising from factors such as size, shape, and inertia can contribute to the sorting of floating plastic materials and subsequent accumulations in the oceans (Pattiaratchi et al., 2022). The findings in this paper suggest that floating plastics of different sizes, shapes, and submergence might follow different drift patterns. Specifically, larger debris with deeper submergence and less streamlined shapes are likely to drift faster and advance over other debris. This phenomenon may lead to the accumulation and formation of patches of plastic with similar characteristics that move together.

Accurate prediction and forecasting of ice conditions are pivotal for maritime operations, climate change studies, and the monitoring of oceanographic and biological conditions (Hebert et al., 2015). This thesis study may contribute to a better understanding of sea ice drift in regions like the Southern Ocean, Arctic, and Antarctic (Spreen et al., 2011; Holland and Kwok, 2012; Kwok et al., 2017). Additionally, it may provide insights into explaining discrepancies observed in drifting buoys and satellite-derived sea-ice motion data (Heil et al., 2001; Schwegmann et al., 2011; Hebert et al., 2015). The findings in this paper may contribute to explaining the enhanced drift of the icebergs, some of which have not yet been fully understood, such as the one in Wadhams (1983).

6.3 Recommendations for future work

The suggestions for future study are listed below:

- In Chapter 3, we evaluate drift in a steady state while introducing unsteadiness in Chapter 5. The mechanism associated with diffraction, identified in Chapter 3, suggests a momentum exchange between the waves and the object. However, a detailed analysis of the force and momentum balance leading to the objects' (enhanced) drift motion has not been conducted. The analysis based on momentum flux resulting from wave reflection might explicitly explain the mechanisms uncovered in Chapter 3 and provide deeper insight into enhanced drift.

- Chapter 3 explored the effect of viscosity and quantitatively compared the present results with the predictions of Calvert et al. (2021). However, this comparison is restricted to the group of round objects under low wave steepness conditions. To enhance our understanding of the viscosity effect, further comparisons should be conducted with the equivalent geometry dimensions (either reducing the 3D model of Calvert et al. (2021) to 2D or extending our 2D numerical simulations to 3D), taking account of Reynolds number (considering both laboratory scales and field scales) and wave steepness.

- A significant contribution of the Stokes drift in a coupled wave and ocean-current model is related to the vortex force term (Craik and Leibovich, 1976), which is essential for the interpretation of Langmuir cells initially observed by Langmuir (1938). The vertical shear of the

Stokes drift, when subjected to a (weak) disturbance, can convert vertical vorticity to horizontal vorticity, consequently inducing the CL2 type instability when the laminar Langmuir number falls below a critical threshold (Leibovich, 1983). However, in nature, Langmuir cells normally occur within the oceanic boundary layer where turbulence develops (Mcwilliams et al., 1997). It is of interest to explore the effects of Langmuir cells induced by CL2 instability mechanism on the Lagrangian transport of floating objects near the free surface. Rather than exploring Langmuir turbulence in a complicated large ocean model system, future work is recommended to enhance the understanding of the influence of Langmuir turbulence on wave-induced transport for objects with finite size.

- According to the theoretical analysis by Longuet-Higgins (1953, 1960), viscosity plays a significant role in drift velocity, and the gradient of the drift near the water surface was twice that of drift in irrotational waves. Supporting this theoretical perspective, experiments by Grue and Kolaas (2017) indicate the presence of streaming effects and pronounced vertical shear within a thin layer on the water surface. Potential future work should investigate the development of such boundary layer and its effect on the drift of objects with various degrees of submergence. This investigation might shed light on the interplay between viscosity, boundary-layer dynamics, and object drift for various objects.

- Chapter 4 has pinpointed a critical transition and turning point in both size and wave steepness, revealing fundamentally different mechanisms governing enhanced drift. Notably, the theoretical model developed in Chapter 3 encounters limitations for larger objects. Future work is required to find out the prevailing mechanisms beyond the transition size. Given that the present theoretical model is based on linear theory, it is of interest to explore the influence of introducing nonlinearities into the model, which might affect the diffraction field and drift amplification factors for larger objects and higher wave steepness.

- Chapter 5 has reported the unsteadiness of drift caused by the vorticity and turbulence. However, the specific mechanisms causing this unsteadiness and the time scale required for the object to attain force and moment balance remain unresolved questions. Future work is required to look at the dynamics of momentum exchange between the object and waves in the

presence of vorticity for the bluff body and investigate the effect of different geometry gradients, size, submergence, and wave steepness on trajectory modeling and drift unsteadiness.

- In the open ocean, one of the dominant transport mechanisms is ocean currents which include geostrophic, tidal, baroclinic, wind-driven currents, and wave-induced currents. Some currents exhibit a strong vertical profile, exerting an impact on the transport of floating objects in the open sea (Van der Mheen et al., 2020). There is a rich literature in the study of wave-current interactions (Huang and Mei, 2003; Ridler and Sleath, 2000) and surface current drift (Huang, 1979, 2007). To provide more insights into realistic forecasting of floating trajectories, future work is recommended to explore the drift of floating objects in the presence of both waves and currents and wave-current interactions. Besides, wave breaking occurs at a large range of scales on the world's oceans and is known to transport particles much faster than non-breaking waves (Pizzo, 2017; Deike et al., 2017a; Pizzo et al., 2019). The present thesis study only deals with non-breaking waves. Future study on the effects of wave breaking on the drift of inertial objects is therefore recommended. The Stokes drift in wave group is divergent, which induces the Eulerian-mean return flow immediately and thus will change the Lagrangian drift of the object (e.g., van den Bremer and Taylor (2015); Van den Bremer and Taylor (2016)). In addition, the drift with large 3D object in irregular waves is examined by Tanizawa et al. (2001); Le Boulluec et al. (2008). The drift velocity is explored as a function of relative wave length and relative significant wave height. Limited to regular waves, the current study is recommended to be extended to consider wave group and irregular waves.

- While the focus of this thesis study is on two-dimensional geometries, particularly relevant for scenarios like icebergs, it is acknowledged that such geometries are too restrictive to understand wave-induced drift in realistic environments. Although the transition between two-dimensional and three-dimensional geometries can be facilitated in the hybrid numerical model and experimental investigation by releasing the restriction of the third dimension, future work is recommended to initially investigate how the presence of the third dimension influences the diffraction-based mechanisms and the influence of object width. This is essential as the diffraction pattern may change with the introduction of an additional dimension, we expect the drift enhancement due to the diffraction effects to be reduced in 3D compared to 2D for a

unidirectional incident wave field, as waves can diffract around the object in 3D instead of just being either reflected or transmitted (2D). Also, the radiation wave field might be affected. It would also be of interest to examine the drift of the objects exposed to waves with directional spreading.

- To examine the extent to which Lagrangian mean flow is affected by the introduction of the finite object size in the current study, we first analyze its effects on the Stokes drift. In this thesis, It is found that the Stokes drift is affected on a scale of l/λ up to 30%, indicating that $l/\lambda = O(1)$ represents the extent to which waves and thus Stokes drift are affected by object size. For the Eulerian-mean flow, under extreme conditions where the object size is very large, and prohibits fluid passage. This could result in flow blockage, the Eulerian-mean flow would exhibit distinctly different structures compared to those observed in the current study. This suggests that the Eulerian flow is relevant to l/d, where d is the water depth. Evaluating the order of l/d in the current scenario, we find $l/d = \frac{l}{\lambda} \cdot \frac{\lambda}{d} = \frac{l}{\lambda} \cdot \frac{2\pi}{kd}$. Given that deep water wave conditions are considered where $kd >> 1$, we have $1/(kd) = O(\epsilon')$, with ϵ' representing a small number $\epsilon' << 1$. Consequently, we have $l/d = O(\epsilon')$ indicating the extent to which Eulerian-mean flow is affected by the object size. We hypothesize that the effect of finite object size on the Eulerian-mean flow field is more evident in shallow water depths, where the contribution of the second-order velocity potential to drift cannot be neglected (Pessoa and Fonseca, 2015). Therefore, we recommend it be examined in future work in both deep water and shallow water scenarios. The effect of finite depth to the Lagrangian drift is explored by van den Bremer and Taylor (2015). It is found that the Stokes drift dominates in the surface while the Eulerian current increases with depth. The finite depth is expected to affect the drift of object with finite size and thus recommended to be considered in the future.

References

Y. Agnon, H. S. Choi, and C. C. Mei. Slow drift of a floating cylinder in narrow-banded beam seas. *J. Fluid Mech.*, 190:141–163, 1988.

J. Alsina, C. E. Jongedijk, and E. van Sebille. Laboratory measurements of the wave-induced motion of plastic particles: Influence of wave period, plastic size and plastic density. *J. Geophys. Res-Oceans*, 125(12):e2020JC016294, 2020.

J. A. P. Aranha. A formula for 'wave damping' in the drift of a floating body. *J. Fluid Mech.*, 275:147–155, 1994.

A.I. Arikainen. Wave drift of an isolated floe. *AIDJEX Bulletin*, 1(16):125–131, 1972.

R. A. Bagnold. Sand movement by waves: Some small-scale experiments with sand of very low density. *J. Inst. Civ. Eng.*, 27(4):447–469, 1947.

J. Bai, N. Ma, X. Gu, et al. Numerical study of the interaction between combined wave-current and a horizontal cylinder close to the free surface. In *The 26th Int. Ocean Polar E.* International Society of Offshore and Polar Engineers, 2016.

C. K. Batchelor and G. K. Batchelor. *An introduction to fluid dynamics*. Cambridge University Press, 2000.

P. W. Bearman, J. M. R. Graham, E. D. Obasaju, and G. M. Drossopoulos. The influence of corner radius on the forces experienced by cylindrical bluff bodies in oscillatory flow. *Appl. Ocean Res.*, 6(2):83–89, 1984.

S. E. Belcher, A. L. M. Grant, K. E. Hanley, B. Fox-Kemper, L. Van Roekel, P. P. Sullivan, W. G. Large, A. Brown, A. Hines, D. Calvert, et al. A global perspective on Langmuir turbulence in the ocean surface boundary layer. *Geophys. Res. Lett.*, 39(18), 2012.

L. Bellomo, A. Griffa, S. Cosoli, P. Falco, R. Gerin, I. Iermano, A. Kalampokis, Z. Kokkini, A. Lana, M. G. Magaldi, et al. Toward an integrated HF radar network in the Mediterranean Sea to improve search and rescue and oil spill response: the TOSCA project experience. *J. Oper. Oceanogr.*, 8(2):95–107, 2015.

A. Bøckmann, C. Pâkozdi, T. Kristiansen, H. Jang, and J. Kim. An experimental and computational development of a benchmark solution for the validation of numerical wave tanks. In *International Conference on Offshore Mechanics and Arctic Engineering*, volume 45400, page V002T08A092. American Society of Mechanical Engineers, 2014.

Ø. Breivik, A. A. Allen, C. Maisondieu, and J. C. Roth. Wind-induced drift of objects at sea: The leeway field method. *Appl. Ocean Res.*, 33(2):100–109, 2011.

Ø. Breivik, A. A. Allen, C. Maisondieu, and M. Olagnon. Advances in search and rescue at sea. *Ocean Dynam.*, 1(63):83–88, 2013.

M. T. Brooks, V. J. Coles, and W. C. Coles. Inertia influences pelagic sargassum advection and distribution. *Geophys. Res. Lett.*, 46(5):2610–2618, 2019.

O. Bühler. *Waves and Mean Flows*. Cambridge University Press, Cambridge, UK, 2nd edition, 2014.

R. Calvert, M. L. McAllister, C. Whittaker, A. Raby, A. G. L. Borthwick, and T. S. van den Bremer. A mechanism for the increased wave-induced drift of floating marine litter. *J. Fluid Mech.*, 915, 2021.

X. Chen and H. Xia. A hybrid LES-RANS study on square cylinder unsteady heat transfer. *Int. J. heat mass tran.*, 108:1237–1254, 2017.

X. Chen, R. C. Zhu, J. Zhao, W. J. Zhou, and J. Fan. Study on weakly nonlinear motions of ship advancing in waves and influences of steady ship wave. *Ocean Eng.*, 150:243–257, 2018.

X. B. Chen. Approximation on the quadratic transfer function of low-frequency loads. In *Proceedings of 7th International BOSS Conference, 1994*, 1994.

M. Cole, P. Lindeque, C. Halsband, and T. S. Galloway. Microplastics as contaminants in the marine environment: a review. *Mar. pollut. bull.*, 62(12):2588–2597, 2011.

G. Colicchio, M. Greco, and O. M. Faltinsen. A BEM-level set domain-decomposition strategy for non-linear and fragmented interfacial flows. *Int. J. Numer. Meth. Eng.*, 67(10):1385–1419, 2006.

A. D. D. Craik. *Wave interactions and fluid flows*. Cambridge University Press, 1988.

A. D. D. Craik and S. Leibovich. A rational model for Langmuir circulations. *J. Fluid Mech.*, 73(3):401–426, 1976.

M. R. Dai, H. H. Shen, M. A. Hopkins, and S. F. Ackley. Wave rafting and the equilibrium pancake ice cover thickness. *J. Geophys. Res.-Oceans*, 109(C7), 2004.

D. G. Danmeier, R. K. M. Seah, T. Finnigan, D. Roddier, A. Aubault, M. Vache, and J. T. Imamura. Validation of wave run-up calculation methods for a gravity based structure. In *International Conference on Offshore Mechanics and Arctic Engineering*, volume 48234, pages 265–274, 2008.

D. DeBok and S. Roehrig. Numerical modelling of coast guard buoys in shallow water. In *OCEANS 81*, pages 174–179. IEEE, 1981.

L. Deike, N. Pizzo, and W. K. Melville. Lagrangian transport by breaking surface waves. *J. Fluid Mech.*, 829:364–391, 2017a.

L. Deike, N. Pizzo, and W. K. Melville. Lagrangian transport by breaking surface waves. *J. Fluid Mech.*, 829:364–391, 2017b.

N. K. Delany and N. E. Sorensen. Low-speed drag of cylinders of various shapes. Technical report, National Advisory Committee for Aeronautics., 1953.

B. Devolder, P. Schmitt, P. Rauwoens, B. Elsaesser, and P. Troch. A review of the implicit motion solver algorithm in OpenFOAM to simulate a heaving buoy. In *NUTTS conference*, volume 2015, page 18th, 2015.

M. H. DiBenedetto and N. T. Ouellette. Preferential orientation of spheroidal particles in wavy flow. *J. Fluid Mech.*, 856:850–869, 2018.

M. H. DiBenedetto, N. T. Ouellette, and J. R. Koseff. Transport of anisotropic particles under waves. *J. Fluid Mech.*, 837:320–340, 2018.

M. H. DiBenedetto, J. R. Koseff, and N. T. Ouellette. Orientation dynamics of nonspherical particles under surface gravity waves. *Phys. Rev. Fluids*, 4:034301, 2019.

M. H. DiBenedetto, L. K. Clark, and N. Pujara. Enhanced settling and dispersion of inertial particles in surface waves. *J. Fluid Mech.*, 936:A38, 2022.

D. Dobler, T. Huck, C. Maes, N. Grima, B. Blanke, E. Martinez, and F. Ardhuin. Large impact of stokes drift on the fate of surface floating debris in the South Indian Basin. *Mar. Pollut. Bull.*, 148:202–209, 2019.

I. Eames. Settling of particles beneath water waves. *J. Phys. Oceanogr.*, 38:2846–2853, 2008.

D. O. Edmund, K. J. Maki, and R. F. Beck. A velocity-decomposition formulation for the incompressible Navier–Stokes equations. *Comput. Mech.*, 52(3):669–680, 2013.

D. Eeltink, R. Calvert, J. E. Swagemakers, Q. Xiao, and T. S. van den Bremer. Stochastic particle transport by deep-water irregular breaking waves. *J. Fluid. Mech.*, 971:A38, 2023.

M. S. EI-Tahan, H. W. EI-Tahan, S. Venkatesh, et al. Forecast of iceberg ensemble drift. In *Offshore Technology Conference*. Offshore Technology Conference, 1983.

M. Eriksen, L. C. M. Lebreton, H. S. Carson, M. Thiel, C. J. Moore, J. C. Borerro, F. Galgani, P. G. Ryan, and J. Reisser. Plastic pollution in the world's oceans: more than 5 trillion plastic pieces weighing over 250,000 tons afloat at sea. *PloS one*, 9(12):e111913, 2014.

O. M. Faltinsen and A. E. Løken. *Drift forces and slowly varying horizontal forces on a ship in waves*. Norske Veritas, Research Division, 1977.

O. M. Faltinsen and A. E. Løken. Slow drift oscillations of a ship in irregular waves. *Appl. Ocean Res.*, 1(1):21–31, 1979.

C. I. Fraser, A. K. Morrison, A. M. Hogg, E. C. Macaya, E. van Sebille, P. G. Ryan, A. Padovan, C. Jack, N. Valdivia, and J. M. Waters. Antarctica's ecological isolation will be broken by storm-driven dispersal and warming. *Nat. clim. change*, 8(8):704–708, 2018.

V. Futch and A. Allen. Search and rescue applications: on the need to improve ocean observing data systems in offshore or remote locations. *Frontiers in Marine Science*, 6:301, 2019.

R. Geyer, J. R. Jambeck, and K. L. Law. Production, use, and fate of all plastics ever made. *Science advances*, 3(7):e1700782, 2017.

Y. Goda and Y. Suzuki. Estimation of incident and reflected waves in random wave experiments. In *Coastal Engineering 1976*, pages 828–845. Coastal Engineering Research Council, 1976.

J. Gong, S. Yan, Q. W. Ma, and Y. Li. Added resistance and seakeeping performance of trimarans in oblique waves. *Ocean Eng.*, 216:107721, 2020.

M. K. Gough, F. J. Beron-Vera, M. J. Olascoaga, J. Sheinbaum, J. Jouanno, and R. Duran. Persistent Lagrangian transport patterns in the northwestern Gulf of Mexico. *J. Phys. Oceanogr.*, 49(2):353–367, 2019.

R. Grotmaack and M. H. Meylan. Wave forcing of small floating bodies. *J. Waterw. Port C.*, 132(3):192–198, 2006.

J. Grue and J. Kolaas. Experimental particle paths and drift velocity in steep waves at finite water depth. *J. Fluid. Mech.*, 810:R1, 2017.

M. Hann, D. Greaves, and A. Raby. Snatch loading of a single taut moored floating wave energy converter due to focussed wave groups. *Ocean Eng.*, 96:258–271, 2015.

R. Hannah. How much plastic waste ends up in the ocean? *Our World in Data*, 2023. https://ourworldindata.org/how-much-plastic-waste-ends-up-in-the-ocean.

V. W. Harms. Steady wave-drift of modeled ice floes. *J. Waterw. Port C.*, 113(6):606–622, 1987.

M. D. Haskind. The hydrodynamic theory of ship oscillations in rolling and pitching. *Prikl. Mat. Mekh*, 10:33–66, 1946.

T. H. Havelock. The wave-making resistance of ships: a theoretical and practical analysis. *P. Roy. Soc. A-Math. Phy.*, 82(554):276–300, 1909.

T. H. Havelock. The drifting force on a ship among waves. *The London, Edinburgh, and Dublin Philosophical Magazine and Journal of Science*, 33(221):467–475, 1942.

M. He, B. Ren, and D. H. Qiu. Experimental study of nonlinear behaviors of a free-floating body in waves. *China Ocean Eng.*, 30(3):421–430, 2016.

D. A. Hebert, R. A. Allard, E. J. Metzger, P. G. Posey, R. H. Preller, A. J. Wallcraft, M. W. Phelps, and O. M. Smedstad. Short-term sea ice forecasting: An assessment of ice concentration and ice drift forecasts using the U.S. Navy's Arctic Cap Nowcast/Forecast System. *J. Geophys. Res.-Oceans*, 120(12):8327–8345, 2015.

P. Heil, C. W. Fowler, J. A. Maslanik, W. J. Emery, and I. Allison. A comparison of East Antarctic sea-ice motion derived using drifting buoys and remote sensing. *Ann. Glaciol.*, 33: 139–144, 2001.

C. Higgins, J. Vanneste, and T. S. van den Bremer. Unsteady Ekman-Stokes dynamics: Implications for surface wave-induced drift of floating marine litter. *Geophys. Res. Lett.*, 47(18): e2020GL089189, 2020.

P. Higuera, J. L. Lara, and I. J. Losada. Realistic wave generation and active wave absorption for Navier–Stokes models: Application to OpenFOAM®. *Coastal Engineering*, 71:102–118, 2013.

A. Hildebrandt, V. Sriram, T. Schlurmann, et al. Simulation of focusing waves and local line forces due to wave impacts on a tripod structure. In *The Twenty-third Int. Offshore Polar E.* International Society of Offshore and Polar Engineers, 2013.

P. R. Holland and R. Kwok. Wind-driven trends in Antarctic sea-ice drift. *Nat. Geosci.*, 5(12): 872–875, 2012.

J. C. Hu, Y. Zhou, and C. Dalton. Effects of the corner radius on the near wake of a square prism. *Exp. fluids*, 40(1):106–118, 2006.

G. Huang and A. W.K. Law. Wave-induced drift of large floating objects in regular waves. *J. Waterw. Port. C.*, 139(6):535–542, 2013.

G. Huang, A. W. Law, and Z. Huang. Wave-induced drift of small floating objects in regular waves. *Ocean Eng.*, 38(4):712–718, 2011.

4734 G. Huang, Z. H. Huang, and A. W. Law. Analytical study on drift of small floating objects
4735 under regular waves. *J. Eng. Mech.*, 142(6):06016002, 2016.

4736 J. Huang, P. M. Carrica, and F. Stern. Coupled ghost fluid/two-phase level set method for
4737 curvilinear body-fitted grids. *Int. J. Numer. Meth. Fl.*, 55(9):867–897, 2007.

4738 J. Huang, P. M. Carrica, and F. Stern. Semi-coupled air/water immersed boundary approach
4739 for curvilinear dynamic overset grids with application to ship hydrodynamics. *Int. J. Numer.*
4740 *Meth. Fl.*, 58(6):591–624, 2008.

4741 N. E. Huang. On surface drift currents in the ocean. *J. Fluid Mech.*, 91(1):191–208, 1979.

4742 Z. Huang. An experimental study of the surface drift currents in a wave flume. *Ocean Eng.*, 34
4743 (2):343–352, 2007.

4744 Z. Huang and C. C. Mei. Effects of surface waves on a turbulent current over a smooth or
4745 rough seabed. *J. Fluid Mech.*, 497:253–287, 2003.

4746 E. Huse. Wave induced mean force on platforms in direction opposite to wave propagation.
4747 *Norwegian Maritime Research*, 5(1), 1977.

4748 M. Inoue, N. Baba, and Y. Himeno. Experimental and numerical study of viscous flow field
4749 around an advancing vertical circular cylinder piercing a free-surface. *Journal of the Kansai*
4750 *Society of Naval Architects of Japan*, 220:57–64, 1993. in Japanese.

4751 M. Isaacson. Measurement of regular wave reflection. *J. Waterw. Port C.*, 117(6):553–569,
4752 1991.

4753 M. D. Isaacson. Wave-induced forces in the diffraction regime. *Editor TL Shaw, University of*
4754 *Bristol, England, Pitman Publishing Ltd., London, Printed in UK, ISBN: 0 273 08433 X*,
4755 1979.

4756 A. Isobe and S. Iwasaki. The fate of missing ocean plastics: Are they just a marine environ-
4757 mental problem? *SCI. TOTAL ENVIRON.*, 825:153935, 2022.

4758 A. Isobe, K. Kubo, Y. Tamura, E. Nakashima, N. Fujii, et al. Selective transport of microplastics
4759 and mesoplastics by drifting in coastal waters. *Mar. pollut. bull.*, 89(1-2):324–330, 2014.

IUCNPlastic. Marine plastic pollution. *International Union for Conservation of Nature: Issues Brief*, 2021. Available at https://www.iucn.org/resources/issues-brief/marine-plastic-pollution (accessed 15 November 2023).

S. Iwasaki, A. Isobe, S. Kako, K. Uchida, and T. Tokai. Fate of microplastics and mesoplastics carried by surface currents and wind waves: A numerical model approach in the Sea of Japan. *Mar. Pollut. Bull.*, 121(1-2):85–96, 2017.

N. G. Jacobsen, D. R. Fuhrman, and J. Fredsøe. A wave generation toolbox for the open-source CFD library: OpenFoam®. *Int. J. Numer. Meth. Fl.*, 70(9):1073–1088, 2012.

J. R. Jambeck, R. Geyer, C. Wilcox, T. R. Siegler, M. Perryman, A. Andrady, R. Narayan, and K. L. Law. Plastic waste inputs from land into the ocean. *Science*, 347(6223):768–771, 2015.

H. Jasak. Dynamic mesh handling in openFOAM. In *47th AIAA aerospace sciences meeting including the new horizons forum and aerospace exposition*, page 341, 2009.

M. L. A. Kaandorp, D. Lobelle, C. Kehl, H. A. Dijkstra, and E. van Sebille. Global mass of buoyant marine plastics dominated by large long-lived debris. *Nat. Geosci.*, 16(8):689–694, 2023.

M. Kandasamy, T. Xing, and F. Stern. Unsteady free-surface wave induced separation: coherent vortical structures and instabilities. *J. Fluid. Struct.*, 2005.

T. Kataoka and T. R. Akylas. On three-dimensional internal gravity wave beams and induced large-scale mean flows. *J. Fluid. Mech.*, 769:621–634, 2015.

T. Kawamura, S. Mayer, A. Garapon, and L. Sørensen. Large eddy simulation of a flow past a free surface piercing circular cylinder. *J. Fluids Eng.*, 124(1):91–101, 2002.

M. S. Kim and W. I. Lee. A new VOF-based numerical scheme for the simulation of fluid flow with free surface. Part I: New free surface-tracking algorithm and its verification. *Int. J. Numer. Meth. Fl.*, 42(7):765–790, 2003.

Y. Kim and K.-H. Kim. Numerical stability of Rankine panel method for steady ship waves. *Ships Offshore Struc.*, 2(4):299–306, 2007.

E. B. Kraus and J. A. Businger. *Atmosphere-ocean interaction*, volume 27. Oxford University Press, 1994.

R. Kwok, S. S. Pang, and S. Kacimi. Sea ice drift in the Southern Ocean: Regional patterns, variability, and trends. *Elem Sci Anth*, 5:32, 2017.

I. Langmuir. Surface motion of water induced by wind. *Science*, 87(2250):119–123, 1938.

B. E. Larsen, D. R. Fuhrman, and J. Roenby. Performance of interfoam on the simulation of progressive waves. *Coast. Eng. J.*, 61(3):380–400, 2019.

A. W. Law and G. Huang. Observations and measurements of wave-induced drift of surface inextensible film in deep and shallow waters. *Ocean Eng.*, 34(1):94–102, 2007.

K. L. Law. Plastics in the marine environment. *Annu. Rev. Mar. Sci.*, 9:205–229, 2017.

K. L. Law, S. Morét-Ferguson, N. A. Maximenko, G. Proskurowski, E. E. Peacock, J. Hafner, and C. M. Reddy. Plastic accumulation in the North Atlantic subtropical gyre. *Science*, 329 (5996):1185–1188, 2010.

M. Le Boulluec, B. Forest, and E. Mansuy. Steady drift of floating objects in waves: Experimental and numerical investigation. In *International Conference on Offshore Mechanics and Arctic Engineering*, volume 48210, pages 321–328, 2008.

L. Lebreton, M. Egger, and B. Slat. A global mass budget for positively buoyant macroplastic debris in the ocean. *SCI. REP-UK*, 9(1):12922, 2019.

S. Leibovich. The form and dynamics of Langmuir circulations. *Annu. Rev. Fluid Mech.*, 15 (1):391–427, 1983.

L. Lenain, N. Pizzo, and W. K. Melville. Laboratory studies of Lagrangian transport by breaking surface waves. *J. Fluid Mech.*, 876:R1, 2019. doi: 10.1017/jfm.2019.544.

D. M. Lewis and S. E. Belcher. Time-dependent, coupled, Ekman boundary layer solutions incorporating Stokes drift. *Dynam. Atmos. Oceans*, 37(4):313–351, 2004.

Q. Li, J. H. Wang, S. Q. Yan, J. Y. Gong, and Q. W. Ma. A zonal hybrid approach coupling FNPT with OpenFOAM for modelling wave-structure interactions with action of current. *Ocean Systems Engineering*, 8(4):381–407, 2018.

Y. Liang, L. Tao, L. Xiao, and M. Liu. Experimental and numerical study on flow past four rectangular columns in diamond configuration. In *International Conference on Offshore Mechanics and Arctic Engineering*, volume 49927, page V001T01A044. American Society of Mechanical Engineers, 2016.

P. Lin and C. W. Li. Wave–current interaction with a vertical square cylinder. *Ocean Eng.*, 30 (7):855–876, 2003.

Z. H. Liu, Y. Zhuang, and D. C. Wan. Numerical study of focused wave interactions with a single-point moored hemispherical-bottomed buoy. *Int. J. Offshore Polar*, 30(01):53–61, 2020.

M. S. Longuet-Higgins. Mass transport in water waves. *Philos. T. R. Soc. S-A.*, 245(903): 535–581, 1953.

M. S. Longuet-Higgins. Mass transport in the boundary layer at a free oscillating surface. *J. Fluid Mech.*, 8(2):293–306, 1960.

M. S. Longuet-Higgins and R. W. Stewart. Radiation stress and mass transport in gravity waves, with application to 'surf beats'. *J. Fluid. Mech.*, 13(4):481–504, 1962.

D. A. Lyn, S. Einav, W. Rodi, and J. H. Park. A laser-Doppler velocimetry study of ensemble-averaged characteristics of the turbulent near wake of a square cylinder. *J. Fluid Mech.*, 304: 285–319, 1995.

Q. W. Ma and S. Yan. Quasi ALE finite element method for nonlinear water waves. *J. Comput. phys.*, 212(1):52–72, 2006.

Q. W. Ma and S. Yan. QALE-FEM for numerical modelling of non-linear interaction between 3D moored floating bodies and steep waves. *Int. J. Numer. Meth. Eng.*, 78(6):713–756, 2009.

Q. W. Ma and S. Yan. QALE-FEM method and its application to the simulation of free-responses of floating bodies and overturning waves. In *Advances in Numerical Simulation of Nonlinear Water Waves*, pages 165–202. World Scientific, 2010.

EPD MANSARD. The measurement of incident and reflected spectra using least square method. *Proc. 17th Coastal Eng., Sydney, Australia, 1980*, 1:154–172, 1980.

A. V. Marchenko. The floating behaviour of a small body acted upon by a surface wave. *J. Appl. Math. Mech.*, 63(3):471–478, 1999.

S. Martin and P. Becker. High-frequency ice floe collisions in the Greenland Sea during the 1984 marginal ice zone experiment. *J. Geophys. Res.-Oceans*, 92(C7):7071–7084, 1987.

E. Martinez, K. Maamaatuaiahutapu, and V. Taillandier. Floating marine debris surface drift: convergence and accumulation toward the South Pacific subtropical gyre. *Mar. Pollut. Bull.*, 58(9):1347–1355, 2009.

M. R. Maxey and J. J. Riley. Equation of motion for a small rigid sphere in a non-uniform flow. *Phys. Fluids*, 26(4):883–889, 1983.

J. C. Mcwilliams, P. P. Sullivan, and C. Moeng. Langmuir turbulence in the ocean. *J. Fluid Mech.*, 334:1–30, 1997.

M. H. Meylan, L. J. Yiew, L. G. Bennetts, B. J. French, and G. A. Thomas. Surge motion of an ice floe in waves: comparison of a theoretical and an experimental model. *Ann. Glaciol.*, 56(69):155–159, 2015.

J. H. Michell. XI. The wave-resistance of a ship. *The London, Edinburgh, and Dublin Philosophical Magazine and Journal of Science*, 45(272):106–123, 1898.

P. Miron, F. J. Beron-Vera, M. J. Olascoaga, and P. Koltai. Markov-chain-inspired search for MH370. *Chaos: An Interdisciplinary J. Nonlinear Sci.*, 29(4), 2019.

M. Mohseni, P. T. Esperanca, and S. H. Sphaier. Numerical study of wave run-up on a fixed and vertical surface-piercing cylinder subjected to regular, non-breaking waves using OpenFOAM. *Appl. Ocean Res.*, 79:228–252, 2018.

S. G. Monismith. Stokes drift: theory and experiments. *J. Fluid Mech.*, 884, 2020.

N. Moradi, T. Zhou, and L. Cheng. Effect of inlet configuration on wave resonance in the narrow gap of two fixed bodies in close proximity. *Ocean Eng.*, 103:88–102, 2015.

J. R. Morison, J. W. Johnson, and S. A. Schaaf. The force exerted by surface waves on piles. *J. Petrol. Technol.*, 2(05):149–154, 1950.

J. Murray, G. Guy, and D. Muggeridge. Response of modelled ice masses to regular waves and regular wave groups. In *Proceedings OCEANS'83*, pages 1048–1052. IEEE, 1983.

NASA. Europa: Water World Infographic. *NASA Europa Clipper*, 2019. Available at https://europa.nasa.gov/resources/148/europa-water-world-infographic (accessed 9 June 2023).

J. H. Nath. Drift speed of Buoys in waves, with Appendix by MS Longuet-Higgins. *Coastal Engineering Proceedings*, 1(16):49–49, 1978.

J. N. Newman. The drift force and moment on ships in waves. *J. Ship Res.*, 11(01):51–60, 1967.

J. N. Newman. Second-order slowly varying forces on vessels in irregular waves. In *Proceedings of the international symposium on dynamics of marine vehicles and structures in waves. London, UK, 1974*, 1974.

J. N. Newman. *Marine hydrodynamics*. The MIT press, 2018.

J. Nossen, J. Grue, and E. Palm. Wave forces on three-dimensional floating bodies with small forward speed. *J. Fluid Mech.*, 227:135–160, 1991.

T. F. Ogilvie. Second order hydrodynamic effects on ocean platforms. *International Work Shop on Ship and Platform Motions, 1983*, pages 205–343, 1983.

M. J. Olascoaga and G. Haller. Forecasting sudden changes in environmental pollution patterns. *P. Natl. A. Sci.*, 109(13):4738–4743, 2012.

M. J. Olascoaga, F. J. Beron-Vera, P. Miron, J. Triñanes, N. F. Putman, R. Lumpkin, and G. J. Goni. Observation and quantification of inertial effects on the drift of floating objects at the ocean surface. *Phys. Fluids*, 32(2):026601, 2020.

V. Onink, D. Wichmann, P. Delandmeter, and E. van Sebille. The role of Ekman currents, geostrophy, and Stokes drift in the accumulation of floating microplastic. *J. Geophys. Res.-Oceans*, 124(3):1474–1490, 2019.

C. Ostle, R. C. Thompson, D. Broughton, L. Gregory, M. Wootton, and D. G. Johns. The rise in ocean plastics evidenced from a 60-year time series. *Nat. commun.*, 10(1):1622, 2019.

J. Palm, C. Eskilsson, G. M. Paredes, and L. Bergdahl. CFD simulation of a moored floating wave energy converter. In *Proceedings of the 10th European Wave and Tidal Energy Conference, Aalborg, Denmark*, volume 25, 2013.

J. Palm, C. Eskilsson, G. M. Paredes, and L. Bergdahl. Coupled mooring analysis for floating wave energy converters using CFD: Formulation and validation. *International Journal of Marine Energy*, 16:83–99, 2016.

J. Palm, C. Eskilsson, L. Bergdahl, and R. E. Bensow. Assessment of scale effects, viscous forces and induced drag on a point-absorbing wave energy converter by CFD simulations. *J. Mar. Sci. and Eng.*, 6(4):124, 2018.

G. Pasternak, D. Zviely, A. Ariel, E. Spanier, and C. A. Ribic. Message in a bottle–the story of floating plastic in the eastern Mediterranean sea. *Waste Manage.*, 77:67–77, 2018.

C. B. Pattiaratchi, M. van der Mheen, C. Schlundt, B. Narayanaswamy, A. Sura, S. Hajbane, R. White, N. Kumar, M. Fernandes, and S. Wijeratne. Plastics in the Indian Ocean–sources, transport, distribution and impacts. *Ocean science*, 18:1–28, 2022.

W. Perrie and Y. Hu. Air–ice–ocean momentum exchange. Part II: Ice drift. *J. Phys. Oceanogr.*, 27(9):1976–1996, 1997.

J. Pessoa and N. Fonseca. Second-order low-frequency drift motions of a floating body calculated by different approximation methods. *J. Mar. Sci. Technol.*, 20(2):357–372, 2015.

O. M. Phillips. *The dynamics of the upper ocean.* Cambridge University Press, 1966.

J. A. Pinkster. Low-frequency second order wave exciting force on floating strutures. *Neth. ship Model Bain Pub.*, 650:19–60, 1980.

J. A. Pinkster and J. P. Hooft. Low frequency second order wave forces on vessels moored at sea. In *11th Symposium on Naval Hydrodynamics, ONR, London, England, 1976*, 1976.

J. A. Pinkster and R. H. Huijsmans. Wave drift forces in shallow water. *Boss 1992*, 1992.

J. A. Pinkster and R. H. M. Huijsmans. The low frequency motions of a semi-submersible in waves. In *Proceedings of 3rd International Conference of Behavior of Offshore Structures*, volume 1, pages 447–466, 1982.

J. A. Pinkster and G. Van Oortmerssen. Computation of the first and second order wave forces on bodies oscillating in regular waves. 2nd int. In *Conf. Numerical Ship Hydrodynamics, Berkeley, USA*, pages 136–456, 1977.

N. Pizzo, W. K. Melville, and L. Deike. Lagrangian transport by nonbreaking and breaking deep-water waves at the ocean surface. *J. Phys. Ocean.*, 49(4):983–992, 2019.

N. E. Pizzo. Surfing surface gravity waves. *J. Fluid Mech.*, 823:316–328, 2017.

N. Pujara and J. Thiffeault. Wave-averaged motion of small particles in surface gravity waves: Effect of particle shape on orientation, drift, and dispersion. *Phys. Rev. Fluids*, 8:074801, Jul 2023. doi: 10.1103/PhysRevFluids.8.074801. URL `https://link.aps.org/doi/10.1103/PhysRevFluids.8.074801`.

H. C. Raven. Variations on a theme by Dawson: Recent improvements of a potential flow calculation method for ships. In *Proceedings of the 17th Symposium on Naval Hydrodynamics*, 1988.

S. Reddy, W. Lau, and PEW C. Trusts. Breaking the plastic wave: Top findings for preventing plastic pollution. *Pew Research Center https://www. pewtrusts. org/en/research-and-analysis/articles/2020/07/23/breaking-theplastic-wave-top-findings, accessed July*, 23:2020, 2020.

B. Ren, M. He, P. Dong, and H. Wen. Nonlinear simulations of wave-induced motions of a freely floating body using WCSPH method. *Appl. Ocean Res.*, 50:1–12, 2015.

E. L. Ridler and J. F. A. Sleath. Effect of bed roughness on time-mean drift induced by waves. *J. waterw. port. c.*, 126(1):23–29, 2000.

P. J. Roache. Perspective: A method for uniform reporting of grid refinement studies. *J. Fluid. Eng. (United States)*, 116(3), 1994.

J. Röhrs, K. Hå. Christensen, L. R. Hole, Gö. Broström, M. Drivdal, and S. Sundby. Observation-based evaluation of surface wave effects on currents and trajectory forecasts. *Ocean Dynam.*, 62:1519–1533, 2012.

A. Roshko. *On the Development of Turbulent Wakes from Vortex Streets*. PhD thesis, California Institute of Technology, 1952.

R. R. Rumer, R. D. Crissman, and A. Wake. *Ice transport in great lakes*. Great Lakes Environmental Research Laboratory, National Oceanic and ..., 1979.

I. I. Rypina, S. R. Jayne, S. Yoshida, A. M. Macdonald, E. Douglass, and K. Buesseler. Short-term dispersal of Fukushima-derived radionuclides off Japan: modeling efforts and model-data intercomparison. *Biogeosciences*, 10(7):4973–4990, 2013.

S. Ryu, M. H. Kim, and P. J. Lynett. Fully nonlinear wave-current interactions and kinematics by a BEM-based numerical wave tank. *Comput. mech.*, 32(4):336–346, 2003.

F. Santamaria, G. Boffetta, M. M. Afonso, A. Mazzino, M. Onorato, and D. Pugliese. Stokes drift for inertial particles transported by water waves. *EPL (Europhysics Letters)*, 102(1): 14003, 2013.

H. Schlichting and J. Kestin. *Boundary layer theory*, volume 121. Springer, 1961.

S. Schwegmann, C. Haas, C. Fowler, and R. Gerdes. A comparison of satellite-derived sea-ice motion with drifting-buoy data in the Weddell Sea, Antarctica. *Ann. Glaciol.*, 52(57): 103–110, 2011.

H. H. Shen and S. F. Ackley. A one-dimensional model for wave-induced ice-floe collisions. *Ann. Glaciol.*, 15:87–95, 1991.

H. H. Shen and Y. Zhong. Theoretical study of drift of small rigid floating objects in wave fields. *J. Waterw. Port C.*, 127(6):343–351, 2001.

J. T. Sinnis, L. Grare, L. Lenain, and N. Pizzo. Laboratory studies of the role of bandwidth in surface transport and energy dissipation of deep-water breaking waves. *J. Fluid Mech.*, 927: A5, 2021. doi: doi:10.1017/jfm.2021.734.

J. E. Sonke, A. M. Koenig, N. Yakovenko, O. Hagelskjær, H. Margenat, S. V. Hansson, F. De Vleeschouwer, O. Magand, G. Le Roux, and J. L. Thomas. A mass budget and box model of global plastics cycling, degradation and dispersal in the land-ocean-atmosphere system. *Microplastics and Nanoplastics*, 2(1):28, 2022.

P. R. Spalart. Airplane trailing vortices. *Annu. Rev. Fluid Mech.*, 30:107, 1998.

G. Spreen, R. Kwok, and D. Menemenlis. Trends in Arctic sea ice drift and role of wind forcing: 1992–2009. *Geophys. Res. Lett.*, 38(19), 2011.

V. Sriram, Q. W. Ma, and T. Schlurmann. A hybrid method for modelling two dimensional non-breaking and breaking waves. *J. Comput. phys.*, 272:429–454, 2014.

C. T. Stansberg and T. Kristiansen. Non-linear scattering of steep surface waves around vertical columns. *Appl. Ocean Res.*, 27(2):65–80, 2005.

C. T. Stansberg and T. Kristiansen. Experimental study of slow-drift ship motions in shallow water random waves. In *International Conference on Offshore Mechanics and Arctic Engineering*, volume 44359, pages 815–823, 2011.

C. T. Stansberg and F. G. Nielsen. Nonlinear wave-structure interactions on floating production systems. In *ISOPE International Ocean and Polar Engineering Conference*, pages ISOPE–I. ISOPE, 2001.

C. T. Stansberg, R. Baarholm, T. Kristiansen, E. W. M. Hansen, and G. Rortveit. Extreme wave amplification and impact loads on offshore structures. In *Offshore Technology Conference*, pages OTC–17487. OTC, 2005.

F. Stern, R. V. Wilson, H. W. Coleman, and E. G. Paterson. Comprehensive approach to verification and validation of CFD simulations—part 1: methodology and procedures. *J. Fluids Eng.*, 123(4):793–802, 2001.

G. G. Stokes. On the theory of oscillatory waves. *Trans. Camb. Phil. Soc.*, 8:411–455, 1847.

C. Strong, D. Foster, E. Cherkaev, I. Eisenman, and K. M. Golden. On the definition of marginal ice zone width. *J. Atmos. Ocean. Tech.*, 34(7):1565–1584, 2017.

B. M. Sumer et al. *Hydrodynamics around cylindrical structures*, volume 26. World scientific, 2006.

K. Suyehiro. The drift of ships caused by rolling among waves. *Trans. Inst. Naval Arch*, 66, 1924.

I. B. A. Svendsen. Mass flux and undertow in a surf zone. *Coast. Eng.*, 8(4):347–365, 1984.

S. Szanyi, J. V. Lukovich, and D. G. Barber. Lagrangian analysis of sea-ice dynamics in the Arctic Ocean. *Polar Res.*, 35(1):30778, 2016.

T. Tamura and T. Miyagi. The effect of turbulence on aerodynamic forces on a square cylinder with various corner shapes. *J. Wind Eng. Ind. Aerod.*, 83(1-3):135–145, 1999.

T. Tamura, T. Miyagi, and T. Kitagishi. Numerical prediction of unsteady pressures on a square cylinder with various corner shapes. *J. Wind Eng. Ind. Aerod.*, 74:531–542, 1998.

K. Tanizawa, M. Minami, and Y. Imoto. On the drifting speed of floating bodies in waves. *Journal of the Society of Naval Architects of Japan*, 2001(190):151–160, 2001.

K. Tanizawa, M. Minami, T. Imoto, et al. On the drift speed of floating bodies in waves. In *The Twelfth Int. Offshore Polar E.* International Society of Offshore and Polar Engineers, 2002.

F. Tong, L. Cheng, C. Xiong, S. Draper, H. An, and X. Lou. Flow regimes for a square cross-section cylinder in oscillatory flow. *J. Fluid Mech.*, 813:85–109, 2017.

J. A. Trinanes, M. J. Olascoaga, G. J. Goni, N. A. Maximenko, D. A. Griffin, and J. Hafner. Analysis of flight MH370 potential debris trajectories using ocean observations and numerical model results. *J. Oper. Oceanogr.*, 9(2):126–138, 2016.

O. Ubbink. *Numerical prediction of two fluid systems with sharp interfaces.* PhD thesis, Imperial College of Science Technology and Medicine, University of London, 1997.

O. Ubbink and R. I. Issa. A method for capturing sharp fluid interfaces on arbitrary meshes. *J. comput. phys.*, 153(1):26–50, 1999.

UNCTADstat. Global plastics trade hits record $1.2 trillion. *UNCATD*, 2022. Available at https://unctadstat.unctad.org/EN/Index.html (accessed 15 November 2023).

N. Untersteiner. *The geophysics of sea ice*. Springer, 2013.

T. S. van den Bremer and Ø. Breivik. Stokes drift. *Philos. T. R. Soc. A*, 376(2111):20170104, 2018.

T. S. van den Bremer and P. H. Taylor. Estimates of Lagrangian transport by surface gravity wave groups: The effects of finite depth and directionality. *J. Geophys. Res.-Oceans*, 120(4): 2701–2722, 2015.

T. S. Van den Bremer and P. H. Taylor. Lagrangian transport for two-dimensional deep-water surface gravity wave groups. *P. Roy. Soc. A-Math. Phy.*, 472(2192):20160159, 2016.

T. S. van den Bremer, C. Whittaker, R. Calvert, A. Raby, and P. H. Taylor. Experimental study of particle trajectories below deep-water surface gravity wave groups. *J. Fluid. Mech.*, 879:168–186, 2019.

M. Van der Mheen, C. Pattiaratchi, S. Cosoli, and M. Wandres. Depth-dependent correction for wind-driven drift current in particle tracking applications. *Frontiers in Marine Science*, 7:305, 2020.

E. Van Sebille, C. Wilcox, L. Lebreton, N. Maximenko, B. D. Hardesty, J. A. Van Franeker, M. Eriksen, D. Siegel, F. Galgani, and K. L. Law. A global inventory of small floating plastic debris. *Environ. Res. Lett.*, 10(12):124006, 2015.

E. Van Sebille, S. Aliani, K. L. Law, N. Maximenko, J. M. Alsina, A. Bagaev, M. Bergmann, B. Chapron, I. Chubarenko, A. Cózar, et al. The physical oceanography of the transport of floating marine debris. *Environ. Res. Lett.*, 15(2):023003, 2020.

V. Vukčević, H. Jasak, and I. Gatin. Implementation of the Ghost Fluid Method for free surface flows in polyhedral Finite Volume framework. *Comput. Fluids*, 153:1–19, 2017.

P. Wadhams. A mechanism for the formation of ice edge bands. *J. Geophys. Res.-Oceans*, 88 (C5):2813–2818, 1983.

P. Wadhams. *Ice in the Ocean*. CRC Press, 2014.

J. Wang, Q. W. Ma, and S. Yan. A hybrid model for simulating rogue waves in random seas on a large temporal and spatial scale. *J. Comput. phys.*, 313:279–309, 2016.

Y. Watanabe. Some contributions of the theory of rolling. *Trans. Inst. Naval Arch*, 80:408–432, 1938.

A. Webb and B. Fox-Kemper. Wave spectral moments and Stokes drift estimation. *Ocean Model.*, 40(3-4):273–288, 2011.

A. Webb and B. Fox-Kemper. Impacts of wave spreading and multidirectional waves on estimating Stokes drift. *Ocean Model.*, 96:49–64, 2015.

C. H. Wiliamson. Vortex dynamics in the cylinder wake. *Annu. Rev. Fluid Mech.*, 28(1): 477–539, 1996.

W. Wilson. Numerical modelling of drifting buoys and its relevance to Lagrangian tracking. In *Proceedings of the 1982 IEEE Second Working Conference on Current Measurement*, volume 2, pages 95–97. IEEE, 1982.

H. Xiao, W. Huang, J. Tao, and C. Liu. Numerical modeling of wave–current forces acting on horizontal cylinder of marine structures by VOF method. *Ocean Eng.*, 67:58–67, 2013.

Q. Xiao, R. Calvert, S. Q. Yan, T. A. A. Adcock, and T. S. van den Bremer. Surface gravity wave-induced drift of floating objects in the diffraction regime. *J.Fluid Mech.*, 980:A27, 2024.

S. Xie. code for Holistically-Nested Edge Detection and pretrained model, 2015. `https://github.com/s9xie/hed`, Last accessed on 2023-3-30.

S. Xie and Z. Tu. Holistically-nested edge detection. In *Proceedings of the IEEE international conference on computer vision*, pages 1395–1403, 2015.

S. Yan and Q. W. Ma. Numerical simulation of fully nonlinear interaction between steep waves and 2D floating bodies using the QALE-FEM method. *J. Comput. phys.*, 221(2):666–692, 2007.

S. Yan and Q. W. Ma. Numerical simulation of interaction between wind and 2D freak waves. *Eur. J. Mech. B-Fluid.*, 29(1):18–31, 2010a.

S. Yan and Q. W. Ma. QALE-FEM for modelling 3D overturning waves. *Int. J. Numer. Meth. Fl.*, 63(6):743–768, 2010b.

S. Yan, Q. Ma, et al. A hybrid approach coupling MLPG-R with QALE-FEM for modelling fully nonlinear water waves. In *The 27th Int. Ocean Polar E.* International Society of Offshore and Polar Engineers, 2017.

S. Yan, Q. W. Ma, J. Wang, and J. Wang. Numerical modelling of wave resonance in a narrow gap between two floating bodies in close proximity using a hybrid model. In *International Conference on Offshore Mechanics and Arctic Engineering*, volume 58882, page V009T12A009. American Society of Mechanical Engineers, 2019.

S. Yan, Q. W. Ma, and J. Wang. Quadric SFDI for laplacian discretisation in lagrangian meshless methods. *Journal of Marine Science and Application*, 19(3):362–380, 2020a.

S. Yan, J. Wang, J. Wang, Q. W. Ma, Z. Xie, et al. CCP-WSI Blind Test using qaleFOAM with an Improved Passive Wave Absorber. *Int. J. Offshore Polar*, 30(01):43–52, 2020b.

S. Yang, S. Luo, F. Liu, and H. Tsai. Euler solutions of flow around a rectangular wing with square tip. In *45th AIAA Aerospace Sciences Meeting and Exhibit*, page 896, 2007.

Y. T. Yang, R. C. Zhu, and L. Hong. A frequency-domain hybrid HOBEM for motion responses and added resistance of ships sailing in head and oblique waves. *Ocean Eng.*, 194:106637, 2019a.

Y. T. Yang, R. C. Zhu, L. Hong, and S. Huang. A semi-analytical high-order translating-pulsating source method for forward-speed ship motions. *Ocean Eng.*, 182:627–644, 2019b.

S. C. Yen and C. W. Yang. Flow patterns and vortex shedding behavior behind a square cylinder. *J. Wind Eng. Ind. Aerod.*, 99(8):868–878, 2011.

5096 D. H. Yoon, K. S. Yang, and C. B. Choi. Flow past a square cylinder with an angle of incidence.
5097 *Phys. fluids*, 22(4):043603, 2010.

5098 S. H. Yoon, D. H. Kim, H. Sadat-Hosseini, J. Yang, and F. Stern. High-fidelity CFD simulation
5099 of wave run-up for single/multiple surface-piercing cylinders in regular head waves. *Appl.*
5100 *ocean res.*, 59:687–708, 2016.

5101 D. L. Youngs. Time-dependent multi-material flow with large fluid distortion. *Numerical*
5102 *methods for fluid dynamics*, 1982.

5103 Y. H. Yu and Y. Li. Reynolds-Averaged Navier–Stokes simulation of the heave performance of
5104 a two-body floating-point absorber wave energy system. *Comput. Fluids*, 73:104–114, 2013.

5105 N. Zhang, S. Yan, X. Zheng, Q. W. Ma, et al. A 3D hybrid model coupling SPH and QALE-
5106 FEM for simulating nonlinear wave-structure interaction. *Int. J. Offshore Polar*, 30(01):
5107 11–19, 2020.

5108 X. S. Zhang, P. Bandyk, and R. F. Beck. Seakeeping computations using double-body basis
5109 flows. *Appl. ocean res.*, 32(4):471–482, 2010.

5110 Y. H. Zheng, Y. G. You, and Y. M. Shen. On the radiation and diffraction of water waves by
5111 a rectangular buoy. *Ocean Eng.*, 31(8-9):1063–1082, 2004.

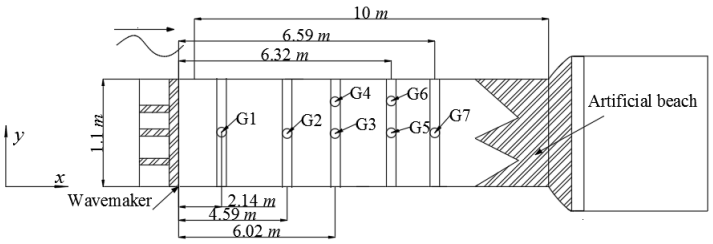
Appendix A

Calibration and testing of the new Wave and Current Flume

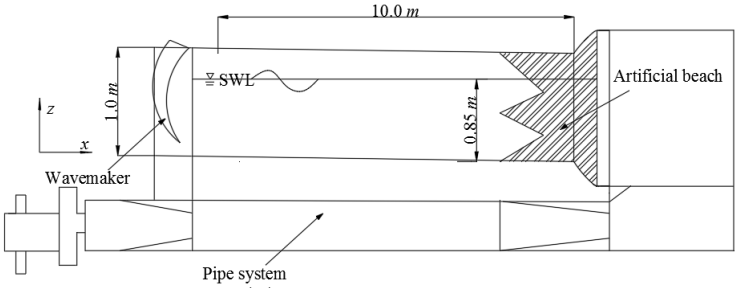
As mentioned in Chapter 4, the experiment conducted for this thesis took place in a newly constructed wave tank, which necessitated significant preliminary work. The testing process involved two primary aspects: assessing the dimensions of the wave tank, with particular emphasis on maintaining a consistent width throughout its entirety, and evaluating the properties of the waves. To begin, we will provide comprehensive measured data pertaining to the tank's dimensions at various sections, accompanied by a report on the manufactured tolerance. This information holds critical importance since the design of our objects and the experiment itself are based on these measurements. Subsequently, we will present an analysis of the wave properties, encompassing a frequency range spanning from 0.5 Hz to 1.8 Hz, with increments of 0.1 Hz. Additionally, we systematically vary the wave steepness, covering a range from 0.02 to 0.35. While not inherently novel in itself, documenting the characterization of this new facility will be valuable for future users seeking to utilize the wave tank.

A.1 Flume Dimensions

The Wave and Current Flume at the Department of Engineering Science, University of Oxford, is a medium-scale, high-flow quality (and low turbulence intensity) facility. It serves as a combined wave and current flume, supporting a wide range of research endeavors. These include investigations into the transport of floating objects by waves, wave-structure interaction



(a) Top plan view.



(b) Front profile view.

Figure A.1.1: Schematic layout of the wave flume, indicating the positions of the wave gauges, the coordinate system, and the pipe system.

for surface-piercing bodies, wake behind hydrokinetic turbines, and 3D turbine flows. It is also utilized for undergraduate teaching, outreach events, and open days. The flume has a working section of 10 m long, 1.1 m wide and 1 m in depth. The normal working water depth for waves is 0.85 m. At one end of the flume, a hinged flap-type wave-maker, measuring 3×700 mm, is installed, while the opposite end features a three-layer mesh wave-absorbing beach complemented by a removable honeycomb screen. For enhanced observation capabilities, the flume uses glass side walls and bottom, allowing flow visualization. The entire flume is composed of four panes of glass seamlessly joined into one piece by four stainless steel columns painted blue. Continuous stainless steel rails running along the top edges of both sides of the flume support gauge settings and model towing. The flume is equipped with water taps located at both ends for tank filling, accompanied by flexible hoses that can be directed into the tank from above and conveniently rolled back once the process is completed. There are also drain exits positioned at all four corners of the tank to aid in efficient emptying when necessary. The flume is not fully enclosed. Instead, it incorporates a pipe system with twin pipes sitting beneath the tank. This system enables the pumping of fluid to create a current beneath the flume, thereby facilitating flow circulations when waves are generated. Figure A.1.1 provides a schematic diagram of the wave flume and pipe system.

However, the effective length of the flume is shorter than the designated test session length

for wave testing, which is typically 10 m. This is due to the presence of wave-absorbing beaches positioned at the end of the flume, which reduces the working length to 8.145 m. From the location where the wave-makers are situated to the starting point of the testing session (marked by the first blue column), there is a distance of 1.8 m. In actuality, the total distance between the wave-maker and the beaches measures 9.945 m. To ensure accurate reporting, we conducted width measurements at five different locations for each glass pane and documented the results in Table A.1.1. The pane of the glass is not perfectly joined in parallel, resulting in steps where the width of the tank changes every two panes. Consequently, we identified the narrowest and widest parts of the flume, situated at x=4.32 m and x=11.32 m, respectively. Though the variation of each pane is very small, it imposes a significant influence on our object design. Therefore, we report the variation here. The final pane is almost occupied by the beaches, rendering the effective testing session happening at pane 1 to pane 4. From the table, we can see that significant variation happens at the second and third pane as well as the variations at the joints. This variation necessitates special care when designing our 2D floating objects. For this study, we did not conduct specific tests to assess the verticality of the flume since the working depth employed was based on a fixed value of 0.85 m.

A.2 Wave properties

Following a comprehensive examination of the flume dimensions, our focus shifts towards testing various wave properties within the flume. To accomplish this, we set up a series of resistance-type wave gauges to measure and analyze key parameters, including reflection coefficient, half of the wave height $H/2$, wave frequency f, the time history of the monochromatic waves, flume lateral variation, and repeatability in turn. We begin by examining the reflection coefficient as it plays a crucial role in understanding other wave properties in the flume. The wave gauges sample the surface elevation at 128 Hz, corresponding to a time step of 0.0078 s. We define a coordinate system, as plotted in figure A.1.1, labeled oxy, where the x-axis runs parallel to the length of the flume, starting from the position of the wave marker and pointing positively towards the beaches. The y-axis is parallel to the width of the flume, starting from the middle of the flume and pointing positively towards the left. Five rows of gauges are mounted on the top stainless rails with steel frames. The third and fourth rows utilize

	x [m]	Width [m]	Variation [%]
	1.82	1.095	
	2.3	1.095	
First pane	2.8	1.095	0
	3.3	1.095	
	3.78	1.095	
	3.82	1.093	
	4.32	1.090	
Second pane	4.82	1.096	0.2503
	5.32	1.097	
	5.78	1.094	
	5.82	1.098	
	6.32	1.093	
Third pane	6.82	1.094	0.2271
	7.32	1.098	
	7.78	1.098	
	7.82	1.096	
	8.32	1.096	
Fourth pane	8.82	1.096	0.1000
	9.32	1.098	
	9.78	1.098	
	9.82	1.098	
	10.32	1.098	
Fifth pane	10.82	1.098	0.0644
	11.32	1.099	
	11.78	1.097	

Table A.1.1: Detailed width dimensions of the flume for each pane. The beaches sit from x=9.945 m to the end x =11.8 m. The variation is calculated by $\delta_{width}/\overline{width}$, $\delta_{width} = \sqrt{\frac{\sum_{i=1}^{5}\left(width_i - \overline{width}\right)^2}{5-1}}$, where $width_i$ represents the i-th location of the corresponding pane and $\overline{width}$ denotes the mean value of the five locations in each pane.

a pair of gauges to assess flume lateral variation, while the remaining rows employ a single gauge. Therefore, a total of seven wave gauges are deployed, positioned at the following coordinates $(x_{gj}, y_{gj}, j = 1, 2, 3, 4, 5, 6, 7)$ in meters: (2.14,0); (4.59,0); (6.02,0); (6.02,0.275); (6.32,0); (6.32,0.275); (6.59,0), as depicted in figure A.1.1. The wave maker is capable of generating waves up to a height of 0.2 m across frequencies ranging from 0.2 to 3.0 Hz. However, due to the limited length of the flume (around 10 m), we opt not to generate excessively long waves. As a result, we select frequencies ranging from 0.5 to 1.8 Hz with intervals of 0.1 Hz. For each frequency, we choose 13 different wave steepness values ka_w ranging from 0.02 to 0.32, with intervals of 0.2 when $ka_w \leq 0.2$, and intervals of 0.4 when $0.2 < ka_w \geq 0.32$. Specifically, the chosen wave steepness values are ka_w=0.02, 0.04, 0.06, 0.08, 0.10, 0.12, 0.14, 0.16, 0.18, 0.20, 0.24, 0.28, 0.32. In terms of repeatability analysis, aside from the frequencies $f = 0.9$, 1.0, 1.05 and 1.1 Hz employed in Chapter 4 where we chose 4 wave steepness (ka_w =0.06, 0.10, 0.20 and 0.32), we select every other frequency (i.e. f=0.5, 0.7, 0.9, 1.1, 1.4, 1.6, 1.8 Hz). For each of these frequencies, we examine only one wave steepness value $ka_w = 0.06$ to investigate repeatability. To assess repeatability, we conduct five repeats of the experiment and examine the 1/2 heights and frequencies of the generated waves. During each measurement, the wave-maker is triggered in conjunction with the wave gauges, and the duration of each measurement is set to $150T_w$ (T_w is the wave period). Each run of the experiment was separated by a 5-minute wait time to allow the flume to settle.

A.2.1 Reflection analysis

To conduct the reflection analysis of unidirectional waves, we use two approaches. The first approach is an extended least squares method based on the frequency-domain manipulation of one-sided surface elevation spectrum, as proposed by MANSARD (1980). This method uses linear theory for wavenumber and wave elevation superposition calculations, allowing for an arbitrary number of wave gauges and accommodating non-colinear gauge spacing. We consider a total of p wave gauges, with the position of the $j-$th gauge given as $(x_{gj}, y_{gj}), j = 1, ..., p$. We define $\Delta x_{1j} = x_{gj} - x_{g1}$, where gauge 1 acts as the reference gauge. The wavenumber k_n of the n-th frequency component and the complex Fourier coefficient B_{jn} of the measured spectrum are obtained by conducting discrete FFT analysis for a given time signal collected by the j-th

wave gauges. To optimize the performance of the discrete FFT analysis, we choose a time signal length N to be an integer power of 2. According to the linear theory dispersion equation, we obtain wavenumber by $\omega_n^2 = gk_n \tanh k_n h$, in which $\omega_n = 2\pi f_n$ is the round frequency of the n-th component, g is the gravitational acceleration and h the water depth. We then calculate incident wave amplitude a_{In}, reflection coefficient C_{rn} and phase shift of the n-th component γ_n by:

$$a_{In} = |Z_{In}|; C_{rn} = \frac{|Z_{Rn}|}{|Z_{In}|}; \gamma_n = \arg(Z_{Rn}) - \arg(Z_{In}) - 2k_n x_{g1}, \tag{A.1}$$

where Z_{In} and Z_{Rn} represent the complex number of Fourier coefficients of the incident and reflected time signals at the reference gauge (gauge 1), respectively. $||$ and arg() give the magnitude and phase of the complex number, respectively. Z_{In} and Z_{Rn} can be calculated by:

$$Z_{In} = \frac{s_{Bzn}s_{dzn} - s_{zn}s_{Bdn}}{{s^2}_{dzn} - s_{dn}s_{zn}}; Z_{Rn} = \frac{s_{Bdn}s_{dzn} - s_{dn}s_{Bzn}}{{s^2}_{dzn} - s_{zn}s_{dn}}, \tag{A.2}$$

in which

$$\begin{aligned} s_{dzn} &= \sum_{j=1}^{p} w_{jn}; s_{dn} = \sum_{j=1}^{p} w_{jn} e^{-2ik_n \Delta x_{1j}}; s_{zn} = \sum_{j=1}^{p} w_{jn} e^{2ik_n \Delta x_{1j}}; \\ s_{Bdn} &= \sum_{j=1}^{p} w_{jn} B_{jn} e^{-ik_n \Delta x_{1j}}; s_{Bzn} = \sum_{j=1}^{p} w_{jn} B_{jn} e^{ik_n \Delta x_{1j}}, \end{aligned} \tag{A.3}$$

in which i is the imaginary unit, w_{jn} is the weighting function coefficient corresponding to the j-th wave gauges and n-th frequency component. We assume equal weighting calculations and set all w_{jn} to 1 for simplicity following MANSARD (1980) and Isaacson (1991). According to the equation A.2, in order to make the calculation based on equation A.1 effective, the denominator should not be zero, we then have:

$$D = {s^2}_{dzn} - s_{zn}s_{dn} = 4\sum_{j=2}^{p}\sum_{q=1}^{j-1} w_{jn}w_{qn} \sin^2(k_n \Delta x_{qj}) \neq 0, \tag{A.4}$$

in which $\Delta x_{qj} = x_{gj} - x_{gq}$ represents the distance between the q-th and j-th wave gauges. Obviously, this requires $\sin k_n \Delta xqj \neq 0$, which can be achieved by choosing suitable uneven wave gauge spacing or ensuring the frequencies where zero denominators occur are high enough to be safely filtered out. We finally obtain our reflection coefficient C_{rw} based on equation A.1 for the corresponding peak frequency (the measured input wave frequency f_w i.e. when f_n=f_w).

The second approach employs the ratio of incident and reflected wave energies to estimate

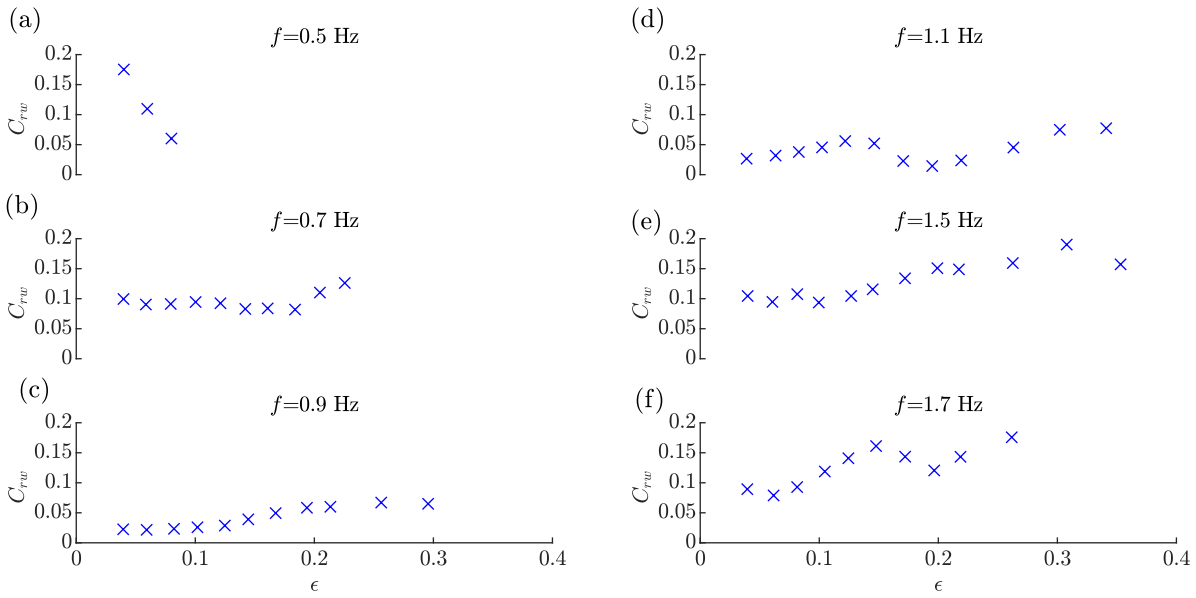


Figure A.2.1: Reflection coefficient C_{rw} of the fundamental wave frequency as a function of wave steepness for different frequencies. The calculations are based on approach 1, where the condition $\sin k_n \Delta xqj = 0$ is satisfied. In cases where the condition fails to be satisfied, we use approach 2 as an alternative).

the overall reflection coefficient based on a simultaneous recording of wave elevations at two adjacent wave gauges according to Goda and Suzuki (1976). Linear dispersion relation and wave superposition are also assumed in this approach. Following the same denotation as the previous approach, for each pair of wave gauges located at two adjacent positions, their distance is $\Delta x_{qj} = x_{gj} - x_{gq}$ where q and j are the chosen wave gauges as a pair. We then have the input wave amplitude a_{In} and reflected wave amplitude a_{Rn}:

$$
\begin{aligned}
a_{In} &= \frac{1}{2|\sin k_n \Delta x_{qj}|}\sqrt{(I_{jn} - I_{qn}\cos k_n\Delta x_{qj} - R_{qn}\sin k_n\Delta x_{qj})^2 + (R_{jn} + I_{qn}\sin k_n\Delta x_{qj} - R_{qn}\cos k_n\Delta x_{qj})^2};\\
a_{Rn} &= \frac{1}{2|\sin k_n \Delta x_{qj}|}\sqrt{(I_{jn} - I_{qn}\cos k_n\Delta x_{qj} + R_{qn}\sin k_n\Delta x_{qj})^2 + (R_{jn} - I_{qn}\sin k_n\Delta x_{qj} - R_{qn}\cos k_n\Delta x_{qj})^2},
\end{aligned}
\tag{A.5}
$$

where $I_{jn} = image(B_{jn})$ and $R_{jn} = real(B_{jn})$ are the imaginary and real part of the complex FFT coefficient B_{jn}, and similarly $I_{qn} = image(B_{qn})$, $R_{qn} = real(B_{qn})$ the imaginary and real part of the complex coefficient B_{qn}. After the spectra of the incident and reflected waves obtained according to equation A.5, we obtain the reflection coefficient $C_{rw} = |a_{Rn}|/|a_{In}|$ on the fundamental wave frequency when $f_n = f_w$. Generally, the positions of wave gauges are recommended to be at least 0.2λ (wavelength) away from both the test structure and wave paddle in regular wave tests and the distance between each pair of gauges is supposed to be in the range of $0.05\lambda < \Delta x_{qj} < 0.45\lambda$. As the positions of the wave gauges remain constant for all

f_w [Hz] \ ϵ	0.02	0.04	0.06	0.08	0.10	0.12	0.14	0.16	0.18	0.20	0.22	0.24	0.28	0.32
0.5	-	0.18	0.11	0.06	-	-	-	-	-	-	-	-	-	-
0.6	-	0.08	0.08	0.08	0.07	-	-	-	-	-	-	-	-	-
0.7	-	0.21	0.10	0.09	0.09	0.09	0.09	0.08	0.08	0.08	0.11	0.13	-	-
0.8	-	0.03	0.02	0.01	0.02	0.02	0.03	0.03	0.05	0.06	-	0.05	-	-
0.9	-	0.02	0.02	0.02	0.03	0.03	0.04	0.05	0.06	0.06	-	0.07	0.06	-
1.0	-	0.02	0.04	0.05	0.05	0.05	0.04	0.04	0.03	0.03	-	0.03	0.07	-
1.05	-	0.05	0.08	0.08	0.08	0.08	0.05	0.05	0.06	0.07	-	0.10	0.14	0.18
1.1	-	0.03	0.03	0.04	0.05	0.06	0.05	0.02	0.01	0.02	0.05	0.07	0.08	-
1.2	-	-	0.08	-	0.06	-	0.05	-	0.05	-	0.06	-	-	-
1.3	-	0.21	0.18	0.16	0.15	0.14	0.13	0.10	0.08	0.08	-	0.16	0.25	0.25
1.4	-	0.10	0.12	0.16	0.22	0.23	0.23	0.23	0.09	0.12	-	0.08	0.12	0.06
1.5	-	0.10	0.09	0.11	0.09	0.10	0.12	0.13	0.15	0.15	-	0.16	0.19	0.16
1.6	-	0.42	0.38	0.33	0.29	0.23	0.16	0.07	0.08	0.13	-	0.25	0.26	0.09
1.7	-	0.09	0.08	0.09	0.12	0.14	0.16	0.14	0.12	0.14	-	0.18	-	-
1.8	0.05	0.04	0.05	0.08	0.14	0.18	0.16	0.16	0.15	0.15	-	0.12	0.09	0.09

Table A.2.1: Reflection coefficient C_{rw} of the fundamental wave frequency for all wave conditions. The calculations are based on approach 1, where the condition $\sin k_n \Delta xqj = 0$ is satisfied. In cases where the condition fails to be satisfied, we use approach 2 as an alternative). The values of $C_{rw} \leq 0.05$ are marked by Green, those of $0.10 \leq C_{rw} \leq 0.20$ are marked by light red, and of $C_{rw} \geq 0.20$ are marked by bright red.

wave conditions, there are instances where the distance between the wave gauges fails to meet the requirement of the approaches previously introduced, rendering the analysis ineffective. Overall, we primarily use the first method for most cases. However, in situations where the gauge distance fails to satisfy the requirements, we resort to the second approach and selected the pair(s) of gauges that satisfy its working range. Also, when using the time series to conduct the analysis, we leave out the time it takes for the reflected waves to reach the first wave gauges (closest to the wave maker) for one complete trip. The reflection coefficient as a function of wave steepness for different frequencies is plotted in figure A.2.1. The reflection coefficient of all wave conditions is given in table A.2.1.

From the figure and the table, we observe that the reflection coefficients for frequency ranging from f =0.8 to 1.2 Hz are generally smaller than 5%, while those in the range of f = 0.5 to 0.7 Hz are slightly larger with some over 10%. For frequencies ranging from f=1.3 to 1.8 Hz the reflection coefficients are notably larger, mostly beyond 10% and some even over 20%. The reflection coefficient does not vary much with the wave steepness except for very low and very high wave steepness. In the case of very low wave steepness, the wave amplitude is too small to be accurately measured by the wave gauges. On the other hand, for very steep waves, we could even observe the beaches moving during wave generation which undoubtedly

affects its absorbing efficiency.

A.2.2 1/2 wave height

To analyze the wave heights under different wave conditions, we examine the time history measured by the wave gauges. There is a delay between the generation of the waves by the wave-maker and their arrival at the gauges. Therefore, we begin our data analysis from a specific time, t_0, which is calculated as $t_0 = 25T_w + x_g/c$, where x_g represents the x position of the wave gauges, c is the wave celerity (calculated as w/k with w being the wave round frequency and k being the wave number). This starting time allows us to disregard the initial transient period. Next, we evaluate the wave height by calculating the difference between the crest and trough wave elevations. This is done by conducting up zero-crossing analysis on the time history data. We then average the wave height over a period of 120 T_w to obtain a representative value. In order to gain a comprehensive understanding of the wave characteristics within the flume, we examine half of the wave height as a function of the wave gauges positions for various wave steepness and frequency combinations shown in figure A.2.2. Furthermore, we calculate the characteristic 1/2 height, denoted as $\overline{a}_g$, by averaging the 1/2 height measured at all seven wave gauges. This characteristic 1/2 wave height is then analyzed as a function of wave steepness for different wave frequencies, which is present in figure A.2.3. The formula for calculating is given by $\bar{a}_g = \frac{1}{7}\sum_{i=1}^{7} a_{gi}$, in which a_{gi} is the 1/2 wave height examined in the i-th wave gauges. To ensure clarity and focus on key results, we present a subset of the data obtained. Specifically, we display results for frequencies f =0.5, 0.7, 0.9, 1.1, 1.5, 1.7 Hz, and wave steepnesses ka_w = 0.06, 0.10, 0.18, 0.24. Table A.2.2 gives the measured 1/2 wave height for all wave conditions. To evaluate the position variation, we calculate the relative Standard deviation of 1/2 wave height measured by the gauges and present it in table A.2.3. The standard deviation is calculated by $\delta_{a,g} = \sqrt{\frac{\sum_{i=1}^{7}(a_{gi}-\bar{a}_g)^2}{7-1}}$.

It deserves mentioning that in our experiments, we have limited the wave height up to 0.1 m to prevent the waves from flapping over the wave gauges. As a result, for f=0.5 Hz, we only have three data points available. From figure A.2.2, it is found that, compared to the input incident wave amplitude, the actual 1/2 wave height is generally smaller and varies with wave frequency and steepness. Specifically, for frequencies in the range of f=0.5 to 1.1 Hz, the

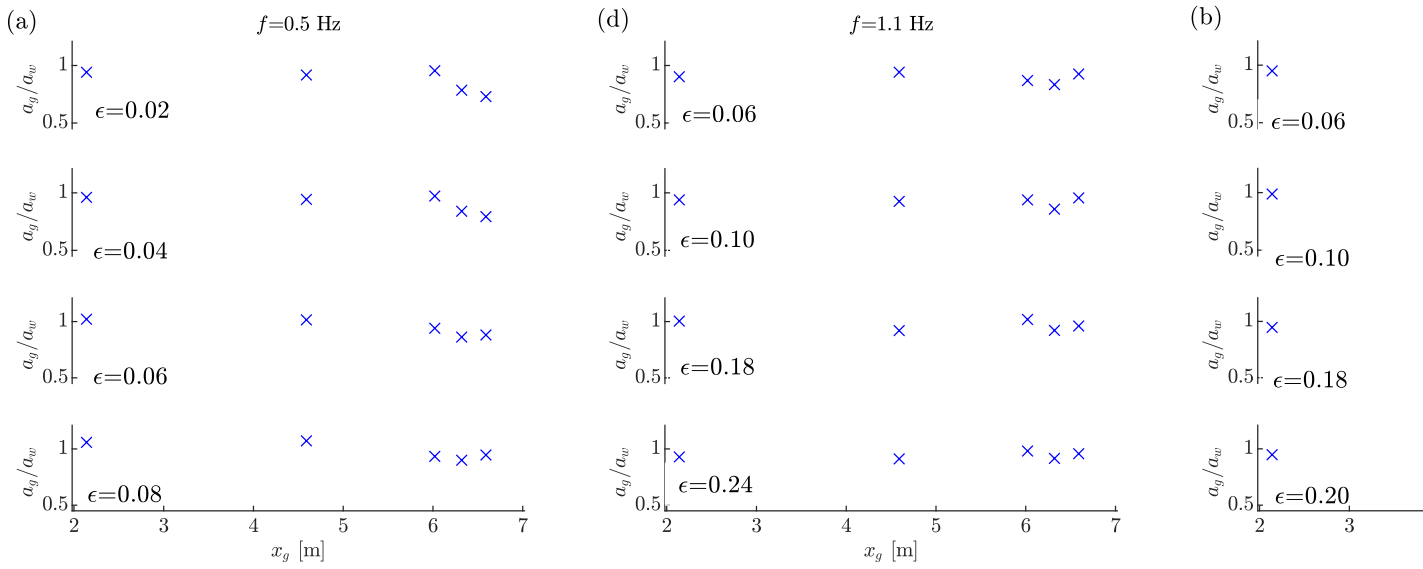


Figure A.2.2: Measured gauge 1/2 wave heights as a function of gauge positions in x axis for different wave steepnesses and wave frequencies. a_g is the examined 1/2 wave heights based on time histories of wave gauges and a_w is the input wave amplitude set to the wavemaker system.

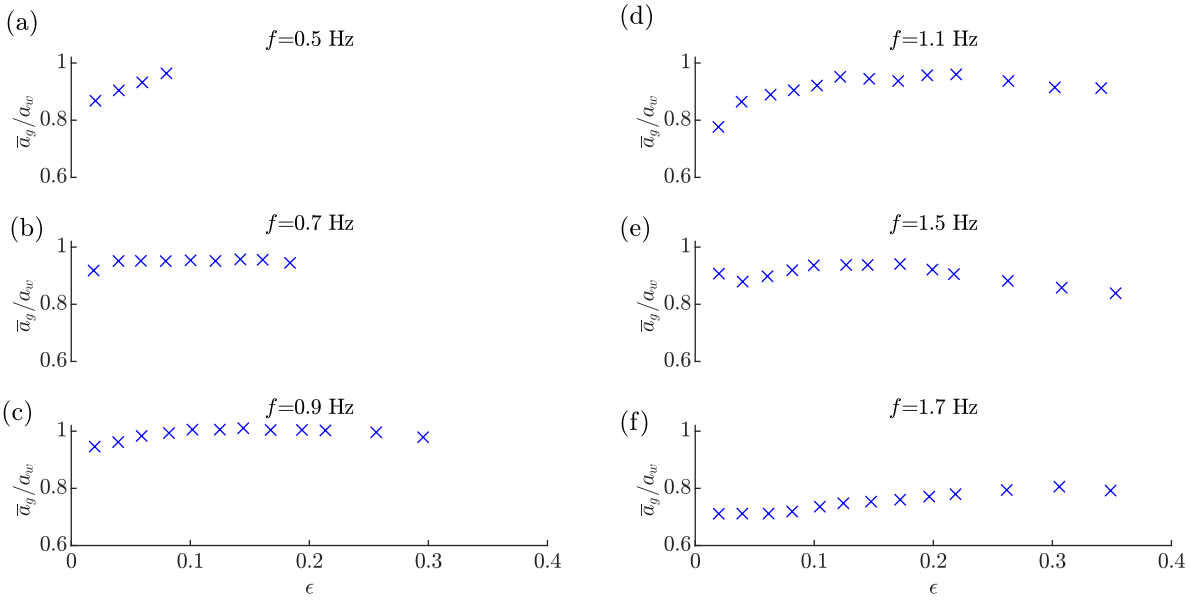


Figure A.2.3: 1/2 Wave heights averaged over all wave gauges as a function of wave steepness ϵ for different wave frequencies. $\overline{a}_g$ is the 1/2 wave heights averaged over a_g of 7 wave gauges and a_w is the input wave amplitude set to the wavemaker system.

f_w [Hz] \ ϵ	0.02	0.04	0.06	0.08	0.10	0.12	0.14	0.16	0.18	0.20	0.22	0.24	0.28	0.32
0.5	0.87	0.90	0.93	0.96	-	-	-	-	-	-	-	-	-	-
0.6	1.09	1.09	1.10	1.11	1.10	-	-	-	-	-	-	-	-	-
0.7	0.93	0.95	0.95	0.95	0.95	0.95	0.96	0.96	0.94	0.80	0.59	-	-	-
0.8	0.95	0.97	0.98	0.99	1.00	1.00	1.00	1.00	1.00	1.00	-	0.62	-	-
0.9	0.95	0.96	0.98	0.99	1.01	1.01	1.01	1.00	1.00	1.00	-	1.00	0.98	-
1.0	0.80	0.91	0.95	0.97	0.97	0.99	0.99	0.99	0.98	0.98	-	0.96	0.95	-
1.05	-	0.88	0.96	0.94	0.98	0.96	0.97	0.95	0.98	0.97	-	0.95	0.97	0.94
1.1	0.78	0.86	0.89	0.90	0.92	0.95	0.94	0.94	0.96	0.96	-	0.94	0.91	0.91
1.2	0.81	-	0.95	-	0.98	-	1.01	-	1.01	-	1.03	-	-	-
1.3	0.95	0.99	1.00	0.99	0.99	0.98	0.95	0.94	0.90	0.91	-	0.86	0.83	0.80
1.4	0.69	0.71	0.76	0.77	0.79	0.80	0.82	0.83	0.86	0.86	-	0.89	0.94	0.93
1.5	0.91	0.88	0.90	0.92	0.94	0.94	0.94	0.94	0.92	0.91	-	0.88	0.86	0.84
1.6	0.83	0.78	0.78	0.79	0.82	0.82	0.84	0.85	0.86	0.87	-	0.89	0.88	0.87
1.7	0.71	0.71	0.71	0.72	0.74	0.75	0.75	0.76	0.77	0.78	-	0.79	0.81	0.79
1.8	0.75	0.76	0.77	0.77	0.78	0.79	0.79	0.79	0.79	0.79	-	0.79	0.79	0.80

Table A.2.2: 1/2 wave heights averaged over all wave gauges $\overline{a}_g/a_w$ for all wave frequencies f_w and wave steepness ϵ. The values of $0.95 \leq \overline{a}_g/a_w \leq 1.05$ are marked by Green, those of $0.8 \leq \overline{a}_g/a_w \leq 0.9$ and $1.1 \leq \overline{a}_g/a_w \leq 1.2$ are marked by light red, and of $\overline{a}_g/a_w \leq 0.8$ are marked by bright red.

f_w [Hz] \ ϵ	0.02	0.04	0.06	0.08	0.10	0.12	0.14	0.16	0.18	0.20	0.22	0.24	0.28	0.32
0.5	0.10	0.08	0.07	0.07	-	-	-	-	-	-	-	-	-	-
0.6	0.07	0.05	0.05	0.04	0.03	-	-	-	-	-	-	-	-	-
0.7	0.14	0.05	0.04	0.04	0.05	0.04	0.04	0.05	0.02	0.18	0.19	-	-	-
0.8	0.13	0.03	0.03	0.04	0.05	0.06	0.06	0.06	0.06	0.06	-	0.08	-	-
0.9	0.14	0.02	0.02	0.02	0.03	0.03	0.04	0.04	0.04	0.05	-	0.06	0.04	-
1.0	0.13	0.03	0.03	0.04	0.04	0.03	0.04	0.04	0.03	0.03	-	0.02	0.03	-
1.05	-	0.05	0.06	0.06	0.06	0.05	0.04	0.04	0.04	0.05	-	0.06	0.07	0.06
1.1	0.09	0.03	0.04	0.03	0.04	0.04	0.05	0.03	0.04	0.03	-	0.03	0.02	0.01
1.2	0.24	-	0.18	-	0.17	-	0.15	-	0.12	-	0.14	-	-	-
1.3	0.31	0.29	0.27	0.25	0.24	0.24	0.23	0.21	0.20	0.20	-	0.19	0.18	0.17
1.4	0.19	0.18	0.19	0.19	0.18	0.18	0.18	0.17	0.17	0.16	-	0.17	0.18	0.14
1.5	0.17	0.17	0.18	0.18	0.18	0.18	0.17	0.15	0.13	0.14	-	0.11	0.08	0.09
1.6	0.14	0.11	0.12	0.11	0.09	0.08	0.08	0.06	0.07	-	0.07	0.06	0.09	0.09
1.7	0.13	0.11	0.09	0.09	0.09	0.09	0.08	0.08	0.07	0.07	-	0.05	0.05	0.07
1.8	0.20	0.18	0.16	0.15	0.13	0.10	0.09	0.08	0.08	0.09	-	0.09	0.09	0.07

Table A.2.3: Gauge variation: Relative standard deviation of 1/2 wave heights examined over all wave gauges $\delta_{a,g}/a_w$ for all wave frequencies f_w and wave steepness ϵ. The values of $\delta_{a,g}/a_w \leq 5\%$ are marked by Green, those of $10\% \leq \delta_{a,g}/a_w \leq 20\%$ are marked by light red, and of $\overline{a}_g/a_w \geq 20\%$ are marked by bright red.

values of a_g/a_w at positions closer to the wave maker are generally larger than those located near the beaches. This behavior may be attributed to wave energy loss. However, for waves of f=1.5 to f=1.8 Hz, it is the opposite that the values near the wave maker are smaller than those near the beaches, which may be due to relatively larger wave reflections (see §A.2.1). The variation of wave gauges in table A.2.3 provides clearer evidence that for waves of f=0.7 to 1.3 Hz, the variation between wave gauges is small whereas for $f \geq 1.4$Hz, the variation becomes significant.

Regarding the value of $\overline{a}_g/a_w$, according to table A.2.2, for frequencies ranging from f=0.7 to 1.3 Hz, the measured wave is generally very similar to the input theoretical values whereas for frequencies $f \geq 1.4$ Hz, significant wave deviation from the theoretical value can be observed. This can be partly explained by the relatively larger reflection coefficient. From figure A.2.3, we can see that such deviation depends on wave steepness. For either very small or very steep waves, the deviation is more significant.

Besides, we observed peculiar wave behavior for wave frequencies of $f_w = 1.2$ Hz and 1.3 Hz. These waves exhibited unusual characteristics that deviated from regular wave behaviors as the wavelengths of these waves were approximately 1.08 m and 0.9238 m, respectively, which are close to the width of the tank 1.1 m. We suspect that this anomalous wave behavior results from resonance occurring due to the interaction between the waves and the tank width. From figure A.2.4, it is evident that the time history of the wave elevation is unstable. The wave signal exhibits significant variations across different wave gauge positions, indicating non-uniformity and inconsistency. It is, hence, recommended to avoid generating monochromatic regular waves with these frequencies for accurate and reliable experimentation.

A.2.3 Wave frequency

To examine the wave frequencies, we analyze the time signal in frequency domain and utilize the discrete Fourier transform analysis. Prior to conducting a proper discrete Fourier transform analysis in MATLAB, we perform signal pre-processing on the wave elevation time history data obtained from the wave gauges. We first remove the initial transient effects and discard the first 25 T_w of the time history. Then, we mirror the signal after conducting the up-zero-crossing analysis to ensure its periodicity. Once the pre-processing is complete, we use the fft function

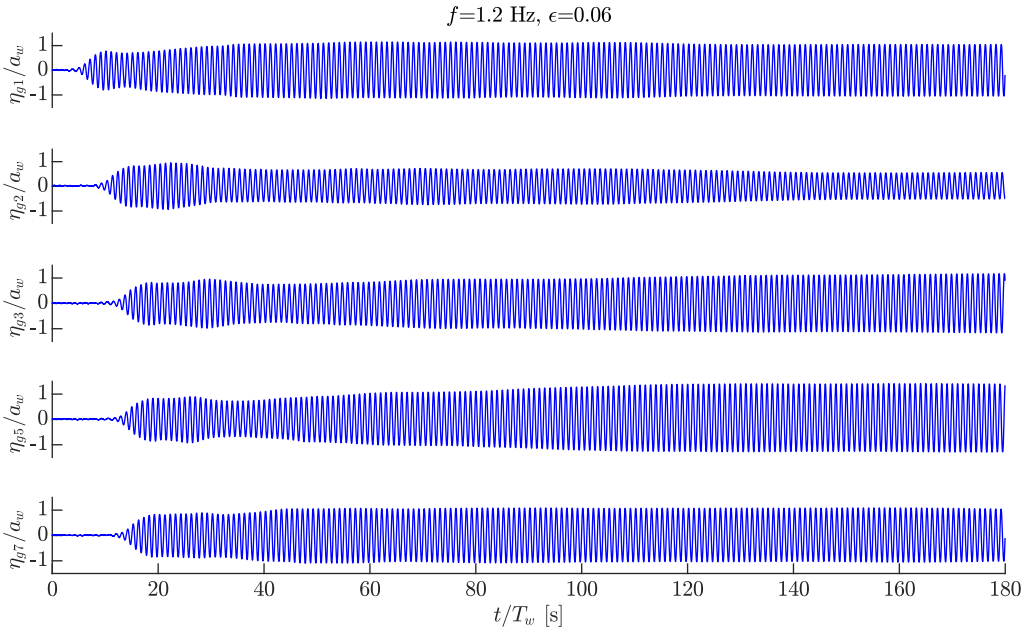


Figure A.2.4: Time history of the surface elevation collected by different wave gauges for the wave of $f = 1.2$ Hz and ka_w=0.06. The surface elevation from the i-th wave gauges is denoted as $\eta_{gi}(i = 1, 2, 3, 5, 7)$ and a_w is the input wave amplitude set to the wavemaker system.

in MATLAB and take only half of the length of the results. By identifying the frequency that corresponds to the maximum absolute value of the result, we determine the peak frequency of the measured signal, which corresponds to the frequency of the wave. Applying this procedure to the signals measured by all wave gauges for different wave conditions, we find a remarkably high agreement between the measured frequencies and the input frequencies. Specifically, the data demonstrate the average measured frequency $\bar{f}_g$ over all wave gauges is equal to the input frequency f_w for all wave conditions. Mathematically, this can be expressed as $\overline{f}_g/f_w$=1.00. Here, $\bar{f}_g = \frac{1}{7}\sum_{i=1}^{7} f_{gi}$ and f_{gi} is the wave frequency examined in the i-th wave gauges. The maximum relative standard variation of the measured frequencies among different wave gauges, denoted as $\delta_{f,g}/f_w$, is found to be 0.0029. This value is obtained by $\delta_{f,g} = \sqrt{\frac{\sum_{i=1}^{7}\left(f_{gi}-\bar{f}_g\right)^2}{7-1}}$.

A.2.4 Time variation

To gain a more comprehensive understanding of how waves evolve over time within the flume, we evaluate the time variation in wave elevation. This analysis entails dividing the entire time duration of $150T_w$ into multiple sections, denoted as N. We then calculate the average 1/2 wave height of each section to track changes in the wave signal over time and to identify when

the wave reaches a stable state. Within our analysis, we focus on gauge 3 positioned at the middle of the tank ($x_{g3} = 6.02$ m, $y_{g3} = 0.0$ m) as the representative signal. Additionally, we explore differences among different wave gauges. The average 1/2 wave heights of each section are plotted against time, normalized by the wave period T_w, with specific frequencies and wave steepnesses, shown in figure A.2.4. To understand the time variation, we plot the time t_0 taken by waves to travel from wavemaker to gauge 3. We also mark the time t_f required for reflected waves to complete a round trip and reach gauge 3. Accounting for the transient time required for the wavemaker to generate constant waves, we observe that the signal becomes stable shortly after t_f when the reflected waves hit gauge 3.

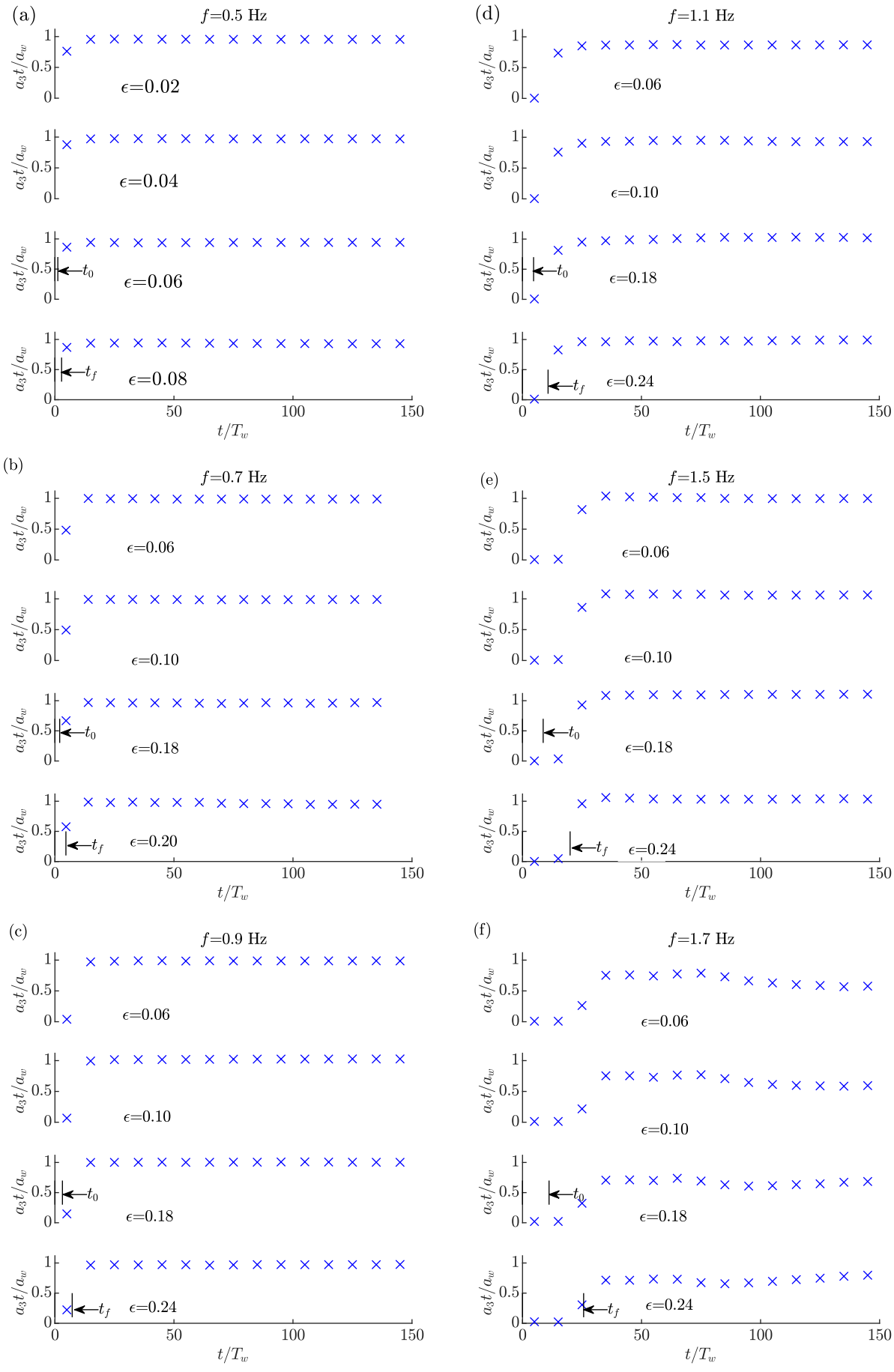

(a)
f=0.5 Hz
ϵ=0.02
ϵ=0.04
ϵ=0.06
ϵ=0.08
(b)
f=0.7 Hz
ϵ=0.06
ϵ=0.10
ϵ=0.18
ϵ=0.20
(c)
f=0.9 Hz
ϵ=0.06
ϵ=0.10
ϵ=0.18
ϵ=0.24
(d)
f=1.1 Hz
ϵ=0.06
ϵ=0.10
ϵ=0.18
ϵ=0.24
(e)
f=1.5 Hz
ϵ=0.06
ϵ=0.10
ϵ=0.18
ϵ=0.24
(f)
f=1.7 Hz
ϵ=0.06
ϵ=0.10
ϵ=0.18
ϵ=0.24
$a_3 t/a_w$
t_0
t_f
t/T_w
0
0.5
1
50
100
150

Figure A.2.4 *(previous page)*: Time variation of the 1/2 wave height over N sections for different wave steepness and wave frequencies based on signals collected by gauge 3, in which N=15. This means the 1/2 wave height of each section is evaluated and averaged by 10 T_w. The scatter data corresponds to the mean value of the time and 1/2 wave height evaluated on the corresponding sections. Time for the waves generated by the wave maker first reach gauge 3, denoted t_0, is calculated by $t_0 = x_{g3}/c$, where $c = w/k$ is the wave celerity, w the wave angular frequency and k wave number. Time for the reflected wave to make a round trip back the gauge 3, denoted by t_f, is calculated by $t_f = t0 + x_f/c$, where $x_f = (9.945 - 6.02) * 2$ m is the traveling distance from the position of gauge 3, hitting the beaches and bouncing back.

To explore time variation discrepancies across different horizontal positions, we compare data collected by various wave gauges for different frequencies in figure A.2.5, in which $\epsilon = 0.10$ is chosen as the representative wave steepness for plotting. As indicated in figure A.2.5, the smallest time variation difference between different gauges is observed at $f = 0.9$ Hz, where gauges exhibit a consistent time-dependent pattern. For frequencies f =0.5, 0.7 and 1.1 Hz, signals between different wave gauges manifest similar time-dependent patterns, albeit stable at slightly varying values. This variation can be attributed to the corresponding reflection analysis and gauge variations for each frequency, with energy dissipation having a minor impact due to the small flume size. Referring to figure A.2.1 (or table A.2.1) and figure A.2.2 (or table A.2.3), waves with a frequency of f =0.9 Hz exhibit a small overall reflection coefficient, leading to rapid stabilization and minimal gauge-based variations. Waves with frequencies f=0.5, 0.7 and 1.1 Hz maintain reasonably low reflection coefficients and gauge variations. In contrast, for f =1.5 Hz, signals in different wave gauges display distinct time-variant patterns and end in a significantly different stable value. This behavior can be attributed to a large reflection coefficient and gauge variations. Additionally, for f=1.7 Hz, signals across all wave gauges fail to achieve stability and exhibit high time dependency across the evaluated sections. These divergent behaviors of the signals within different wave gauges suggest that, for this wave frequency, even though the reflection coefficient and gauge variation share some similarities with waves of $f = 1.5$ Hz, the signal remains highly unstable over the entire measured 150 T_w period. This instability might be associated with the performance of the wavemaker at such a high frequency.

To evaluate the time variation of the wave more comprehensively, we first determine the number of sections required for the wave to achieve a stable status. It is found that for frequencies ranging from 0.5 Hz to 1.0 Hz, it takes at least 1 section (equivalent to $10T_w$) to reach

f_w [Hz] \ ϵ	0.02	0.04	0.06	0.08	0.10	0.12	0.14	0.16	0.18	0.20	0.22	0.24	0.28	0.32
0.5	0.13	0.15	0.24	0.53	-	-	-	-	-	-	-	-	-	-
0.6	0.13	0.26	0.44	0.48	0.21	-	-	-	-	-	-	-	-	-
0.7	0.94	0.50	0.25	0.39	0.19	0.73	0.52	1.19	0.48	1.44	6.69	-	-	-
0.8	1.16	0.39	0.63	0.18	0.36	0.31	0.24	0.26	0.33	0.88	-	-	-	-
0.9	0.32	0.27	0.15	0.25	0.38	0.19	0.58	0.62	0.24	0.20	-	0.31	2.61	-
1.0	0.35	0.51	0.37	0.15	0.41	0.43	0.87	0.55	1.05	0.51	-	0.69	0.74	-
1.05	-	0.10	0.13	0.24	1.01	0.66	1.27	0.60	0.57	1.51	-	2.07	0.94	0.32
1.1	1.55	1.27	0.26	1.08	0.91	1.27	0.26	1.97	1.99	1.43	0.98	1.23	1.00	-
1.2	6.44	-	11.84	-	13.04	-	13.17	-	12.60	-	13.07	-	-	-
1.3	3.61	2.65	3.18	2.45	2.81	2.39	2.16	4.22	3.09	1.70	-	2.16	3.39	3.64
1.4	3.11	2.54	2.03	2.06	1.37	1.53	2.03	1.52	2.84	1.96	-	0.93	0.98	2.40
1.5	3.20	2.22	1.40	1.22	0.78	0.50	0.66	0.86	0.61	0.71	-	0.87	1.23	0.93
1.6	1.60	1.61	1.23	0.71	0.62	0.89	0.83	0.66	0.92	0.87	-	1.95	1.24	1.07
1.7	8.79	9.23	8.47	8.20	7.77	6.76	5.50	4.66	4.22	3.46	-	4.25	5.40	3.97
1.8	5.83	7.43	7.78	7.78	6.97	5.72	5.38	4.71	4.07	3.97	-	2.80	2.67	1.58

Table A.2.4: Time variation: Relative standard deviation (expressed in units of 100%) of 1/2 wave height examined over different time sections after the signal becomes stable, which is denoted as $\delta_{a,t}/a_w$, for all wave frequencies f_w and wave steepness ϵ. The values of $\delta_{a,t}/a_w \leq 1\%$ are marked by Green, those of $3\% \leq \delta_{a,t}/a_w \leq 5\%$ are marked by light red, and of $\delta_{a,t}/a_w \geq 5\%$ are marked by bright red.

a stable condition. For the frequency of f =1.1 Hz, it requires 2 sections (equivalent to 20 T_w). However, for frequencies between f=1.3 Hz and 1.8 Hz, the waves need 3 sections to stabilize. Notably, waves with a frequency of 1.2 Hz do not achieve a good stable condition within the analyzed time frame (not presented here). To further evaluate the time variation, we calculate the standard deviation of the 1/2 wave height over the remaining sections. Specifically, we focus on data collected by gauge 3 and calculate the standard deviation for sections 4 to 15. The standard deviation is denoted as $\delta_{a,t}$ and is calculate by $\delta_{a,t} = \sqrt{\frac{\sum_{i=4}^{1} 5(a_{ti}-\bar{a}_t)^2}{12-1}}$ where a_{ti} represents the 1/2 wave height evaluated over i-th section, and $\bar{a}_t$ is the mean value of sections 4 to 15. Table A.2.4 gives the standard deviation of the section 1/2 wave heights based on the time signal of gauge 3 for all wave conditions.

It is found that for low frequencies ranging from f=0.5 to 1.1 Hz, the wave signal remains stable with minimal variations over time. However, for high frequencies of f=1.7 to 1.8 Hz, the signal exhibits significant time variations. The nature of this time variation appears to be influenced by wave steepness, but the patterns are not clear.

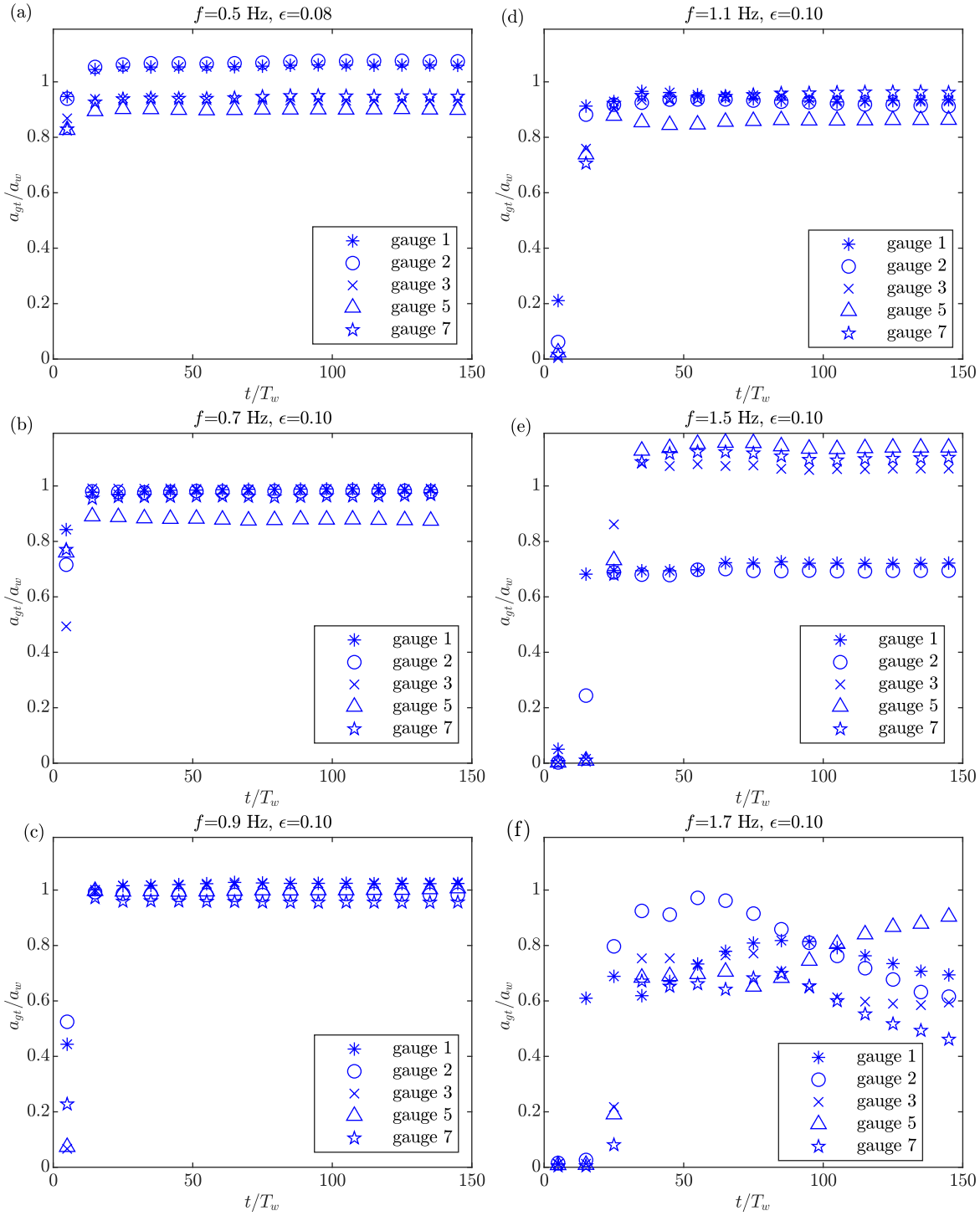


Figure A.2.5: Time variation of the 1/2 wave height over N sections for different wave frequencies when $\epsilon = 0.10$ ($\epsilon = 0.08$ for $f = 0.5$ Hz as this is the largest wave that we have for this frequency). The data is based on signals collected by different wave gauges (data for gauge 4 and gauge 6 are not presented here as they share the same x-location with gauge 3 and gauge 5), in which N=15. This means the 1/2 wave height of each section is evaluated and averaged by 10 T_w. The scatter data corresponds to the mean value of the time and 1/2 wave height evaluated on the corresponding sections.

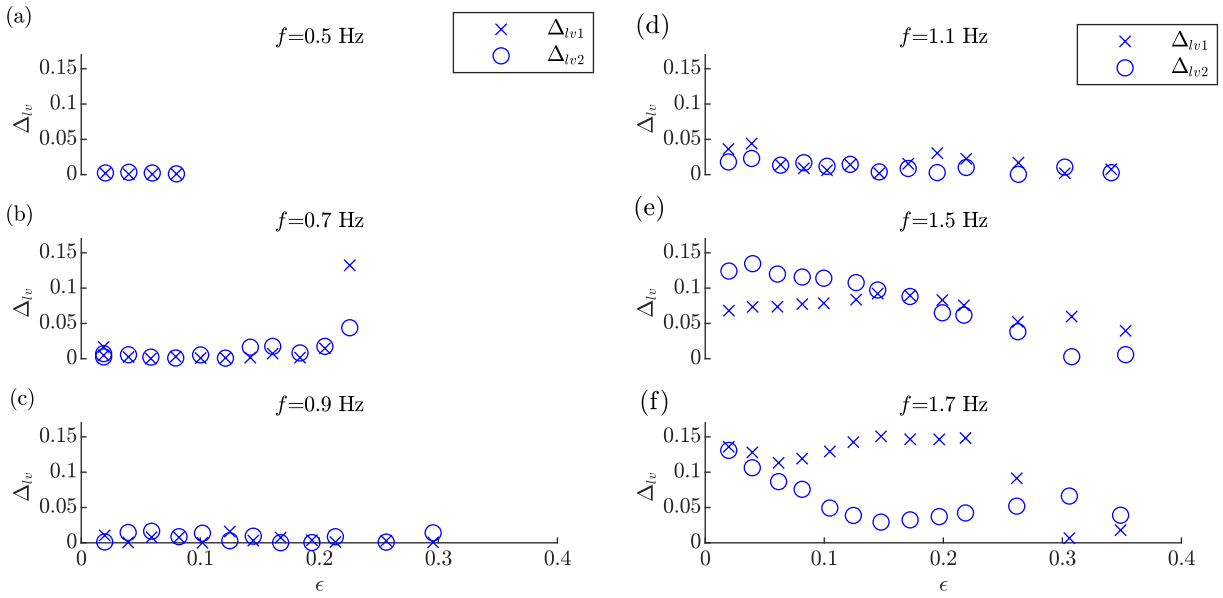


Figure A.2.6: Lateral variations Δ_{lv} as a function of wave steepness for different frequencies based on signals collected by two pairs of gauges 3,4 and gauges 5,6.

A.2.5 Lateral variation

To assess the lateral variation of the flume for unidirectional monochromatic waves, we use the time signal collected by two pairs of wave gauges located at (x_{g3} = 6.02 m,y_{g3} = 0 m); (x_{g4} = 6.02 m, y_{g4} = 0.275 m) and (x_{g5} = 6.32 m, y_{g5} = 0 m); (x_{g6} = 6.32 m, y_{g6} = 0.275 m) respectively. As suggested by §A.2.3, the measured frequencies show little deviation from the input frequencies and the variation among different gauges is minimal. Therefore, we primarily focus on the 1/2 wave height variation in this analysis. To evaluate the lateral variations at different longitudinal positions, we calculate two relative difference values $\Delta_{lv1} = |(a_{w3} - a_{w4})|/((a_{w3} + a_{w4})/2)$ and $\Delta_{lv2} = |(a_{w5} - a_{w6})|/((a_{w5} + a_{w6})/2)$, in which ($a_{wj}$ denotes the time-averaged 1/2 wave height measured by gauge j. We plot the Δ_{lv} values as a function of wave steepness for different wave frequencies in figure A.2.6. This provides a visual representation of the 1/2 wave height variation at different longitudinal positions. Furthermore, we present the specific values of Δ_{lv1} and Δ_{lv2} for all wave conditions in table A.2.5 and table A.2.6, respectively.

It is found, according to figure A.2.6, when wave frequency is low, like for waves of frequencies in the range of f=0.5 to 1.1 Hz, the lateral variation of row 1 and of row 2 is similar and the overall variation is small (smaller than 5%), which does not vary much with the wave steepness. However, for higher frequencies of f=1.5 and 1.7 Hz, the lateral variation of row

f_w [Hz] \ ϵ	0.02	0.04	0.06	0.08	0.10	0.12	0.14	0.16	0.18	0.20	0.22	0.24	0.28	0.32
0.5	0.19	0.06	0.07	0.11	-	-	-	-	-	-	-	-	-	-
0.6	1.55	0.78	0.15	0.13	0.43	-	-	-	-	-	-	-	-	-
0.7	1.68	0.48	0.25	0.02	0.30	0.10	0.12	0.16	0.73	0.16	1.48	13.23	-	-
0.8	0.76	0.05	0.21	0.60	0.32	0.07	0.26	0.41	0.15	0.30	-	11.06	-	-
0.9	1.04	0.07	0.79	0.77	0.01	1.60	0.32	0.74	0.38	0.10	-	0.28	0.06	-
1.0	0.05	0.59	0.51	1.11	0.25	2.03	0.05	0.04	0.90	0.04	-	0.00	3.34	-
1.05	-	0.06	0.06	0.06	0.06	0.05	0.04	0.02	0.03	0.05	-	0.03	0.05	0.06
1.1	3.63	4.41	1.40	0.90	0.61	1.40	0.20	1.54	3.05	2.25	1.70	0.20	0.76	-
1.2	2.15	-	5.75	-	5.43	-	6.00	-	5.34	-	9.34	-	-	-
1.3	26.80	28.54	25.70	21.46	20.75	19.92	17.38	17.51	14.77	10.39	-	8.46	5.51	5.45
1.4	1.98	1.96	1.37	0.06	2.63	5.14	7.84	11.03	10.00	14.46	-	17.43	16.45	10.23
1.5	6.81	7.34	7.36	7.73	7.86	8.37	9.22	8.95	8.31	7.56	-	5.22	5.97	3.96
1.6	12.94	10.36	12.37	11.18	9.59	8.41	8.16	4.79	3.97	2.51	-	1.75	4.29	5.81
1.7	13.60	12.80	11.33	11.92	12.93	14.25	15.08	14.67	14.65	14.83	-	9.13	0.66	1.79
1.8	17.80	20.71	19.64	23.09	22.13	17.46	16.41	13.61	11.66	10.49	-	4.53	1.36	6.26

Table A.2.5: Lateral variations of the first pair of gauge 3,4 Δ_{lv1} (expressed in units of 100%) for all wave frequencies f_w and wave steepness ϵ. The values of Δ_{lv1} ≤1% are marked by Green, those of 3% ≤ Δ_{lv1} ≤ 5% are marked by light red, and of Δ_{lv1} ≥ 5% are marked by bright red.

f_w [Hz] \ ϵ	0.02	0.04	0.06	0.08	0.10	0.12	0.14	0.16	0.18	0.20	0.22	0.24	0.28	0.32
0.5	0.25	0.33	0.24	0.11	-	-	-	-	-	-	-	-	-	-
0.6	0.06	0.60	0.31	0.10	0.02	-	-	-	-	-	-	-	-	-
0.7	0.72	0.26	0.56	0.23	0.10	0.54	0.08	1.64	1.75	0.82	1.75	4.39	-	-
0.8	1.02	0.11	0.48	0.38	0.07	0.53	0.65	0.75	0.39	0.39	-	2.68	-	-
0.9	0.12	1.46	1.64	0.86	1.36	0.29	0.94	0.01	0.04	0.86	-	0.10	1.41	-
1.0	0.35	0.82	0.68	1.14	1.05	2.16	1.33	0.59	0.47	1.73	-	1.60	0.46	-
1.05	-	0.04	0.04	0.04	0.03	0.01	0.01	0.03	0.02	0.01	-	0.04	0.03	0.02
1.1	1.80	2.29	1.34	1.69	1.18	1.46	0.39	0.87	0.29	1.02	0.05	1.07	0.28	-
1.2	23.36	-	20.34	-	19.41	-	18.27	-	15.62	-	15.37	-	-	-
1.3	24.26	19.48	16.40	14.42	11.82	8.91	6.62	2.09	0.90	2.98	-	8.95	8.45	10.39
1.4	12.64	14.41	15.27	18.29	18.77	19.83	19.55	17.51	16.30	13.81	-	8.72	7.32	1.89
1.5	12.42	13.46	11.99	11.57	11.40	10.78	9.74	8.81	6.50	6.17	-	3.83	0.29	0.57
1.6	5.04	5.19	6.72	7.15	5.50	4.45	3.31	0.47	0.11	2.38	-	4.77	5.23	5.45
1.7	13.08	10.63	8.66	7.58	4.92	3.87	2.94	3.25	3.71	4.23	-	5.19	6.62	3.91
1.8	38.39	30.22	23.59	18.49	9.65	2.71	1.18	7.75	11.82	14.83	-	18.97	18.71	11.50

Table A.2.6: Lateral variations of the second pair of gauge 5,6 Δ_{lv2} (expressed in units of 100%) for all wave frequencies f_w and wave steepness ϵ. The values of Δ_{lv2} ≤1% are marked by Green, those of 3% ≤ Δ_{lv2} ≤ 5% are marked by light red, and of Δ_{lv2} ≥ 5% are marked by bright red.

1 differs from that of row 2 and they are generally larger than 5%. And the lateral variation changes with wave steepness. From table A.2.5 and A.2.6, it is further demonstrated that for lower frequencies like f=0.5 to 1.1 Hz, the lateral variation is small whereas for high frequency, the lateral variation becomes significantly large (over 20%).

A.2.6 Repeatability

To assess the repeatability of the waves in the flume and evaluate the variations in the data obtained from the wave gauges, we conduct repeat experiments as described earlier and choose the 1/2 wave heights averaged among all wave gauges $a_{wr} = \sum_{j=1}^{7} a_{wj}/7$ as our evaluating target

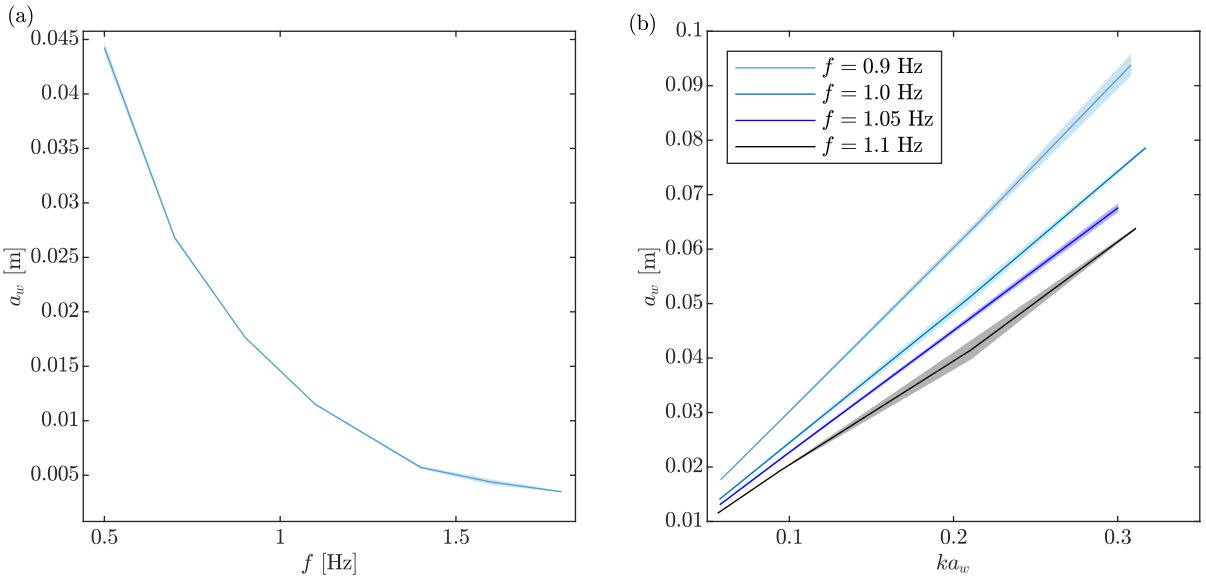


Figure A.2.7: Confidence bands on the 1/2 wave heights (a) as a function of wave frequency for ka_w=0.06 and (b) as a function of wave steepness for waves of $f = 0.9, 1.0, 1.05, 1.1$ Hz. Each case is obtained by 5 repeats with its mean value denoted by the solid lines. The error bars correspond to two standard deviations on either side of the mean as shown in the shading area.

here. Specifically, we denote a_{wrm} as average 1/2 wave heights of the m-repeat (m=1,2,...,5), then we calculate its mean value and standard variation by:

$$\begin{aligned} \bar{a}_{wr} &= \tfrac{1}{5}\sum_{m=1}^{5} a_{wrm} \\ \delta_{wr} &= \sqrt{\frac{\sum_{m=1}^{5}(a_{wrm}-\bar{a}_{wr})^2}{5-1}}, \end{aligned} \tag{A.6}$$

Figure A.2.7 gives the confidence bands for all the repeat experiments. It is shown, by figure A.2.7 (a), that for low wave steepness ka_w=0.06, the wave is highly repeatable and the repeatability gets slightly reduced for high frequency. According to figure A.2.7 (b) that generally, the repeatability gets reduced for intermediate and high wave steepness.